University of Sussex

High Voltage Breakdown in the Ramsey Cell of the CryoEDM experiment.

- An experimental study of some relevant parameters.

Andrew John Davidson

Submitted for the degree of Doctor of Philosophy
School of Mathematical and Physical Sciences
University of Sussex
September 2011
Supervisors: M Hardiman and P G Harris

Declaration

I hereby declare that this thesis describes my own original work, except where explicitly stated. No part of this work has previously been submitted, either in the same or different form, to this or any other University in connection with a higher degree or qualification.

Signed: …… Date: …….

Andrew John Davidson 30/09/2011

UNIVERSITY OF SUSSEX

ANDREW JOHN DAVIDSON, DOCTOR OF PHILOSOPHY

HighVoltage Breakdown in the Ramsey Cell of the CryoEDM experiment.

- An experimental study of some relevant parameters.

Abstract

A pressure cell apparatus has been designed, constructed and commissioned to measure the dielectric strength of liquid helium as a function of pressure for various temperatures in He I and He II. Breakdown experiments between a set of stainless steel parallel plate Rogowski profile electrodes with a separation of 1.27 mm have been made for temperatures ranging between 1.7 K to 4.2 K and applied pressures of SVP to ~ 2.2 bar. All pressure data taken above and below the λ-point exhibit similar features. At low pressure, near the SVP, breakdown voltage rapidly increases with applied pressure. This behaviour is linear for all temperatures and has an average gradient of 0.176 ± 0.0096 $kVtorr^{-1}$. This regime changes at a pressure dependant kink point. Above this point a more gradual increase in breakdown voltage with pressure is observed. Data for all temperatures normalised to 50 kV and 1200 torr have an average gradient of 0.01693 ± 0.00092 $kVtorr^{-1}$ with an average intercept of 29.69 ± 0.88 kV. A linear relationship is observed between the normalised kink pressure and the density of the helium (-34.4 ± 1.4 kg $m^{-3}torr^{-1}$ and intercept of 5130 ± 200 kg m^{-3}). The normalised kink pressure as a function of SVP produces a linear relationship with a gradient consistent with unity (0.97 ± 0.04 $torr^2$ with an intercept of 88 ± 13 torr). High voltage breakdown initiating at the cathode triple junction (CTJ) has been investigated in He I, He II and LN_2 under SVP. Breakdown tests were made between parallel plate Rogowski profile electrodes with an Al_2O_3 ceramic spacer between them. Chips, cracks and tracks across the ceramic have been observed. LN_2 breakdown tests cause catastrophic damage. Calculations of the E-fields in any gap between the ceramic and electrode show E-field enhancements of up to a factor of ~ 4.5. The end of a ceramic sample was sputtered with Gold in an attempted to prevent any E-field in the gap. This work has been carried out within the UK CryoEDM Collaboration and was aimed at understanding better the parameters which will ultimately limit the E-field in the Ramsey Cell of the main experiment.

Acknowledgments

The work carried out in this thesis has only been possible because of the huge amount of help and support that has been provided by a number of individuals.

I would like to thank both my supervisors Mike Hardiman and Phillip Harris for the huge amount of time and effort they have given me through the course of this DPhil.

I benefited enormously from the vast experimental experience of the team here at Sussex especially Mike Hardiman, Ian Wardell, Christopher Townsley and James Karamath. For all the help, discussion and advice I am truly thankful.

The PC apparatus worked perfectly. This is down to the enormously skilled team that made it. To John Knight, Bob Woodhouse, Alan Mayers and Keith Nie thank you for your first rate job.

Throughout my DPhil I have had a huge amount of help, support and assistance from some top undergraduate students. In particular I need to give a massive thank you to Debbie Hill, Lee Suttle and Lydia Munday. Their enthusiasm hard work and commitment helped get us through those many late nights in the Lab. I would also like to thank Markus Vogt and James Sinclair for their help.

I would like to thank all members of the Sussex CryoEDM collaboration for the help and guidance they have provided over the course of this DPhil. In particular I would like to thank Simon Peeters, Mike Pendelbuery, Peter Smith and Dave Shiers for their expertise and their friendly approachable nature.

When working on the CryoEDM experiment at the ILL I was always welcomed and encouraged to get stuck in. For help in understanding the apparatus I would like to thank Maurits van der Grinten, Keith Green, Vishal Francis, Sergei Ivanov, Sergei Balashov, Mark Tucker and Andrei Khazov.

To my fellow DPhils colleagues Kat and Matt thanks for everything over the years.

I would like to thank Chen-Yu Liu from the IUCF for her discussion on the dielectric strength of liquid helium under pressure.

Contents

Contents

Contents

Contents

Contents

Contents

Contents

1 Introduction

A simple cosmological question yet to be explained is why the Universe is made up of matter and not antimatter. Although antimatter can be created in a laboratory or in the upper atmosphere, as a result of a comic shower, there is no evidence of antimatter Planets or Galaxies.

After the big bang some under lying law of nature decided that for every 10^9 particle antiparticle annihilations 1 particle would be left over. To this 1 particle we and our Universe owe our existence. The mechanism capable of producing a matter-dominated Universe is called CP violation. One way of making a direct measurement of CP violation is by measuring the neutron Electric Dipole Moment (nEDM).

Chapter 2 discusses the motivation for carrying out a nEDM experiment. Experimental evidence of previously observed P and CP violation are described. The mechanism for CP violation is outlined along with some predicted values of CP violation. CP violation in the Standard Model (SM) is orders of magnitude below any experimental capabilities thus a direct observation of a nEDM would indicate new physics beyond the SM.

As the neutron is electrically neutral it makes it experimentally favourable to be used as a probe of CP violation. Currently the best place to get neutrons is the Institut Laue-Langevin (ILL). Their 56 MW reactor produces a dense beam of neutrons. The cryogenic neutron electric dipole moment (cryo-edm) experiment takes advantage of this beam. High densities of very low energy ($\leq$ 335 neV, $\leq$ 4 mK) ultracold neutrons (UCN) are produced in the experiment when 8.9 Å (10^{-3} eV, 11 K) cold neutrons from a collimated beam interact with liquid helium at ~ 0.5 K. Once formed UCN can be confined to the experiment. The whole cryo-edm apparatus is submerged in liquid helium at ~ 0.5 K. The Ramsey method of oscillatory fields is then used to manipulate the neutrons.

Chapter 1 Introduction

In chapter 3 the method of conducting a nEDM measurement is given. The physical principles and experimental techniques used in the cryo-edm experiment are reviewed. The Ramsey Cell, which is the main focus of investigation for this thesis, is examined. The Ramsey method of oscillating fields is described which should enable the cryo-edm experiment to reduce the upper limit set on the nEDM by two orders of magnitude down to 10^{-28} ecm.

It is not surprising that the sensitivity of measuring a nEDM is directly proportional to the applied E-field. The work in this thesis investigates the electrostatics of the Ramsey cell in order to increase the E-field across it to a maximum value. Previous work carried out on high voltage breakdown in liquid helium is reviewed in Chapter 4, the main literature review. The parameters that affect the dielectric strength of liquid helium are discussed and all known data taken as a function of pressure in liquid helium are reviewed.

The main investigation of this thesis is to study the effect that pressure has on the dielectric strength of liquid helium. In order to do this, an apparatus had to be designed, manufactured and commissioned that is capable of taking high voltage breakdown measurements in liquid helium as a function of both temperature and pressure. These parameters had to be able to be changed independently. The electrodes used for the measurements were parallel plate electrodes. The high voltage electrode was a Rogowski profile. Great care was taken in the design to ensure the electrodes remained parallel during assembly. This apparatus, the pressure cell (PC), runs in a bath cryostat. It is capable of doing breakdown measurements at temperatures between 1.7 K and 4.2 K and can be pressurised up to a least ~ 2.4 bar. The design of the PC is detailed in chapter 5. The method used to take data using the PC is also outlined.

The cryo-edm experiment has a BeO ceramic tube sandwiched between the electrodes to act as both a spacer and the external walls of the Ramsey cell to trap the neutrons. The

possible effect of this spacer on breakdown has also been investigated using Al_2O_3 ceramic spacers. The point where the electrode surface, liquid helium and Al_2O_3 ceramic meet, the cathode triple junction (CTJ), is generally thought to be the weak point for high voltage breakdown.

A series of experiments have been carried out using parallel plate Rogowski profile electrodes and ceramic tubes to investigate the electrostatics of the CTJ. The electrodes have grooves which are used to locate on Al_2O_3 tube spacer. The groove profiles have been scaled to those of the Ramsey cell electrodes. The grooves help to shield the CTJ.

Two sets of parallel plate Rogowski profile electrodes were used. One set is smaller than the other. The apparatus used for the Al_2O_3 tests is described at the end of chapter 5.

The PC was used to take high voltage breakdown data in liquid helium at temperatures between 1.7 K and 4.2 K and all pressures between the SVP at the relevant temperature and ~ 2.4 bar. As the emphasis is on finding a pressure dependence at constant temperature all other parameters are kept constant. The high voltage breakdown data is presented in chapter 6.

The results of the Al_20_3 ceramic tests are shown in the final section of chapter 6. Measurements were made in He I, He II and LN_2 under SVP.

Analysis of the data from chapter 6 is carried out in chapter 7. Breakdown pressure effect data taken at any constant temperature between 1.7 K and 4.2 K have a similar form; the form of the pressure dependence is the same in He I and He II. The general form displays two distinct regions that change at a temperature-dependent kink pressure. As the pressure is increased above SVP a rapid increase in breakdown voltage is observed. This behaviour increases linearly with pressure to a kink point. As the pressure is increased above the kink point the breakdown voltage again increases linearly with pressure, however this dependence

is much more gradual. Analysis of each temperature showed that the second, gradually increasing, linear region was the same for all temperatures.

The results of CTJ breakdown tests using Al_2O_3 ceramics are also presented and discussed in chapter 7. The most significant discovery from the tests, using the small electrodes, is that high voltage breakdown can damage, chip and catastrophically break the Al_2O_3 ceramics. In general the discharge seems to have initiated from the CTJ. The data taken with Al_2O_3 ceramics between parallel plate electrodes have been compared to data at similar electrode separations without any Al_2O_3 ceramic.

The small electrodes used for the Al_2O_3 ceramic tests have been electrostatically modelled using Opera vector fields. Using the experimentally observed breakdown values the magnitude of the E-field at breakdown has been calculated.

Implications of the data, presented in this thesis, in regards to the cryo-edm experiment are discussed in chapter 8. If the form of the pressure dependence data continues down to 0.5 K then increasing the pressure of the liquid helium in the cryo-edm apparatus could significantly increase the E-field and thus reduces the statistical uncertainty. The effect that pressure has to UCN is also discussed. Some suggestions for future experiments in regards to understanding and improving the E-field in the Ramsey cell are presented.

Appendix A is a report of high voltage data taken from the cryo-edm experiment in June 2009 and December 2010.

Opera vector field models of the PC 30 kV feedthroughs and modifications to cryo-edm experiment are shown in Appendix B.

A report on damage caused to an electrode surface is shown in Appendix C. SEM pictures and AFM analysis of damage carters on the surface of an electrode are presented.

A very interesting discovery of a superfluid leak is shown in Appendix D. It is a good example of the two fluid model of liquid helium and its dependence on temperature.

Appendix E and F are technical drawings of Rogowski profile electrodes. The former shows the design of new electrodes for the PC. These have grooves and are capable of holding an Al_2O_3 ceramic spacer between. The latter are the electrodes used for the ceramic tests in this thesis.

An investigation of the electrostatics of the Ramsey Cell has been carried out in appendix G. The actual electrode groove profile was measured and then used to calculate the magnitude of the E-field.

2 The Search for the Electric Dipole Moment of the Neutron

2.1. The Neutron

The neutron was discovered by Chadwick (1932) and was the last of the three atomic particles to be found. Prior to this, the popular belief was that the only particles present in the atom and atomic nucleus were the proton and the electron.

This hypothesis had problems, for example, the observed spin of C^{14} could not be satisfied by any combination of protons and electrons. When, in 1920 Rutherford predicted the existence of a nuclear particle with mass approximately that of the proton but electrically neutral, the search was on to find this particle.

Although Chadwick is credited with the actual discovery, a number of other results lead to this. In 1929 Viktor Hambardzumyan and Dmitri Ivanenko explained the atomic nuclei could not be made of protons and electrons.

Bothe and Becker carried out an experiment in 1930 in which they exposed a beryllium target to alpha particles. The radiation that was ejected from the beryllium target could penetrate lead and was not deflected by a magnetic field. At first, this was thought to be very high energy gamma radiation.

The Joliot-Curies decided to repeat this experiment in 1932. They observed that this strange radiation emitted from the beryllium target was capable of removing protons from a secondary paraffin wax target (Lavrakas 1952). After calculating the velocity of the emitted protons, they concluded that the protons were being removed from the atomic nucleus of the paraffin wax in a manner similar to Compton scattering (Burcham and Jobes 1995).

Chadwick had a problem with this hypothesis as it violated the conservation of momentum. However, if this radiation was a neutral particle with mass approximately that of the proton it could quite easily remove a proton from the nucleus and conserve momentum. Chadwick had discovered the neutron and was awarded the Nobel Prize in Physics in 1935.

The neutron is now very well understood: it has a mass of 1.00866491578(55) amu (Nakamura et al 2010) and is not an elementary particle but made from 1 up (+ 2/3e) and two down quarks (-1/3e and -1/3e), and has an overall charge of zero.

The moment and spin of the quarks within the neutron contribute to give it a spin ½ and magnetic dipole moment μ_n of $-1.91\mu_N$, where μ_N is the nuclear magneton

$$\mu_N = \frac{e\hbar}{2m_p}$$

and m_p is the proton rest mass.

One property that has been predicted but not found to date is the neutron electric dipole moment (nEDM).

2.2. The Electric Dipole Moment of the Neutron

Although the overall charge of the neutron is zero, if the centres of the positive and negative charge do not coincide, this will give rise to an electric dipole moment (EDM) (Ramsey 1982). The EDM is defined as the distance separating the centres of mass of the positive and negative charges multiplied by the magnitude of their charge, in the direction of the spin axis.

This can be written as

$$d_n = x \cdot q$$

where d_n is the nEDM, x is the distance separating the centres of charge and q the magnitude of the charge and is illustrated in fig 2.1.

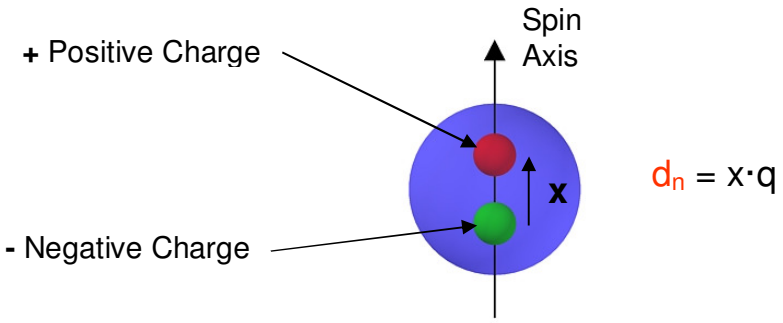

Fig..2.1. Classical representation of the Neutron Electric Dipole Moment (nEDM).

As we shall see below, a successful observation of a non-zero nEDM would be of enormous interest. It would represent the first direct observation of the violation of Time Reversal Symmetry and hence CP violation.

Furthermore a variety of magnitudes for the nEDM are predicted by all High Energy theories and hence a measurement of the actual magnitude or indeed simply setting a new upper limit will shed light on the correctness of each theory.

2.3. The Baryon Asymmetry of the Universe

One of the most fundamental questions in physics is why the Universe is made from matter and not antimatter. Although antimatter can be created in a laboratory and tiny amounts observed in cosmic showers there is no evidence of any antimatter galaxies. It is widely accepted that the Universe came into existence 13.7 billion years ago and the Big Bang Theory (BBT) (Morris 2002) is backed up by Hubble's law, the discovery of the cosmic microwave background (CMB) and the natural abundance of light elements in the Universe.

Chapter 2 The Search for the Electric Dipole Moment of the Neutron

In 1929 Hubble deduced a relationship between the observed redshift of distant galaxies and their receding velocity from Earth. This relationship showed that the farthest galaxies are moving away from Earth at higher velocity than nearer ones and provided sound evidence that the Universe is expanding.

The fact that the Universe is bigger now than previously, and as it is expanding throughout all space, led to the suggestion that it came into existence at a single point (The Big Bang).

The CMB, predicted by Gamow Alpher and Herman in 1948, was discovered by radio astronomers Penzias and Roberts in 1965 and is the electromagnetic background left behind by the formation of the early Universe after the Big Bang. It fills the Universe almost uniformly with a mean temperature of ~ 2.7 K.

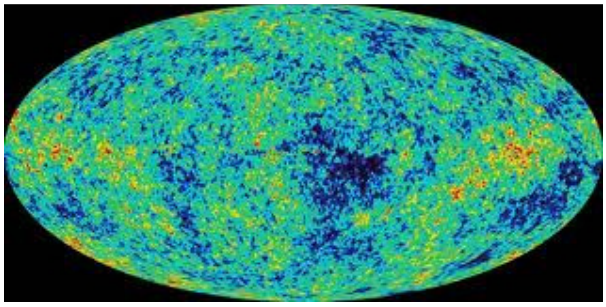

Fig..2.2. WMAP image of the CMB (WMAP 2010).

Now we encounter the problem. The number of particles and antiparticles created by pair production should be identical so why do we observe a universe made from matter and not antimatter?

This dominance of matter over antimatter is called the baryogenesis of the Universe, or more baryons than antibaryons. The average density of matter in the Universe is ~ 10^{-31} gcm^{-3} which produces an average baryon number density of $n_B \sim 10^{-7}$ cm^{-3}. Calculations of the CMB show a γ background density $n_\gamma \sim 400$ cm^{-3} (Burcham and Jobes 1995). One way to

describe the leftover matter from the big bang is to state the experimentally found ratio of baryon to γ density, η (Perepelitsa 2008).

$$\eta = \frac{n_B - n_{\bar{B}}}{\gamma} = 6 \times 10^{-10}$$

This number implies that for every ~ billion particle and particle annihilation 1 matter particle was left. The question is why?

Baryon number (B) is defined as the number of baryons minus the number of antibaryons. In 1967 Andrei Sakharov (Sakharov 1967) outlined three conditions that had to be satisfied to allow for a Universe which went from B = 0 to B > 0. The first was there had to be at least one B number violating process. This is quite a clear assumption. If the Universe had B = 0 at creation and B > 0 now, there needs to be some process that violates B. The second is that charge conjugation operation C and the combined operations of C and parity P, CP, had to be violated. This is required such that the rate of baryogenesis is greater the reverse process antibaryogenesis. The final condition needed for a B > 0 universe is that the interaction occurred outside of thermal equilibrium. The Boltzmann factor states that at thermal equilibrium the amount of matter and antimatter should be equal. So to have greater amounts of matter the reactions must have occurred outside thermal equilibrium.

These requirements are needed to produce a B > 0 Universe. Trying to investigate these conditions can give valuable clues about the birth of the Universe. Therefore studying the fundamental symmetries and violations of these symmetries of particles, such as the neutron, will help to understand and explain the level of CP violation in the Universe and help answer why is B > 0.

2.4. C, P and T symmetries and the CPT theorem

CPT invariance is a very important assumption of all quantum field theories. It states that under the combine operations of C (charge conjugation), P (parity) and T (time reversal) the final system will be invariant to that of the initial state.

The C operator changes a particle into its antiparticle and vice versa. P rotates all spatial coordinates 180˚about a point in space, x,y,z goes to -x,-y,-z. T symmetry is invariant if a state remains the same irrespective of the direction of time.

It is a fundamental requirement of QFT that any system acted on by all three operators C P and T in any order will be indistinguishable from the initial system. From the CPT theorem it ensures that for every antiparticle there is a particle that has identical mass, spin and half-life but has opposite quantum numbers.

Hence, due to the CPT invariance, if there is a violation in CP there must also be a violation of T.

2.5. Observed P, CP and T violation in nature

The strong and electromagnetic interactions conserve P and it was assumed that the weak interaction also conserved P. Lee and Yang (1956) had proposed that the strange decay products of the K mesons might be a sign of P violation in the weak interaction but it was not confirmed.

In 1957 Wu decided to test P conservation in the weak interaction in the β decay of ^{60}Co (Wu et al 1957). A sample of ^{60}Co was introduced into a cerium magnesium nitrate sample and it was cooled to ~ 10 mK. The addition of a relative low magnetic field of ~ 0.05 T produced a local field of 10-100 T in sample which polarised the ^{60}Co. The polarisation was monitored by observing the anisotropic γ emission from the decay of ^{60}Ni. The observed β decay emitted preferentially in the direction of the magnetic field providing clear evidence

of P violation in the weak interaction. It was then assumed that combining C and P the weak system would remain invariant.

In 1964 Christenson et al (Christenson et al 1964) observed CP violation in the decay of K mesons. They are the lightest strange mesons and so decay via the flavour changing weak interaction. The particle and antiparticle do not form a weak CP eigenstate (Das and Ferbel 1994).

$$CP|\overline{k^0}> = -C|\overline{k^0}> = |\mathrm{k}^0>$$

$$CP|\mathrm{k}^0> = -C|\mathrm{k}^0> = |\overline{k^0}>$$

However, weak CP egienstates can be formed by a linear combination of the particle and antiparticle (Giansiracusa 2003). $|k_1>$ having a CP value to +1 and the $|k_2>$ -1.

$$|k_1> = \frac{1}{\sqrt{2}}\left(|k^0> - |\overline{k^0}>\right) \qquad CP|k_1> = +|k_1>$$

$$|k_2> = \frac{1}{\sqrt{2}}\left(|k^0> + |\overline{k^0}>\right) \qquad CP|k_2> = -|k_2>$$

It has been experimentally observed that there are two decay modes for neutral K mesons. One mode decays into two pions. Due to the negative intrinsic parity of the pion this mode is found to have a CP value of +1. It therefore concluded that $|k_1>$ with a weak CP value of +1 will decay into two pions of weak CP of +1. $|k_2>$ decays into three pions. This decay path has CP of –1. Thus $|k_1>$ of CP -1 decays into three pions of CP -1.

The life times of the two decay modes are different. The lifetime of $|k_1>$ is 0.9×10^{-10}s and that of $|k_2>$ is 0.5×10^{-7}s. Due to the difference in decay times, all the $|k_1>$ decays well before the $|k_2>$. This leaves a pure – CP beam. However, the amazing observation by Christenson et al was that very occasionally the $|k_2>$ state decayed into 2 pions. The

probability of observing two pions was very small, 1×10^{-3}, but it was finite and was the first true indication of CP violation of the weak interaction.

2.6. Quark generations and the CKM matrix

The CKM matrix is a 3 × 3 unitary matrix describing the relationship between the quark mass eigenstates (d s b) and the weak interaction eigenstates (d′ s′ b′) (Buras 2002). The weak eigenstates are not pure mass eigenstates but linear combination of the mass eigenstates.

$$\begin{pmatrix} d' \\ s' \\ b' \end{pmatrix} = \begin{pmatrix} \mathrm{V}_{ud} & \mathrm{V}_{us} & \mathrm{V}_{ub} \\ \mathrm{V}_{cd} & \mathrm{V}_{cs} & \mathrm{V}_{cb} \\ \mathrm{V}_{td} & \mathrm{V}_{ts} & \mathrm{V}_{tb} \end{pmatrix} \begin{pmatrix} d \\ s \\ b \end{pmatrix} = \hat{V}_{CKM} \begin{pmatrix} d \\ s \\ b \end{pmatrix}$$

In order to satisfy the experimentally observed suppression of strangeness changing currents, ΔS = 1, to those with no change in strangeness, ΔS = 0, in the decays of K^+ and π^+ Cabibbo (1963) proposed the weak egienstates were not pure mass egienstates but a linear superposition of the strong eigenstats. This is shown as weak isospin doublet (Burcham and Jobes 1995),

$$\begin{pmatrix} u \\ d' \end{pmatrix} = \begin{pmatrix} u \\ d\cos\theta_c + s\sin\theta_c \end{pmatrix}$$

where θ_c is the Cabibbo angle which is ~ 13˚.

There was a problem with this model. The strangeness changing neutral current decay of $K_L \rightarrow \mu^+ \mu^-$ was suppressed in respect to the charge current decay of $K^+ \rightarrow \mu\ \upsilon_\mu$. The decay path of K^+ was ~10^8 times more probably than that of K_L.

Chapter 2 The Search for the Electric Dipole Moment of the Neutron

In 1970 Glashow, Iliopulos and Maiani (Glashow et al 1970) proposed the existence of a fourth quark, charm. They predicted it would have the same charge as the down quark and form a second generation doublet with the strange quark. Given as,

$$\begin{pmatrix} c \\ s' \end{pmatrix} = \begin{pmatrix} c \\ s\cos\theta_c - d\sin\theta_c \end{pmatrix}$$

This second generation doublet combined with the first generation doublet forms a 2 × 2 rotational mixing matrix known as the GIM mechanisms (Burcham and Jobes 1995). Given by;

$$\begin{pmatrix} d' \\ s' \end{pmatrix} = \begin{pmatrix} \cos\theta_c & \sin\theta_c \\ -\sin\theta_c & \cos\theta_c \end{pmatrix}\begin{pmatrix} d \\ s \end{pmatrix}$$

The introduction of the charm quark cancels the unobserved strangeness changing neutral currents.

The mass of the charm quark has to be different to that of the down quark. If they were the same they would exactly cancel. The mass of the charm was predicted by Glashow, Iliopulos and Maiani to be in the region of 1 to 3 GeV. This was confirmed in 1974 with the discovery of the J/ψ particle (bound state of charm anticharm) with a mass of 3.097 GeV/c^2.

In 1973, before the discovery of the charm quark, Kobayashi and Maskawa (1973) extended the mixing matrix to include three quark generations. They were trying to show the mechanism for CP violation in the weak interaction. As a $n \times n$ unitary matrix will have $\frac{(n(n-1))}{2}$ Euler angles (real parameters) and $\frac{((n-1)(n-2))}{2}$ phase angles. Therefore in the 3 × 3 CKM matrix there are 3 real parameters, θ_{12} θ_{13} θ_{23} and 1 CP violating complex phase angle δ.

The three quark generations are shown as 3 doublets.

$$\begin{pmatrix} u \\ d' \end{pmatrix}\begin{pmatrix} c \\ s' \end{pmatrix}\begin{pmatrix} t \\ b' \end{pmatrix}$$

$$\begin{pmatrix} d' \\ s' \\ b' \end{pmatrix} = \begin{pmatrix} \mathrm{V}_{ud} & \mathrm{V}_{us} & \mathrm{V}_{ub} \\ \mathrm{V}_{cd} & \mathrm{V}_{cs} & \mathrm{V}_{cb} \\ \mathrm{V}_{td} & \mathrm{V}_{ts} & \mathrm{V}_{tb} \end{pmatrix}\begin{pmatrix} d \\ s \\ b \end{pmatrix} = \hat{V}_{CKM}\begin{pmatrix} d \\ s \\ b \end{pmatrix}$$

V_{ij} indicates the coupling between the quarks. V_{ud} is the interaction between the u and d quarks mediated by the W^{+} boson.

The CKM matrix has been parameterised in a number of ways. The parameterisation by the Particle data group (Nakamura K et al 2010) is given by;

$$\hat{V}_{CKM} = \begin{pmatrix} c_{12}c_{13} & s_{12}c_{13} & s_{13}e^{-i\delta} \\ -s_{12}c_{23} - c_{12}c_{23}s_{13}e^{i\delta} & c_{12}c_{23} - s_{12}s_{23}s_{13}e^{i\delta} & s_{23}c_{13} \\ s_{12}s_{23} - c_{12}c_{23}s_{13}e^{i\delta} & -s_{23}c_{12} - c_{12}c_{23}s_{13}e^{i\delta} & c_{23}c_{13} \end{pmatrix}$$

Where c_{ij} and s_{ij} are $\cos\theta_{ij}$ and $\sin\theta_{ij}$ and i,j are generations 1,2 and 3. If $\theta_{13} = \theta_{23} = 0$ and $\theta_{12} = \theta_c$ then the matrix reduces back the 2×2 mixing mechanisms with only two generations of quarks.

Another widely used parameterisation is the Wolfenstein parameterisation (Wolfenstein 1983). The coupling of V_{ud} is found experimentally and called λ. Using experimental observations all the other components are found in terms of powers of λ. To bring all experimental observations into agreement with the unitary conditions terms A, ρ and η are introduced. The CP violating phase is included in λ^3 terms.

$$\hat{V} = \begin{pmatrix} 1 - \frac{\lambda^2}{2} & \lambda & A\lambda^3(\varrho - i\eta) \\ -\lambda & 1 - \frac{\lambda^2}{2} & A\lambda^2 \\ A\lambda^3(1 - \varrho - i\eta) & -A\lambda^2 & 1 \end{pmatrix} + O(\lambda^4)$$

The orthogonal quark states (d′ s′ b′) result in $(V^{-1}(V^{T})^*)$. Therefore the product of row i with the complex conjugate of column j will produce a unitary triangle.

$$\begin{pmatrix} V_{ud}^* & V_{cd}^* & V_{td}^* \\ V_{us}^* & V_{cs}^* & V_{ts}^* \\ V_{ub}^* & V_{cb}^* & V_{tb}^* \end{pmatrix} \begin{pmatrix} V_{ud} & V_{us} & V_{ub} \\ V_{cd} & V_{cs} & V_{cb} \\ V_{td} & V_{ts} & V_{tb} \end{pmatrix} = \begin{pmatrix} 1 & 0 & 0 \\ 0 & 1 & 0 \\ 0 & 0 & 1 \end{pmatrix}$$

One of these unitary triangles is given by (Battaglia et al 2003)

$$V_{ud}V_{ub}^* + V_{cd}V_{cb}^* + V_{td}V_{tb}^* = 0$$

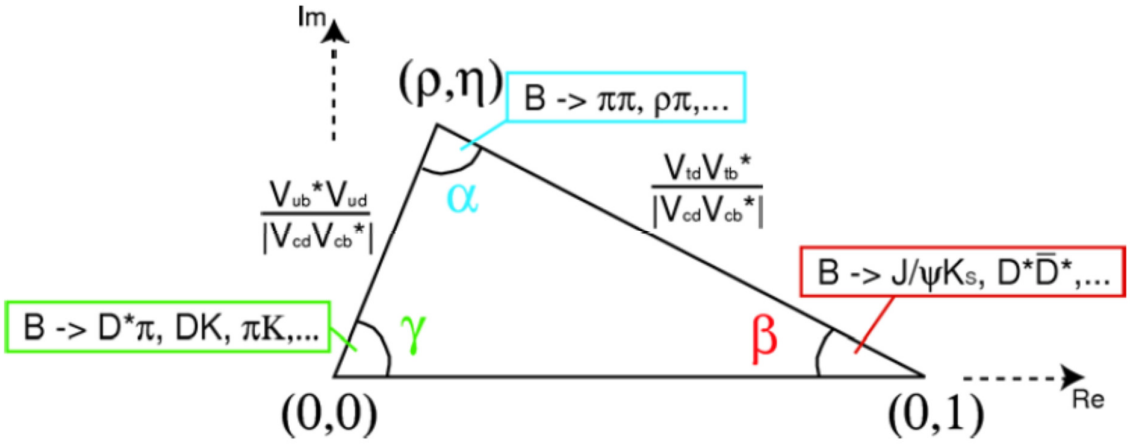

Fig..2.3. An example of a unitary triangle in the complex plane. The relevant mixing elements for the slopes are shown along with some decays used to study the angles (Karamath 2007).

In the complex plane the real and imaginary parts add to give 0 separately. This produces the three lines in the complex plane. They close to form the triangle. As $V_{cd}V_{cb}^*$ is known to a high accuracy the unitary triangle can be rescaled such that the vertices fall on (0,0), (1,0) and (ρ,η).

The CKM matrix is required to be unitary by the SM. Any deviation away from unitary would indicate new physics beyond the standard model. The current status of each component along with the experimental technique for constraining its value is shown on table 2.1.

Quark Coupling	Experimental observation method.	Value
V_{ud}	Nuclear β decay	0.97425 ± 0.00027
V_{us}	Semileptonic kaon decay	0.2252 ± 0.0009
V_{cd}	Neutrino and antineutrino interactions	0.230 ± 0.011
V_{cs}	Semileptonic D or D_s decays	1.023 ± 0.036
V_{cb}	Semileptonic B decays	$(40.6 \pm 1.3) \times 10^{-3}$
V_{ub}	$B \rightarrow X_u l\upsilon$(anti) decays	$(3.89 \pm 0.44) \times 10^{-3}$
V_{td}	B – B(anti) oscillations / loop-mediated rare K and B decays	$(8.4 \pm 0.6) \times 10^{-3}$
V_{ts}	B – B(anti) oscillations / loop-mediated rare K and B decays	$(38.7 \pm 2.1) \times 10^{-3}$
V_{tb}	Top decays	0.88 ± 0.07

Table..2.1. Particle data group values of the magnitude of CKM elements with the experimental technique used to constrain these values (Nakamura K et al 2010).

2.7. CP violation of the neutron and expected values

Measuring a neutron electric dipole moment (nEDM) is a direct observation of CP violation. The interaction Hamiltonian of a neutron placed in magnetic and electric field changes under the operation of T or the combined operations of CP, Fig. 2.4. Acting T or CP

upon the neutron flips the spin but the spatial charges remain in the same position. In effect, the energy state of the Neutron is now different to what is was. As a result of the Pauli exclusion principle there is only one energy state for the neutron thus T and therefore CP is violated.

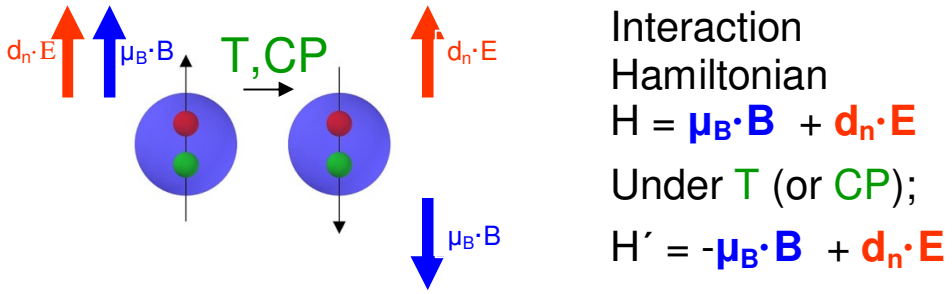

Fig..2.4. Interaction Hamiltonian of the neutron under magnetic and electric fields.

In the standard mode a nEDM can be produced by W boson exchange. As there is no overall favour change from first order interactions, an additional second order interaction such as an additional gluon loop or interactions containing more than one quark is required (Harris 2007).

From dimensional requirements Donoghue et al (1992) predicts the magnitude of a nEDM (d_n) arising from second order interaction in the standard model is

$$d_n \sim e \frac{G_F^2}{\pi^4} \frac{m_t^2}{M_W^2} \, Im\Delta^{(4)} \mu^3 \sim 10^{-31}$$

Where $Im\Delta^{(4)} = A^2\lambda^2\eta = c_1 c_2 c_3 s_1^2 s_2 s_3 \sim 10^{-4}$ is a required CP violating factor A, λ and η are terms from the Wolfenstein CKM matrix and c_i and s_i are the cos and sin of the mixing angles of CKM matrix. The term $\frac{m_t^2}{M_W^2}$ comes from the GIM mechanism. The factor π

is included from loop diagrams and μ is the "typical hadronic scale" (0.3 GeV) making the term dimensionally correct.

This predicted value for a permanent nEDM of 10^{-31} ecm is well outside any current experimental measurements. However, many other theories have predicted nEDM values which will be explored in the next generation of nEDM experiments. Indeed since Ramsey first publication (Smith et al 1957) of the upper limit of the neutron edm in 1957 of 5×10^{-20} ecm the current upper limit has been improved experimentally by ~ 6 orders of magnitude, Fig. 2.5. The current upper limit, held by the Sussex-RAL collaboration, is 2.9×10^{-26} ecm (Baker et al 2006).

The Strong sector can also produce a nEDM. The QCD Lagrangian has a $\bar{\theta}$ phase that is both P and CP violating (Harris 2007, Sinclair 2010). This phase cannot produce CP violation in the neutral kaons as it occurs in the ΔS = 0 operator however it can produce a nEDM

$$d_{n\approx\bar{\theta}\frac{m_u m_d m_s}{m_u m_d+m_u m_s+m_d m_s}\frac{e\mu_n}{\Delta M}\sim\bar{\theta}\times10^{-15}\ ecm}$$

Due to the experimental upper limit the $\bar{\theta}$ has to be < 10^{-10} radians. As $\bar{\theta}$ can be anything between 0 and 2π this extremely small value is known as the strong CP problem. The $\bar{\theta}$ can be constrained to 0 however this requires the assistance of theoretically predicted, but not yet observed, axion particle.

The next generation of nEDM experiments should be capable of reducing the upper limit to 10^{-28} ecm. One theory outside the standard model which is being increasing put under pressure by improving nEDM upper limits is Supersymmetry. In the supersymmetric model the addition of superpartners for all fermions and boson allows one loop contributions to quark EDMs, producing a nEDM ~ 10^{-23} to 10^{-24} ecm. These values disagree with

experiment by orders of magnitude. However, a minimal supersymmetric model predicts an nEDM of order 10^{-27} to 10^{-25} ecm (Pospelov 2005).

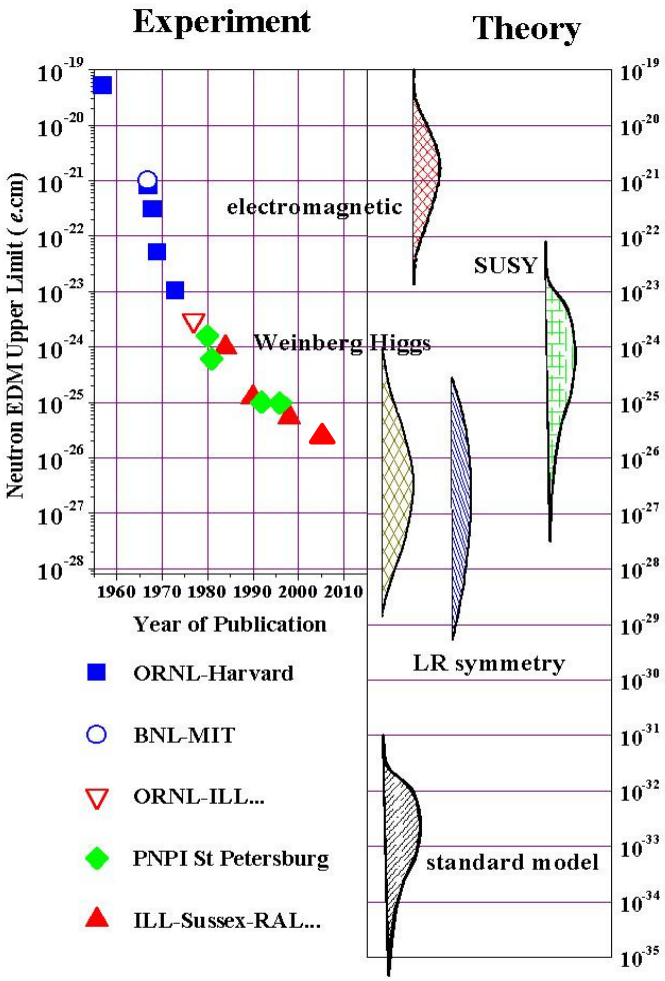

Fig..2.5. The experimental upper limit set on the Neutron electric dipole moment (nEDM) as a function of the year of publication. Included is the ILL-Sussex-RAL current upper limit of 2.9×10^{-26} ecm. Also shown on the right hand side are theoretical predictions of the nEDM (STFC 2009).

This is well within the range of the next generation of nEDM experiment. If a nEDM is observed at this level it will be a direct observation of physics beyond the standard model. Many theories predict a nEDM to be approximately of this magnitude as a nEDM of this magnitude is thought to be needed to explain the extent of the baryon asymmetry of the Universe.

3 Background to the Cryogenic nEDM Experiment

3.1. Conducting a nEDM Experiment

This sections looks at how to perform an experiment to determine the magnitude of the nEDM. An overview of the NMR technique used to measure the precession frequency of the Neutron in a stable magnetic field is given. This technique is then combined with a parallel or antiparallel electric field to produce a slight change to the precession frequency.

In order to gain an understanding of the level of sensitivity needed to measure a nEDM some realistic experimental values for the magnetic and electric fields are estimated to generate a measurable value for the change in precession frequency expected for an nEDM of 1×10^{-27} e cm.

3.1.1. Neutrons in a magnetic field

In order to do a nEDM measurement, we first take advantage of the known properties of the magnetic dipole moment (μ_n). Polarised UCN trapped in a bottle made from material with a high Fermi potential (Pendlebury 1993) and in a known magnetic field (B) will try to align with this field, figure.3.1.

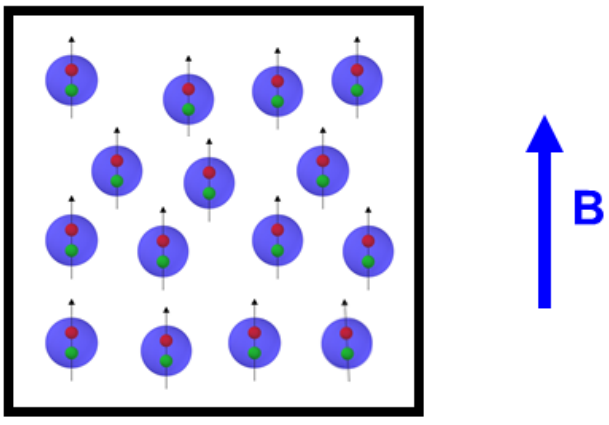

Fig..3.1. Polarised UCN trapped in a high Fermi potential material bottle.

This causes a torque (τ) created by the μ_n trying to align with the B field, given by

$$\tau = \mu_n \times B$$

$$where\ \mu_n = -1.91\mu_N = -9.66 \times 10^{-27}\ J\ T^{-1}$$

μ_N is the nuclear magneton

$$\mu_N = \frac{e\hbar}{2m_p} = 5.05 \times 10^{-27}\ J\ T^{-1}$$

e is the elementary charge and m_p the proton rest mass.

The torque causes the neutron spin to precess about B. The rate of this precession is governed by the gyromagnetic constant (γ_n) and the applied magnetic field. The rate of precession of the Neutron in a known magnetic field is known as the Larmor precession frequency (ω_L) and is given by

$$\omega_L = \gamma_n B$$

where

$$\gamma_n = \frac{2|\mu_n|}{\hbar} = 1.83 \times 10^{8}\ Hz\ T^{-1}$$

If a magnetic field of 5×10^{-6} T is applied then

$$\omega_L = (1.83 \times 10^{-8})(5 \times 10^{-6}) = 916\ rad\ s^{-1}$$

Therefore the frequency is

$$\nu = \frac{916}{2\pi} = 145.8\,Hz.$$

So a neutron placed in a known magnetic field of 5×10^{-6} T will precess about the B field at frequency of 145.8 Hz.

3.1.2. Neutrons in magnetic and electric fields

In order to perform a nEDM experiment an electric field is required. This field must be parallel or anti parallel to the B field, figure.3.2. It is produced by two parallel plate electrodes. They are located at either end of the material bottle.

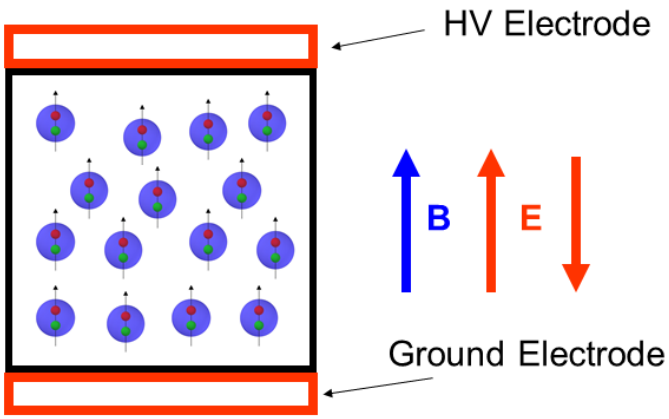

Fig..3.2. Polarised UCN in a material bottle. The direction of the applied magnetic and electric fields is shown.

The addition of an electric field either parallel or antiparallel to the magnetic field creates an additional torque. This changes the precession frequency. The easiest way to examine the affect this has on the precession frequency is to look at the change to the interaction Hamiltonian energy caused by Zeeman and Stark shifts, figure.3.3.

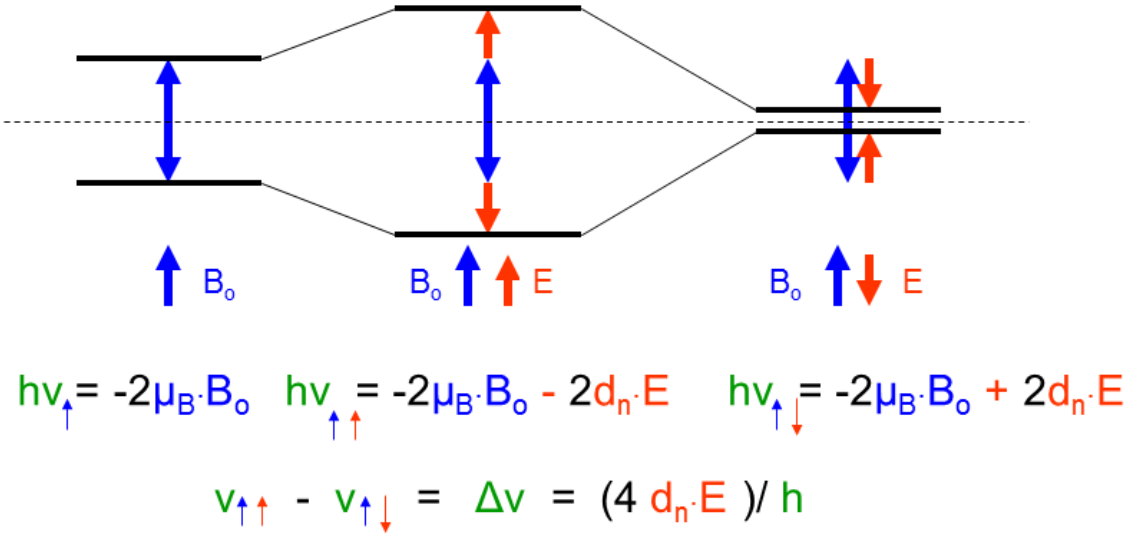

Fig..3.3. Zeeman splitting and Stark shift for a neutron placed in electric and magnetic fields.

The interaction of the neutron magnetic dipole with a magnetic field produces an energy level splitting, the Zeeman affect. The application of a parallel or anti-parallel electric field, with respect to the magnetic field, will cause the electric dipole moment (d_n) to interact with the E-field and cause an additional Stark shift of the interaction energy, figure.3.3. If a change in interaction energy and therefore precession frequency is detected on application of an applied electric field this is a positive indication of a permanent electric dipole moment.

The difference in interaction energy caused by the parallel and antiparallel electric fields can be used to work out the expected change in precession frequency ($\Delta\nu$) for a d_n of 1×10^{-27}ecm and an electric field across the cell of 50 kV cm^{-1}.

$$\Delta\nu = \frac{(4 \times (1 \times 10^{-27}) \times 50000)}{\mathrm{h}} = 48\,nHz$$

If the nEDM is 1×10^{-27} ecm the difference in the precession frequency between parallel and antiparallel fields of 50 $kVcm^{-1}$ is ~ 48×10^{-9} Hz. We are therefore looking for a tiny signal of 48×10^{-9} Hz on top of a signal of 145.8 Hz. This is indeed an extremely small change in precession frequency. To measure such a small variation the Ramsey resonance technique is used (section 3.1.7.)

3.1.3. Ultra cold neutrons (UCN) and storage

In our experiment free neutrons are realised from the deuterated fission reaction in the core of the ILL 56 MW nuclear reactor. A Maxwellian spread of neutrons with different energies is produced. However, in order to do a nEDM experiment the neutrons have to be stored in material walls. This requires very low energy neutrons ~10^{-7} eV. These neutrons that reflect from the surface of a material wall at all angles of incidence are called Ultracold Neutrons (UCN) (Golub and Pendlebury 1979).

This sections looks at the principle involved in storing UCN. Thus, allowing probing of their properties by electric and magnetic fields.

Neutrons interact via the strong, gravitational, weak and magnetic force. These properties have been used over the years to develop experiments capable of studying the neutron and also to use the neutron as the tool to probe other structures (Neutron scattering).

When a UCN comes into near proximity to a material surface its long wavelength samples a number of nuclei in the surface as a result of the strong nuclear force. The wavelength can penetrate the surface up to ~ 100 Å. If the Fermi potential (V_f) experienced by the neutron over the total sampling area is greater than the neutron energy E_n the neutron will be scattered from the surface (Golub and Pendlebury 1979). V_f is given by (Fermi 1936, Golub and Pendlebury 1979)

$$V_f = \left(\frac{2\pi\hbar^2}{m_n}\right)\sum_i N_i a_i$$

Where m_n is the mass of the neutron N is the molecular number density and a is the scattering length.

Unlike the high energy experiments at the LHC where particles are accelerated to extremely high velocities UCN move at ~ 5 ms^{-1}. Therefore gravity strongly affects the way they bounce around in high V_f stored volumes. The neutron gravitational potential is given by V_g and is in the usual form.

$$V_g = mgh$$

where m is the neutrons mass. If a neutron freely falls under gravity for 1 meter it will gain energy of ~ 1.03×10^{-7} eV (Pendelbury 1993). This is quite an increase in total energy. A meter free fall under gravity provides the neutron with enough energy to now penetrate the containment walls. However, this can be an advantage. If a Neutron detector is placed at the bottom of a meter drop the energy gained by the neutrons, due to gravity, increases the probability that the neutrons will pass through the surface of the detector and therefore be detected.

The length of time a UCN spends in a material bottle is governed by the β decay of the neutron into a proton via the weak interaction, Fig. 3.4. A down quark changes to an up quark with the exchange of a W^- boson and emission of an electron and an electron anti neutrino. The current accepted value for this decay lifetime is $\tau_n = 885.7 \pm 0.8$ s (Nakamura K et al 2010).

In practice gaining these long τ_n experimentally is very difficult. There are a number of loss mechanisms. These are reviewed in section 3.1.5.

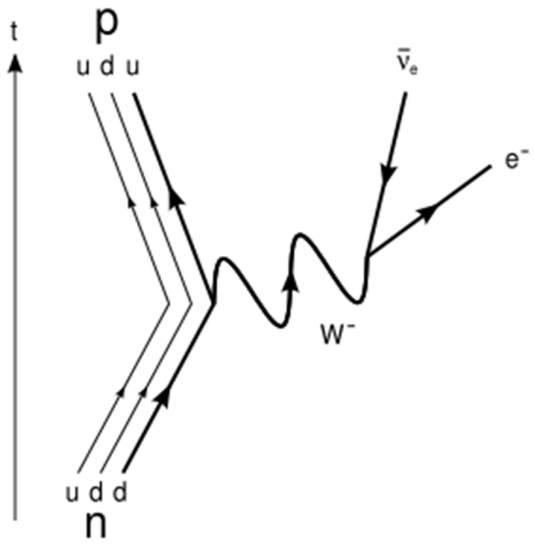

Fig..3.4. Feynman diagram of neutron β decay (Schools).

As mentioned above the magnetic dipole of the neutron interacts with the magnetic field and creates a potential V_m.

$$V_m = -\mu \cdot B$$

Where μ is the magnetic dipole moment and B is the magnetic field. As we will see in the next section this is also advantages as the magnitude of V_m is spin dependent.

3.1.4. Polarisation

The magnetic interaction of the neutron with a magnetic field is spin dependent. For a magnetic material an additional term has to be added to V_f. The total potential U that a neutron sees when it comes into contact with a magnetic material surface is given by

$$U = V_f \pm \mu_n \cdot B$$

The sign of the second term is the spin depend part which is measured relative to the B field. This property can be used, and is used by our cryoEDM experiment, to produce a polarised sample of neutrons. For some magnetic materials (e.g. Fe) a neutron with its spin aligned parallel to the B field will feel a high U causing it to be reflected back into the storage volume while a neutron with spin anti parallel will have E_n greater than U and therefore be able to pass into the material surface and be absorbed.

Neutrons with higher energies can also be reflected off material walls. This occurs if the component of their velocity vertical to the wall is low with respect to V_f. Therefore if $E_\perp < V_f$ reflection from the surface will occur.

Similar to optics total reflection of a neutron will occur from the surface of a magnetic material at any angle of incidence to the surface up to the critical angle θ_c given by (Golub and Pendlebury 1979)

$$\sin\theta \leq \lambda \left(\frac{Na}{\pi} \pm \frac{m_n}{2\pi\hbar^2}\,\mu B\right)^{1/2} = \sin\theta_c$$

Where λ is the neutron wavelength. This means UCN and neutrons with higher energies with a small glancing angle of incidence to a magnetic guide tube can be formed into a beam of polarized neutrons that can be transported to the an experiment.

3.1.5. UCN production in He II and losses

The number of UCN produced by the ILL reactor is very low. However, a large number of cold neutrons are produced. Pendlebury and Golub (Golub and Pendlebury 1977) theoretically investigated the production of UCN by the interaction of cold neutrons with He II. They noticed the dispersion curves for a free neutron and He II crossed at two points,

figure 3.5. Cold neutrons of wavelength 8.9 Å can down scatter to UCN by giving up virtually all of their energy to the He II by the emission of 11 K phonon. An extra advantage of this process is that it does not change the polarisation of the neutrons. Therefore a polarised beam 8.9 Å cold neutrons will down scatter to UCN whilst remaining in the same spin state. This is due to the coherent scattering properties of He II.

Of course the reverse up scattering process is also possible. However, if the temperature of the He II is ≤ 0.5 K this processed is suppressed by the Boltzmann factor. At these low temperatures there are not enough 11 K phonons in the bulk He II to up scatter the UCN. In fact the UCN see the He II as an inert matrix in which they do not interact (Liu 2009). Multi phonon down scattering does also occur for neutrons with higher energies. However, single phonon emission is most likely (Golub and Pendlebury 1979).

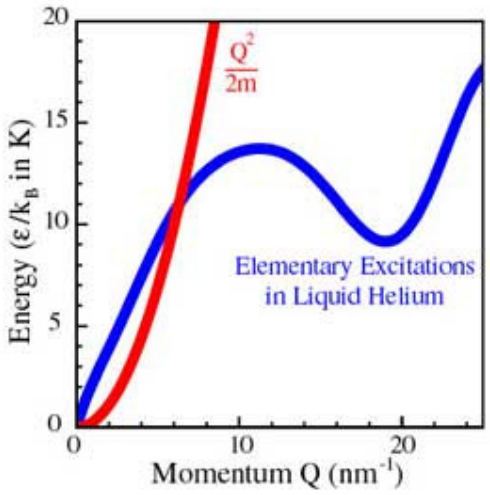

Fig..3.5. Energy versus momentum for a free neutron, red line, and He II, blue line, (Harvard).

Although up scattering of UCN is suppressed in 0.5 K He II other processes can cause losses in neutron numbers. When a UCN comes in contact with the material wall there is some probability that it will be captured by a nucleus in the material wall or from a nucleus of a frozen gas particle on it. UCN can also be up scattered from the material wall. The 2 mK

UCN can gain enough energy from the 0.5 K wall to penetrate the material container and escape. This process does not occur every time the neutron hits the wall. The long wavelength of the neutron interacts with ~ 10^7 particles on the surface. The total centre of mass velocity of the ~ 10^7 particles is far less than that of the UCN. Thus the UCN coherently scattered from its surface back in the He II medium.

Impurities in the He II can also affect the UCN numbers. Although ^{4}He has no capture cross section to UCN ^{3}He has a spin dependant cross section. When the spin of the ^{3}He and the UCN are parallel there is no cross section. However, when the spins are antiparallel it has a high capture cross section of 5×10^6 b. This makes it important to filter out the ^{3}He from the ^{4}He when filling the production volume. Gaps between the UCN containment volume apparatus will also cause UCN to escape.

The total number density of UCN (Korobkina et al 2002) in the He II volume is given by

$$\rho_{UCN} = P\tau_n$$

where P is the production rate in UCN cm^{-1}s^{-1} and τ_n the experimental UCN lifetime in the He II after accounting for all losses.

3.1.6. Transportation of UCN and the Ramsey cell

Polarised UCN will stay in the same spin state if an external magnetic holding field is applied. As long as the fields are set up correctly the neutrons will remain polarised throughout the experiment.

The method of moving UCN around the experiment is relatively simple. UCN act as an ideal gas in He II at a temperature $\leq$ 0.5 K. They bounce around within their containment

walls. A sealed UCN production volume is used to build up the density of UCN. After a period of time this volume is opened up to the experimental cell, the Ramsey cell. The UCN can now spread out through the containment volume. Some of them make it into the Ramsey cell. This is where they are subjected to both magnetic and electric fields.

The Ramsey cell is made from two cylindrical parallel plate electrodes. These are made from Beryllium which has a high V_f (252 neV) to UCN. A BeO ceramic spacer, also with a high V_f (261 neV), is used to keep the neutrons between the electrodes. The E field is created by charging one of the electrodes to HV while keeping the other grounded. The E field acts either parallel or anti parallel to the B field. The B field is created by a ~ 2.6 m long superconducting solenoid (Katsika 2011).

3.1.7. The Ramsey technique and nEDM measurements

A nEDM of 10^{-27} e cm in an E-field of ~ 50 $kVcm^{-1}$ would produce a change in precession frequency $\Delta\nu$ of ~ 48 nHz. This is a very small signal, especially if it is on top of the Larmor precession frequency of ~ 145 Hz. In order to increase the level of sensitivity by many orders of magnitude Ramsey (Ramsey 1956) proposed a technique using transverse oscillatory magnetic fields (Ramsey resonance) that manipulates the spin axis of the precessing particle while being able to monitoring its precession rate.

A spin polarised neutron subjected to a static B field in the z direction, with its spin axis also in the z direction, will presses about it at ω_L, Fig.3.6. part 1. Two current loops in opposite directions are set up such that the components of their fields cancel in the z axis and produce a second transverse field B_1 in the xy plan. The currents are pulsed at ω_L. The neutron sees B_1 as a stationary field in its rest frame. As a result the neutron also starts to presses about B_1. As the neutron is now precessing about the static B and the transverse B_1, which it sees as a static field in its rest frame, it causes the neutrons spin axis to spiral out of

alignment of the B (z direction). The process continues for a time $\tau = \frac{1}{4\gamma B_1}$, where γ is the gyromagnetic ratio. At this point the neutrons spin axis has been flipped by 90˚. It now is aligned with the xy plan. The oscillating transverse field is turned off but remains running in the signal generator, figure 3.6 part 2. This is known as the $\frac{\pi}{2}$ pulse. Although the spin axis is now in the xy plane it still precesses about B at ω_L.

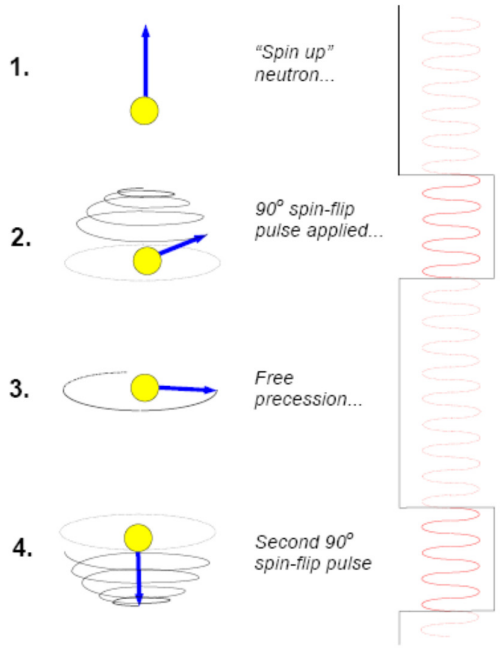

Fig..3.6. Illustration of the separate oscillating fields Ramsey resonance technique (Harris 2007).

The neutron has a period of free precession, figure 3.6 part 3. The length of this period is restricted by the τ_n in the apparatus. A second $\frac{\pi}{2}$ pulse is applied from the signal generator which is in phase with the first pulse. The neutron again sees the static field in phase with the first $\frac{\pi}{2}$ pulse and once again precesses about it. It continues to spiral until its spin axis is now opposite to B (-z direction). At this point the second $\frac{\pi}{2}$ pulse is turned off.

If an E field, either parallel or anti parallel to the static B field, is also applied across the neutron during this period of free precession the additional torque created by the nEDM

will cause a change in phase between the precession frequency of the neutron and the signal generator frequency.

If this signal is large enough to be detected this is a positive indication of a permanent nEDM.

Figure 3.7 shows a Ramsey resonance curve (Harris 2007). The number of flipped neutrons, those in the opposite spin state after experimental manipulation, is plotted against the frequency of the oscillating field applied. The minimum number of neutrons counted, i.e. the maximum number flipped, occurs at ω_L. A nEDM signal is observed by looking for a shift in the Ramsey curve. i.e. maximum number of flipped neutrons occurs at a different frequency. In summary a shift of the Ramsey curve proportional to the applied electric field indicates a nEDM signal. On Fig. 3.7 a detectable nEDM will cause the Ramsey curve to shift either left or right depending on the direction of the applied E field.

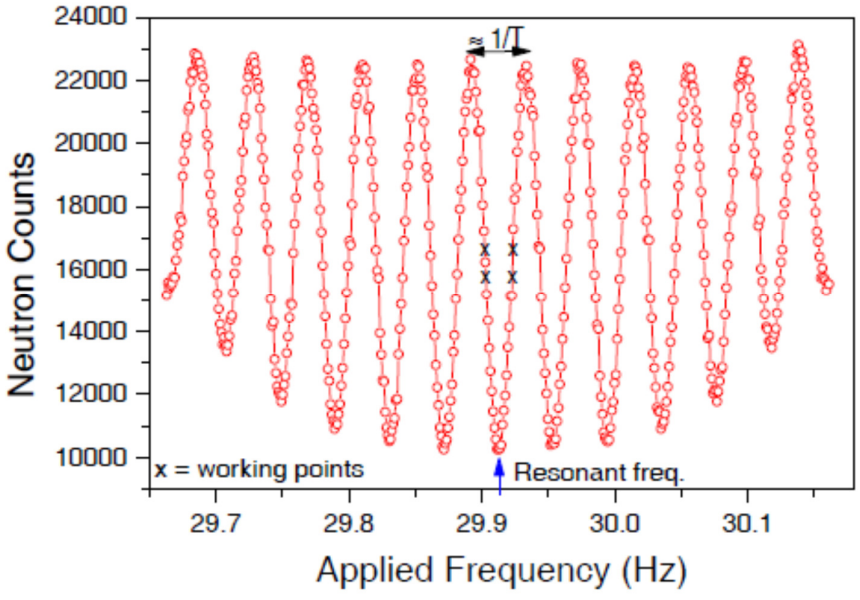

Fig..3.7. Example of a Ramsey resonance curve (Harris 2007)**.**

3.1.8. nEDM statistical uncertainty

The statistical uncertain on an nEDM measurement (σ_{d_n}) is given by

$$\sigma_{d_n} = \frac{\hbar}{2\alpha E T_s \sqrt{N}}$$

Where α is product of polarisation defined as

$$\alpha = \frac{(N_\uparrow - N_\downarrow)}{(N_\uparrow + N_\downarrow)}$$

E is the electric field applied across the cell. T_s is the storage time of the neutrons and N is the number of neutrons, $N_\uparrow$ is spin up and $N_\downarrow$ is spin down. For a full derivation of the statistical uncertainty see (Grozier 2007). It is clear from σ_{d_n} that sensitivity of the nEDM measurement is improved by maximising the E-field, storage time and the number of neutrons.

3.2. cryoEDM Apparatus

In this section the main parts of the CryoEDM apparatus will be explained.

3.2.1. Overview of the cryoEDM apparatus – Production of UCN and their movement to the Ramsey cell

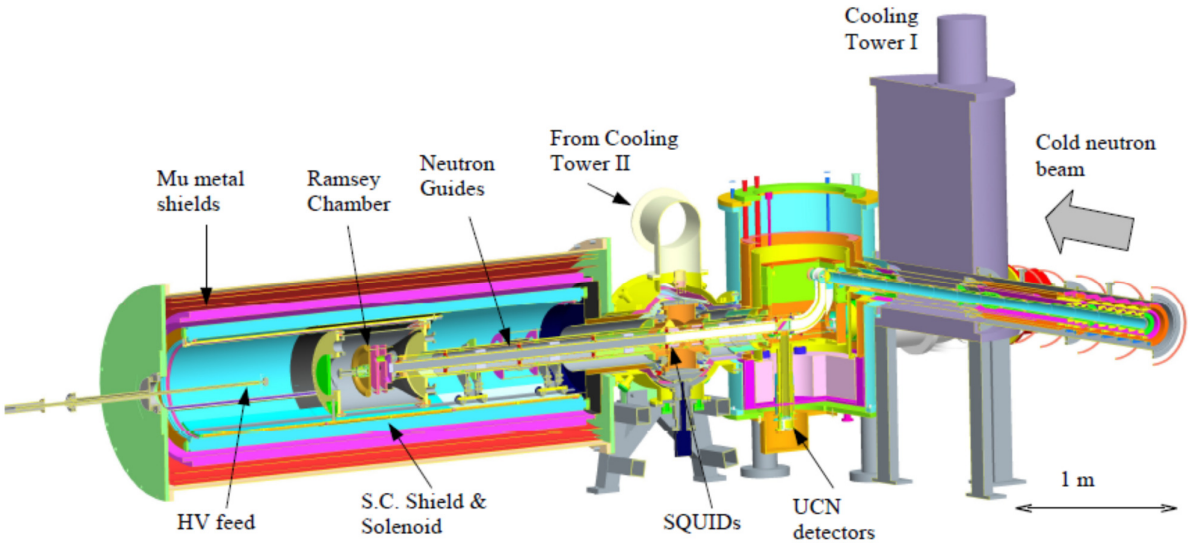

Fig..3.8. Section through the cryo-edm experiment apparatus (Baker et al 2009).

The ILL produces a neutron flux of 1.5×10^{15} neutrons cm^{-2} s^{-1}. From this the 8.9 Å cold neutrons are guided from the reactor core to the Cryoedm experiment (Baker et al 2009, Baker et al 2010). Just before entering the UCN production volume they pass through a polarizer. This is made up from layers of Fe foil and intercalated graphite. Due to the magnetic properties Fe the V_F seen by the cold neutrons is spin depended. The neutrons in one spin state see a V_F of > 350 neV while that of the other spin state see ~ 90 neV. Thus

neutrons of one spin state are reflected back along the guide tubes while the other pass through and are absorbed by surrounding material.

Although magnetised in one direction the ferromagnetic magnetic domains in the Fe layer may not all be aligned. By increasing the number of layers of Fe the probability of reflection by neutrons of required spin state can be improved from 90 % to 95 %.

As well as selecting neutrons of one spin state the 2.3 m long polariser acts as a cut off for higher energy neutrons. Neutrons with wavelength < 4.5Å have enough energy to pass through the Fe layers and are absorbed into the polariser wall.

Once polarised the cold neutrons pass through a beryllium window into the super thermal UCN source filled with He II. This is where the cold 8.9 Å neutrons down scatter to UCN. Indeed the entire experiment from this point on is submerged in He II at ~ 0.5 K. The source is sealed at both ends to allow the number density to UCN to build up. Although cold neutrons can pass through the beryllium window the UCN having lower KE are reflected by the high V_F of the beryllium. The UCN maintain their spin orientation via a set of holding coils positioned around the super thermal UCN source.

A number of valves are used to control the movement of UCN throughout the apparatus. Once the density of the UCN is sufficiently high, the source valve is opened. UCN are now able to disperse through guides tubes to the Ramsey cell. The UCN guide tubes are made from copper. The inner surface of the tube is coated with beryllium. After leaving the source the UCN first encounter a 90˚ elbow. This ensures only UCN pass to the Ramsey cell. Higher energy neutrons cannot get around the 90˚ bend and penetrate the walls of the experiment. This prevents excitations and reduces γ radiation, from neutron capture, in the Ramsey cell. The neutrons make their way along this guide tube until they reach the Ramsey cell where the nEDM experiment takes place.

3.2.2. Overview of the cryoEDM apparatus – The Ramsey cell

The Ramsey cell actually consists of two cells, Fig.3.9. Both are exposed to the magnetic fields while only one has an E field across it. Therefore the high voltage cell is where the nEDM experiment takes place. The other cell is used for comparison.

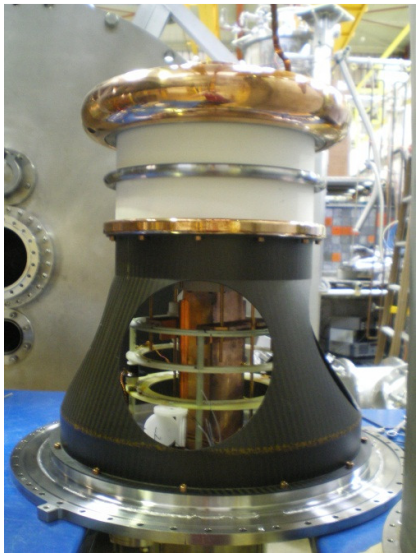

Fig..3.9. Photograph of the cryo-edm Ramsey Cell.

The probability of detecting a nEDM is proportional to the applied E-field. Increasing the E-field across the cell improves the probability of detecting a nEDM. The experiment should run at the maximum voltage possible. Therefore an understanding of the electrostatics of the Ramsey cell is very important. Indeed the thrust of this thesis has been to investigate the electrostatics of the cell.

The HV cell is made up of two parallel plate Beryllium electrodes with a diameter of 29 cm. The HV electrode is surrounded by a CuBe corona dome. The electrodes are kept 4.5 cm apart. They are separated by a BeO cylindrical spacer. The spacer has an inner diameter

of 25 cm and an outer diameter of 26.1 cm. Machined into the face of the electrode is a 5 mm deep groove of radius 10 mm. This helps to locate the BeO and keep the electrodes parallel. However, the primary purpose is to reduce any high E fields and thus prevent breakdown at the cathode triple junction (CTJ). This is the triple point where the BeO, liquid Helium and electrode meet.

The HV electrode has a corona ring around it made from CuBe. It is charged during a nEDM run. The HV supply and feeds are the same as that used in this thesis (section 5.5.). The middle electrode is grounded. This creates an E field across the cell perpendicular to the surface of the electrodes. This is along the same axis as the static B field.

The second cell is similar in geometry to the HV cell. It has the same separation as the HV cell. The BeO spacer is the same size and the groove geometry is the same. However, in this case both electrodes are grounded producing no E field between the electrodes.

The magnetic holding field, B, is created from a 2.6 m long super conducting solenoid. It is set up to produce a field of 5 μ T. This B field should remain homogenous and static over the total experimental period. Failure to do so can result is a false nEDM signal. Any change in the magnetic environment will change the ω_L. This will result in a shift to the Ramsey resonance curve. The stability of the magnetic field should be 0.1 pT (Katsika 2011). This is achieved by a combination of superconducting lead shield, mu metal shields and a set of compensations coils. The stability of the magnetic environment is detected via SQUIDS.

The neutrons are guided to the Ramsey cell where they are manipulated by electric and magnetic fields. After a period of time, ~ 300 seconds, they are realised form the cell and guided back along the guide tube to the detectors.

3.2.3. Overview of the cryoEDM apparatus – The UCN detectors

The UCN detector is a solid state Si detector, figure 3.10, (Baker et al 2003). A layer of ^{6}Li is sandwiched between the detector and layer of Fe. The Fe is magnetised and therefore only allows one spin state through it. The ^{6}Li has a very large cross section for UCN of ~ 10^{5} b. The reaction with UCNs is

$$^{6}Li + n \rightarrow \alpha + T + 4.8\,MeV$$

Either α or T trigger the Si detector. The low KE of the neutrons ensures the emission products are back to back. Therefore either α or T will hit the detector and indicate the presences of a UCN.

Fig..3.10. Solid state UCN Si detector (Baker 2010).

A period of time is allowed to count all the neutrons of one spin state. Then an activation coil is turned on at the top of the detector guide tube. As the UCN pass through it flips their spin. This process allows all UCN to be counted. This helps with the statistics and ensures all UCN have emptied out of the cell and guide tubes prior to the release of UCN from the second cell. After both cells are empty the measurement cycle can start again.

3.2.4. The High Voltage and liquid Helium requirements and rationale behind this DPhil study

This thesis investigates the electrostatics of the Ramsey cell. As the σ_{d_n} is proportional to the applied electric field it should be maximised. The HV electrode should be charged to a maximum voltage without any chance of breakdown.

A discharge across the cell causes a number of problems. From a physical point of view the sudden current causes the magnetic environment the neutron samples to change. This in turn has an effect on the ω_L. Discharge will also dump a lot of energy in the He II at 0.5 K. It is therefore important to keep the capacitance of the HV feed line as low as possible or to limit the current available on discharge by adding a large resistor into the cell end of the HV line.

Each breakdown event causes a crater on the both sets of electrodes. An increased number of discharges reduces the maximum voltage the electrodes can hold. It has also been calculated (Munday 2010) that the electrode material is emitted into the He II after discharge. Material impurities will also cause problems as they will charge in the E-field and can assist in triggering breakdown.

On an experimental level any discharge has a chance of finding its way back to ground via sensitive electronics. This can kill instrumentation it encounters on its way.

It is therefore very important to apply the maximum E field possible but have no chance of any breakdown. The two main aspects of this thesis have been to increase the E-field by investigating the factors affecting the dielectric strength of liquid helium at 0.5 K, and therefore improving it, and investigating the breakdown voltage the BeO spacer is likely to withstand.

4 Factors Affecting High Voltage Breakdown in Liquid ^{4}He and Other Liquids

4.1. Breakdown in Dielectric Liquids

4.1.1. Introduction

When the electric potential is increased between a pair of electrodes submerged in a dielectric liquid it can cause breakdown. Catastrophic discharge from one electrode to the other happens in the order of ns and hence extremely high peak currents can be produced. This thesis investigates this type of discharge. Sustained discharges can also occur and this process is sometimes used to remove spikes and asperities from the surface of a HV electrode prior to use and is called current-limit conditioning.

It is generally accepted that high voltage breakdown across a dielectric liquid is through a gas "streamer" which eventually connects the two electrodes. This gas phase starts with a bubble which can be created within the bulk of the liquid. More often, this initial bubble forms at one of the electrodes and a variety of mechanisms are thought to be responsible. The most obvious of these is field emission of electrons from asperities on the cathode. In this case, when the local current density is sufficiently high, heat input to the liquid from the electrons leads to formation of a gas bubble on the asperity. Both the surface tension of the liquid and the hydrostatic pressure in the liquid will try to collapse the bubble and this is counteracted by the heating effect of the current tending to expand the gas and vaporise more liquid, thereby increasing the gas pressure within the bubble. In addition, electrostatic forces on the bubble will also tend to increase its size. Clearly, under these circumstances, whether the initial bubble grows, collapses or remains at a stable size depends on many parameters. The thermal conductivity and specific heat of the liquid will be

important and it is simple to show that an increase in hydrostatic pressure of the liquid will lead to a decrease in initial bubble size, all other factors remaining equal.

A second mechanism thought to be important involves impurities in the liquids, especially microscopic particles which become charged. Once this happens, they can be attracted to one of the electrodes, thereby causing local heating and leading to initial bubble formation.

There are obvious technological reasons for work on dielectric strength of liquids, ranging from transformer oils to liquid cryogens for possible use in superconducting machines. Much of the work on breakdown in liquids has been done with point-to-plane geometries in order to have more control on the geometry.

In this thesis, we are interested in the properties of liquid ^{4}He at 0.5 K when between two rather large plane electrodes. In general, there are arguments that the dielectric strength of any liquid in such a cell should decrease with both increasing electrode surface area and with volume. The basic idea is that the larger the area, the greater the number of asperities, and that the larger the volume, the more impurity particles present.

As is well known, liquid ^{4}He has some very unusual properties, many of which are relevant to us. It has very low latent heat, high ionisation potential and, below 2.17K, it exhibits a superfluid phase in which the thermal conductivity is essentially infinite. In addition, isolated electrons in liquid helium form their own unique type of bubble.

4.1.2. Some properties of Liquid ^{4}He

With its high zero point energy and low van der Waals force liquid Helium can remain liquid down to absolute zero. Helium can be solidified although this requires a pressure of ~ 25 bar (Wilks and Betts 1987). There are two naturally occurring stable

isotopes of Helium. ^{3}He and ^{4}He with a ~ abundance 1:10^7 respectively. Under normal atmospheric conditions ^{4}He boils at 4.2 K while ^{3}He boiling point is lower at 3.32 K.

In practice, when using ^{3}He, a lower temperature can be reached for the same pumping power in comparison to ^{4}He. This technique is used in the cryoEDM experiment. ^{3}He is pumped on to reduce the temperature to ~ 0.5 K and then thermal conduction to the ^{4}He in the main volume is used to reduce its temperature.

Of course ^{3}He cannot be used as the cryogenic medium in the cryoEDM experiment. With its lack of a neutron ^{3}He has an extremely high capture cross sections for neutrons. On the other had once neutrons are in the UNC state they see the ^{4}He as nothing more than an inert medium.

In order to filter ^{3}He out of ^{4}He a superleak is used. This takes advantage of the fact that ^{4}He under goes the phase transition into the superfluid at 2.17 K from normal state He I to superfluid He II while ^{3}He does not until ~ 2.6 mK. As He II has a lower viscosity than He I it can flow through tiny capillaries, ~ nm. This has the advantage of being able to filter the normal state ^{3}He from the mixture. It can also be problematic. Any superfluid seal has to be tested to show leak tight integrity before being installed into the cryoEDM apparatus (Appendix D).

The phase transition occurs at the λ-point. The specific heat of the liquid is observed to rapidly increase at this point then fall away just as quickly after passing through it. Due to its similarity with the Greek letter lambda it was named after it. The superfluid transition can be visually observed when ^{4}He passes from He I into He II. With its relatively low thermal conductivity He I bubbles vigorously as the liquid approaches the λ transition. After passing into the He II phase there is an instantaneous stop of bubbling. The He II is motionless and still. This remarkable change is due to the change in the thermal conductivity of the He II.

The high conductivity means there are no thermal gradients in the liquid and boiling can only occur from the surface of the liquid.

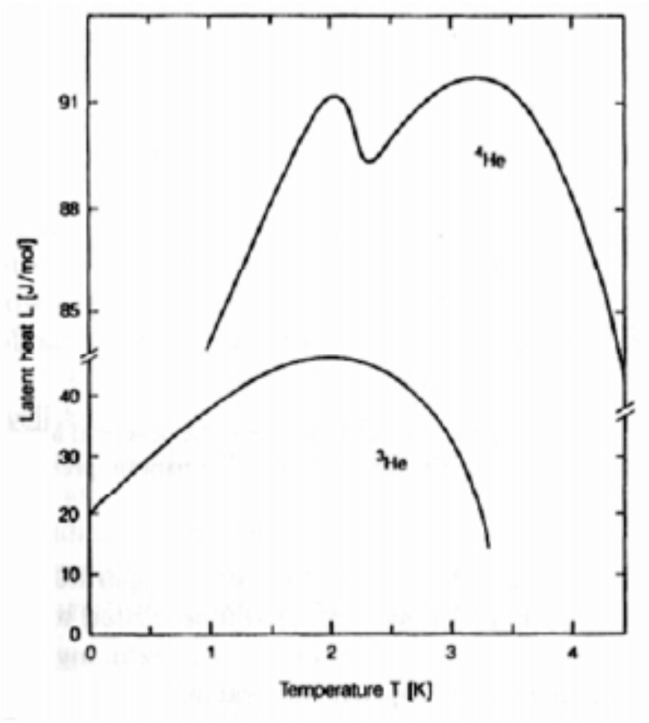

Fig..4.1. Latent heats of ^{3}He and ^{4}He. (Wilks and Betts, 1987)

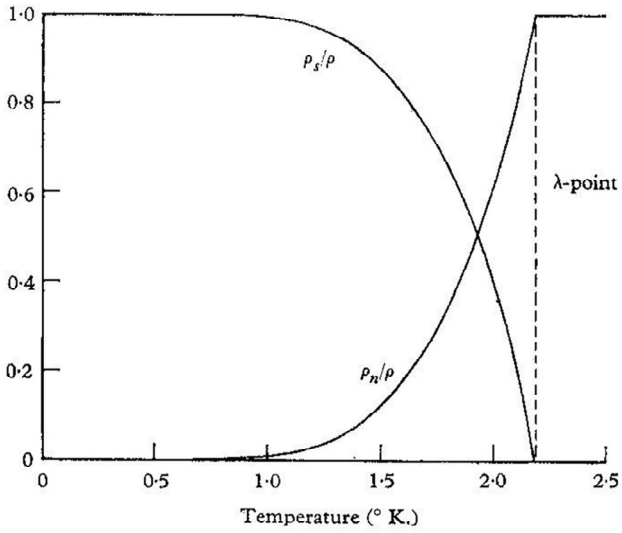

Fig..4.2. Normalised densities of the superfluid and normal components of ^{4}He as functions of temperature below the lambda point. (Atkins, 1959)

The latent heat of liquid helium is very low in both phases of the liquid, Fig. 4.1. Only a small amount of energy is therefore needed to vaporise the liquid and create vapour. Below the λ-point the liquid is a mixture of He I and He II. The normal density (ρ_n) and the superfluid density (ρ_s) are observed in the fluid by their individual characteristics. The ρ_n creates a drag force in the liquid while ρ_s enables the He II to easily pass through tiny gaps. The properties of this mixture are explained by the two fluid model of superfluid liquid Helium (Landau 1941). The density of each component is a function of temperature, Fig. 4.2.

4.1.3. Electron Field Emission and Field Ionisation

For an excellent discussion on field emission and field ionization in liquid ^{4}He see Phillips and McClintock 1974 (Phillips and McClintock 1974). Application of a high E-field over a point or spike on the cathode electrode enables electrons in the cathode to escape from its surface. This process is known as electron field emission. They escape via a tunnelling process of which the barrier thickness is a function the electric field. Once free of the metal surface the electron accelerates away from the anode. Alternatively when a positive potential is applied to the anode the high E-field around the tip or spike on its surface can cause electrons to tunnel out of an atom in the dielectric medium. This leaves behind an ion which then accelerates away from the anode under the E-field.

The well known Fowler Nordeheim (FN) (Latham 1995) equation gives the emission current density (J) as

$$J = A \left(\frac{E_F}{\Phi}\right)^{1/2} (E_F + \Phi)^{-1} E^2 \exp\left(\frac{\left(-B\Phi^{3/2}\right)}{E}\right)$$

where E_F is the Fermi energy, Φ is the work function of the surface, E the E-field and A and B constants. We can see that J is proportional to the exponential of the E-field. This

equation assumes a flat electrode surface. In practice experiments differ from calculation due to an increased E-field as a result of the electrode surface roughness.

4.1.4. Breakdown in Liquid ^{4}He under SVP

Many authors have studied liquid ^{4}He breakdown under SVP. These measurements were all made in pumped helium baths at temperatures between 4.2 K (760 torr) and 1.2 K (< 1 torr). In such measurements the liquid ^{4}He in the main bath acts both as the dielectric medium and the cryogenic coolant. To reduce the temperature below 4.2 K the LHe^4 is pumped on and cools by evaporation. Hence, as the temperature is reducing so too does the pressure in the liquid. Karamath (2007) has collated all the available data and Fig 4.3 displays breakdown voltage as a function of electrode separation and temperature. The highest breakdown voltage data points taken by Long et al (2006) are noteworthy. They obtained breakdown at ~ 700 kV between large (45.8 cm) diameter parallel plate electrodes at relatively large electrode separation (≤ 7.2 mm). This reduced to ~ 250 kV when the liquid ^{4}He was in the superfluid state.

In his own work on breakdown voltage as a function of temperature, shown in Fig.4.4, Karamath (2007), found that for a set of quasi-parallel plate electrodes a reduction in V_{bd} by a factor of ~ 2 on going from 4.2 K to 1.4 K. The indicated pressure in this Fig is actually the SVP above the liquid Helium bath, whereas the total pressure in the helium between the electrode is

$$P_{total} = \rho g h + P_{SVP}$$

where $\rho g h$ is the hydrostatic pressure and P_{SVP} is the SVP. On first inspection the data might be interpreted as a temperature dependence of the breakdown voltage, with some indication of a plateau below the superfluid transition at 2.17 K. However, as Karamath

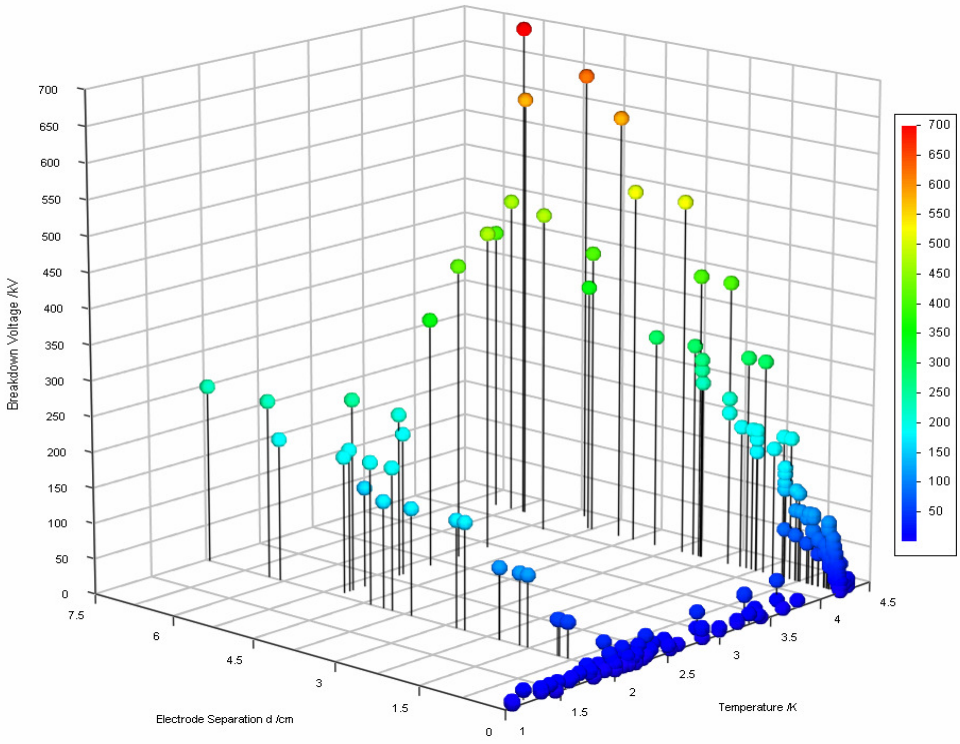

Fig..4.3. Plot of $V_{bd}(d,T)$ from Karamath (2007) of all known voltage breakdown events as a function of electrode separation and temperature in uniform electric fields.

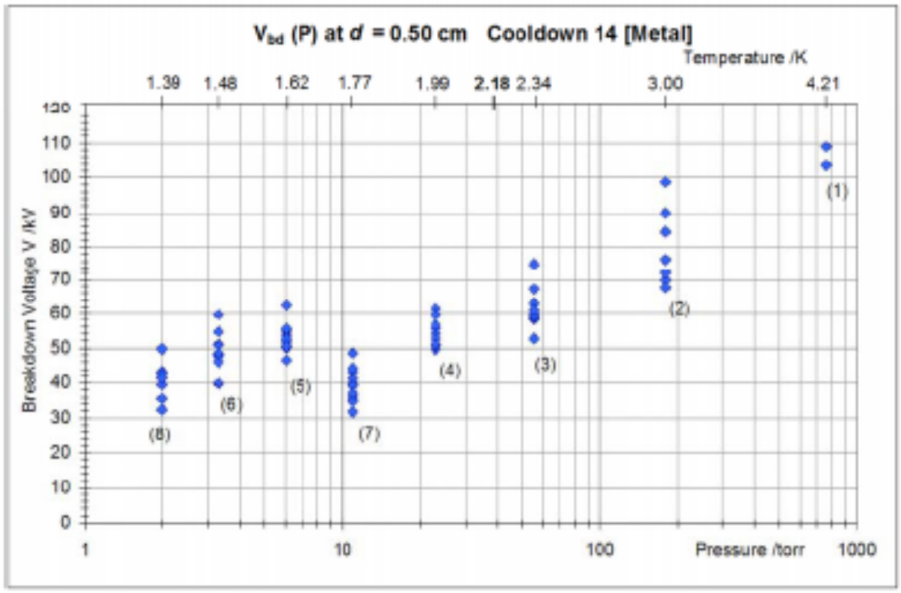

Fig..4.4. Breakdown as a function of temperature and SVP for quasi-parallel plate electrodes at 5mm separation. The measurements were made in a pumped bath cryostat (Karamath 2007).

points out, the estimated hydrostatic contribution in this particular experiment was about 10 torr, Hence, it is not possible to say from such data whether the primary variation is due to temperature or pressure. For a detailed review of breakdown in liquid ^{4}He under SVP see Karamath (2007).

4.1.5. Electrode Surface Roughness, Material and Area

It is widely accepted that each breakdown is triggered from the "weakest" point on the electrode surface, where the local field is highest. Therefore, breakdown voltages can be increased by reducing the number of such points, thus making the surface finish an important parameter. May and Krauth (1981) have carried out breakdown experiments on spherical Niobium electrodes with differing surface finishes in liquid ^{4}He. Over a range of separations between 0.5 mm and 2.5 mm the difference in breakdown voltage between electropolished and mechanically polished electrodes is between 12% and 20%, as shown in Fig.4.5. The electropolished electrodes have a surface finish of the order of 10 nm and that of mechanically polished is of the order 100 nm.

Gerhold (1989) has also completed tests on electrodes with different surface finishes in liquid ^{4}He with a polished electrode showing a factor of ~ 2 improvement over a mechanically ground one.

Similar reductions in breakdown voltage have been observed by other authors for other dielectric liquids (Hayakawa et al, 1997; Hara, 2008). It is therefore fairly clear that the dielectric strength of a cell can be increased by having extremely smooth electrodes and the data suggest that electropolishing produces the highest breakdown voltages.

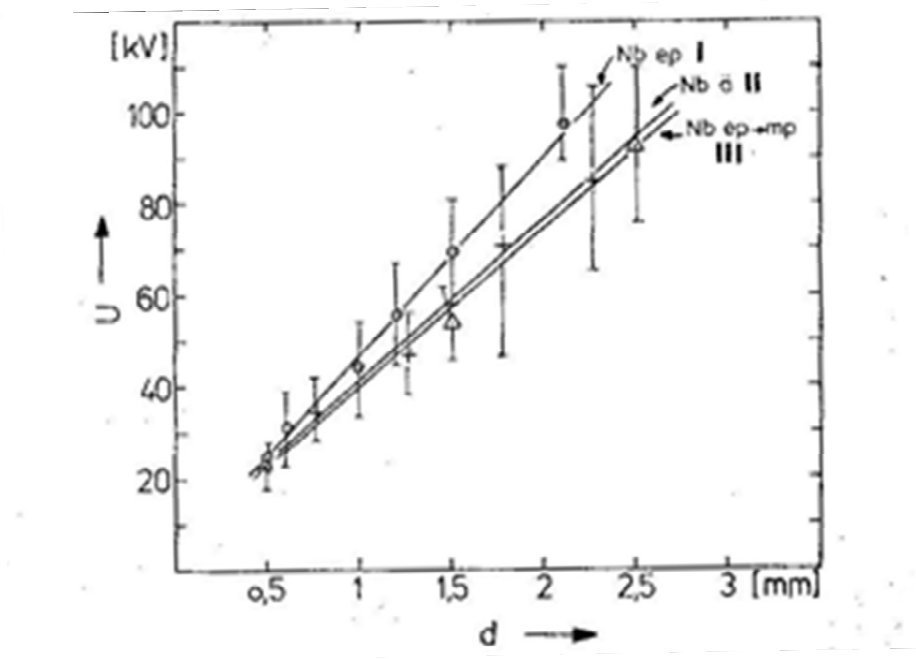

Fig..4.5. AC breakdown voltage in liquid helium as a function of separation for Nb spheres with different surface finishes. Nb ep I: electropolished; Nb ä II: etched electrodes; Nb ep →mp III: electropolished then mechanically polished. (May and Krauth, 1981).

May and Krauth (1981) also investigated 50mm diameter electrodes made from different material to compare the effect this has on the breakdown in liquid helium, as shown in Fig.4.6.

These authors found that electropolished Niobium had the highest breakdown voltage but that ball bearing steel (sample K in the Fig. 4.6.) also exhibited high values.. They suspected this to be due to an oxide layer over the surface. A stainless steel sample (CrNi) had a lower breakdown voltage which was not improved even after extensive mechanical polishing. This was attributed to the rougher microscopic structure of the steel. Two Brass electrode pairs were tested (Ms). One was cooled slowly and the other very quickly. A large reduction in breakdown voltage is observed for the electrodes that were cooled rapidly. On inspection, these electrodes had micro-cracks on the surface, thought to have been formed during the cool down from stresses induce by large thermal gradients.

Chapter 4 Factors Affecting High Voltage Breakdown in Liquid ^{4}He and Other Liquids

In a classic paper, Weber and Endicott (1956), presented breakdown voltage as a function of electrically stressed electrode surface area in transformer oil. This paper is notable for the rigor of the statistical analysis and of the experimental technique used.

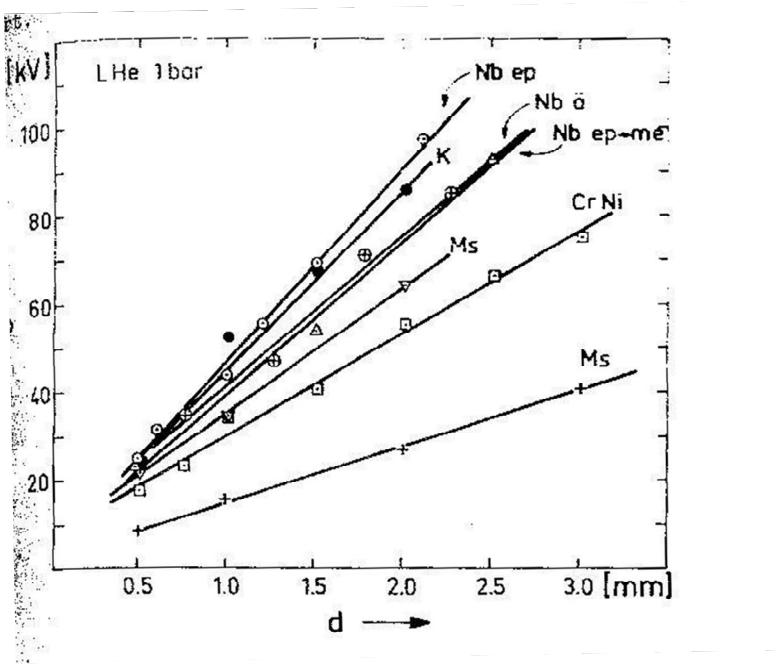

Fig..4.6. AC breakdown voltage in liquid helium at 4.2K under SVP as a function of separation for different electrode materials. (May and Krauth, 1981) .

Four pairs of different area Rogowski profile (see section 5.2.3.) electrodes were used, each pair with the same separation of ~ 1.9 mm. After a large numbers of measurements between each set of electrodes, they found that the average breakdown voltage showed a weak decrease with increasing area, as shown in Fig. 4.7. The mode breakdown value dropped from 55.65 kV to 45.56 kV when the relative areas changed by a factor of 20.

They also observed a reduction in breakdown strength of between 2 % and 6 % over a run of 200 breakdowns. This was attributed to either roughening of the electrode surface due to breakdown or a buildup of discharge products in the high-field region, or to a combination

of these factors. No significant differences were found when the orientation of the electrodes was changed from horizontal to vertical.

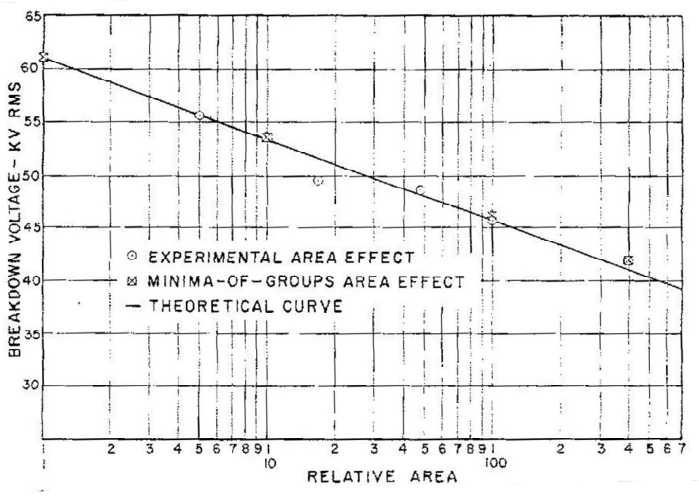

Fig..4.7 The effect of the relative electrode area on the breakdown voltage in transformer oil. (Weber and Endicott, 1956).

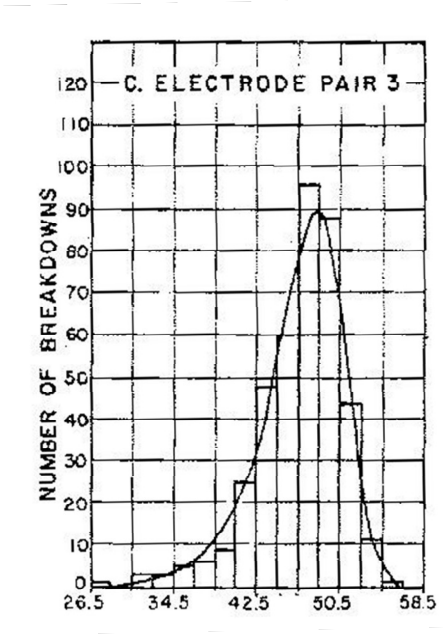

Fig..4.8 Extremal value probability distribution observed for breakdown between a set of parallel plate electrodes in transformer oil. (Weber and Endicott, 1956)

Weber and Endicott also showed clearly that their data were best represented by an extreme value distribution, rather than a normal one, as shown in Fig.4.8. This is understandable qualitatively: As breakdown always initiates from the weakest point in the system at any particular time, the distribution is skewed towards lower voltages.

Similar trends in breakdown fields with electrode area have been found by (Hayakawa et al, 1997) in liquid N_2. They correlated their measurements with those from other workers and deduced that $E_b = 105(A)^{(-1/6.23)}$ kVpeak mm^{-1} over five orders of magnitude in area as shown in Fig. 4.9.

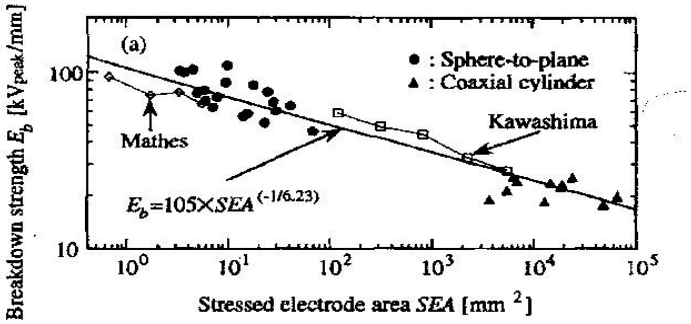

Fig..4.9 Breakdown field as a function of electrode area for liquid N_2. (Hayakawa et al, 1997)

4.1.6. Liquid Purity and Stressed Volume

As mentioned above, the purity of the dielectric liquid also affects breakdown strength since charged matter will accelerate in high field regions and the resulting impact with an electrode can trigger breakdown. Since the total number of impurities will increase with cell volume, a decrease in breakdown fields might be expected for larger cells.

Yoshino et al (1982) measured breakdown fields in commercial grade and purified liquid ^{4}He using 6 μs pulsed fields, finding a factor of ~ 2 higher in the purer material. They

also found a weak dependence on electrode separation, as shown in Fig.4.10, which appears to be approximately the same for both grades of helium. It should be noted that they were using very small cells.

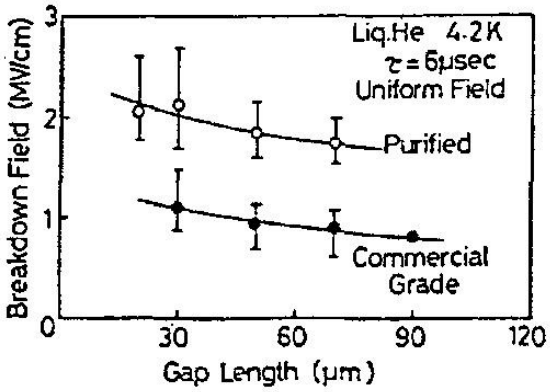

Fig. 4.10. Breakdown in different purities of liquid ^{4}He at 4.2K as a function of electrode separation. (Yoshino et al 1982)

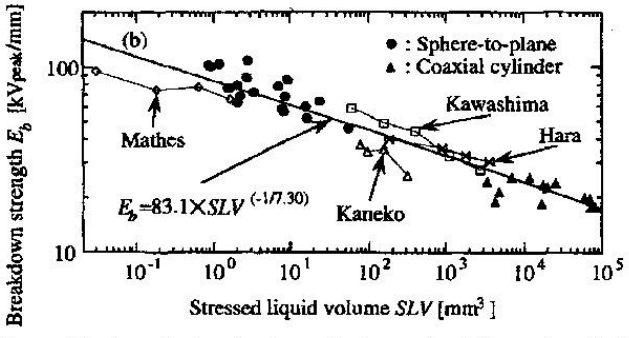

Fig. 4.11. Deduced breakdown fields in LN_2 as a function of stressed liquid volume. (Hayakawa et al, 1997)

A study of breakdown as a function of the level of particulate contamination in liquid ^{4}He has been made by Wu (1996). A parallel plate geometry with 1 mm separation was used and particles between 50μm and 200μm were introduced into the helium. Such particles of non-metallic fiberglass (G-10CR) showed no effect on the breakdown field. However,

similar sized metallic particles of aluminium or Sn:Pb alloy (solder) reduced the breakdown field by up to a factor of 2. The experiments were carried out at 4.2 K and 2.15 K under 1 bar pressure but there was no evidence for any temperature dependence.

Hayakawa et al (1997) have examined the effect of stressed volume on breakdown in LN_2 by comparing their work and that of others, as shown in Fig.4.11. In a similar manner to their analysis of the stressed area effect, they find the power law dependence of the breakdown field on volume as $E_b = 83.1\ (S)^{(-1/7.30)}$ kVpeak mm^{-1}, where S is the stressed liquid volume, in this case is over seven orders of magnitude.

4.1.7. Breakdown Repetition Rate, Polarity and Geometry

Coletti et al (1982) looked at the effect of varying time intervals between adjacent breakdowns in liquid ^{4}He. They found that short intervals resulted in a reduction in breakdown voltage but that would recover after ~ 4 minutes. Furthermore, they found no degradation in breakdown voltage as a function of run time for 80 breakdowns taken 4 minutes apart, arguing that this interval is sufficient to restore maximum dielectric strength. This finding differs from that of Weber and Endicott (1956) who saw a reduction in the mean breakdown voltage as a function of event number in transformer oil. However, Weber and Endicott did take 2.5 times more data points during each run.

Oliver (1981) also looked at breakdown voltage as a function of run number for spherical 20 mm diameter brass and steel electrodes in liquid ^{4}He. The trend is generally the same for both sets of electrodes and is shown in Fig. 4.12. A higher breakdown voltage is observed at the start of the run which reduces sharply over about 8 breakdowns. Thereafter, the voltage decreases with a weak linear dependence.

The shape and polarity of the electrodes also affects the breakdown voltage. The general consensus is that breakdown in liquid ^{4}He is initiated at the cathode. Data from

Yoshino et al (1982) are shown in Fig. 4.13. This shows lower breakdown for a point-to-plane geometry when the needle is negative. This finding is also reported by Hara et al (1993). Yoshino et al's data also showed that the surface finish of the negative electrode has a more important effect on breakdown than that of the anode.

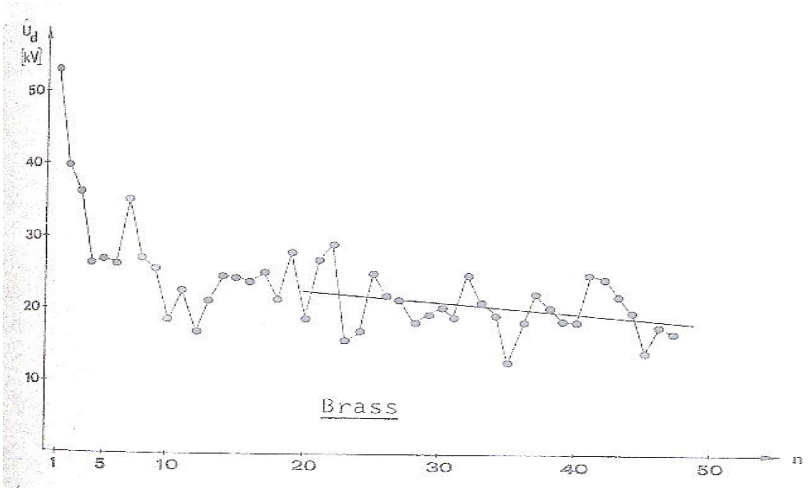

Fig..4.12. Breakdown voltage as a function of run number for spherical brass electrodes in liquid ^{4}He. (Oliver 1981)

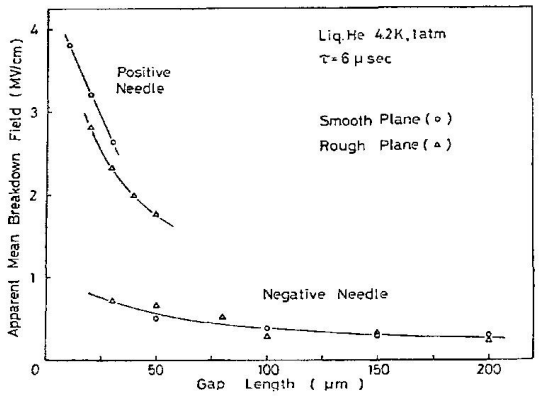

Fig..4.13. Effect of polarity and surface finish on breakdown in liquid ^{4}He at 4.2K. (Yoshino et al,1982)

The orientation of the electrodes may also influence breakdown. Horizontal electrodes may collect impurities on their surface and trap vapour bubbles whilst vertical electrodes will allow dust and impurities to fall out of the E-field region and allow vapour bubbles to rise to the surface. However, Weber and Endicott (1956) found no dependence on orientation for tests in transformer oil, but they went to considerable lengths to ensure that all debris was removed from the breakdown cell after each run.

4.2. High Voltage Breakdown as a Function of Pressure in Liquid ^{4}He and Other liquids

4.2.1. Pressure Dependence of Breakdown in Liquid ^{4}He

Breakdown of pressurised liquid ^{4}He above and below the λ-point has been investigated by a number of groups and all the work is reviewed here. A full list is given in Table 4.1, towards the end of this chapter. These studies were prompted by a number of applications ranging from superconducting magnets for energy storage and fusion science, superconducting power devices and, most recently, for the US collaboration nEDM experiment.

Data from Wu (1996), Hara (1993) and Huffer (2008) is discussed first since their measurements were in pressurised He II. Wu carried out tests for The Superconducting Magnetic Energy Storage – Engineer Test Model (SMES-ETM) project. These were conducted under similar conditions to that expected in the operation of this system, with a pressure of ~ 1 atmosphere being held over the liquid ^{4}He at all temperatures ranging from 1.8 K to 4.2 K. Hara's investigations were related to the electrostatic properties of large scale superconducting magnets for nuclear fission applications. The minimum temperature at which Hara recorded breakdown data in He II was 2.03 K at 1 atmosphere and 1.7 K at SVP.

The group based at the Indiana University Cyclotron Facility (IUCF) have carried out work on pressurised He II for the SNS Neutron Electric Dipole Moment (nEDM) experiment. (Huffer 2008, Karcz et al 2009).

Hara and Huffer see a clear dependence with changing pressure whereas Wu works at a constant pressure. However, by comparing Wu's data as a function of temperature at a constant 1 atmosphere with work at SVP, it is possible to infer a pressure dependence at constant temperatures below 4.2K.

The apparatus used by Wu, Hara and Huffer have some similarities. All implement a similar principle to cool the liquid helium while being able to vary the pressure above SVP by using a double helium volume. The outer volume, the main bath, is used to control the temperature of the liquid in the inner volume. However, it is not completely clear how Wu or Hara pressurise the ^{4}He in the cell volume. Huffer does this using helium gas from a gas bottle at room temperature, via a small capillary.

In Wu's case three electrode geometries, parallel plate, point-to–plane and coaxial were used. The electrodes were made from polished Al and their separation could be adjusted at low temperature. Hara used stainless steel sphere-to-sphere and electrodes and a point-to-plane pair made from tungsten and stainless, respectively. It is unclear exactly which electrode geometry Huffer used as reference is made to both parallel plate and sphere-to-plane stainless electrodes (Karcz et al, 2009). It is likely that this groups measurements were limited to about 20kV by the HV feedthrough used.

4.2.2. Wu - Pressure Dependence of Breakdown in Liquid ^{4}He

Figure 4.14 shows breakdown voltage against electrode separation at 1.93K under 1 bar. The data clearly shows that as the separation, d, is reduced V_{bd} decreases. A curved trend line is drawn through the data and it is stated that the relationship is not linear. However, given the scatter in the data, this conclusion seems unwarranted.

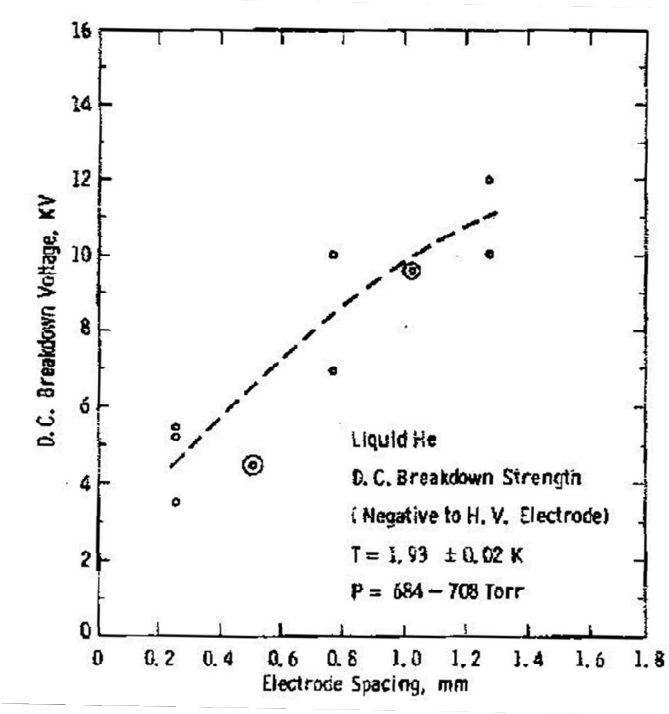

Fig..4.14. Breakdown voltage as a function of electrode spacing in liquid ^{4}He at 1.93K under 1 bar pressure. (Wu, 1996)

Figure 4.15 shows Wu's data for V_{bd} from 4.2 K to just below 2 K for different parallel plate electrode separations, with the pressure being kept at 1 bar throughout.

Although different trend lines have been drawn for each separation, the scatter in the raw data points do not seem to justify these differences. The only clear trend seems to be that

the V_{bd} values remains fairly stable as the liquid ^{4}He temperature reduces from 4.2 K to below 2 K (and hence into the superfluid phase). For a separation of 1.27 mm the average V_{bd} is ~14 kV, corresponding to ~110kV/cm and at 0.254 mm the V_{bd} of ~ 3.75 kV is equivalent to ~147 kV/cm.

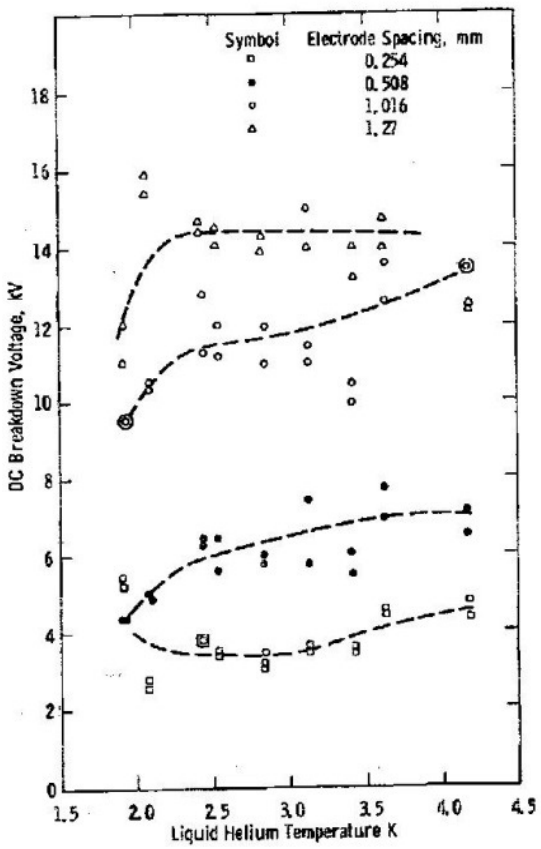

Fig..4.15. Breakdown voltage as a function of temperature for liquid ^{4}He under 1 bar pressure. (Wu 1996)

Although Wu compares the indicated trends with temperature in Fig. 4.15. to the results of Blank and Edwards (1960) and those of Hwang (1978), both of these latter studies were conducted on liquid ^{4}He under SVP and so follow similar behaviour to that shown in Fig. 4.4.

4.2.3. Hara - Pressure Dependence of Breakdown in Liquid ^{4}He

Hara (1993) carried out breakdown tests from 4.2 K to just below the λ transitions with the pressure held at 1 bar. Four different separations of sphere-to-sphere electrodes were used and in all cases no significant change in breakdown field was seen as the temperature was reduced. These data are shown in Fig. 4.16 and essentially agrees with Wu's data in Fig.4.15, as the breakdown voltage remains fairly constant with reduced temperature, in Fig.4.15 although Hara shows very few data points

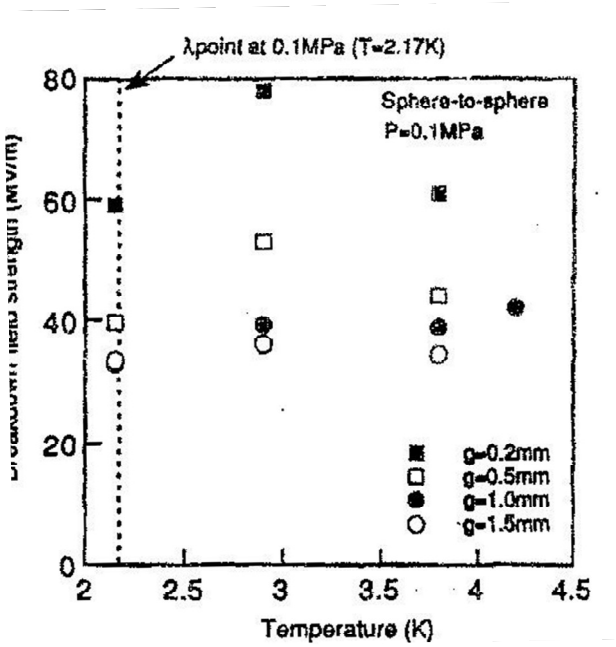

Fig. 4.16 Sphere-to-sphere breakdown field as a function of temperature for liquid ^{4}He under 1 bar pressure. (Hara 2008)

Figure 4.17 shows Hara's data for breakdown field against electrode separation for sphere-to-sphere geometry. In this case the temperature was held at ~2 K while the pressure was varied from SVP to 1 bar. At electrode separations above 0.5 mm there is clear pressure

dependence. The overall breakdown field reduces with increased gap length and Hara attributes this to a volume effect. However, at electrode separations ≤ 0.1 mm there is very little pressure dependence. Hara points out that, although there is only a small dependence on pressure at small separations, the breakdown field is still higher than those of larger electrode separations with applied pressure.

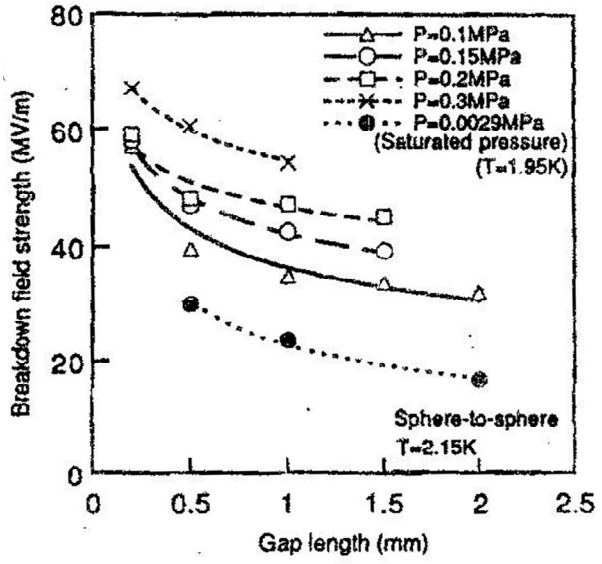

Fig..4.17. Sphere-to-sphere breakdown fields in superfluid liquid ^{4}He at various separations and pressures. (Hara, 2008)

A point-to-plane electrode geometry was also investigated by Hara. Data were taken at constant temperature as a function of pressure, shown in Fig.4.18, and at constant pressure as a function of temperature, Fig.4.19. At a constant temperature, and with the needle negative, there was little or no pressure dependence. For positive polarity, a slight increase in breakdown voltage was observed with increasing pressure. At constant pressure, with the needle negative, there was no change in breakdown behaviour when the temperature was

reduced from 4.2 K to below the superfluid transition. However, for the positive needle, an increase in breakdown voltage was observed with reducing temperature.

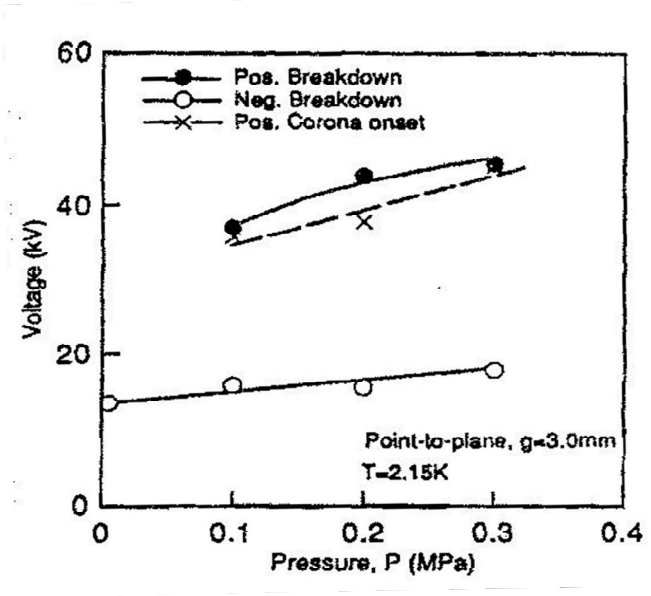

Fig..4.18. Point-to-plane breakdown voltages as functions of pressure for liquid ^{4}He at 2.15K. (Hara 2008)

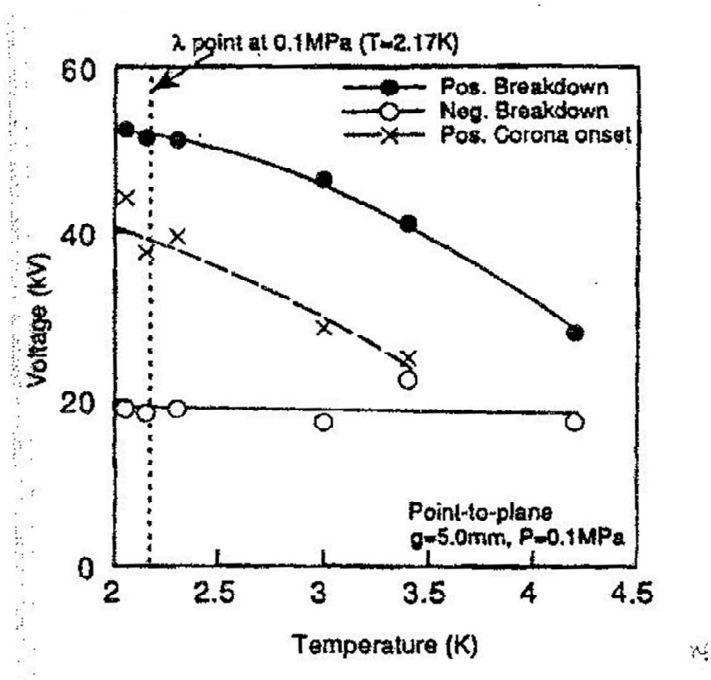

Fig..4.19. Point to-plane breakdown voltages as functions of temperature for liquid ^{4}He under 1 bar pressure. (Hara 1993)

Hara argues that when the needle is negative, breakdown is initiated by field emitted electrons from the cathode tip and that this current is independent of the temperature and pressure of the helium. When the tip is positive, he proposes that the pressure dependence is due to breakdown occurring in a bubble created around the positive tip. This bubble hypothesis is strengthened by the fact that at a larger electrode separation Hara observes a stable glow caused by corona discharge around the positive tip. To maintain such a vapour bubble, a certain amount of energy is required and he proposes two mechanisms. The first of these is Joule heating by field ionisation of helium atoms and the second is the movement of dielectric particles by dielectrophoresis (Gerhold 1972).

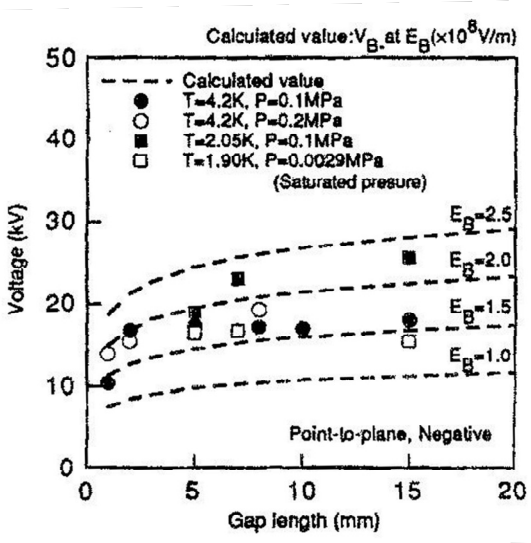

Fig..4.20. Calculated and measured point to-plane breakdown voltages as functions of electrode separation in liquid ^{4}He. $E_B(\times10^8\,\mathrm{V m^{-1}})$ is the field at the tip (Hara 2008).

For the uniform field case of the parallel plate electrodes, Hara suggests that at very small separations there is no pressure dependence as the breakdown is caused by field emission from the cathode surface. At larger electrode separations there is a greater stressed volume of liquid between the electrodes and the number of impurity particles between the

electrodes is larger. Hara suggested this increases the probability of bubble creation and the size of the bubble is then affected by variations in pressure.

Figure 4.20 shows Hara's calculated breakdown voltages as a function of electrode separation for a negative tip, together with his data. The breakdown values were calculated using a charge simulation method but no details of this are presented. Hara argues that the calculated breakdown voltages agree with the data if the electric field producing field emission from the tip is higher than 10^8 Vm^{-1}.

4.2.4. Huffer (IUCF) - Pressure Dependence of Breakdown in Liquid ^{4}He

Figure 4.21 shows the breakdown fields obtained by Huffer (2008) as a function of temperature and pressure. Data was taken first at 4.2 K at SVP. The breakdown cell was then cooled to below 2 K under SVP and data taken again. Next the cell was gradually pressurised and a sequence of data taken below the lambda transition at several pressures.

The cell was then warmed to just above the transition and further data were taken at ~ 1 bar. Finally, the cell was depressurised back to SVP and data taken as the temperature (and SVP) rose. The factor of 2.5 drop in breakdown field on cooling under SVP is as expected from previous data. Pressurising the superfluid to 125 torr appears to restore it fully to its 4.2 K breakdown value whilst further increase in pressure has little effect on the breakdown E-field. On releasing the pressure, the warm-up data under SVP closely resembles that taken by Karamath (2007) and others.

The cell was then warmed to just above the transition and further data were taken at ~ 1 bar. Finally, the cell was depressurised back to SVP and data taken as the temperature (and SVP) rose. The factor of 2.5 drop in breakdown field on cooling under SVP is as expected

from previous data. Pressurising the superfluid to 125 torr appears to restore it fully to its 4.2 K breakdown value whilst further increase in pressure has little effect on the breakdown E-field. On releasing the pressure, the warm-up data under SVP closely resembles that taken by Karamath (2007) and others.

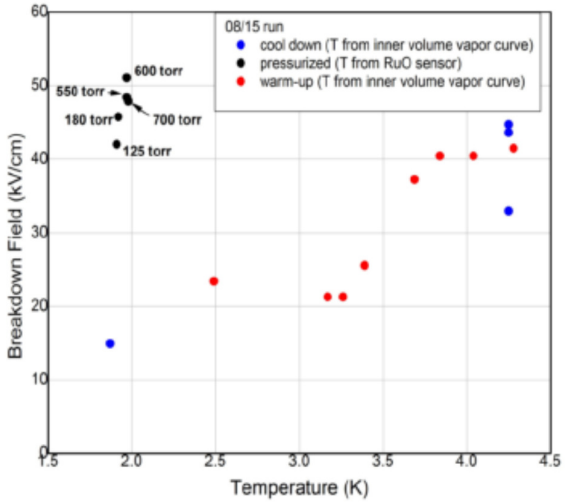

Fig..4.21. Breakdown field measurements as a function of temperature and pressure in liquid ^{4}He. Blue symbols: cooling under SVP; Black symbols: increasing pressure at T >2.17K; Red symbols: warming under SVP. (Huffer, 2008)

After modifications to their apparatus, Huffer took further data, shown in Fig.4.22 and which he claims exhibits hysteresis in the breakdown field as a function of pressure at roughly constant temperature. The sequence of measurements was broadly the same, cool under SVP to the superfluid phase, pressurise at approximately constant temperature, depressurise at constant temperature and then warm. The main difference in this second set of data was that the breakdown field was reported to remain at a high value after depressurising (the green symbols in Fig.4.22).

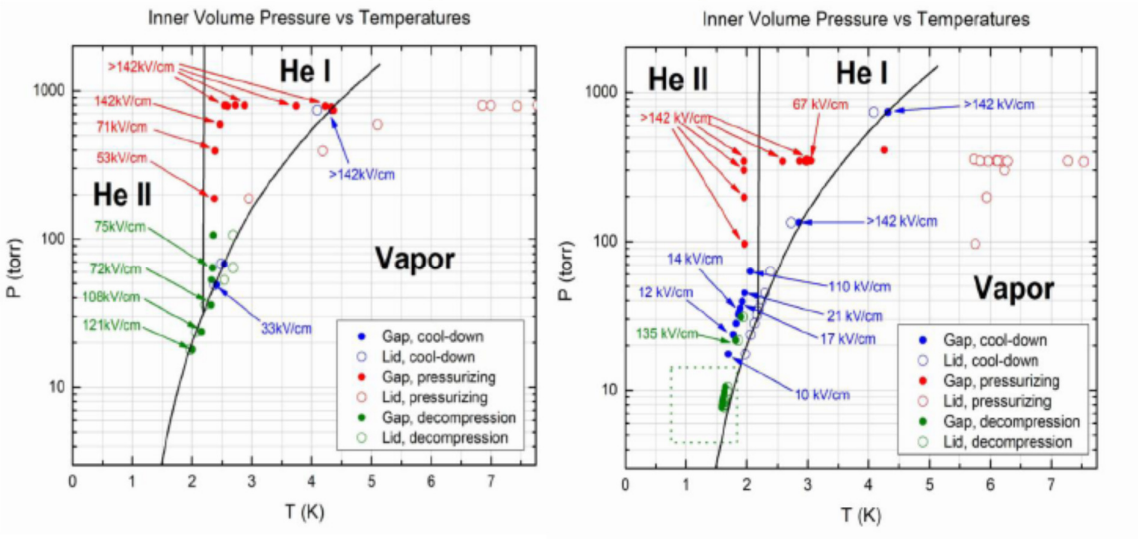

Fig..4.22. Second breakdown field measurements as a function of temperature and pressure in liquid ^{4}He. Blue symbols: cooling under SVP; Red symbols: increasing pressure at T < 2.17K; Green symbols: after depressurisation. (Huffer, 2008)

In this second data set, the breakdown field varied by more than a factor of 4 on cooling under SVP and on pressuring at low temperature.

The IUCF group have hypothesised that the apparent hysteretic behaviour is related to the suppression of quantum vortices in the superfluid. We shall return to this topic when discussing our results in section 7.1.4 and will present a more prosaic possible explanation for the observations.

4.2.5. Summary of Pressure Dependent Studies of High Voltage Breakdown in Liquid ^{4}He

A number of other authors have made breakdown measurements in pressurised liquid He I. These have mostly been made at 4.2 K and in general some increase in breakdown voltage is observed at higher pressures. Burnier et al, (1970) found a factor of 1.3 increase on changing the pressure from 1 to 3bar, Meats (1972) a factor of 1.9 between 1 and 8 bar.

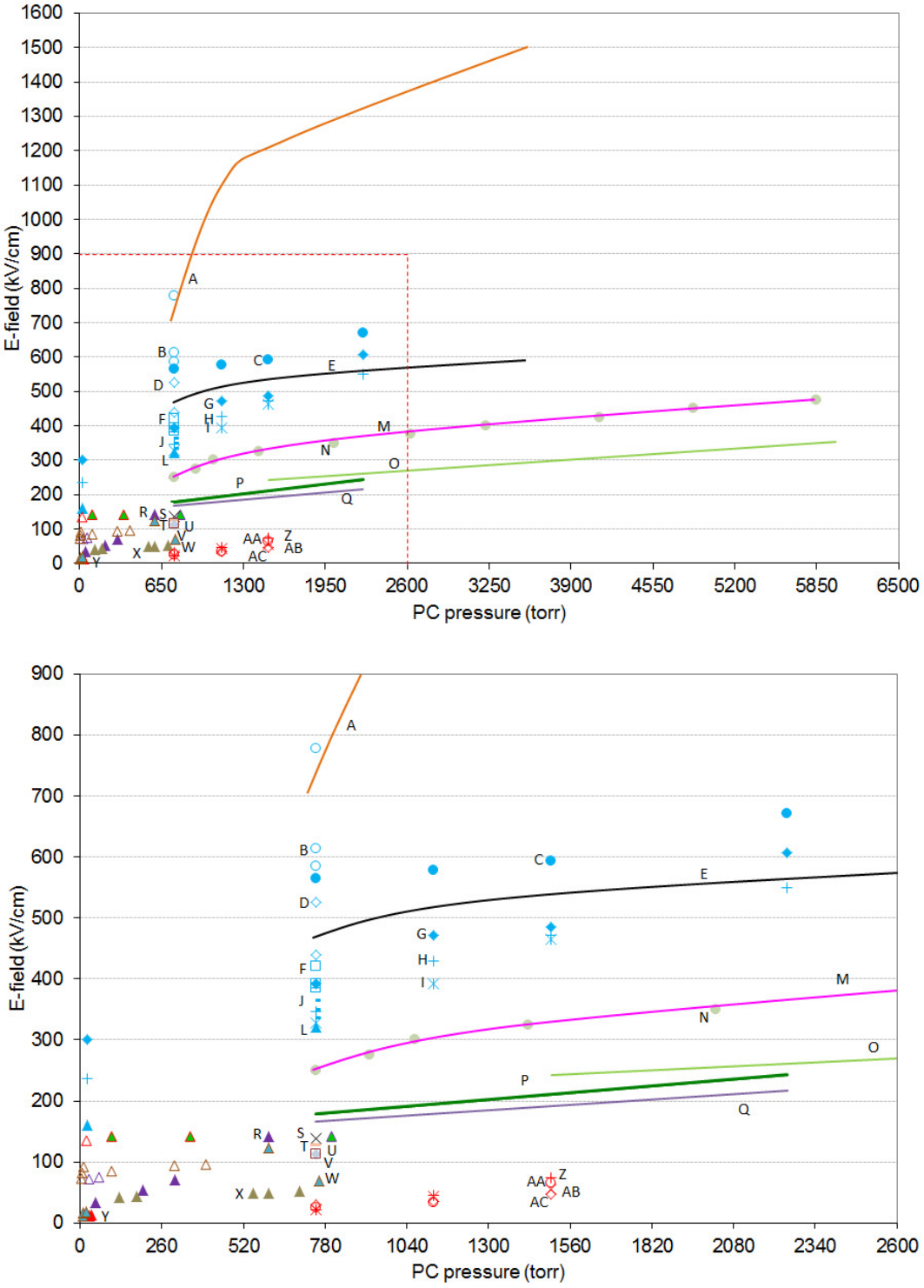

Fig..4.23. Summary plots of all known data for breakdown field in liquid ^{4}He as a function of pressure. The key to the symbols are given in Table 4.1 below.

Data Set	*Symbol*	*Separation (mm)*	*Temperature (K)*	*Electrode Profile*	*Comments*	*reference*
A	(line)	0.1	4.2	Plane/Sphere	6 µs Pulsed.	Yoshino (1982)
B		0.2	2.1 to 3.8	Sphere/Sphere	25 mm Ø dc	Hara (1993)
C		0.2	1.95	Sphere/Sphere	25 mm Ø dc	Hara (1993)
D		0.5	2.1 to 3.8	Sphere/Sphere	25 mm Ø dc	Hara (1993)
E	(line)	0.5	4.2	Sphere/Sphere	50 mm Ø dc	Gerhold (1989)
F		1	2.9 to 4.2	Sphere/Sphere	25 mm Ø dc	Hara (1993)
G		.5	1.95	Sphere/Sphere	25 mm Ø dc	Hara (1993)
H		1	1.95	Sphere/Sphere	25 mm Ø dc	Hara (1993)
I		1.5	1.95	Sphere/Sphere	25 mm Ø dc	Hara (1993)
J		1.5	2.1 to 4.2	Sphere/Sphere	25 mm Ø dc	Hara (1993)
L		2	1.95	Sphere/Sphere	25 mm Ø dc	Hara (1993)
M	(line)	1	4.2	Plane/Plane	60 mm Ø dc	Meats (1972)
N		1	4.2	Plane/Plane	60 mm Ø dc	Meats (1972)
O	(line)	1.7	4.2	Plane/Sphere	15 mm Ø ac	Fallou (1970)
P	(line)	1	4.2	Sphere/Sphere	62.5 mm Ø	Burnier (1970)
Q	(line)	2	4.2	Sphere/Sphere	62.5 mm Ø	Burnier (1970)
R		Not stated	2.3	Not stated		Huffer (2008)
S		0.254	2 to 4.2	Plane/Plane	62.6 mm Ø dc	Wu (1996)
T		0.508	2 to 4.2	Plane/Plane	62.6 mm Ø dc	Wu (1996)
U		1.016	2 to 4.2	Plane/Plane	62.6 mm Ø dc	Wu (1996)
V		1.27	2 to 4.2	Plane/Plane	62.6 mm Ø dc	Wu (1996)
W		Not stated	1.8 to 2.1	Not stated		Huffer (2008)
X		Not stated	2	Not stated		Huffer (2008)
Y		Not stated	1.8	Not stated		Huffer (2008)
Z		5	4.2	Uniform field	Electrode/ Superconducting Wire coil. dc	Chigusa (1999)
AA		3	4.2	Uniform field	Electrode/ Superconducting Wire coil. dc	Chigusa (1999)
AB		7	4.2	Uniform field	Electrode/ Superconducting Wire coil. dc	Chigusa (1999)
AC		9	4.2	Uniform field	Electrode/ Superconducting Wire coil. dc	Chigusa (1999)

Table..4.1 Key to Fig.4.23.

Yoshino (1982) presented data obtained using pulsed voltage on a sphere-to-plane geometry with a 0.1 mm gap. Yoshino found field values of 70 kV/cm at 1 bar, increasing to 1500 kV/cm at 4.7 bar. These extremely high fields are probably a result of the very small gap and the pulsed voltage.

Figure 4.23 and Table 4.1 summarise all known data on the pressure dependence of high voltage breakdown in liquid ^{4}He. From this review, it is clear that for both He I and He

II breakdown values increase with increased pressure. In general, the 4.2 K data seems to show the largest differential dE_{bd}/dP near the SVP and then to increase rather slowly at higher pressures. The detailed behaviour below 4.2 K is not yet clear, particularly in the superfluid phase. This is due both to the lack of data and to the wide differences in the experimental configurations used.

4.2.6. Pressure Dependent Breakdown in Other Liquids

In order to understand the pressure dependence of breakdown in liquid ^{4}He, it is useful to consider the behaviour in other dielectric liquids. This section reviews such data taken in transformer oil (Cavallos et al, 2005), liquid N_2 (Hayakawa et al, 1997) and liquid H_2 (Gerhold, 1979).

A point-to-plane geometry was used by Cavallos et al to investigate breakdown in transformer oil under reduced pressure from essentially vacuum to ~1 bar, as shown in Fig.4.24. The point had a radius of 40 µm and the separation between the electrodes was 2.5 mm. With the tip at negative potential, a critical pressure (P_c) was identified at ~ 100 torr, below which the breakdown voltage decreased rapidly, whereas above P_c a linear dependence was observed. A positive tip showed a lower breakdown value but with a linear dependence for all pressures between 2 torr and 760 torr. The gradient of this slope was approximately the same as that found above P_c when the tip is negative.

Cavallos et al also investigated the size and dynamics of vapour bubbles created in transformer oil as a function of pressure and related this to the breakdown voltage (see section 4.2.3.).

Hayakawa et al (1997) looked at breakdown in liquid N_2 as a function of applied pressure in the range from 1 to 5 bar, using AC at 60 Hz. They used both sphere-to-plane electrodes and also pairs of coaxial cylinders whose area and stressed volume was ~ 3 times

larger than the sphere-to-plane configuration. In addition, the coaxial cylinder arrangements were also fitted with a heater which provided a continuous source of thermal bubbles during experiment on these electrodes. Tests were made on both types of electrodes with < 1µm mirror finishes and coaxial electrodes with a rougher surface of ~ 200 µm.

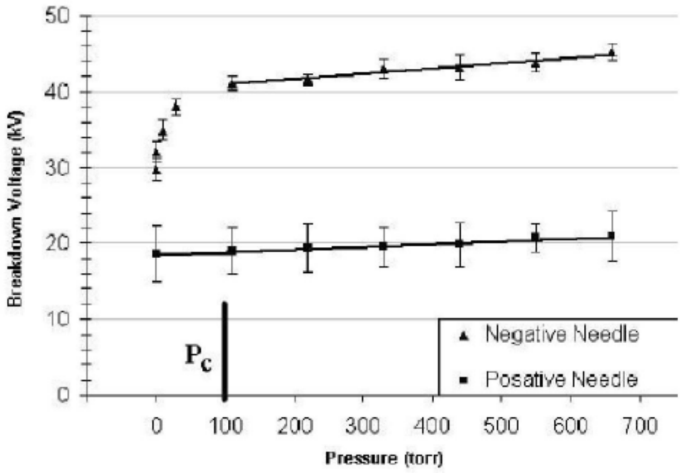

Fig..4.24. Pressure dependence of the breakdown voltage in transformer oil for a point-to-plane geometry with 2.5 mm separation. (Cavallos et al, 2005)

Figure 4.25 shows the breakdown field as a function of pressure for each of the configurations. The mirror-finish coaxial-with-bubbles experiment shows the most rapid initial increase in breakdown with pressure, after which it saturates. The authors argue that thermal bubbles between the electrodes reduce in size and number as a result of pressurisation and that eventually the dominant factor in breakdown changes from bubbles in the gap to impurities in the liquid N_2.

With regard to the sphere-to-plane electrodes, Hayakawa et al, suggest that the small stressed volume leads to breakdown being initiated in bubbles forming on micro-protrusions on the electrode surface, rather than in thermal bubbles in the bulk of the liquid. They then further suggest that the reduction in size of these surface bubbles causes the more gradual

increase in breakdown voltage with pressure. Comparing the data taken with the mirror finish and rougher electrodes it is clear that surface finish has an effect on breakdown voltage.

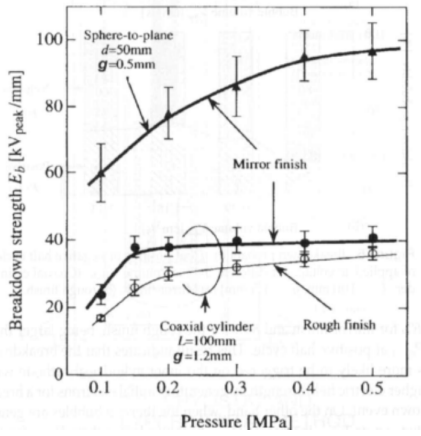

Fig..4.25 Breakdown field in liquid N_2 as a function of applied pressure for the configurations used by Hayakawa et al. (1997)

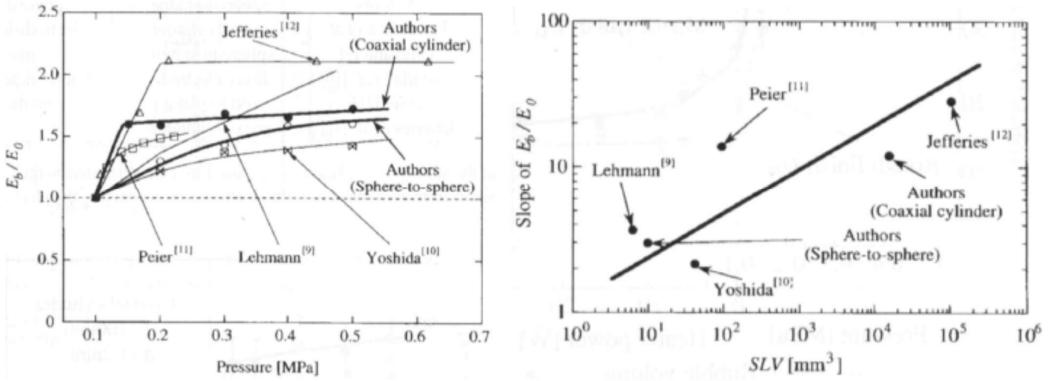

Fig..4.26a Normalised breakdown fields in liquid N_2 as a function of applied pressure.

Fig..4.26b Initial slope of Fig.4.26a as a function of Stressed Liquid Volume From Hayakawa et al. (1997)

Figure 4.26a shows the normalised ac liquid N_2 data taken by Hayakawa et al and other authors whilst Fig. 4.26b shows the initial slope of $E_b/E_0(P)$ plotted as a function of the Stressed Liquid Volume (SLV). From these plots, Hayakawa et al conclude that the

breakdown strength for large stressed volumes increases sharply at lower pressures and then saturates.at higher pressure.

A similar rapid increase and then saturation of the breakdown field with pressure has been observed in other liquids, in particular in liquid H_2. Data by Jeffries and Mathes (1970) and by Burnier et al (1970) is shown in Fig. 4.27, taken from Gerhold (1979). This is for H_2 at 20 K from atmospheric pressure (SVP) to 6 bar, showing an initial slope of about 200 kV/cm/bar and an overall increase of a factor of ~2.3.

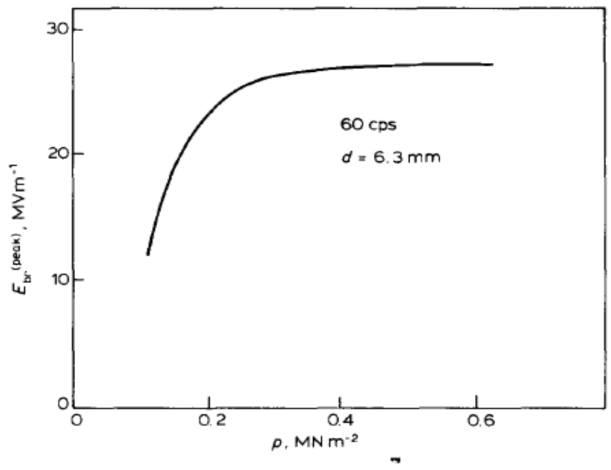

Fig..4.27. AC breakdown field in liquid H_2 at 20K as a function of pressure. From Gerhold (1979)

4.3. Bubble Formation in Liquids

4.3.1. Introduction

The stability and dynamics of bubbles in classical liquids has been, and remains a topic of high interest. Bubble formation is technically important in many areas such as cavitation and thermal transport. It is a challenging theoretical problem due to the number of parameters involved. The result of the competing tendencies of surface tension, hydrostatic pressure and internal gas pressure on the dynamics are usually discussed in terms of the

Rayleigh-Plesset equation (Brennan, 1995). When the bubble is formed as a result of electron injection into the liquid, there may be plasma heating of the gas within the bubble and the thermal effects become much more complicated. In such a case, there will be additional electrostatic forces tending to elongate the bubble (Garton and Krasucki, 1964).

In general, electrostriction leads to an increase in pressure in a dielectric liquid subjected to an electric field (Garton and Krasucki, 1964 and references therein). For a spherical bubble in a dielectric liquid subject to a uniform field E, the electrostrictive pressure is given as

$$P_{es} = \left[\frac{1}{2}\left(\varepsilon_{liq} - \varepsilon_{bubble}\right)\left(\frac{\varepsilon_{liq} + 2\varepsilon_{bubble}}{3\varepsilon_0}\right)\right] E^2$$

The general criterion for bubble stability can then be written

$$P_{\text{hydrostatic}} + P_{applied} + P_{electrostrictive} + \sigma C - P_{bubble} = 0$$

where $P_{hydrostatic} = \rho gh$, $P_{applied}$ is the externally applied pressure, σ is the surface tension, C is the reciprocal of the radius of curvature and P_{bubble} is the pressure of the gas inside the bubble. Hence, the general effect of P_{es} on a spherical bubble is to compress it. However, as Garton and Krasucki have shown both theoretically and experimentally for gas bubbles in oil, that an isolated spherical bubble in a uniform field is unstable and will always deform, roughly elliptically, in the direction of the field. They found that the difference in the curvature at the ends of the major and minor axes C_a and C_b depends on the square of the electric field and on the difference in dielectric constants

$$C_a - C_b \propto \frac{\left[E^2\left(\varepsilon_{liq} - \varepsilon_{bubble}\right)^2\right]}{\sigma\varepsilon_{liq}}$$

For a non-conducting bubble of neutral gas in, say, liquid helium, this difference is relatively small. However, if the gas becomes ionised, then ε_{bubble} diverges and the elongation increases dramatically above a certain field value to yield an unstable bubble. Figure 4.28 shows Garton and Krasucki's calculations of the elongation γ as a function of applied field for various $\frac{\varepsilon_{bubble}}{\varepsilon_{liq}}$ ratios.

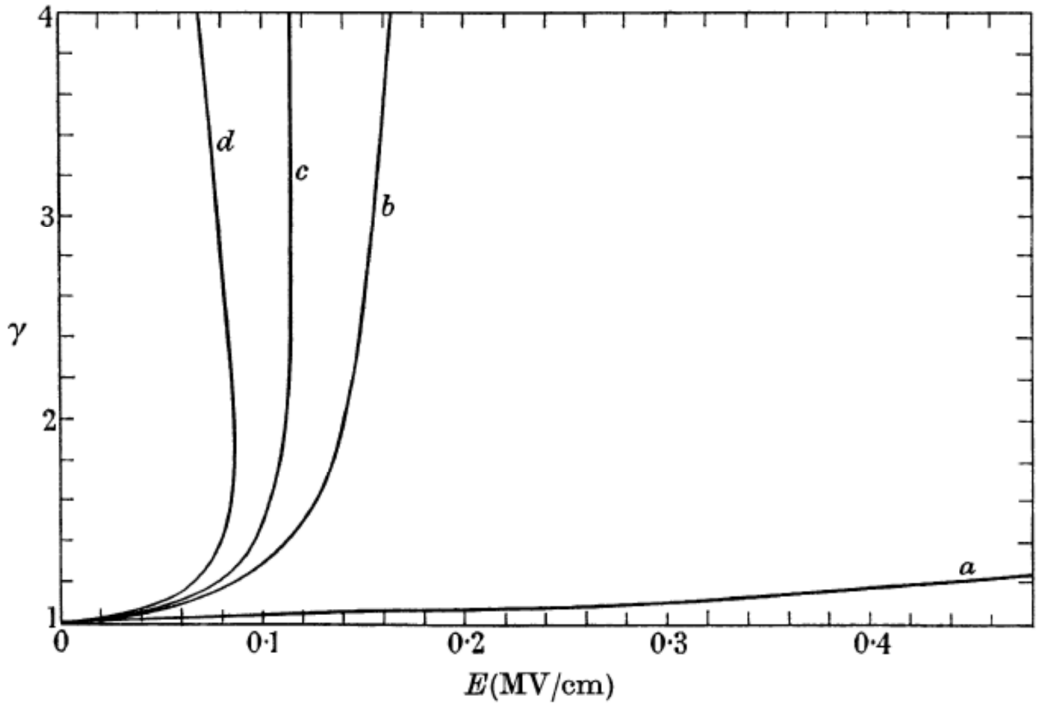

Fig..4.28 Elongation, γ (major:minor axes ratio) for compressible bubbles in a dielectric liquid subject to uniform field. $\varepsilon_{liq} = 1.883$, $\sigma = 18.42 \times 10^{-3}$ Nm^{-1}, $P_0 = (P_{hydro} + P_{app}) = 1$ bar, $r_0 = 10$ μm. Curve (a) $\varepsilon_{bubble}/\varepsilon_{liq} = 0.534$; (b) $\varepsilon_{bubble}/\varepsilon_{liq} = 10$; (c) $\varepsilon_{bubble}/\varepsilon_{liq} = 20$; (d) $\varepsilon_{bubble}/\varepsilon_{liq} = \infty$.

The unusual thermal properties of liquid ^{4}He, in both its normal and superfluid states, make the calculation of bubble size and motion truly challenging. Nevertheless, in their early

classic paper on field emission into liquid helium, Halpern and Gomer (1969a) made the first serious attempt at such a model. This has been developed further by McClintock (1973b) and most recently by Schmidt (1982, 2003).

We review below the available experimental data on bubbles in He I and He II and in some other relevant liquids. First, however, we have to consider the unique case of the electron bubble in liquid ^{4}He.

4.3.2. Isolated charges in Liquid ^{4}He – Electron Bubbles and Snowballs

Field emission of electrons from an electrode tip into liquid Helium has been observed and characterised by many authors (McClintock, 1969, 1971, 1973, Halpern and Gomer 1969). In addition, there have been many direct measurements of the mobilities and effective masses of both negative and positive single charge carriers in liquid He, (Ostermeier 1973, Poitrenaud and Williams, 1972). In general, very high values of effective mass and low values of mobility are found. A single electron emitted into liquid Helium quickly loses energy to excitations of the liquid, after which it finds it energetically favourable to expel Helium atoms from its immediate location. Maris (2008) presents a particularly simple form for the bubble energy:

$$U_{bubble} = \frac{h^2}{(8mR^2)} + 4\pi R^2\alpha + \frac{4}{3}(\pi R^3 P)$$

where $\frac{h^2}{(8mR^2)}$ is the zero point energy of the confined electron, $4\pi R^2\alpha$ is the surface energy of the bubble and $\frac{4}{3}(\pi R^3 P)$ is the work done by the bubble against the liquid. Here, m is the

mass of the electron, R is its radius of the bubble, α is the surface tension of the helium and P the applied pressure. Minimising the energy leads to a bubble radius of ~18 Angstrom at the minimum energy of 0.21eV. The motion of an electron in such an "exclusion bubble" under the influence of an electric field thus involves the motion of a large number of He atoms. This results in low mobility and an effective mass of ~80m_4 arising from the electron bubble structure interacting strongly with the excitations in the liquid (m_4 is the mass of the ^{4}He atom). Typical drift velocities of 10^{-2} and 10^{-3} $cm^2V^{-1}s^{-1}$ are observed (Schmidt 2002, Ostermeier 1973). The electron's mobility exhibits strong pressure and temperature dependences between 4.2 K and 0.5 K (McClintock, 1973b), as the spectrum of the various elementary excitations in the liquid changes.

Positive charge carriers in liquid He attract a "snowball" of ^{4}He atoms clustered around the positive core, and again these have large effective masses and low mobilities.

The formation of these relatively large structures, containing ~50 He atoms, is as a result of the electrostrictive pressure discussed above exceeding the solidification pressure of He (~25 bar at 1.6 K). These "snowballs" and electron bubbles are thought to be responsible for the high dielectric strength of the bulk liquid. Even application of very high electric fields does not result in an isolated negative electron or positive ion acquiring sufficient energy to ionise further ^{4}He atoms, hence an avalanche discharge is never initiated by these carriers.

4.3.3. Vapour Bubble Formation in Liquid Helium

Notwithstanding the above, it is clear that true vapour bubbles play a vital role in liquid ^{4}He breakdown, although the very high thermal conductivity of He II might initially suggest that a vapour bubble within the bulk superfluid is not possible. This section of the review presents evidence for vapour bubbles in both the normal and superfluid states.

Hickson and McClintock (1971) observe a gaseous corona discharge around a fine tip submerged in normal state liquid ^{4}He under a strong E-field. An emission current > 10^{-9} A was enough to sustain a glow discharge. Evidence of sputtering to the end of the tip further confirmed this. The bubble radius was found to be a function of the emission current and measured to be ~ 10^{-2} cm at current and voltage of 10 μA and 3 kV, respectively. Hickson and McClintock also presented a simple calculation which yielded the observed bubble radius. This assumed that all the energy gained by charges moving in the electric field within the gaseous bubble was converted into heat and that this heat was transferred to the liquid only through the surface of the bubble at 1 Wcm^{-2}.

In He I, vapour bubbles have also been observed at the tip but these are not stable and move away from the tip. Their shape is also not always spherical, with some being observed to elongate around the tip.

In the work by Hara et al (1993), reviewed in detail in section 4.2.3 above, they also observed a stable glow around the end of a positive tip in He II. In the case of a negative tip they observed that breakdown in He II is always preceded by a pulsating current and light emission which typical lasts a few μs (see section 4.3.6). In order to create the bubble, energy has to be transferred into the liquid He. Hara et al suggest the possible mechanisms are Joule heating by field ionisation of helium atoms, movement of dielectric particles by dielectrophoresis (Gerhold, 1972) as well as other processes which are not explicitly stated.

Vapour bubbles in He I and He II have been observed and characterised by Abe et al (2008). In their experiments, two piezoelectric transducers are pulsed to produce an acoustic wave. Above a certain threshold, a bubble is created on the surface of the lower transducer. The experimental region is illuminated by a laser and a high speed camera records the characteristics of the bubble at a rate of 1000 frames per second, from creation to collapse. Figure 4.29 shows the data for He I. A 5 ms pulse produces a large bubble at the centre of

the transducer. It is accompanied by many other small bubbles (~70 μm) over the whole surface. The large bubble then gradually rises up and reached the top transducer, after ~100 ms.

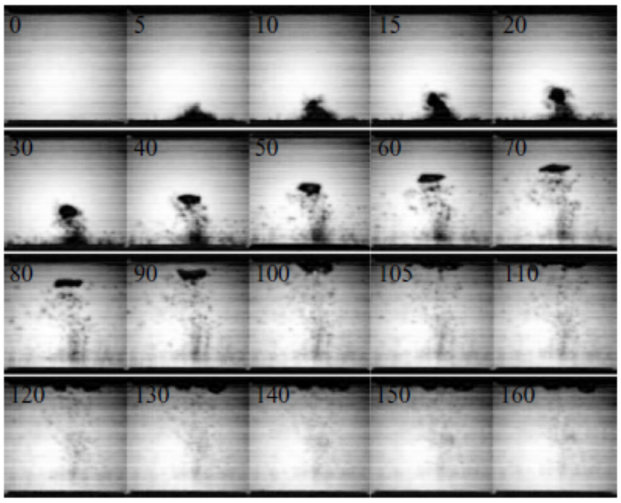

Fig. 4.29 Images of vapour bubbles created on the surface of a piezoelectric transducer in He I at 3.2 K under SVP. The bubbles are generated by a 7.2 V acoustic pulse lasting 5 ms. The time sequence in ms is shown in the top of each frame. The separation of the top and bottom transducers is 10 mm. (Abe et al, 2008).

The authors attribute the behaviour to boiling of the helium on the lower transducer. An increase in temperature created by the pulse together with the low thermal conductivity of the He I causes the surface of the transducer to heat allowing bubbles to form. The large bubble does not collapse but drifts up through the cell to the top transducer.

A similar experiment was carried out in He II at 300 mK under SVP. Figure 4.30 shows the bubbles created by different amplitude pulses.

The smaller pulse creates a smaller bubble which grows from a single point on the bottom transducer then collapses before it reaches the top transducer. The larger pulse produces a larger bubble which oscillates in size and eventually splits into smaller bubbles.

The bubble shape in He II is highly irregular, especially at large size, and Abe et al attribute this to turbulent flow around it.

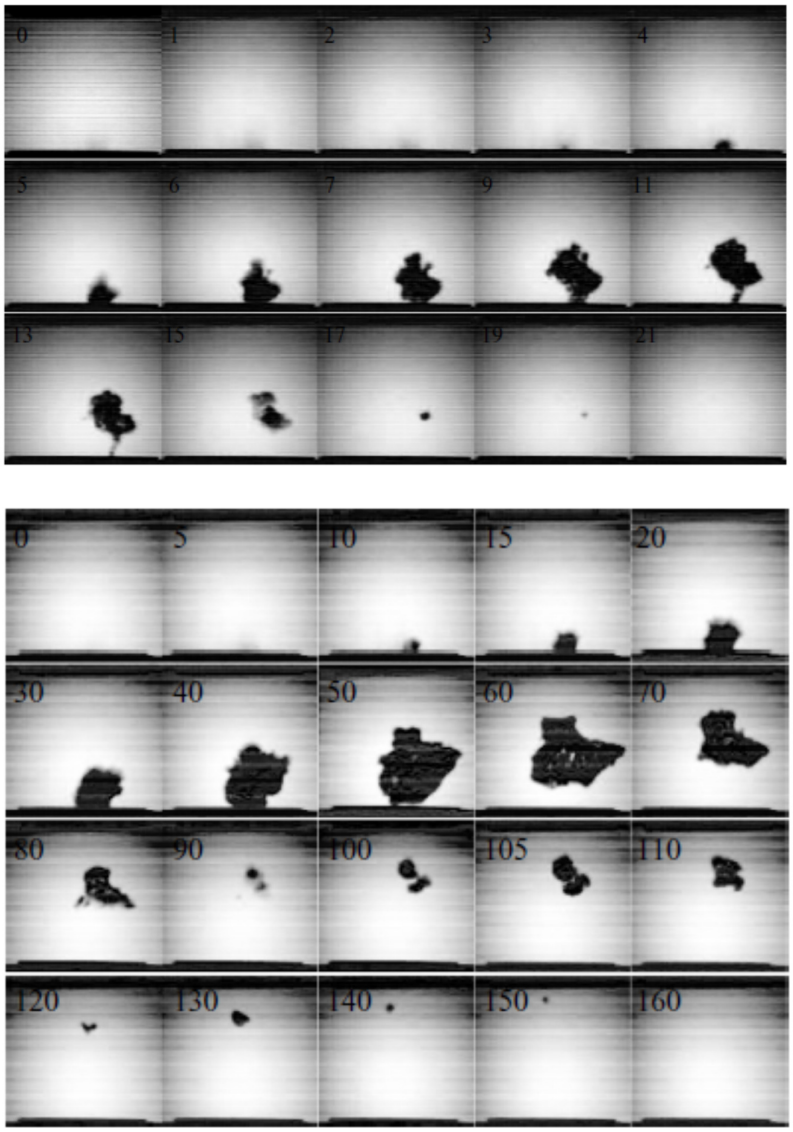

Fig. 4.30 Images of vapour bubbles created on the surface of a piezoelectric transducer in He II at 300 mK under SVP. The time sequence in ms is shown in the top of each frame. The separation of the top and bottom transducers is 10 mm. **Top**: Images of bubbles generated by a 7.2 V acoustic pulse lasting 5 ms; **Bottom**: Images of bubbles generated by a 8.2 V acoustic pulse lasting 5 ms. (Abe et al, 2008).

The difference in the initial bubble formation at the lower transducer in the two ^{4}He states is also striking and is attributed to the differences in the thermal conductivities. The high thermal conductivity of He II dissipates the heat into the liquid and therefore does not allow the surface of the transducer to warm up. Therefore, the bubble is created at the point where the acoustic wave amplitude is maximum.

The bubbles created by the same (7.2 V) amplitude pulse in He I (3.2 K, ~240 torr) and He II (0.3 K, < 1 torr) show a clear size difference (Fig 4.29 and 4.30 Top). Abe et al state that this size is a result of the different temperatures. However, since the data is taken under SVP, the pressure in the liquid differs by three orders of magnitude in the two cases. Hence, it would seem plausible that part of this difference in bubble size is caused by the pressure; particularly since this is well known in other liquids (see section 4.2.3.).

To explore the effect of bubbles formed at the local hot spots or around particulate contaminates in superconducting machines, Hara (2008) made measurements on He I and II using electrodes with heaters and with deliberately added (rather large) particles. Little experimental detail is given but, images are presented of a 1 mm sphere initially on the surface of the lower of the two parallel plate electrodes. As the E-field is increased, the sphere becomes charged and at a critical voltage rises above the plate and a microdischarge occurs at the minor gap.

In summary, relatively large and easily observed bubbles can be created in both He I and He II. They can be formed as a result of field emission, from an acoustic pulse, from direct heating or as the result of charged impurities within the electrode gap and the bubbles in the two phases have different dynamical characteristics.

4.3.4. Bubble Size and Dynamics as a Function of Pressure

This section looks at the behaviour of vapour bubbles as a function of pressure. In general, as the pressure in the liquid increases, bubble size decreases. This has been observed in He I and He II (Abe, 2008), LN_2 (Hara et al 2008, Hong et al 2003), in transformer oil (Cevallos et al 2005a, Cevallos et al 2005b, Butcher et al 2006) and in cyclohexane (Beroual et al 1998).

We have already discussed in section 4.2.6 the pressure dependence of the breakdown voltage observed by Cevallos et al (2005a), which showed a sharp drop below a critical pressure, P_c (Fig 4.22). Figure 4.31 here shows the variation in the sizes and evolution of the bubbles formed at the negative tip, as the pressure is varied. When a bubble is created below P_c, the bubble expands and the rate of expansion is a function of pressure. At P_c (102 torr) and higher pressures there is little or no expansion.

The growth, collapse and radius of the bubble observed by Cevallos agree with that predicted by the Rayleigh equation (see section 4.3.1.).

Hong et al (2003) uses vertical electrodes to study the behaviour of thermally created bubbles in the presence of a high E-field. A stable vapour channel has been observed bridging the gap between electrodes. Increasing the pressure causes the vapour bubble to reduce in size and form a conical shape. It is now conical in shape. At even higher pressures a vapour layer is formed. Thus increasing the pressure greatly reduces the size and shape of the vapour bubble.

Kattan et al (1989) examined the influence of hydrostatic pressure on the bubble dynamics in purified cyclohexane. When the hydrostatic pressure is increased the volume and the lifetime of the bubble significantly reduce.

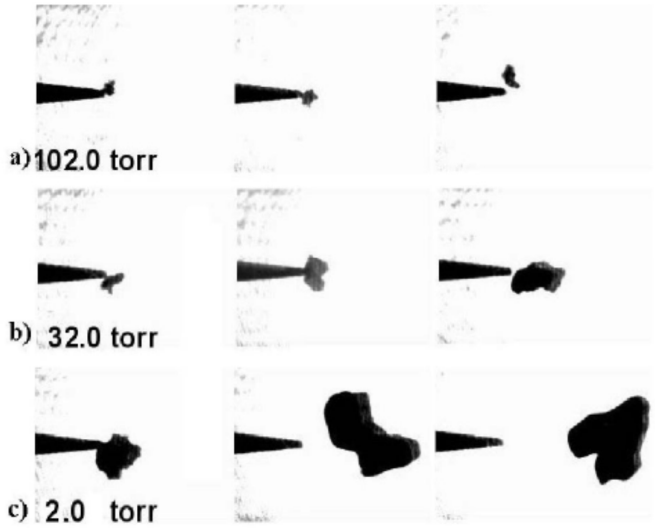

Fig..4.31. Variation of bubble size with pressure for breakdown in transformer oil. Shaft diameter of the needle is 0.51 mm with a tip radius of curvature of 40 μm (Cevallos et al, 2005a)

4.3.5. Breakdown as a function of thermal bubble size

Hayakawa et al (1997) investigate breakdown as a function of the size of thermally induced bubbles in LN_2, Fig.4.32. The measurements were taken at atmospheric pressure and

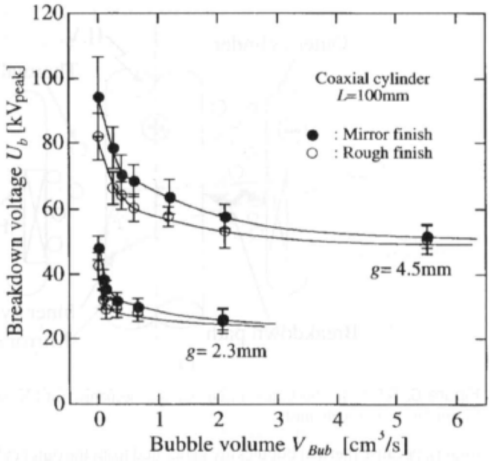

Fig..4.32. Breakdown voltage as a function of bubble volume in LN_2. Bubble created by thermal heating. (Hayakawa, 1997)

the bubble volume was changed by varying power to a heater. The results indicate a strong dependence of breakdown voltage on bubble volume. Initially a small increase in bubble volume causes the breakdown voltage to rapidly reduce. A more gradual decrease in breakdown voltage is observed with bubble volume for higher heater powers.

4.3.6. Pre-breakdown Current and Light Emission

A glow discharge has been observed around the tip of an electrode in liquid ^{4}He in both the He I and He II phases (Hickson and McClintock 1971, Hara 1993).

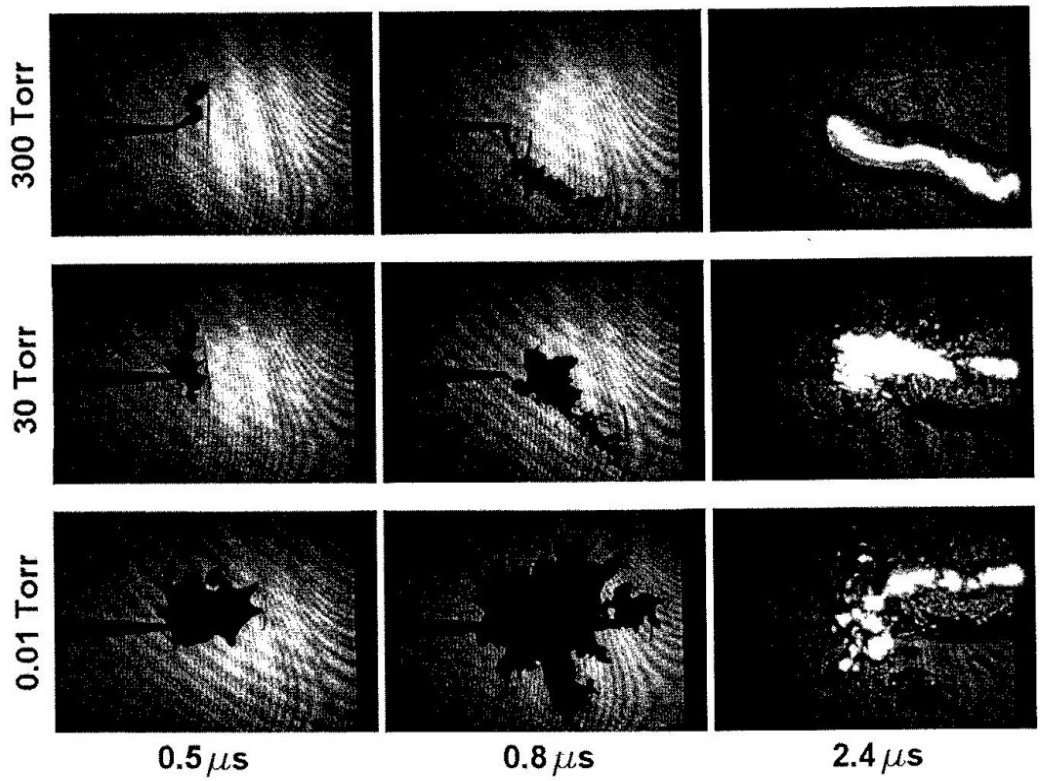

Fig..4.33. Streamer propagations in transformer oil as a function of pressure. (Cevallos et al 2005b)

Hara has investigated pre-breakdown current and light emission at the cathode prior to catastrophic breakdown. Before a negative breakdown event, a pulsating current was seen

which correlated with the level of light emission. This phenomenon lasted a few μs before catastrophic breakdown and was observed prior to every negative event.

The effect of pressure on streamer development in transformer oil has been investigated by Cevallos (2005b). As shown in section 4.3.4, a higher pressure prevents the bubble expanding. Similarly an increase in pressure in transformer oil prevents streamer channels from increasing in volume, Fig.4.33.

The propagation velocity of the streamer across the gap is independent of pressure. In each case breakdown occurs ~ 2.4 μs after streamer initiation. No reference is made to the breakdown voltage at each pressure however, as shown in section (4.2.2) transformer oil breaks down at a higher voltage when pressurised so it is assumed that the breakdown voltage for each pressure in Fig.4.33 are different with the higher pressure having the highest breakdown voltage.

4.3.7. Discussion of proposed high voltage breakdown mechanisms in liquid helium and other dielectric liquids

This section presents possible high voltage breakdown mechanisms mainly in liquid helium, but also in transformer oil. In the case of liquid helium the general consensus is that breakdown occurs through a low density vapour region (a bubble) within the bulk liquid.

Electron emission from the cathode is one way of transferring energy to the bulk liquid. Schmidt (1982) and Schmidt et al (2002, 2003) present a calculation of the energetic considerations of electron emission or field ionization. Schmidt's conclusion is discharge in liquid helium is always triggered by electron emission from the cathode. However, in this

model the breakdown initiating electron that crosses the gap is delocalised (it is not trapped in an electron bubble by helium atoms, see section 4.3.2).

Schmidt presents a simple estimate of the energy lost via electron and helium atom elastic collisions. Schmidt's model suggests that a delocalised electron will dissipate eEd (d is the gap length, E the electric field) on reaching the anode. For a breakdown voltage of 7.5 kV in a uniform E-field of separation 100 µm (data from Yoshino et al 1979) 0.0075 eV nm^{-1} is dissipated. Schmidt assumes the path of the electron between electrodes is straight. As the size of a helium atom is ~ 0.4 nm each atom receives ~ 30 meV. As the latent heat of vaporisation of a helium atom is 0.87 meV each emitted electron is capable of creating vacancies which can lead to gaseous catastrophic breakdown.

Schmidt explains the drift velocity of the delocalised electron is proportional to the E-field at low E-fields and a super linear dependence is observed at higher E-fields. In the case of a 7.5 kV breakdown across a 100 µm gap the breakdown field has a lifetime of ~ 5 ns. In this case the model holds true. However, in the case of a large gap ~ 15 mm (Hara et al 1993) the breakdown voltage is ~ 25 kV (for a negative tip needle). As the electrons moves away from the tip the E-field will considerable reduced. Now the lifetime of the delocalised electron is too short to enable it to bridge the gap across the electrodes before being trapped and localised by helium atoms.

In the case of a pin–plane geometry with a positive tip Schmidt explains that electron emission is still the mechanism of breakdown. A stable glow discharge is created in a stable bubble that forms around the positive tip. The bubble size is a function of the applied voltage. Thus, increasing the voltage increases the size of the positive bubble reducing the effective gap which increases the E-field on the planner electrode thus initiating electron emission and promoting breakdown.

This fact that a stable bubble can be produced around a positive tip and only a unstable bubble lasting a few μs (Schmidt 2003) forms around a negative tip in liquid helium is a strange phenomenon. It can be postulated that field ionisation around a positive tip pulls electrons from the helium atoms into the anode removing them from the liquid. The positive ions remain in the liquid and move away from it under the E-field generating a bubble. In contrast when a positive ion is attracted to the cathode it will remain in the bulk liquid. The charge build up on the surface of the cathode can create a space charge which might cause any bubble to collapse. This might be a possible explanation as to why Hara et al (1993) see a pulsating current with a correlated distribution of light and why Schmidt reports that negative filament type streamers observed around a negative tip last for only a few μs. Halpern and Gomer (1969a) have also argued that this effect is sufficient to cause layers of tens of nm of solid helium to be formed in the high fields around a positive tip in a point-plane geometry.

Gerhold (1972, 1979, 1989, 1991, 1994, 1998a, 1998b) also agrees that breakdown occurs through a gaseous bubble within the bulk liquid. Electron emission from the cathode is thought to be the main source of energy to create the bubble. Gerhold also presents an argument of how high permittivity impurities around and asperity on the cathode can increase the local E-field prompting electron emission. In this case the electrons collide with the impurities and charge them negative creating repulsion force from the surface. This motion generates heat creating the bubble (Gerhold 1972).

In later papers Gerhold (1991,1994) explains that an antibubble barrier (AB), which is an intrinsic liquid phenomena, has to be overcome in order to generate a bubble. Electron emission from the cathode injects an electron into the liquid. This electron produces a vacuous cavity in which no helium atoms are present. This cavity can collapse causing the stored energy from the cavity to be transferred to the bulk liquid and creating a vapour bubble.

After the bubble is created if the density of the gas inside the bubble drops below the Paschen minimum a gaseous breakdown will be initiated.

Hara et al (1993) suggest both negative and positive charge carriers can be injected into liquid helium when using a pin-plan geometry. Electron emission and negative breakdown is caused by field emitted electrons from the cathode. Hara's data showed that the negative breakdown from a tip had little effect on temperature and pressure. Thus, Hara et al argues that the negative breakdown mechanism is not caused by a vapour bubble. In the case of a positive tip Hara et al observe a pressure dependence. They suggest that positive breakdown occurs in a vapour bubble. This is strengthened by their observation of a stable glow around a positive tip. In order to create the bubble Hara et al suggest the energy is transferred to the liquid via Joule heating or, as Gerhold suggest, the movement of charged impurities (dielectrophoresis).

For small gaps < 0.1 mm there is little or no dependence with pressure. Hara et al suggests that breakdown is being triggered by field emission. For gaps > 0.5 mm the breakdown strength decreases and is pressure dependent. In this case Hara states that field-emission initiated breakdown is now not possible at these reduced E-fields. The breakdown mechanism is thought to be a result of enhanced bubble formation created by the increased volume of liquid between the electrodes. Hara et al states that there is no change in breakdown mechanism above and below the lambda point.

Kok et al (1962) presents a discussion on the breakdown mechanism of liquefied gas. It is suggested that contaminants within the liquid make a bridge between electrodes under the force of the E-field. The positive containment in liquid helium is thought to be polarised helium atoms clustered around a positive charge. The negative containments are a cloud of electrons or a O ion trapped by approximately 50 polarised atoms. Kok et al suggest that this bridge can support the flow of charge via the tunnelling of electrons or ions. Kok et

al also point out that heating of liquid helium ions can create an ionised vapour column in which catastrophic breakdown can occur.

Butcher et al (2006) outline their proposed breakdown mechanism in transformer oil for pin-plane geometry. In the case of negative polarity every breakdown is preceded by the creation of a low density bubble caused by a partial discharge into the liquid (Cevallos 2005a). This discharge heats the local oil molecules causing a vapour bubble. The vapour bubble starts to expand until it comes into equilibrium with the liquid. The lifetime and maximum radius of this bubble are shown to fit the classical Rayleigh model (Rayleigh 1917, Kattan et al 1991). Reducing the pressure causes an increase in the rate of bubble expansion. As partial discharge can occur as much as ~ 1 ms before breakdown this allows a sufficient time for the bubble to expand. Further injection of charge into the bubble promotes an electron and ion avalanche causing an elongated streamer and then catastrophic breakdown. In the case of a positive needle in transformer oil positive ions or holes are thought to be the charge carries that bridge the gap between electrodes in the bulk liquid. This is thought to be the case as positive breakdown shows little effect on pressure.

4.4. Surface flash over and breakdown at the CTJ

4.4.1. Introduction to breakdown at the CTJ

The cryoEDM experiment uses BeO spacers to maintain the separation of the Ramsey Cell electrodes and as a captive wall for the UCN (section 3.2.2). The point where the BeO, electrode and liquid helium meet is known as the cathode triple junction (CTJ).

Although the dielectric strength of the pure liquid helium may be sufficient to support a high voltage the inclusion of the insulating spacer between the electrodes may cause this breakdown voltage to drop. The mechanism behind breakdown at the CTJ and surface

flashover has been investigated by a number of authors, particularly in the case of vacuum, (Miller 1989, Yamamoto et al 2000, Neuber et al 1998). At sections along the CTJ where the profile is not uniform it will cause it to be electrostatically weak creating high E-fields that promote electron emission. This in turn can initiate catastrophic breakdown in the form of a surface flash over across the insulator.

This section of the review presents breakdown data for pairs of electrodes with an insulator between them taken in LHe or LN_2

4.4.2. Previous data on surface flash over – LN_2

An investigation of the high voltage breakdown behaviour of a pair of electrodes with and without an insulating spacer submerged in LN_2 has been carried out by Butcher et al (1999a, 1999b). The electrode separation was 1.75 mm. Little detail is given about the precise geometry but this diagram shows electrodes with curved edges that meet the insulating sample at approximately right angles, figure 4.34.

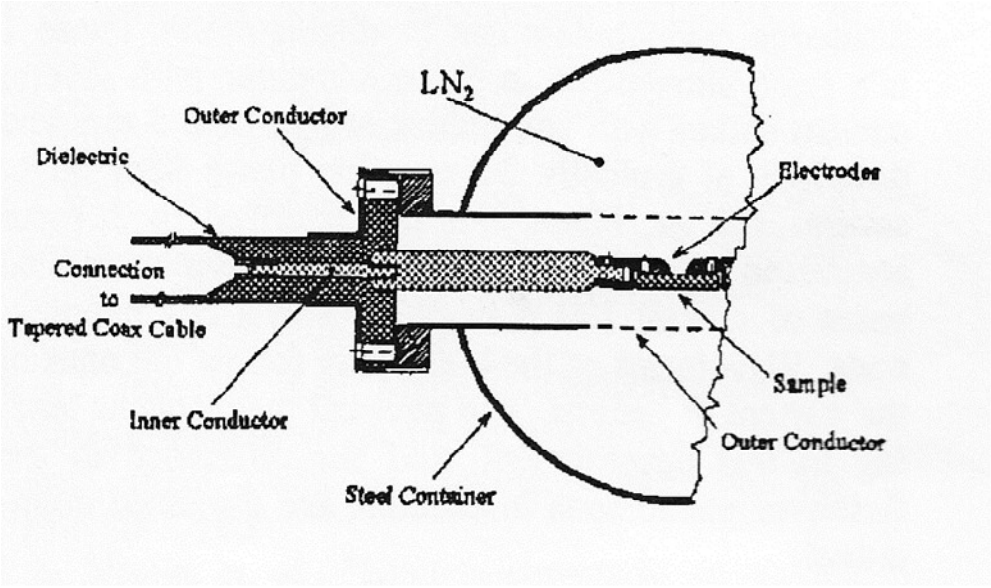

Fig..4.34. Experimental apparatus used by Butcher et al (1999a, 1999b) The electrode geometry and insulating sample configuration are shown.

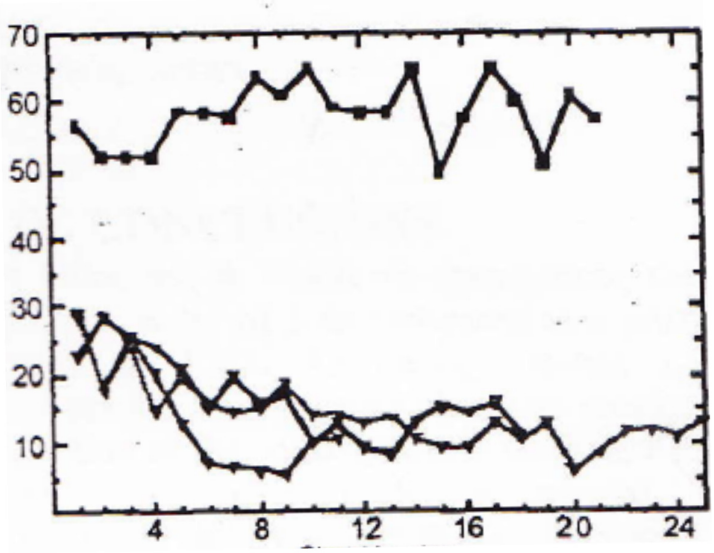

Fig..4.35. Breakdown voltage vs breakdown number for bulk LN_2 and surface flash over across an Alumina insulating sample. Top trace: Breakdown trough the bulk LN_2; Bottom three traces: Breakdown across an Alumina sample. Each trace starts with a new sample. (Butcher 1999a).

The insulators were Lexan and Alumina and were bolted onto the bottom of the electrodes, thus maintaining a permanent gap of 1.75 mm. A calibration test was first carried out to find the breakdown voltage of the bulk LN_2 without any insulating sample. Butcher et al observe an average breakdown E-field of ~ 315 $kVcm^{-1}$ for super cooled LN_2 at 68 K under 255 torr, figure 4.35, similar to that observed by others (Hara et al 1987).

When the insulating sample is present a similar drop in voltage is observed for both Alumina and Lexan. The first two or three breakdowns show a reduction in breakdown E-field by a factor of ~ 2, figure 4.35. As the number of breakdowns increases the breakdown E-field drops until about the 10^{th} breakdown, after which the breakdown E-field is relatively constant, ~ 63 $kVcm^{-1}$. When the temperature of the LN_2 is 77 K (pressure 1 atmosphere) the breakdown E-field increases from ~63 $kVcm^{-1}$ to ~91 $kVcm^{-1}$.

It takes as little as 4 breakdown events for a visible amount of electrode material to be deposited as a track across the sample surface. This track is in the direction of the E-field and Butcher et al estimate the layer thickness to be less than 1 micron. The Alumina suffers considerably more damage than the Lexan, at same value breakdown E-fields. On the Alumina, visible pits can be observed on the surface where material has been ejected as a result of discharge.

In summary, Butcher et al suggest that the inclusion of an Alumina ceramic sample between a pair of electrodes reduces the breakdown E-field by ~ 3.

4.4.3. Previous data on surface flash over – LHe

Migliori et al (1978) have studied dielectric tracking in liquid Helium. An experiment was carried out to compare the breakdown voltage of two, geometrically identical, samples of NEMA G-10 circuit board. One sample was extremely clean (cleaned using trichlorrethylene). The second was contaminated by being rubbed by a copper tube. It was noted that at x10 magnification a large number of metal chips can be seen on the contaminated sample surface. However, no short circuits between the sample sides were observed. The sample was sandwiched between a pair of spring loaded electrodes. The E-field was calculated to be greatest over the sample surface. The sample thickness was stepped. This allowed the tracking distance between the electrodes to be varied in from a minimum of 0.15 mm to a maximum 0.7 mm. For each separation at least 5 breakdowns were taken.

Two types of breakdown were observed. Full breakdown was accompanied by a hissing sound and voltage drop. The second produced a current spike but no drop in voltage. The second type of data only occurred a few times when the clean sample was used. Migliori

et al state the second type of breakdown is caused by charged particles being ejected from the surface of the sample and is therefore not a catastrophic breakdown.

During this experiment, the liquid Helium was under a SVP pressure of 580 torr (3.9 K). The results showed that the ratio of breakdown voltage between the clean and the contaminated sample was similar, 0.9 ± 0.06.

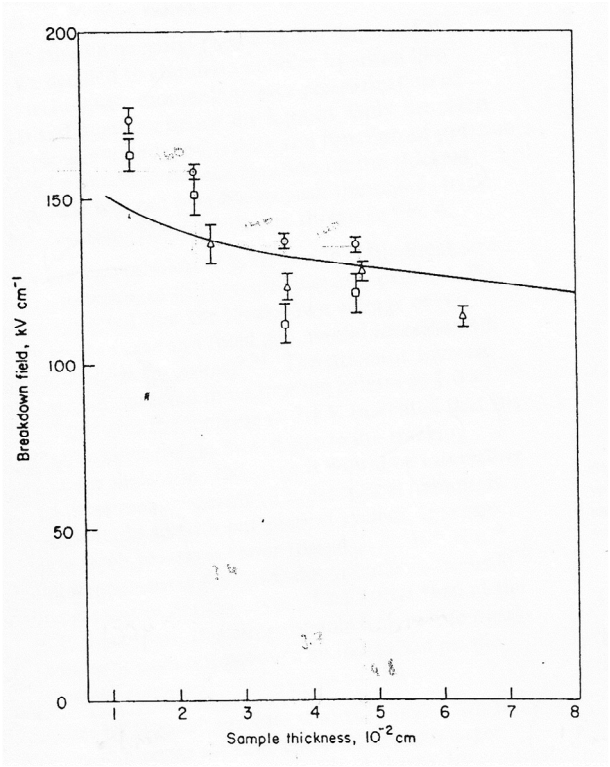

Fig..4.36. Breakdown E-field for tracking across an insulating sample between a pair of spring loaded electrodes vs insulating sample thickness in LHe boiling at 580 torr, (Migliori et al 1978). Circle: G-10 clean sample; Square: G-10 sample contaminated by rubbing with copper particles; Triangle: Crest 475 resin on glass-dacron tape sample; Solid line: Breakdown E-fields from helium gas. Data from Gerhold (1972).

Figure 4.36 shows the slight reduction in breakdown E-field versus the tracking length. The solid line in this figure 4.36 also shows breakdown voltage as a function of length taken in helium gas by Gerhold (1972). Migliori et al suggest their flashover data

correlates well with Gerhold's data. It is clear that the typical E-field breakdown values here of around ~ 150 kVcm^{-1} are less than that expected for the bulk liquid helium. Migiliori et al quote the breakdown voltage for liquid helium under similar conditions and electrode separations without any insulator to be ~ 500 kVcm^{-1} (section 4.1.4), some 3 times greater than with the insulating spacer.

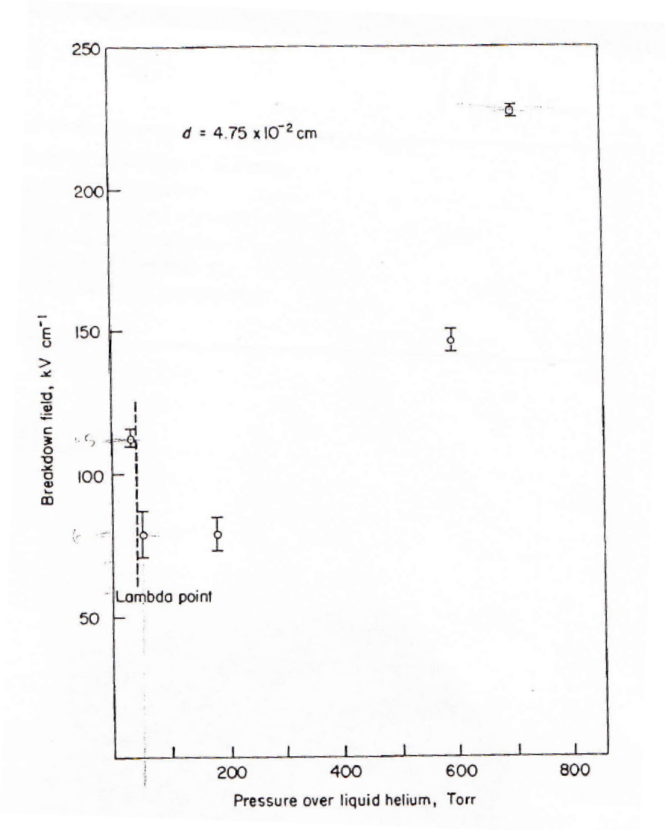

Fig..4.37. Liquid helium breakdown tracking E-field versus SVP for a 0.475mm thick sample of G-10 CR between a pair of spring loaded electrodes. The lambda point is indicated. Migliori (1978).

Migliori et al also used a clean sample of thickness 0.475 mm to investigate the breakdown tracking E-field in liquid helium temperature under SVP, figure 4.37.

Reducing the temperature (SVP) from 4.2 K (760 torr) to ~ 2.2 K (~ 40 torr) reduces the breakdown voltage across the sample by ~ 3. Migliori et al observe the breakdown E-

field to increase after passing through the lambda point. They state that this behaviour is "due to bubbles" but give no explanation.

Wu and Roach (1992) and Wu (1996) present data on surface flash over in liquid helium between 1.9 K and 4.2 K. For all tests the pressure above the liquid is held at ~ 1 atmosphere. A set of parallel plate electrodes, diameter 7.62 cm, have a 1 mm thick sample of G10-CR, diameter 2.54 cm, sandwiched between them. Over a temperature range between 1.93 K and 4.24 K no obvious change in breakdown voltage at fixed pressure is observed.

Wu and Roach compare the breakdown voltage with and without the insulating spacer and state there is no significant observed difference. However, the E-field values for breakdown in bulk liquid helium seem to be relatively low, ~ 120 kVcm^{-1} (see section 4.2.2).

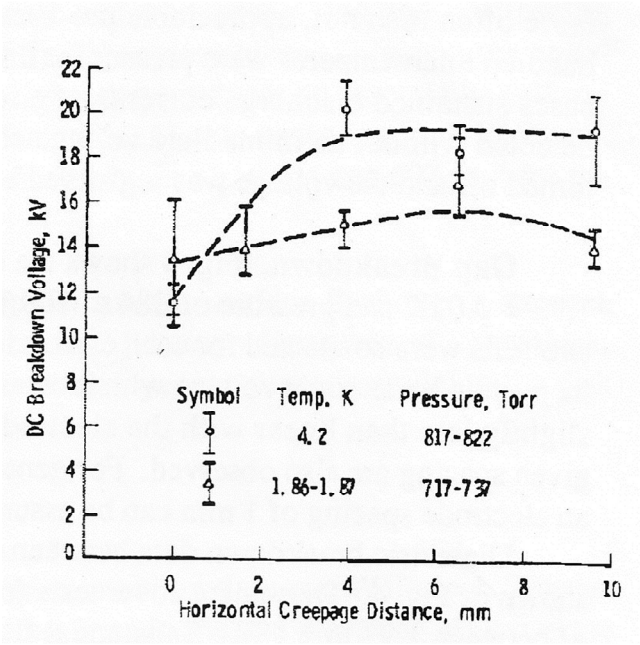

Fig..4.38. Liquid helium breakdown voltage versus tracking length for pin-plane geometry. Circle: Breakdown at 4.2 K; Triangle: Breakdown at 1.9 K. The pressure of the liquid helium is also shown. Wu and Roach (1992).

Surface tracking tests were also made using a pin-plane geometry. The tracking distance along the surface of the G-10 CR was varied. The distance the discharge had to

travel was the product of the horizontal distance across the surface of the electrode plus the thickness of the G-10 CR insulator. Data were taken at 4.2 K and 1.86 K. The trends in the breakdown data are similar, figure 4.38.

The data taken at 4.2 K are generally higher than that taken at 1.86 K. However, comparison of the pressures above the LHe shows it was ~ 100 torr higher for the experiment at 1.86 K. It is therefore hard to deduce if this is a temperature or pressure effect. In general the breakdown voltage increased with the total tracking length up to 5 mm and then flattened off. This is explained as being caused by high E-fields on the pin dominating the voltage breakdown, as might be expected.

4.4.4. Summary of previous surface flash over data

Data have been reviewed on the effect an insulating sample has when placed between two electrodes. Butcher et al (1999a, 1999b) observed a reduction by a factor of ~ 3 in breakdown voltage in LN_2 when an Alumina or Lexan insulator is used. Migliori et al (1978) also saw a reduction by a factor of ~ 3 in the breakdown E-field when a G10 spacer is used in liquid helium. They measured as a function of temperature and pressure and found no difference between clean and contaminated samples.

On the other hand Wu and Roach's data suggest there is no significant change in breakdown voltage for a temperature range between 1.93 K and 4.24 K when the pressure in the liquid is held at approximately 1 atmosphere after the introduction of a 1 mm spacer.

5 Experimental Apparatus and Methods

5.1. Introduction and Overview of the Pressure Cell Rig

The main aim of this thesis is to understand better some of the factors affecting the dielectric strength of liquid helium most relevant to the cryo-edm experiment. Previous work has been reviewed in Chapter 4, and by Karamath (Karamath 2007). In particular, in our laboratory Karamath (Karamath 2007) found an unambiguous reduction in the breakdown strength by a factor of ~ 2 over the temperature range 4.2 K to 1.4 K for liquid helium in equilibrium with its SVP. Long et al (Long et al 2006) have reported similar results over a smaller temperature range. Both of these experiments were carried out in a pumped helium bath, leading to simultaneous changes of the temperature and pressure in the liquid. In order to separate the possible dependences, we have developed an apparatus that can measure dielectric breakdown of liquid helium whilst varying the pressure and the temperature independently.

Our Pressure Cell (PC) rig is designed to investigate V_{bd} (T,P). The pressure in a closed vessel containing the helium under test can be increased from the SVP at any given temperature up to about 2 bar. Inside this vessel, the HV breakdown cell uses essentially a parallel plate geometry with the maximum area possible. The HV electrode accordingly has a "Rogowski" profile (Lux 1998, Ness 2008, Rogowski 1923, Rogowski 1926a, Rogowski 1926b) and the ground electrode is a flat circular cup. A large amount of effort has been made to ensure that the electrodes can first be aligned to be parallel to each other and then to remain so. Both electrodes are electrically isolated from the pressure cell body such that discharges make a safe path back to the HV power supply. The whole arrangement can operate to above 50kV.

The PC was designed to be used either with a metal bath cryostat (the "KEK") or with a large-access Oxford Instruments dilution fridge with a 20 mK base temperature. All data

taken for this thesis was made using the KEK cryostat over the temperature range ~ 1.7 K to 4.2 K.

This chapter gives a detailed account of the challenges involved in the design, construction, commissioning and use of this apparatus.

5.2. The Pressure Cell Rig: Mechanics and Electrostatics

5.2.1. Dimensional Constraints

The first step in the design process was to ensure that the PC vessel could fit either inside the KEK cryostat or onto the cold plate of the dilution refrigerator.

The next aim was to produce a parallel plate HV cell with the largest area possible whilst incorporating a structure to allow xyzθØ rotation of the ground electrode with respect to the HV electrode.

The inner diameter of the KEK cryostat is Ø 200 mm. The dilution fridge inner vacuum can (IVC) is actually smaller than this but, as seen in Fig.5.1, could easily be modified to accommodate a diameter of up to 300 mm. Hence, the diameter of the PC was fixed at 190 mm. The total height of the PC is limited to 300 mm by the length of the IVC in the fridge.

The dilution fridge has three 38 mm ID experimental access ports which run directly from room temperature and through the cold plate, as shown in Fig.5.2. It was decided to use the locations of the two most widely separated ports to define the positions of the HV feed and return lines to the PC. These have a centre to centre separation of 94.85 mm.

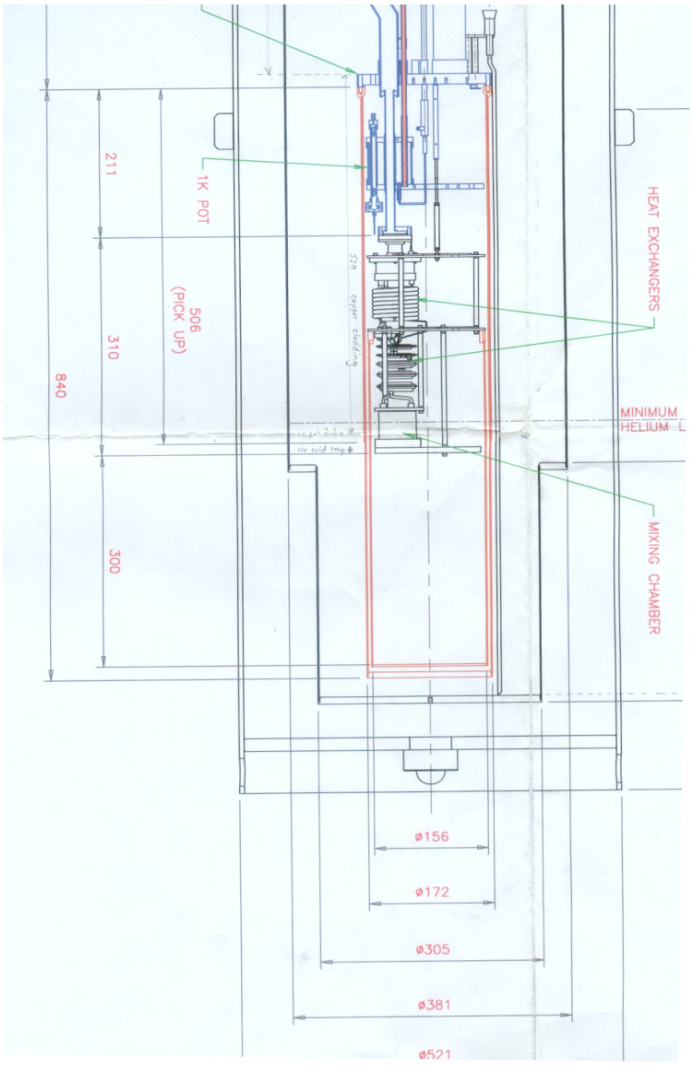

Fig..5.1. Technical drawing of the Oxford Instruments dilution refrigerator.

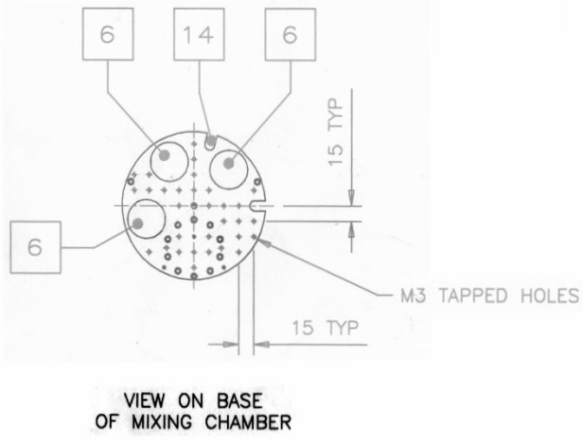

Fig..5.2. View of the base of the mixing chamber on cold plate of the dilution refrigerator. Three 38 mm ID access ports are labelled by the number 6.

5.2.2. HV Cell and Mechanical Alignment

A cross section through an AutoCAD generated model of the whole PC is shown in Fig.5.3.

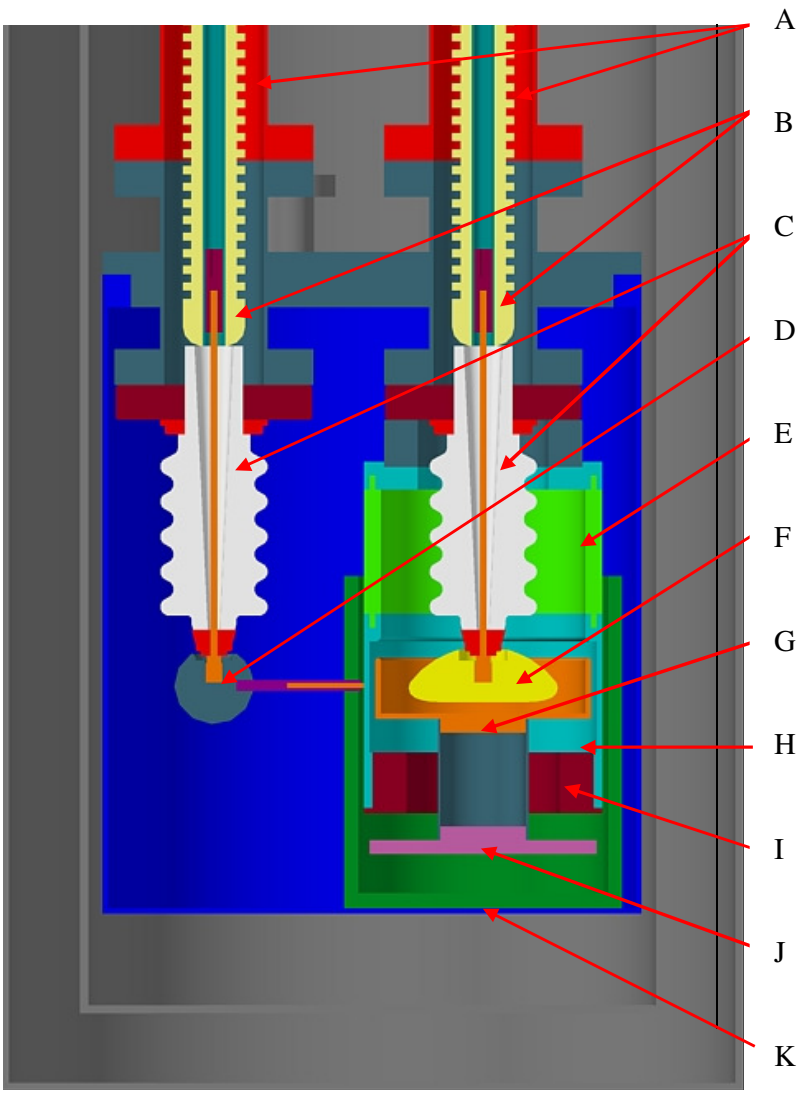

Fig..5.3. AutoCAD generated model of the PC apparatus. A: HV feed vacuum tubes; B: HV feeds; C: ± 30 kV commercial ceramic feedthroughs; D: Return line ball connector; E: G-10 middle section of the PC ground electrode support structure; F: HV Rogowski profile electrode; G: Ground electrode; H: lower section of the PC ground electrode support structure; I: xyzθØ ground electrode positioning ring; J: PC ground electrode positioning plate; K: Insulating PTFE bucket.

The pressure cell is suspended from two evacuated thin-wall stainless tubes (A), down which run the HV input and return lines (B). Each tube is effectively closed by a commercial HV feedthrough (C) with both the tube(s) and the feedthrough(s) being connected to the PC top plate. The HV electrode (F) is attached to the end of the input feedthrough. Details of the Rogowski profile of the HV electrode are given in section 5.2.3. We discuss here the circular cup ground electrode (G) and ground electrode support structure (E and H), and the xyzθØ positioning ring (I) which ensure that the electrodes are always parallel.

The ground electrode, shown in Fig. 5.4, is a circular cup with an inner diameter of 72 mm. It was chosen to be a cup rather than a plate so that the electrostatics of the HV cell would be cylindrically symmetric. It was also machined from solid stainless steel, rather than fabricated, for the same reason.

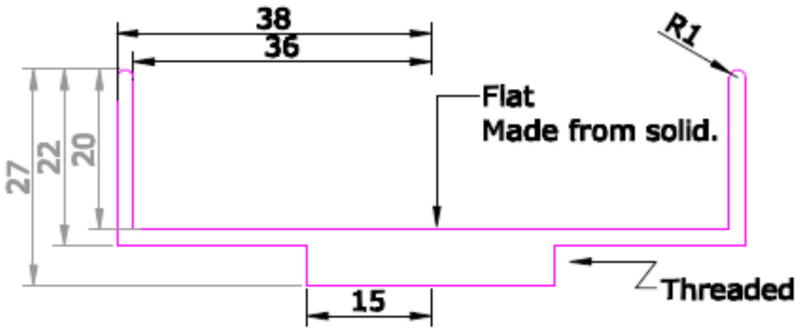

Fig..5.4. AutoCAD drawing of the PC ground electrode.

Figure 5.5 shows the PC with the outer can removed and the ground electrode support structure (E & H) can be clearly seen. This is mounted from the input feedthrough flange and consists of upper and lower stainless steel rings glued to a G-10 tube middle section, thus providing electrical insulation between the HV cell and the PC body. The lower part of the support structure connects to the xyzθØ positioning ring, which in turn is connected to the ground electrode. Hence, both electrodes are effectively mounted on the input feedthrough.

To produce a parallel alignment of the electrodes, the assembly sequence is as follows. The xyzθØ positioning ring is placed over the ground electrode positioning tube prior to the ground electrode and the ground electrode positioning plate being connected together, as shown in Fig.5.6. Three M6 studs are securely screwed into the base of the xyzθØ positioning ring, and protrude through three 10 mm diameter holes on the ground electrode

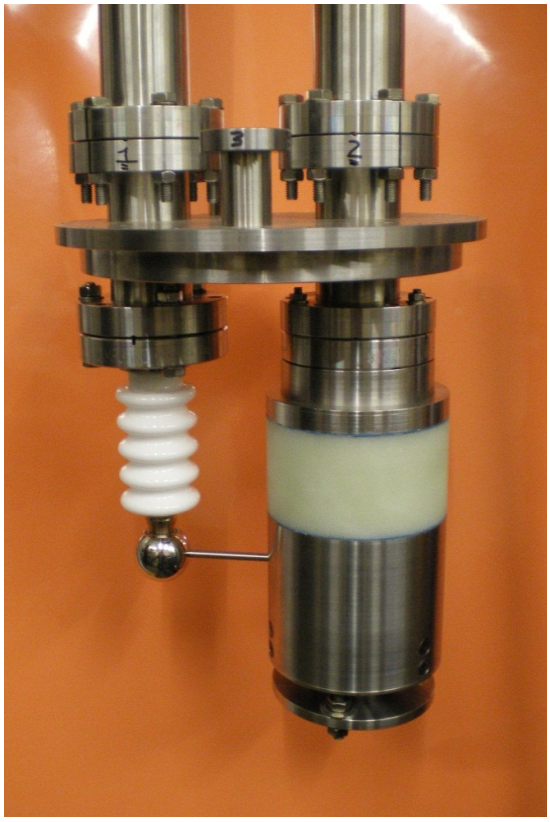

Fig..5.5. The PC with the outer can removed. The ground electrode support structure is suspended from the input (HV) feedthrough flange.

positioning plate. A shim of thickness equal to the desired separation is then placed on the ground electrode. The ground electrode, now connected to the ground electrode positioning plate with the xyzθØ positioning ring between them, is offered up to the HV electrode. Next, the xyzθØ positioning ring is fixed to the lower part of the ground electrode support structure.

The ground electrode is now carefully raised until the shim makes contact with the HV electrode. Once the shim is flat against both electrodes, the positioning plate can be firmly clamped to the xyzθØ positioning ring. This is done with a nut and a large penny washer on either side of the ground electrode positioning plate.

Fig..5.6. Assembly sequence for the PC ground electrode**.** Clockwise from top left: Image 1: PC ground electrode, PC ground electrode tube and PC ground electrode positioning plate; Image 2: PC ground electrode connected to the positing plate. Also shown is the xyzθØ ground electrode positioning ring; Image 3: PC ground electrode connected to the positing plate with the xyzθØ ground electrode positioning ring in place. Also shown is the lower section of the PC ground electrode support (before being glued to the G-10 section); Image 4: PC ground electrode fully assembled and connected to the PC ground electrode support via the xyzθØ rotation ring.

This arrangement has many advantages. As the diameter of the holes on the ground electrode positioning plate are large compared to the M6 stud diameter, x and y adjustment is

possible when aligning the electrodes. The height and angle of the ground electrode can be adjusted by moving the nuts and penny washers up and down the threads on the three M6 studs, thus providing z, θ, Ø adjustment.

The final stage of the cell assembly is to remove the shim. The ground electrode is now firmly attached to the xyzθØ positioning ring via the ground electrode support plate. The xyzθØ positioning ring is released from the lower part of the ground electrode support structure. The ground electrode is removed and the shim taken out. The ground electrode is then placed back in the same position by fixing the xyzθØ positioning ring to the ground electrode support structure. The final result is a parallel separation between electrodes which is equal to that of the thickness of the shim.

5.2.3. Rogowski profile electrode

We require the HV cell to have the largest area compatible with the dimensional constraints. The best way to utilise the space available is to use a so-called Rogowski profile electrode (Lux 1998, Ness 2008, Rogowski 1923, Rogowski 1926a, Rogowski 1926b). Compared to a simple parallel plate geometry, this type of profile effectively increases the volume of uniform E-field within the cell whilst at the same time removing the high fields at the electrode edges. This section gives an overview of the methods used to electrostatically model, design and then manufacture a Rogowski profile electrode for the PC cell.

Normally, to produce a Rogowski profile a finite plate electrode parallel to an infinitely large one is electrostatically modelled. In our case, the ground electrode is not infinite and is cup shaped. Hence, the model was adjusted by reducing the size of the finite electrode until the fields at its edges were only marginally affected by the presence of the ground electrode.

The modelling of the cell, including the lower part of the ground electrode support structure were done using Vector Fields Opera software (Opera v10), as shown in Fig. 5.7. A 0.01 cm thick circular flat plate electrode is placed 0.82 cm from the ground electrode. The flat plate is then raised to 200 kV and the ground electrode the lower part of the ground electrode support structure held at 0 V. The resulting potential and E-field maps are shown in Fig. 5.8 with the highest field being at the edge of the plate electrode.

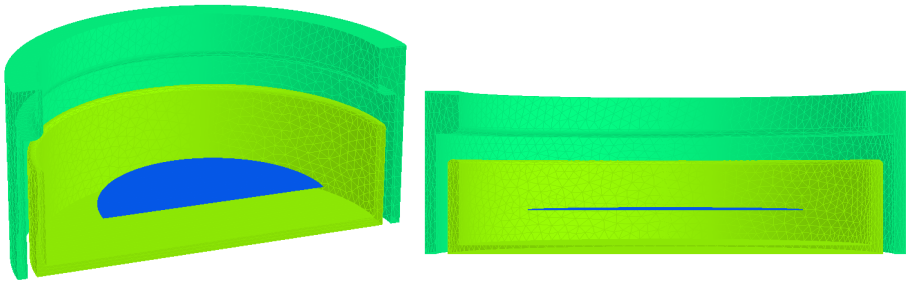

Figure.5.7. Opera geometric model. Pale green: PC ground electrode; Green: Lower part of the ground electrode support; Blue: Parallel plate electrode. The electrodes are separated by 0.82 cm.

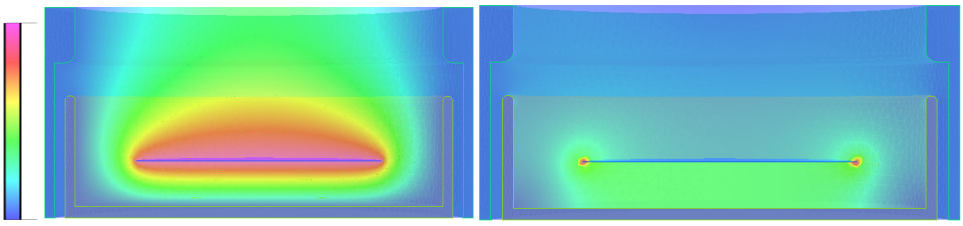

Fig..5.8. Opera output with ground electrode at 0 V, lower part of the ground electrode support at 0 V and the plate electrode at 200 kV. Electrode separation 0.82 cm. Left image: Equipotential map: 200 kV, red; 0 V, blue. Right image: E-Field map: 7.9 x 10^5 kV/cm, red; 0 kV/cm, blue, The highest E-field is at the edge of the plate. The same colour key can be used for both plots.

The left image of Fig.5.9 shows the equipotential contour map (at 25 kV intervals) superimposed on the E-field map. From this figure, an equipotential is then chosen that has the high field edge effects inside the contour and which results in the highest fields outside

the contour being in the region between the equipotential and the ground electrode. Thus the E-field in this region is also more uniform than that in the whole region between the flat plate and the ground electrode.

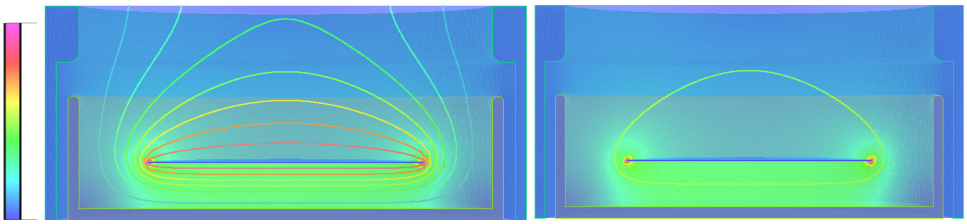

Fig..5.9. Opera output for same configuration as in Fig.5.8. Left image: Equipotential contours superimposed on the E-field map. Contours are at 25 kV intervals. Right image: The 100 kV contour superimposed on the E-field map.

Our choice of parameters was guided by Karamath's (Karamath 2007) observation of breakdown at 100 kV at an electrode separation of 0.41 cm in ^{4}He at 4.2 K under SVP. The right image in Fig.5.9 shows the 100 kV contour only and this is equidistant from the plate at 200 kV and the ground electrode over much of the cell. Hence, an electrode with this profile at 0.41 cm from the ground electrode and at 100 kV will generate the E-Fields shown. Increasing the separation above this value may result in the maximum field being between the HV electrode and the sides of the ground electrode.

A HV cell with this design should thus be capable of doing breakdown tests in ^{4}He at separations of up to 0.41cm and at voltages of 100 kV. Currently the PC apparatus is restricted to 50 kV since the high voltage feedthroughs start breaking down beyond this voltage.

To manufacture the Rogowski electrode, the desired profile was taken from Opera, exported into AutoCAD and digitised. The profile was then programmed into an NC lathe by

the mechanical workshop personnel and the Rogowski profile electrode made out of stainless steel, as shown in Fig.5.10.

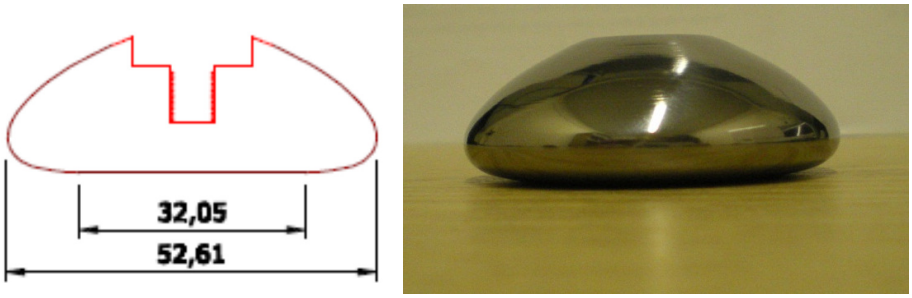

Fig..5.10. Pressure Cell HV Rogowski profile electrode.

The same preparation technique was used for all the electrodes used in this thesis. After mounting on a carrier stub in a lathe, they were mechanically polished with successively finer abrasives culminating in one micron silicon paper. They were then polished with Autosol paste. After the mechanical polishing, the electrodes were cleaned and degreased in a solution of Decon 90 in a an ultrasonic bath for ~ 30 mins. They were then rinsed repeatedly using deionised water and dried in air.

5.2.4. The Pressure Cell Blow-off Valve

In use, the PC contains several litres of liquid helium under pressure. A catastrophic rise in temperature of the main bath would lead to unacceptably high pressures in the cell and hence a blow-off valve is needed. It was decided to have this valve in very close proximity to the PC, rather than at the room temperature end of a capillary which might block. Given the unavailability of a suitable commercial device, a blow-off valve was designed which would be fixed onto one of the mini CF access ports on the top plate of the PC. The design was

influenced by that of (More and Johnson 1998), since their superfluid-tight blow-off valve met all our criteria.

Our valve is made of two parts, as shown in Fig. 5.11. The first is the valve support (f). It is simply an extension of the PC volume to which the blow-off valve top plate seals. This top plate carries the blow-off valve mechanism, consisting of a CuBe spring bellows, a piece of thin 0.025 mm Cu sheet and a chamfered M4 stud with a hole drilled through the middle. One end of the CuBe bellows is hard soldered onto the valve top plate and the other end to the copper support ring. The thin Cu sheet is soft soldered onto the Cu support and the M4 stud is positioned a set distance away from the Cu sheet and held in place by two lock nuts. The blow-off valve mechanism, hanging from the top plate fits inside the valve support and seals to it using Indium.

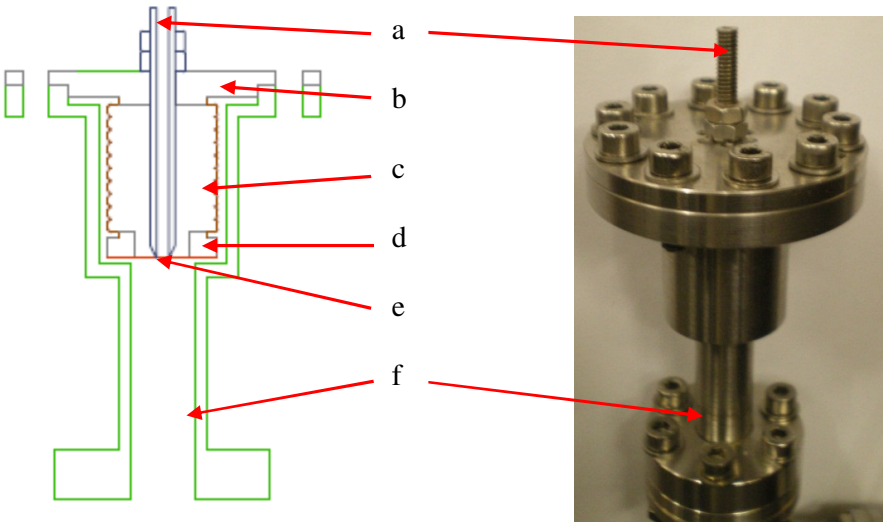

Fig..5.11. Pressure Cell Blow-off Valve. a: M4 chamfered stud with a hole through centre; b: blow-off valve top plate; c: CuBe spring bellows; d: Cu support ring; e: Cu sheet; f: Blow-off valve support.

Increasing pressure in the PC causes the CuBe bellows to squeeze together until the Cu sheet touches the M4 stud and the Cu sheet is eventually punctured, as shown in Fig.5.12. The over pressure is then released into the KEK main bath volume via the hole in the M4 stud

and the 6 holes on the blow-off valve top plate. After puncture the Cu sheet has to be replaced.

Fig..5.12. Tested parts of the PC blow-off valve. Left: Perforated Cu rupture sheets; Right: CuBe spring bellows.

The blow off value was first tested at room temperature. The spring constant was measured and the height of the M4 stud set such that it would puncture at a given pressure. This worked rather reliably at room temperature but in liquid nitrogen, the same separation led to perforation at a higher pressure, presumably due either to differential thermal contraction or to a change in the spring constant of the CuBe bellows.

For cryogenic use a different method is used to determine the required setting. With the stud withdrawn, the valve is connected to a He gas bottle, pressurised to the desired value and then immersed in liquid nitrogen. After boiling has stopped the valve is removed from the nitrogen and the M4 stud screwed in gently until it makes contact with the Cu sheet. The stud is locked in place. the pressure released and the valve allowed to warm.

To test the reproducibility of this technique, the blow off valve is again cooled in liquid nitrogen and the pressure increased until rupture. Such tests proved satisfactory and the valve was set in this manner before being installed on the PC. Given that most of the thermal contraction of stainless and CuBe has occurred by 77K, it was assumed that the rupture pressure at helium temperatures would be very similar to the set value.

5.2.5. Additional parts of the Pressure Cell

For completeness, this section goes through the remaining parts of the PC. As discussed in 5.2.1 the PC top plate, shown in Fig.5.13, was designed to fit into both the KEK and dilution fridge. It is made from stainless and has five access ports: two CF70 flanges on the bottom connect to two HV feedthroughs and three mini CF flanges provide access for the pressurisation system and temperature instrumentation.

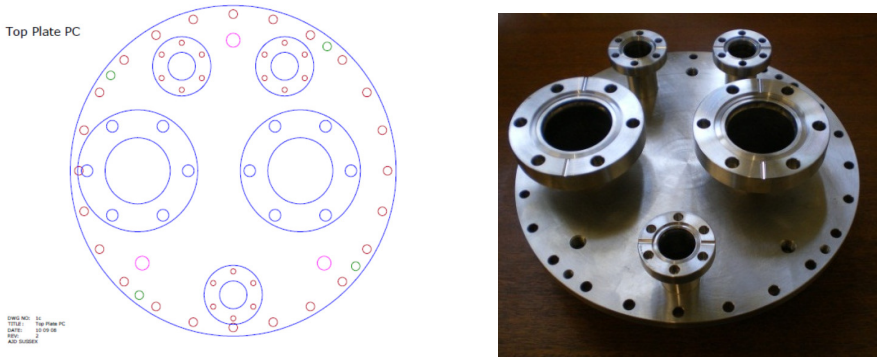

Fig..5.13. Pressure Cell top plate.

Figure 5.14 shows the finished PC being offered up to the cold plate of the dilution fridge, thus confirming the HV access ports were in the correct position and that there are no obvious barriers to use at lower temperatures.

The commercial HV feedthroughs (MDC 2010) have been extensively tested at low temperatures. Although they are rated at only ± 30 kV, they have proven stable to ±50 kV and tests in superfluid ^{4}He confirmed their leak tightness. These feedthroughs were used for all breakdown measurements taken in the PC reported in this thesis. As discussed in section 5.2.3, the PC should work to 100kV but to reach this, higher rated feedthroughs will be needed.

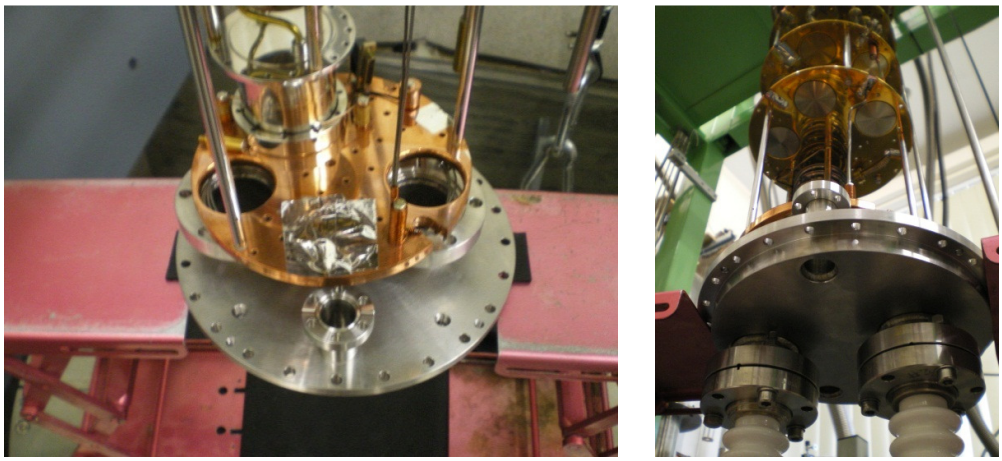

Fig..5.14. The PC top plate positioned under two of the access ports on the cold plate of the dilution refrigerator.

Fig..5.15. The PC top plate and can sealed together and hanging from the HV feed vacuum tubes.

The PC outer can and top plate are sealed using Indium and are shown in Fig. 5.15. Before commissioning the PC was pressure tested to 3 bar.

Figure 5.16 shows the stainless steel top plate to enable the PC to run in the KEK cryostat. The PC hangs from it via a pair of thin wall stainless steel tubes down which the HV feed and return lines pass. The tubes connect the PC and top plate via two CF70 flanges, one

of which is rotatable to ensure alignment. To prevent room temperature radiation hitting the PC a series of baffles is mounted around the HV feed vacuum tubes. These are staggered in height to ensure maximum pumping conductance.

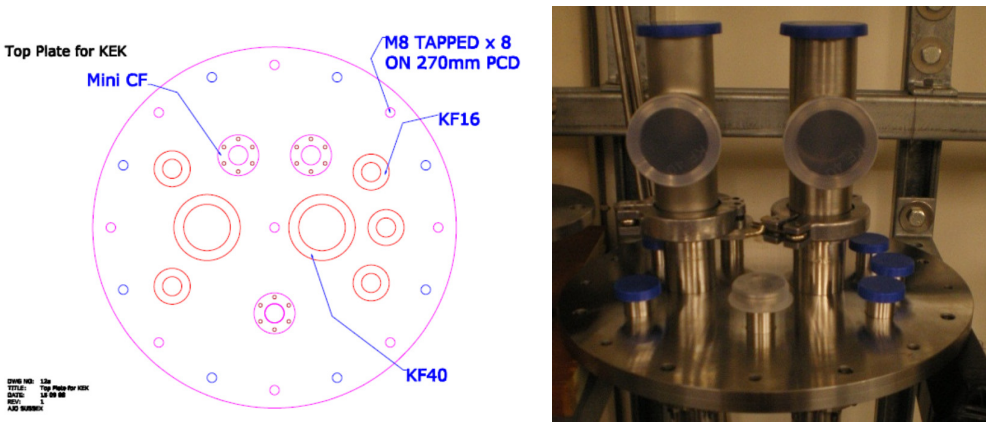

Fig..5.16. The KEK cryostat top plate.

5.3. Pressure Cell Temperature Control

5.3.1. Varying and Measuring the PC Temperature

The temperature of the PC is determined by the temperature of the liquid ^{4}He in the KEK. As long as the PC is in thermal contact with the main bath, the PC and everything inside it is assumed to be at the same temperature. The main bath is cooled by evaporative cooling in the usual manner and a vapour pressure line extending to the base of the KEK cryostat is used to determine the temperature on cooling from 4.2K. The heat input to the main bath is such that even if the cooling is stopped, there is little evidence of the helium remaining supercooled with rising bath pressure. The pumps used are capable of producing a base temperature of ~ 1.7K.

It is relatively easy to hold the temperature of the main bath stable while taking breakdown data by adjusting the flow rate between the main bath and the pumps with a large

and a small valve in parallel. In general the temperature of the bath was not changed rapidly, ensuring the PC and main bath remained in thermal equilibrium.

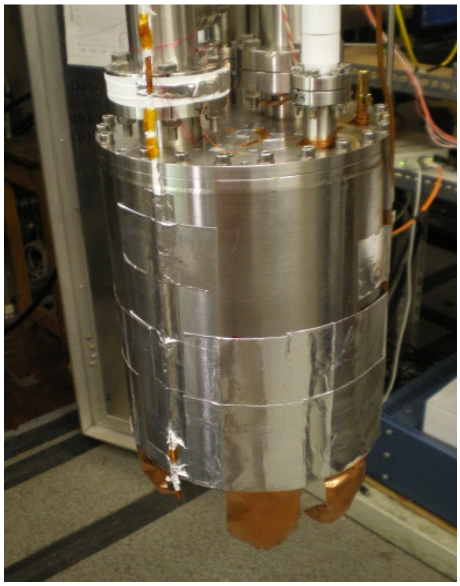

Fig..5.17. Thermally anchoring Cu straps visible at the base of the PC vessel.

Four Cu straps are thermally anchored to the base of the cryostat, as shown in Fig.5.17. These touch the base of the KEK cryostat and extend halfway up the body of the PC vessel. GE varnish secures them to the PC vessel to provide good thermal contact and they were also covered with Al tape. With these straps in place, it reasonable to assume the PC is always in thermal contact with the main bath even if the level of the bath drops below the base of the PC. In practice this situation only occurred during one run and is clearly indicated in the data.

As well as the vapour pressure line, the PC has some other thermometry. A RuO_2 sensor and a K-type thermocouple are each thermally anchored to the top plate. The former works in the range 4.2 K to 50 mK whilst the latter is used down to 70 K. The thermocouple is very useful during pre-cooling and for checking the conditions of the apparatus prior to helium transfer.

The liquid level in both the KEK cryostat and PC are monitored using Alan Bradley level sensors. A separate wire coiled around the level sensor is used to heat it. A four-wire resistance measurement is taken while 1 μA is passed through the resistor. In the gas phase, localised heating of the resistor causes its resistance to change. If this change is more than ~8% the resistor is still in gas. In the liquid phase, the heat from the current is dissipated into the liquid and the change in resistance is far less ~1%. This is a nice and very accurate way of recording the liquid level in both the main bath and the PC.

5.3.2. Filling the Pressure Cell with Liquid Helium

The PC is filled with helium from the main bath via an Oxford Instruments needle valve mounted on one of the mini CF access ports on the PC top plate. It is adjusted by a screw fitting on the KEK top plate. The input tube to the needle valve is a 3 mm copper tube extending to the bottom of the KEK bath. This tube incorporates a filter and it is coupled to the body to the valve by a PTFE jacket.

After pre-cooling, and just before transfer, the PC is filled with approximately 1000 torr of Helium gas and sealed. This acts both as a transfer gas to cool the cell and its contents and as a gas thermometer. Once the level of liquid in the main bath is above the top of the PC the needle valve is opened and the pressure in the cell reduced to ~500 torr. Liquid from the main bath then flows into the PC and the transfer is continued. The aim is to fill the PC completely and to have helium in the main bath up to just below the bottom radiation baffle.

5.3.3. Liquid ^{4}He Density Changes

Once the PC is full with liquid the needle valve is closed and the PC sealed off from the main bath. Breakdown measurements can now be taken at 4.2 K under various pressures

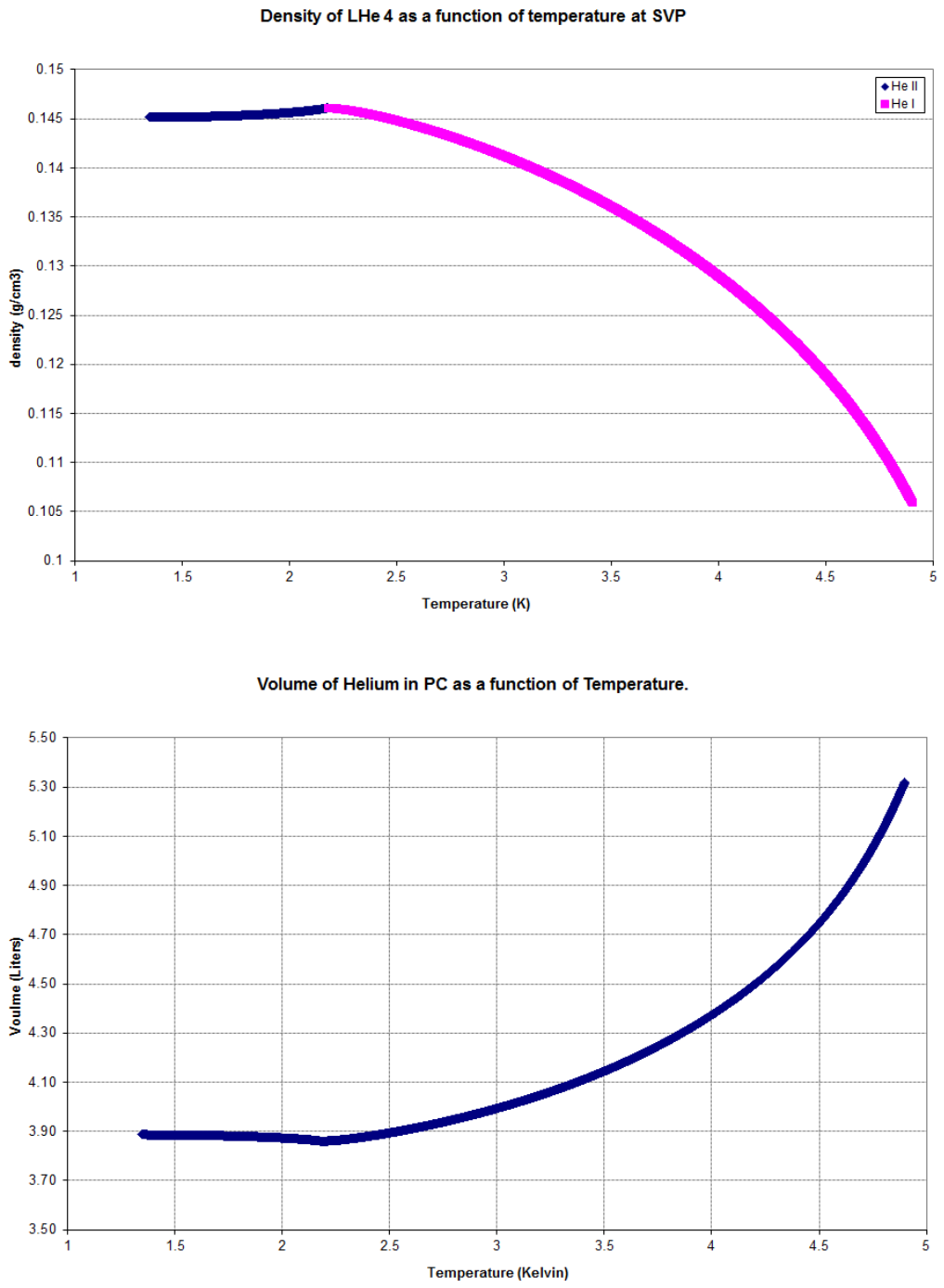

Figure.5.18. Top: Liquid ^{4}He density as a function of temperature, (Donnelly and Barenghi 1998) Bottom: Volume of Liquid ^{4}He in the PC as a function of temperature.

from the SVP at 4.2 K up to 1500 torr. To take measurements at lower temperatures the main bath is pumped on. However, since the density of liquid ^{4}He increases with decreasing temperature, the volume of liquid in a sealed cell will be reduced. Figure 5.18 shows the known change in density (Donnelly and Barenghi 1998) and the 1.4 l volume decrease expected in our cell between 4.2 K and base temperature.

Obviously, the PC has to be completely full before breakdown measurements can be made. Hence, for temperatures below 4.2 K a considerable extra volume of helium has to be slowly condensed into the PC from a gas bottle at room temperature, via a fill capillary line (L_{fc}).

5.4. PC Pressure Control

The helium gas handling circuit along with the connections to the KEK top plate and PC top plate are shown Figure 5.19. A high purity He gas bottle equipped with a high purity stainless steel regulator is coupled into a gas manifold. All seals and valves in direct contact with the input helium gas are of all-metal construction and the manifold can be evacuated with a dry pump. There are two separate capillaries connected to the PC. The 1.56 mm diameter static line (L_{st}) rises straight to the KEK top plate and is used to measure the pressure in the PC using Bourden and Baratron gauges. It was found necessary to install a separate smaller diameter 1.24 mm fill capilliary (L_{fc}) which has a 3 m long cooling coil positioned between the two lowest baffles, as shown in Fig.5.20. Evaporating gas from the main bath cools the coil and therefore the helium gas from room temperature which needs to be condensed as the PC cools below 4.2 K.

At any given temperature the pressure is set on the gas regulator and helium is allowed to flow into the PC via L_{fc}. Once the desired pressure is reached the gas supply is shut off and the pressure measured via L_{st}. Typically, the pressure can drift by ± 3 torr during

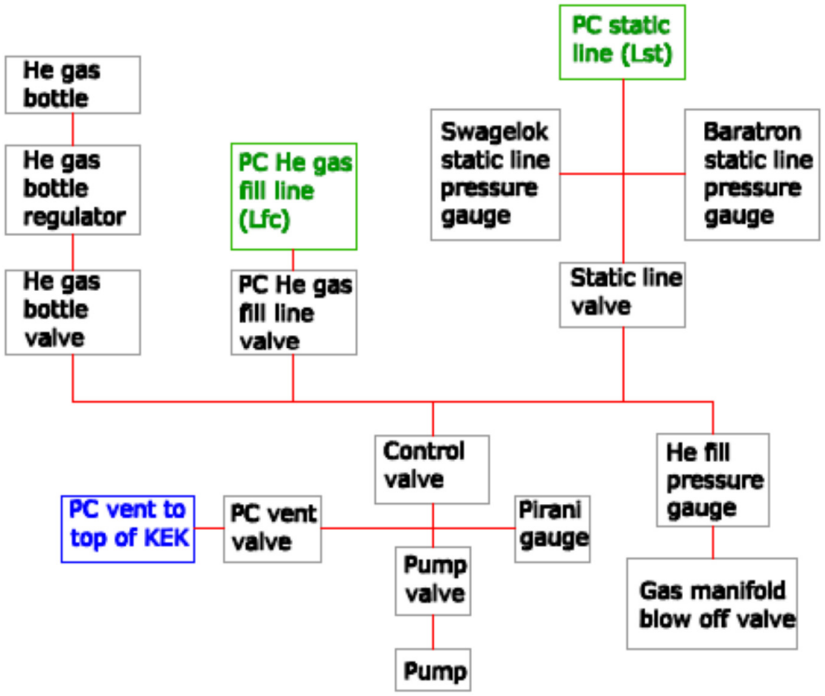

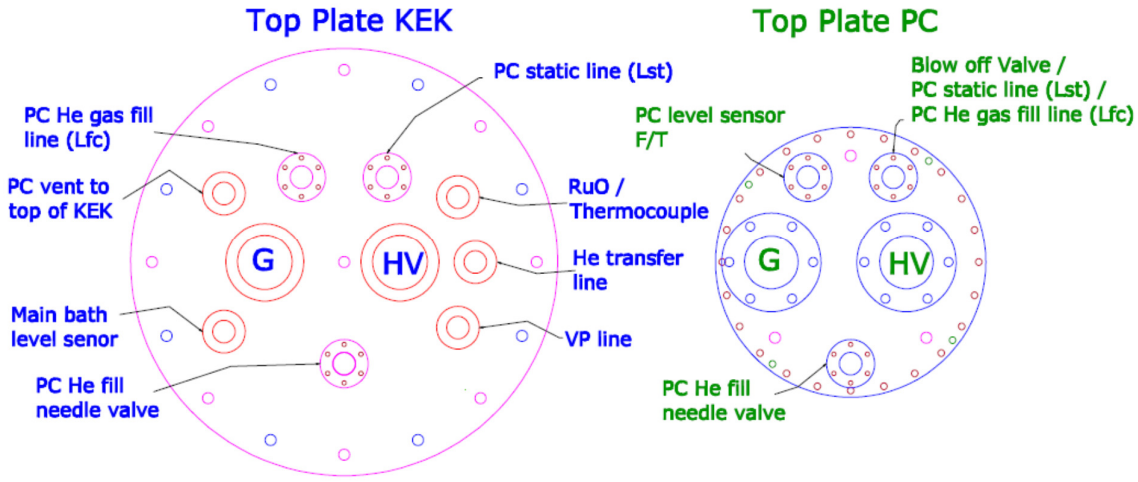

Figure.5.19. Top**:** Flow diagram of the PC He gas handling circuit; Bottom: Access port labels for both KEK and PC top plates.

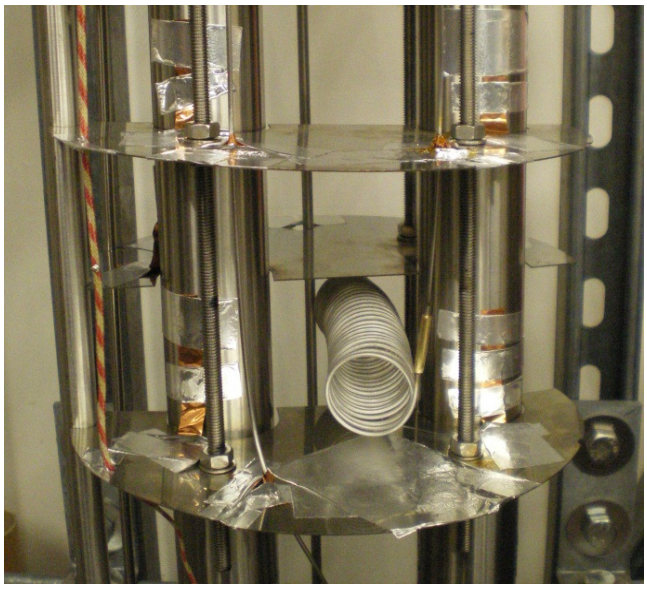

Fig..5.20. The extra 3 meters of length added to the He gas fill line capillary (L_{fc}).

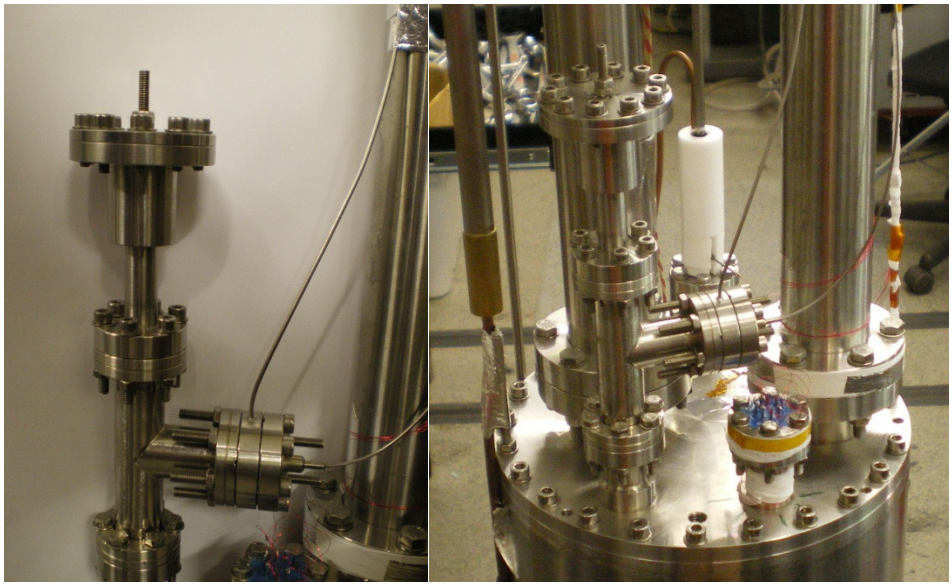

Figure.5.21. Left image: T-piece connecting the He gas fill line capillary (L_{fc}), static line capillary (L_{st}) and blow off valve to the PC vessel; Right image: The fully assembled PC top plate.

the 3 minute interval between data points. Reducing the pressure is usually done by venting the PC to the main bath via the needle valve.

Since there is a large vertical temperature gradient in the cryostat, as the pressure in the PC varies the level of helium liquid in thin capilliaries will rise until it reaches the point where the applied pressure equals the He SVP corresponding to the temperature at that point.

The final assembly of the PC top plate is shown in Fig.5.21. Both capillaries, L_{fc} and L_{st}, are connected to the PC via a T-piece that also connects the blow off valve.

5.5. High Voltage Apparatus

5.5.1. Circuit and Power Supplies

The HV circuit, shown in Fig.5.22, is relatively simple. The most difficult aspect is ensuring that the HV discharge returns safely to the power supply without causing damage to any of the other instrumentation in the rig.

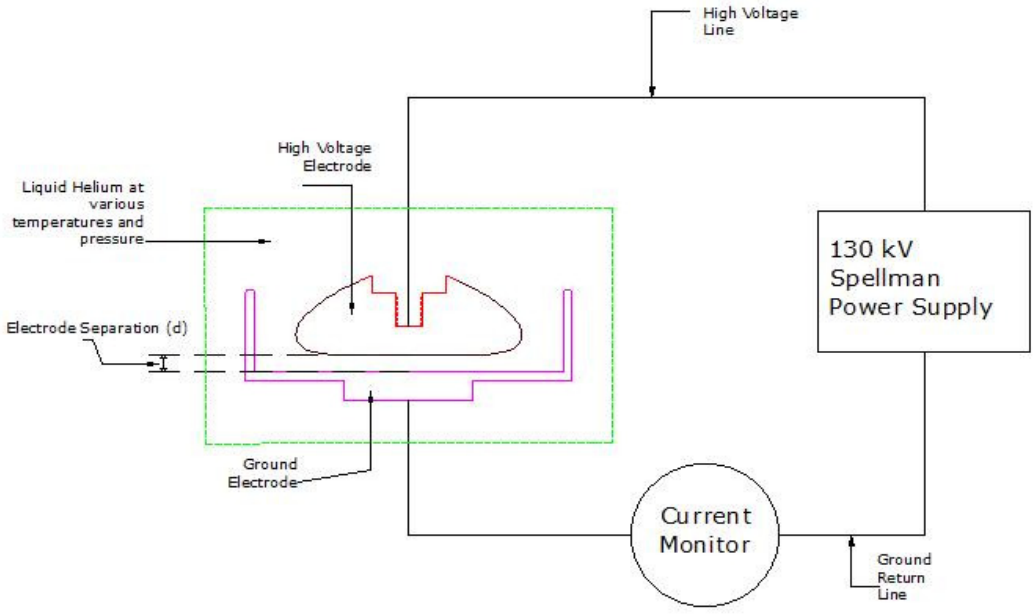

Fig..5.22. The Pressure Cell HV circuit.

Two 130 kV Spellman power supplies (Spellman SL10W) were used, one positive and the other negative polarity. All measurements in the PC were made with the positive voltage on the HV electrode while both polarities were used in the ceramic tests.

The supplies can be run in either current limited or voltage limited mode and have automatic flashover protection. They can be controlled manually or by computer via an optically coupled interface constructed in-house. Karamath (Karamath 2007) has calculated the internal capacitance of the Spellman power supply to be ~ 1 nF.

5.5.2. Pressure Cell HV Feed and Return Line

The cryogenic HV feed was built to Karamath's design (Karamath 2007) which has proved reliable to ± 130 kV in vacuum and has a capacitance of ~0.1 nF. It is made up of a 9.53 mm OD SS tube (0.71 mm wall thickness) squeezed into a 21 mm OD PTFE tube, with ID the same as the SS tube OD. It connects to the HV feedthroughs on the PC via a CuBe connector shown in Fig.5.23. This type of connection provides ample travel. The two legs are spring loaded and push inside the inner stainless steel tube of the HV feed. During any thermal contraction of the HV feed, the legs can move freely along the inner tube thus always ensuring electrical contact.

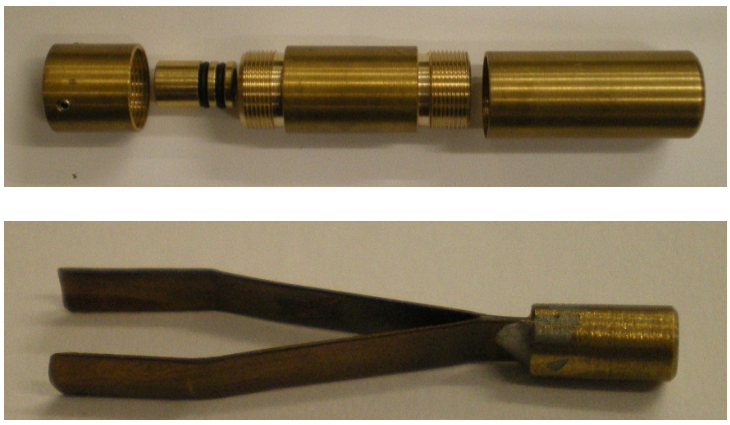

Fig..5.23. Top image: HV feed brass connector prior to assembly (Townsley 2008). Bottom image: Spring loaded CuBe HV feed to feedthrough connector.

This type of connector also enables the inner volume of the feed to be pumped out. The HV feed and return lines were deliberately placed in a vacuum in the initial design. If they were in the main bath volume, where the helium gas pressure varies from atmosphere down to a few torr, breakdown and/or glow discharge would be inevitable at the bottom end of the feed, once the liquid level drops below that of the outer ground. Having the HV feed in vacuum therefore increases the running time and data can be taken until the main bath is practically empty. The top (room temperature) ends of the HV feeds are sealed by a double O-ring HV feed brass connector, see Fig.5.23.

It was found to be essential that the HV feed and return lines are heat sunk to the walls of the feed vacuum tubes to reduce the heat leak into the PC. Prior to doing this the PC could not be filled fully. The level would rise to approximately the height of the electrodes and then stop. Our assumption was that the heat leak down the feeds raised the temperature of the HV electrode and return line ball such that any further helium condensed into the PC immediately boiled off. After the installation of 6 heat sinks on each PTFE feed, equally spaced and fixed firmly to the grounding, it proved relatively simple to fill the PC completely.

Fig..5.24. CuBe spring loaded HV feed heat sinks.

The heat sink, shown in Fig.5.24, is made out of a single strip of CuBe sheet 0.5 mm thick. Four legs are cut from this and the sheet is bent to the diameter of the HV feed. The legs are bent up to make a sprung contact with the inner wall of the feed vacuum tubes. A nut and bolt with a spring washer clamps the heat sink tightly onto the PFTE feed and ensures maximum thermal contact.

The HV feed connects to the Spellman power supply via a ~ 2.5 m HV cable rated at 130 kV and with a total capacitance of ~ 100 pFm^{-1}. The cable mates with the HV feed via our laboratory standard Cu/PTFE connector, see Fig. 5.25.

Fig..5.25. HV Cu connector connected to the HV feed. The return line feed is visible.

When the cell breaks down it is important to direct the discharge safely back to the power supply. For this reason, the characteristics of the return line are essentially identical to the HV feed line. On breakdown, the ground electrode support structure becomes charged. This charge makes its way to the return line via a spring-loaded connect screwed into the return line ball. It then passes through a second feedthrough, up the feed line and back to the power supply.

Practically the whole apparatus, including the cryostat, pumps and all HV parts were inside a grounded Faraday cage. Only the He gas bottle and the computer were outside this enclosure.

5.5.3. Taking Breakdown Data

Before taking breakdown data, the HV circuit was checked by using a current monitor placed in the return line. The voltage to the HV cell was ramped to a modest value and observation of the same value of charging current on the monitor as being delivered by the supply gave confidence that HV was reaching the cell.

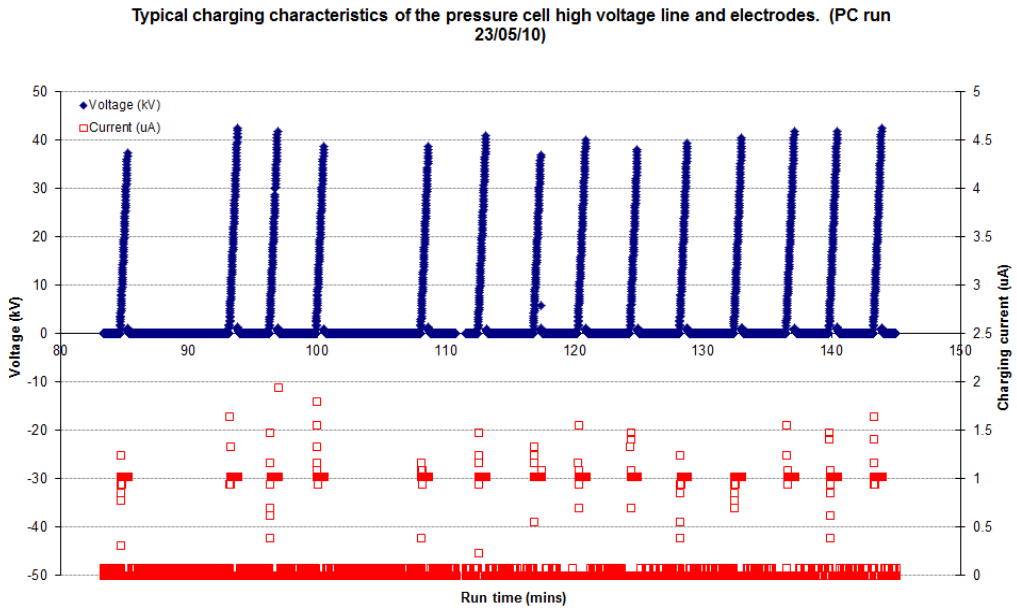

Fig..5.26a. Voltage versus time for a typical charging sequence of the PC HV cell. From PC run 23/03/10. Blue diamonds: Voltage (kV); Red squares: Charging current (μA).

A set of typical breakdown measurements is shown in Fig.5.26. The cycle is repeated about every 3 minutes. The voltage and current limits are set to 50 kV and 1 μA and the voltage ramps in current-limited mode until breakdown. Initially the Spellman power supply

slightly fluctuates, hunts around, before it locks on 1 µA. The breakdown voltage is the highest value reached before the voltage drops catastrophically. This leads to the saw tooth characteristic observed on Fig.5.26a and Fig.5.26b.

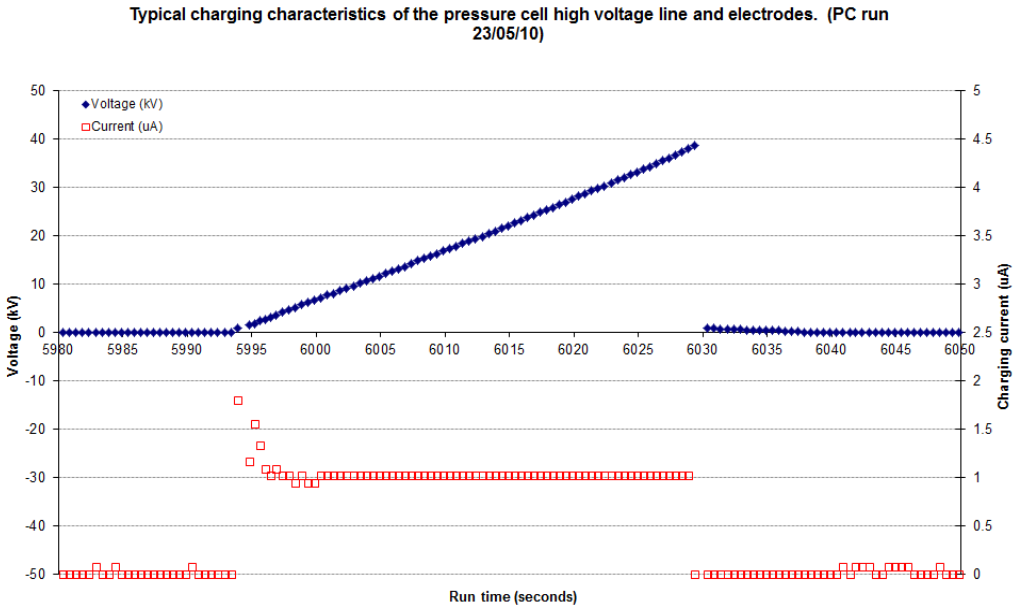

Fig..5.26b. Voltage versus time for a typical charging sequence of the PC HV cell. From PC run 23/03/10. Blue diamonds: Voltage (kV); Red squares: Charging current (µA).

5.6. PC Operation and Apparatus Configurations used

After assembly (section 5.2.), the PC is inserted into the KEK. To flush out all impure gas, the needle valve is shut and the PC volume pumped on through the gas manifold. The pump is then valved off and the PC backfilled to 1000 torr. This process is repeated three times and after the third backfill the gas bottle is left connected. The needle valve is then opened and helium gas flows through the PC into KEK and out via the VP line to ensure this latter is clear. Finally the needle valve is closed and the gas bottle valved off leaving 1000 torr of helium gas in the PC.

The KEK cryostat is then filled with liquid nitrogen. The helium gas in the PC acts as a transfer gas and also as a gas thermometer. The apparatus is cooled for at least 12 hours, after which the nitrogen is blown out. To make sure all the nitrogen is removed the temperature of the KEK is allowed to increase to ~ 90K before helium is transferred. During this warming period a pressure of ~ 800 torr of Helium gas is maintained in the PC with the needle valve cracked open.

The needle valve and the helium gas bottle are then both closed leaving ~ 800 torr in the PC and helium liquid is transferred into the KEK. The pressure in the PC will reduce by ~ a factor of 16 when liquid begins to condense in the bath.

Once the level of helium in the KEK reaches the top of the PC, the needle valve is opened and the PC is filled from the main bath (section 5.3.2.). After filling, the PC can be pressurised (section 5.4.1.). Once the desired temperature and pressure are achieved, voltage is applied to the PC (section 5.3.3.).

The PC apparatus was upgraded four times over the data taking period. Configuration 1 was used for PC runs 1, 2 and 3. The HV feed and return line were in the main bath volume and in contact with the liquid helium. This set up works but does not allow a long running time since the run must be stopped as soon as the liquid drops below the end of the HV feed ground.

Configuration 2 was used for PC runs 4 and 5. The feeds were now in vacuum and PTFE blocks with a volume of 1.5 l were placed in the PC volume to reduce the amount of liquid helium needed to fill it.

The static line (L_{fc}) was added for Configuration 3. From PC run 6 onwards the static line was used to record the pressure in the PC at any point during the run. Prior to this the actual pressure could only be known when the helium gas bottle was valved off. This was only reliable when the PC was full of Helium and not condensing gas to liquid.

The electrostatic integrity of the PC was checked after obtaining the data for this thesis. Configuration 4 was the same as configuration 3 except that both electrodes had been removed, polished and put back together at a larger separation. This configuration was used for PC run 13.

5.7. Tests on Electrodes separated by Ceramic Spacer

5.7.1. Overview of the Ceramic Test Apparatus

A series of breakdown measurements were carried out using pairs of electrodes separated by a cylindrical Al_2O_3 spacer, in a configuration similar to the Ramsey Cell in the main cryoEDM experiment. These experiments were made in liquid helium at 4.2 K and 1.4 K and in liquid nitrogen at 77 K. In all cases, the liquids were under SVP. A glass cryostat with a 90 mm internal bore and the larger diameter KEK were used for the measurements.

The two pairs of electrodes had Rogowski profiles and incorporated grooves which located the ceramic spacers (Hill 2009). Some of the apparatus developed by Karamath (Karamath 2007) was adapted to perform these measurements and is denoted JRK below.

5.7.2. Electrodes for Ceramic Spacer Tests

Full details of the designs of the two pairs of electrodes are given by Hill (Hill 2009) and these are denoted DKH small set (DKHs) and DKH large set (DKHl). The geometry of the groove on each pairs is a scaled version of that on the Ramsey cell. In addition to locating the ceramic spacer, the groove is designed to reduce the E-fields at the CTJ, and hence breakdown. The two sets of electrodes were made from stainless steel in the same manner as described in section 5.2.3 above and are shown in Fig.5.27 and Fig.5.28. Dimensional details of these are given in Appendix F.

5.7.3. Test Rig for DKHs Electrodes

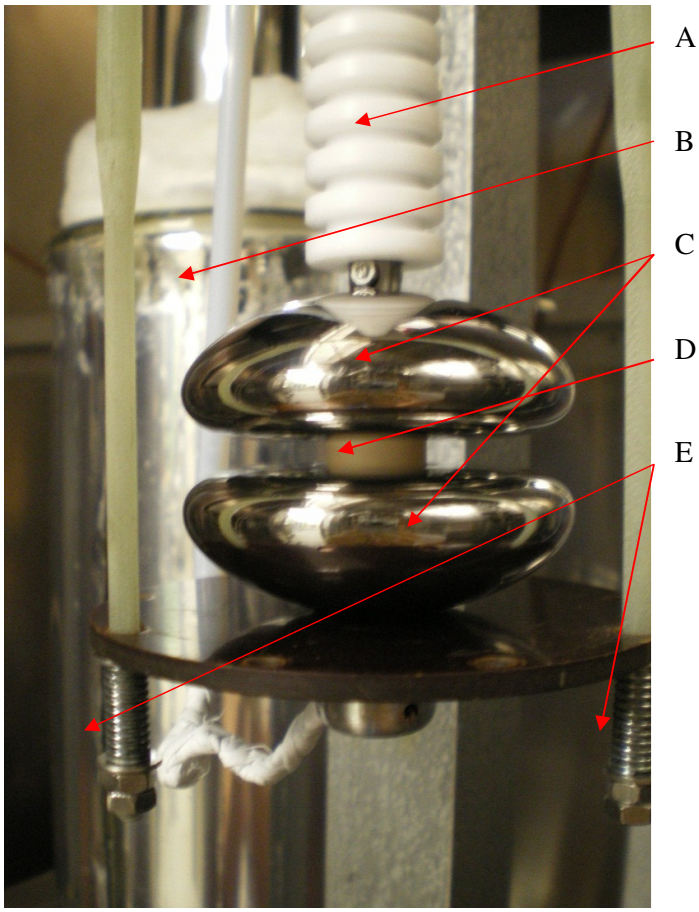

Fig..5.27. The modified JRK setup to measure V_{bd} across a ceramic using the DKHs electrodes. A: HV feed; B: HV return line; C: DKHs electrode; D: 10 × 15 mm diameter Al_2O_3 sample; E: DKHs ground electrode base plate springs.

The lower part of the JRK rig used is shown in Fig.5.27. The upper electrode is connected to the HV feed and a 10 × 15 mm diameter Al_2O_3 ceramic is placed between the electrodes. The rig was modified by adding springs under the insulating base plate which carries the ground electrode. This ensures that the electrodes always remain in contact with the ceramic at low temperatures. This rig was used in a 90 mm bore glass bath cryostat.

In this rig the HV feed can be moved vertically using a manipulator on the cryostat top plate. This adjustment allows us to mechanically load the cell in an accurate manner. The loading can be calculated from the spring constant of the springs and the thermal contraction coefficients of the rig.

A test was made to establish whether the loading or differential contraction causes damage to the ceramic at low temperature. The cell was loaded and dunked in liquid nitrogen until boiling stopped. It was then taken out and inspected and no evidence of any damage was found. The force applied to the cell in this test was ~ 2 times greater than that used during breakdown measurements.

5.7.4. Test Rig for DKHl Electrodes

To run the DKHl electrodes, the JRK rig had to be modified to run in the larger diameter KEK cryostat. In this case the HV electrode simply rests on top of the 60 × 70 mm diameter ceramic. The weight of the electrode alone is sufficient to ensure good contact with the ceramic. A spring contact was made between the HV electrode and HV feed. In one configuration, the spring contact was made using a Coda connector, see Fig.5.28 (G). In a second configuration, the spring contact is made using a connector similar to that used in the PC apparatus, see Fig.5.28 (H).

In both configurations the ground electrode was secured to a plate suspended from the top plate of the KEK cryostat. As the inner height of the KEK is less than that of the glass cryostat, a collar is needed to gain extra height for the JRK insert.

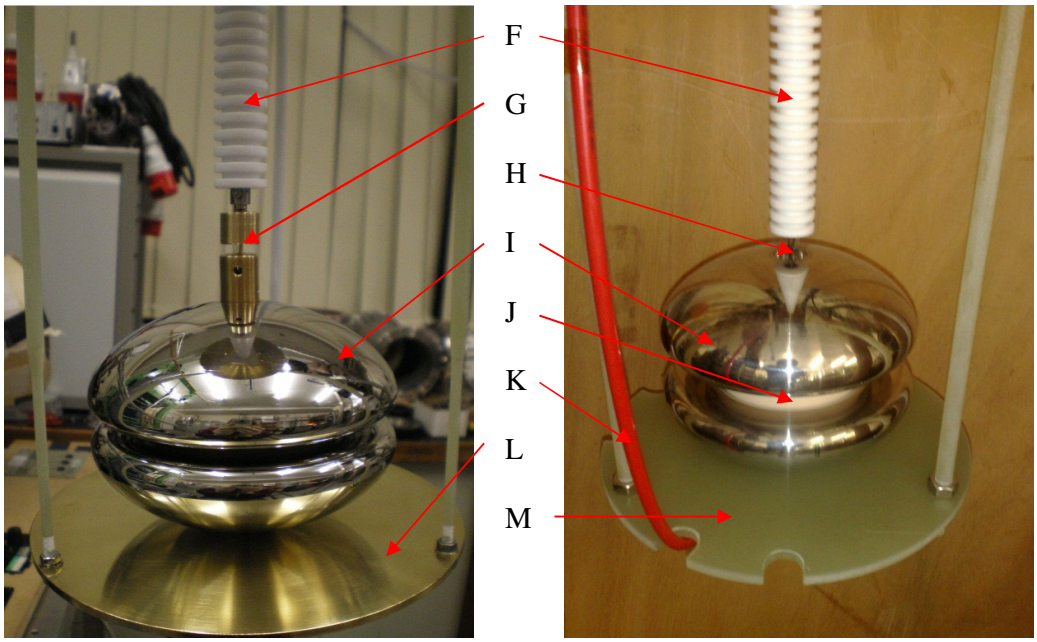

Fig..5.28. The setup to measure V_{bd} across a ceramic sample using the DKHl electrodes. Left image: DKHl apparatus configuration 1; Right image: DKHl apparatus configuration 2. F: HV feed; G: Configuration 1 HV feed to DKHl electrode connector; H: Configuration 2 HV feed to DKHl electrode connector; I: DKHl electrodes; J: Al_2O_3 sample; K: Configuration 2 return line; L: Configuration 1 ground electrode base plate; M: Configuration 2 ground electrode base plate.

5.7.5. Operation of the Ceramic Test Apparatus

Measurements taken in He I, He II and liquid nitrogen were set up in the same manner. Prior to installation the ceramics are cleaned in aqua regia solution for 30 mins and then rinsed repeatedly with deionised water. The electrodes are polished and cleaned in the usual way. The ceramic is mounted between the electrodes and then loaded.

When taking measurements in liquid nitrogen the cryostats are simply filled directly. When using liquid helium, the KEK cryostat is pre-cooled with liquid nitrogen which is then blown out. The glass cryostat has a separate liquid nitrogen jacket and is pre-cooled with the helium volume evacuated. After the helium transfer the temperature can be adjusted in the usually way by evaporative cooling.

6 Data

This chapter presents all data taken for this thesis and has been split into three sections.

Data from PC runs 1 to 5 are displayed in section 6.1. These were taken using the PC before the incorporation of a permanent static line. High voltage breakdown, temperature and pressure are plotted versus event number for each run. At the end of the section, 6.1 data from PC runs 1 to 5 are plotted together to give an overall picture of high voltage breakdown in liquid helium as a function of pressure. The error bars on the pressure for these measurements are large as a result of not having a static line and should be regarded as preliminary data.

The addition of the separate static line allowed the PC pressure to be determined accurately at any point during an experimental run. All the data presented in section 6.2 (PC runs 6 to 13) were taken using this configuration over the temperature range 1.7 K $\leq$ T $\leq$ 4.2 K and at pressures from SVP to 2.2 bar. The variation of the high voltage breakdown as a function of pressure at various fixed temperatures is shown at the end of the section.

Section 6.3 presents all the data taken with the DKHl and DKHs electrodes with and without ceramic spacers, and in liquid helium and liquid nitrogen.

As discussed in Chapter 4 (4.1.5 extremal value distribution), the values of breakdown voltages measured at given fixed pressures and temperatures often follow an extremal, rather than Gaussian, distribution and hence can show a wide range of values. For this reason, in the raw data plots we have shown all the recorded values. Where average values of breakdown voltages are presented, the arithmetic mean of the data set is used and the error bars shown are the standard error of the mean. This is defined as $\frac{\sigma}{\sqrt{n}}$, where σ is the standard deviation of the data set at that temperature and pressure and n is the number of data points.

One of the main objectives of this thesis was to determine the dependence of the high voltage breakdown in liquid helium as a function of pressure. For this, we need to determine how the breakdown voltage distribution shifts as a whole with varying pressure. The arithmetic mean of a given data set, together with its standard error as defined above, is hence a valid parameter from which to determine any such variation with pressure.

It is important to distinguish between the mean of the distribution of observed breakdown voltages and some "voltage rating" or "breakdown voltage". In order to determine this latter value, one has first to specify the acceptable probability that application of the working voltage will lead to a breakdown. If this is, say, 1%, then the "breakdown voltage" will be the point on the distribution below which only 1% of breakdowns occurred. This will obviously be much lower than the mean of the breakdown voltage distribution which we have used.

6.1 $V_{bd}(P,T)$ Data taken without static line

The following section gives an account of all data taken with the PC apparatus between 12/03/2010 and 20/04/2010. These data were taken before the installation of a static line on the PC to measure the pressure. In general, the breakdown voltage, V_{bd}, is shown as triangles, the main bath saturated vapour pressure, P_v is circles and the main bath temperature, T_{mb}, squares. The temperature of the PC, T_{PC}, is deduced from T_{mb}. The PC pressure is shown in the figures as two distinct groups. Group 1 is when the pressures in the PC, P_c, are known precisely and on the figures are shown against a blue background. The Group 2 data were taken at times when $P_v \leq P_c \leq P_t$ where, P_t is the pressure set at the top of the fill capillary (L_{fc}) and are shown against a red background.

6.1.1. PC Run 1 (12/03/2010)

Figures 6.1a and 6.1b show all breakdown data taken from PC Run 1 as a function of the run time.

The first ten data points were taken at a temperature of 4.2 K and under P_v. The pressure in the PC is known precisely. The average V_{bd} for this set is 36.8 ± 1.2 kV.
At time (A), helium gas is released from the gas bottle and P_t set to ~ 1200 torr. This resulted in a sudden jump in the average breakdown voltage of the next twenty data points to 42.68 ± 0.87 kV, this indicated that increasing the pressure of the liquid helium at a fixed temperature does increase V_{bd}.

At time (B) the main helium bath was pumped on and P_t was held at 1200 torr. While cooling thus it was obvious that helium gas was condensing into the PC since a whistling sound was herd through the regulator. This is due to the density of the helium, ρ_H, increasing with decreasing temperature, resulting in a decreased volume of helium in the PC.

V_{bd} data was taken while cooling down after (B) and during this period it was not clear that $P_t = P_c$ so this data is in Group 2. Shortly after cooling had started it was decided to warm back to 4.2 K and refill the cryostat to ensure a longer run time and hence only two data points were taken between (B) and (C). Before refilling, further V_{bd} measurements were taken at 4.2 K under P_v, between (C) and (D) with an average breakdown at 40.00 ± 0.61 kV. Breakdown measurements were resumed once the cryostat had been refilled to maximum level. Between (D) and (E) five measurements were taken at 4.2 K and a pressure just above P_v. Although it was assumed that the pressure at both ends of the capillary was the same, this was not confirmed. For this reason this data has been classed as Group 2.

At (E) the second cooldown of this PC run started. Between (E) and (F) the reduction in temperature was accompanied by a steady decrease in V_{bd}. It should be noted that the regulator setting was not changed after cooling started (E). P_t dropped by ~ 110 torr

from ~ 800 torr to ~ 690 torr, caused by helium gas condensing into the PC. As $P_v \leq P_c \leq P_t$ the data is in Group 2.

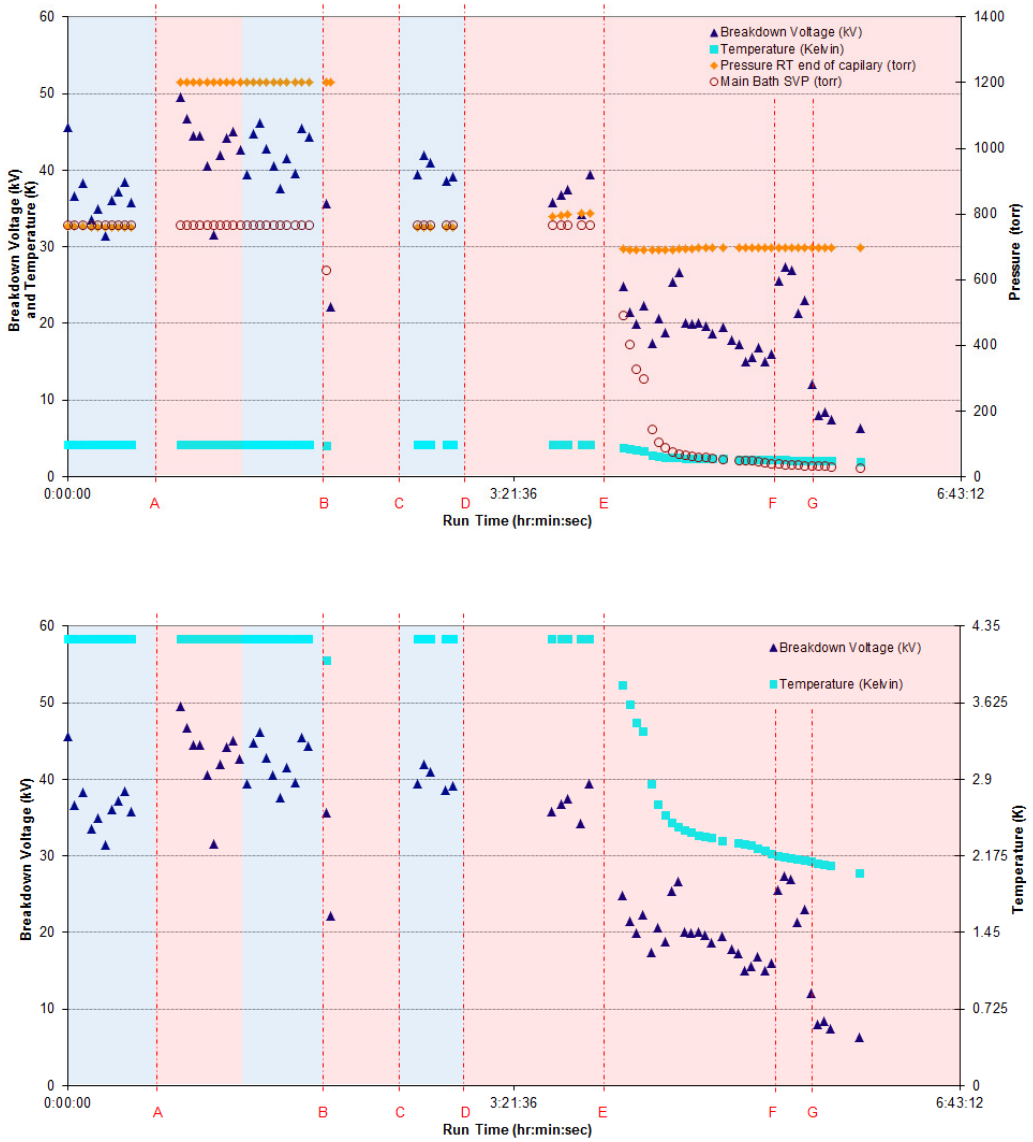

Fig..6.1a. and 6.1b. Breakdown voltage, pressure and temperature as a function of run time for PC Run 1. Blue triangle: Breakdown voltage, V_{bd} ; Orange diamond: Pressure applied at the top of the fill capillary, P_t, (i.e. at room temperature); Red Circle: Main He bath SVP, P_v; Pale blue square: Temperature of the main bath, T_{mb}, and therefore PC temperature, T_{PC}, (deduced from P_v). In the blue shaded area $P_c = P_t$. In the red shaded area $P_v \leq P_c \leq P_t$. The relevance of regions A to G is explained in the text.

A sudden improved jump in breakdown voltage was observed at (F) and this value was maintained for the next five data points. It was thought at this point that the PC was full of superfluid. After these five points, the V_{bd} reduced to values lower than that predicted by JRK's results.

The liquid Helium level senor in the main bath indicated that the end of the HV feed ground was now above the level of liquid Helium. It was assumed that breakdown was occurring at the end of the HV feed and the run was stopped to prevent damage.

6.1.2. PC Run 2 (18/03/2010)

The second PC run was carried out on the 18/03/2010. The setup had not been modified since the Run 1.

All breakdown data taken from the PC Run 2 are shown on Fig.6.2a. and Fig.6.2b. As for PC Run 1 the first ten breakdown data points, between the start of the run and (A), were taken in He I at 4.2 K and P_v. These gave an average breakdown voltage of 36.3 ± 1.2 kV, in agreement with the first ten data points of Run 1. As $P_t = P_c$, this is Group 1.

The aim of this run was to cool the PC to 3.07 K, P_v = 200 torr, and take all data points at that constant temperature. The main bath was cooled to 3.07 K, between (A) and (B). Ten data points were taken at ~3.07 K and SVP, (B) to (C) with the needle valve open to ensure the PC and main bath were at the same pressure. Under these conditions, the average breakdown voltage was 24.1 ± 1.7 kV and since P_c is known precisely this is Group 1.

At (C) the needle valve was closed separating the main bath and PC volumes. Pressure was applied to the PC through L_{fc} , P_t ~ 915 torr. At this point there was a sudden jump in T_{mb} caused by warm RT gas entering the PC and causing its temperature to rise. Over the period (C) to (D) the temperature recovered to 3.07 K. This was achieved by a combination of increasing the pumping speed and the PC filling rate. The average V_{bd} under

these conditions was 32.18 ± 0.98 kV. To check that the PC was full, the fill valve was closed. This was done a number of times between different data points and P_t reduced each time the fill valve was closed. This showed that $P_c < P_t$ and that therefore the PC was not full at any point between (C) and (D).

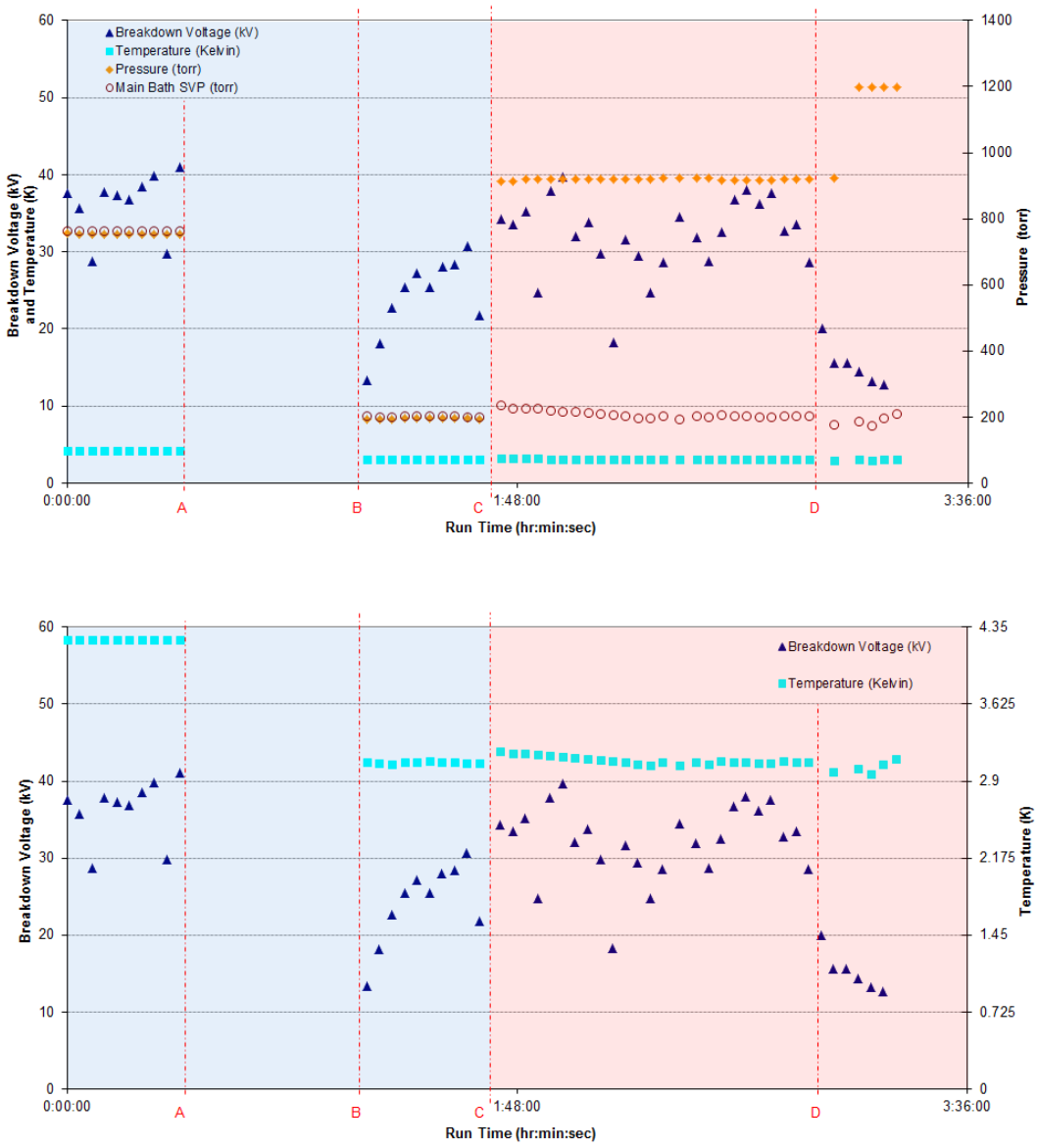

Fig..6.2a. and 6.2b. Breakdown voltage, pressure and temperature as a function of run time for PC Run 2. Blue triangle: V_{bd}; Orange diamond: P_t ; Red Circle: P_v; Pale blue square: T_{mb} and therefore temperature of PC (deduced from P_v). In the blue shaded area $P_t = P_c$. In the red shaded area $P_v \leq P_c \leq P_t$. The relevance of regions A to D is explained in the text.

At D there was a sharp decline in breakdown voltage. Again, this matched the time when the end of the ground on the HV feed came out of the liquid Helium. To confirm the feed was breaking down, the pressure in the PC was increased. However, the breakdown voltage continued to reduce. This continued until the last high voltage ramp. This time it did not breakdown, but instead there was a period of sustained discharge. This suggested that the feed was breaking down rather than the PC cell. It was not confirmed that the PC had refilled fully with helium.

6.1.3. PC Run 3 (21/03/2010)

The aim of this run was to do breakdown measurements at 2.64 K, P_v = 100 torr. Ten breakdown measurements were taken under these conditions. The PC was pressurised while remaining at a constant T_{mb} of 2.64 K (therefore T_{PC} = 2.64 K). V_{bd} was taken for pressurised helium at 2.64 K.

Before cooling down to 2.64 K, seven breakdown measurements were taken at 4.2 K under P_v. These are shown on Fig.6.3. and Fig.6.4. between the start of the run and (A). These points had an average breakdown voltage of 32.4 ± 1.8 kV. The fact that breakdown was occurring at similar values to those observed at 4.2 K under P_v, on PC Runs 1 and 2 suggests that breakdown was occurring in the cell and that the HV feed had not been damaged by the continuous discharge sustain at the end of the Run 2.

The main bath was cooled to ~ 2.64 K, (A to B) and the pumping rate was regulated to hold P_v at ~ 100 torr. The needle valve was open to ensure the main bath and PC were at the same P_v. Once the temperature was stable ten V_{bd} measurements were taken under these conditions (B to C). However, after the third breakdown it was observed that the PC pressure had fallen below the main bath pressure. It was found that the vapour pressure

line (VP) line had become blocked. The VP line plumbing was rearranged. Once fixed, P_v of the main bath was set back to 100 torr and measurements continued.

At (C) the needle valve was closed to separate the PC volume from the main bath. Pressure was then applied to the PC with P_t set to ~ 1086 torr. Again, helium gas condensing in from the bottle at room temperature heated the PC and increased the boil off from the main bath. This can be seen clearly on Fig.6.4. The pumping rate was regulated to bring P_v back to ~ 100 torr and therefore T_{mb} to ~2.64 K.

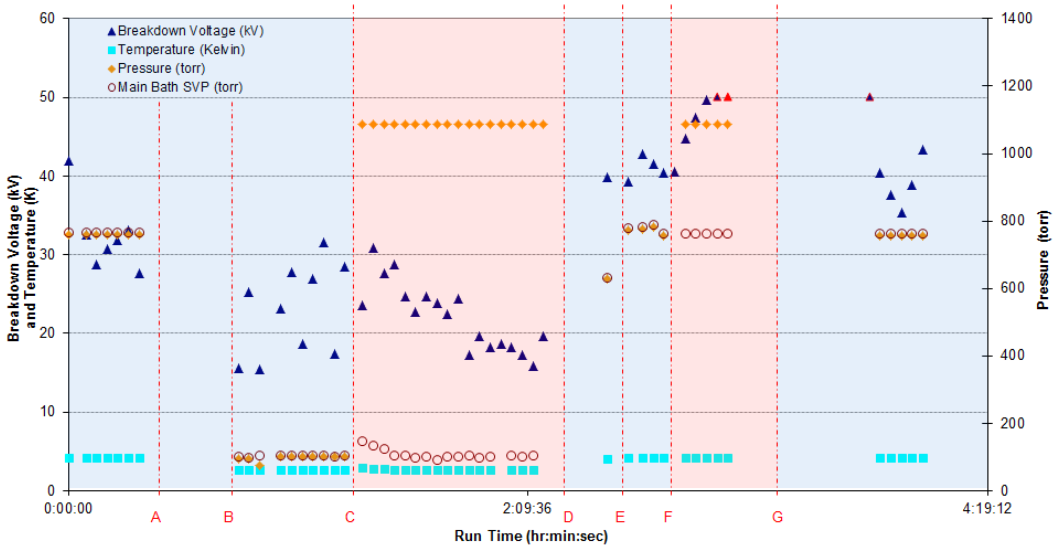

Fig..6.3. Voltage, pressure and temperature as a function of run time for PC Run 3. Blue triangle: V_{bd}; Blue triangle with red outside: Voltage held for a period of time before breakdown, V_{hbd}; Red triangle: Voltage did not breakdown, V_h; Orange diamond: P_t, (i.e. at room temperature); Red Circle: P_v; Pale blue square: T_{mb}, and therefore PC (deduced from P_v). In the blue shaded area $P_t = P_c$ (PC open to main bath). The red shaded area represents $P_v \leq P_c \leq P_t$ (PC closed to main bath and constantly filling through the fill capillary with room temperature He gas). The relevance of regions A to G is explained in the text.

While pressurizing and refilling the PC (C to D) further measurements were taken. There was no obvious sign of any real improvement in breakdown voltage. The fill valve was closed several times over this period to check if the PC could hold pressure. At no point

could it hold its pressure ($P_c < P_{t)}$. It was concluded that at no time was the PC full of liquid helium.

Over (C to D) the breakdown voltage, on average, reduced continuously. This was probably a result of the HV feed ground becoming uncovered. To prevent damage to the HV feed V_{bd} measurements were stopped at this helium temperature and pressure.

The pumps were turned off and the apparatus was warmed back to 4.2 K (D to E). The needle valve was open while the apparatus warmed. This ensured the PC and main bath were at the same P_v. One data point was taken as it warmed and the increase in voltage to ~ 40 kV suggested that the reduction in breakdown voltage over period (C to D) was caused by the HV feed breaking down in low pressure gas (at SVP) above the liquid.

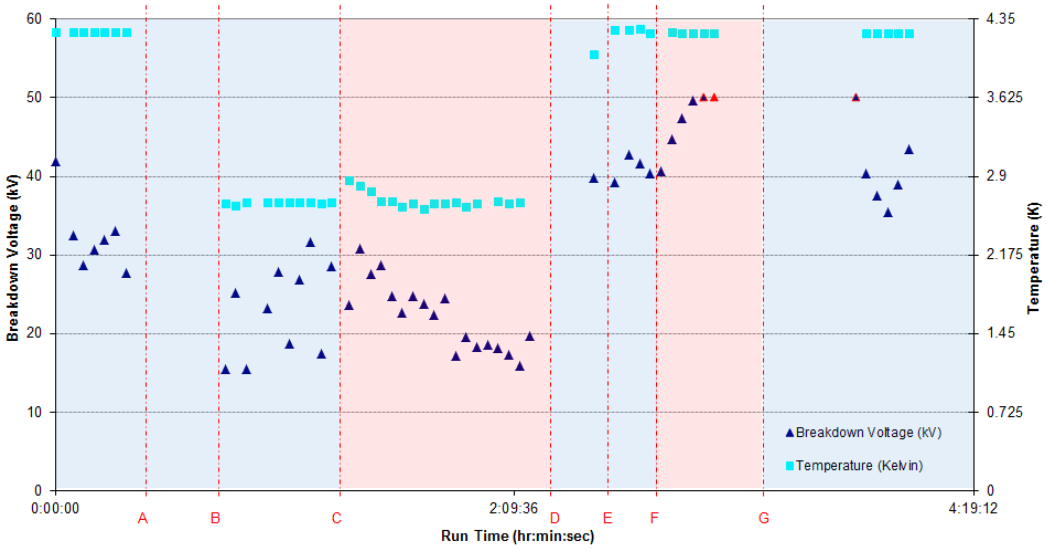

Fig..6.4. Voltage and temperature as a function of run time for PC Run 3. Blue triangle: V_{bd}; Blue triangle with red outside: Voltage held for a period of time before breakdown, V_{hbd}; Red triangle: Voltage did not breakdown, V_h; Pale blue square: T_{mb} and therefore temperature of PC (deduced from P_v). In the blue shaded area $P_t = P_c$ (PC open to main bath). The red shaded area represents $P_v \leq P_c \leq P_t$ (PC closed to main bath and constantly filling through the fill capillary with room temperature He gas). The relevance of regions A to G is explained in the text.

After P_v returned to atmospheric pressure four additional breakdown points were taken (E to F). These lay within the scatter of the first seven points taken under the same temperature and pressure. The cell was then pressurised with P_t set to ~ 1086 torr. V_{bd} increased over this time until it reached the point where it did not breakdown at the maxium applied voltage of 50 kV. These data are shown on Fig.6.3. and Fig.6.4 as red triangles. The triangles with the navy blue inside and red outside are for points where the voltage held for approximately 5 seconds before it breaking down at 50.1 kV. The next data point, a red triangle, ramped up to 50.1 kV and held at this voltage for ten minutes before it was manually ramped down.

The pressure was next reduced to 1 atmosphere by opening the needle valve and connecting the fill capillary back to the main bath (G). Six more voltage ramps were completed. The voltage held at 50.1 kV for ~ 20 seconds before breakdown, after which the breakdown values were all around 40 kV. The data taken in Runs 1, 2 and 3 clearly indicate that pressurising liquid helium increases V_{bd}. However, the apparatus in its then state was not suitable to take low temperature measurements of pressurized liquid helium. After cooling below 4.2 K, the level of the liquid helium fell below the height of the grounding on the HV feed before the PC had time to refill from the RT gas bottle. To make lower temperature measurements some modifications were carried out on the setup to increase the run time.

The first of these was to enclose the HV feed in a vacuum such that the run did not have to finish when the end of the HV feed ground came out of the liquid helium. The run could continue as long as liquid helium in the main bath was in thermal contact with the PC.

The second problem to solve was to reduce the time taken to refill the PC after it reached the required temperature. The free volume inside the PC was decreased by placing 1.5 litres of PTFE spacers in it. The breakdown cell was not disassembled during this modification.

These two modifications to the PC apparatus increased the run time and enabled the PC to fill completely with helium being condensed from the RT gas bottle.

Two PC runs were then carried out with the PC apparatus in the new arrangement on 15/04/2010 and the 20/04/2010.

6.1.4. PC Run 4 (15/04/2010)

Measurements were first carried out at 4.2 K under P_v. P_t was then increased above P_v and further measurements taken. The needle valve was opened to release pressure from the PC and V_{bd} measurements were taken again at 4.2 K under P_v.

The main bath was then refilled and more data was taken at 4.2 K under P_v before the bath was cooled below the superfluid transition. Measurements were then made at P_v and when the PC was being pressurized up to ~1200 torr. The He II was then depressurised and additional data taken at P_v. The data from this run is shown on Fig.6.5. and Fig.6.6.

The initial data at 4.2 K under P_v (start of run to A) was consistent with that taken previously with an average breakdown voltage of 29.6 ± 0.95 kV.

At (A) P_t was set to ~ 1200 bar and again the boil off increased. Monitoring when the boil off falls sharply indicates when the PC is full.

Ten V_{bd} measurements were made at 4.2 K with P_t set to 1200 torr and there was a noticeable improvement in V_{bd}. Over this period P_c was not known (i.e $P_v \leq P_c \leq P_t$). The fill valve was then closed such that the fill capillary was acting as a static line and P_t remained at ~ 1200 torr. Therefore, the PC was full and P_c = 1200 torr. Ten more measurements were taken which produced an average V_{bd} of 43.07 ± 0.68 kV, an increase by a factor of ~ 1. 4 over the SVP value at 4.2 K.

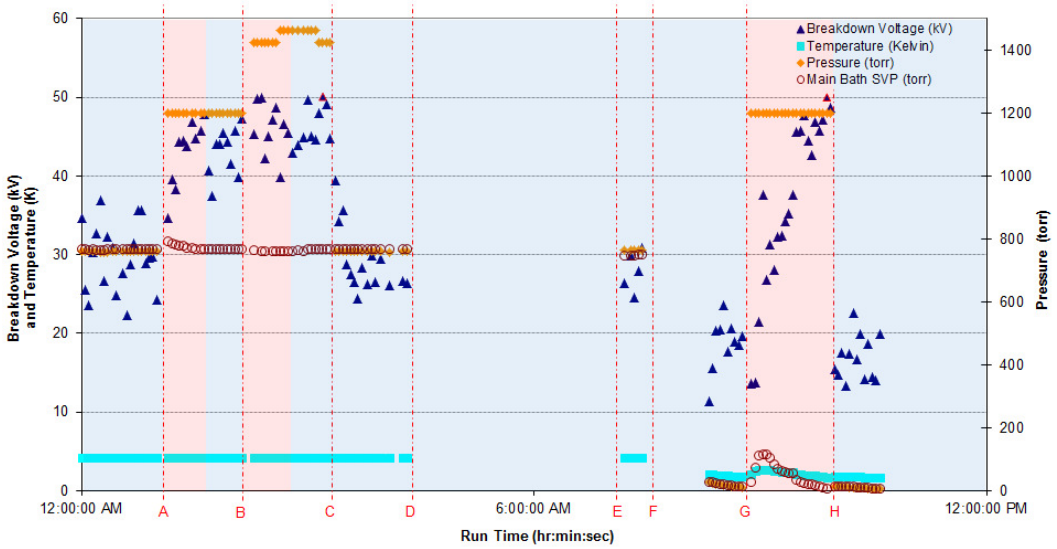

Fig..6.5. Voltage, pressure and temperature as a function of run time for PC Run 4. Blue triangle: V_{bd} ; Blue triangle with red outside: V_{hbd}; Orange diamond: P_t, (i.e. at room temperature); Red Circle: P_v; Pale blue square: T_{mb}, and therefore PC (deduced from P_v). In the blue shaded area $P_t = P_c$ (1: PC open to main bath; or 2: PC closed to main bath with He gas fill valve closed and fill capillary (L_{fc}) acting as a static line). The red shaded area represents $P_v \leq P_c \leq P_t$ (PC closed to main bath and constantly filling through the fill capillary with room temperature He gas). The relevance of regions A to H is explained in the text.

At (B), P_t was increased to ~ 1425 torr. Ten measurements were taken while the cell was being pressurized and P_t drifted up to ~ 1463 torr for the later measurements after which the fill valve was closed. Ten additional measurements were taken at 4.2 K with P_c = 1463 torr for the first six measurements and 1425 torr for the last four. One data point held at 50.1 kV for ~ 0.5 s before breaking down. The average V_{bd} for these ten points was 46.31± 0.59 kV, a slight increase in V_{bd} when this data is compared to that at 4.2 K under 1200 torr.

At (C) the needle valve was opened releasing P_c back to P_v and between (C and D) measurements were taken at 4.2 K under P_v yielding an average of 29.1 ± 1.3 kV, similar to previous. The main bath was refilled with liquid helium and pumped down through the superfluid transition. This section of data from PC Run 4 has been plotted on Fig.6.6.

The first five breakdowns (blue) were taken at 4.2 K under P_v. The next ten data (red) were taken in He II at ~1.8 K to 2 K under P_v with an average V_{bd} 18.7 ± 1.0 kV.

At (G) the PC was sealed off from the main bath and P_t set to 1200 torr. At this point the breakdown voltage increased steadily (red outside blue inside). The temperature of the liquid helium in the bath was also observed to increase rapidly to a maximum of ~ 2.85 K and then fall monotonically. When V_{bd} reached a maximum value (Red outside green inside) it was assumed that the pressure inside the PC was 1200 torr. The average V_{bd} value for this data was 46.47 ± 0.70 kV.

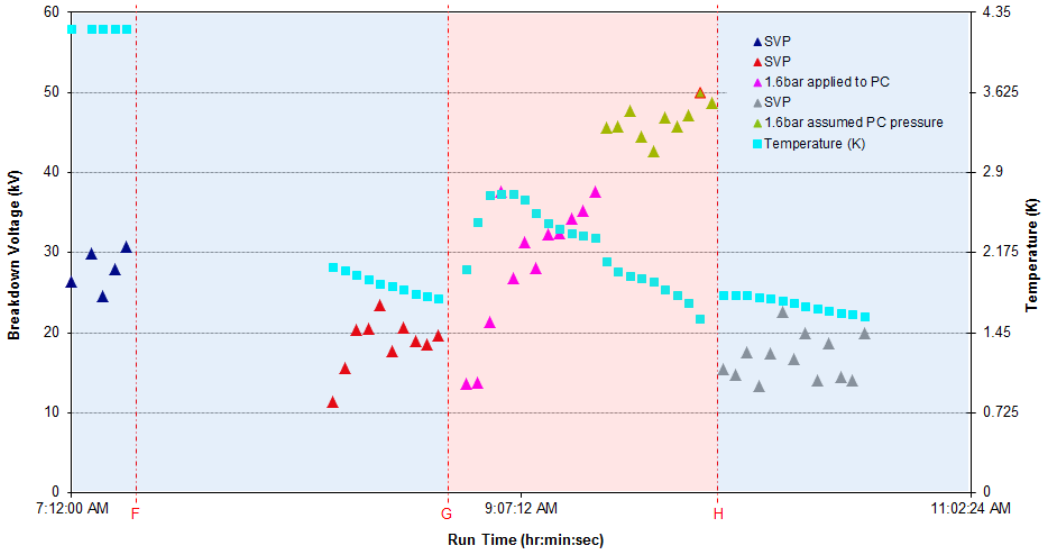

Fig..6.6. Breakdown voltage and temperature as a function of run time for PC Run 4. Blue triangle: V_{bd}, $P_t = P_c$; Red triangle: V_{bd}, $P_t = P_c$; Pink triangle: V_{bd}, $P_v \leq P_c \leq P_t$ (P_t ~ 1200 torr, PC constantly filling with He gas through L_{fc}); Lime triangle: V_{bd}, $P_v \leq P_c \leq P_t$ (P_t ~ 1200 torr, PC assumed to be full); Grey triangle: V_{bd}, $P_t = P_c$; Lime triangle red outside: V_{hbd}, $P_v \leq P_c \leq P_t$ (P_t ~ 1200 torr, PC assumed to be full); Pale blue square: T_{mb}, and therefore PC (deduced from P_v). In the blue shaded area $P_t = P_c$ (PC open to main bath). In the red shaded area $P_v \leq P_c \leq P_t$ (PC closed to main bath and constantly filling through the fill capillary with room temperature He gas). The relevance of regions F to H is explained in the text.

At (H) the PC volume was depressurized by opening it to the main bath. This caused the main bath pressure to increase slightly, Fig.6.7. It then slowly reduced. The helium in the PC was now under P_v and the breakdown voltage again dropped to approximately the same values as before, the average V_{bd} was 16.83 ± 0.79 kV. Pressurizing He II to 1200 torr can thus increase the V_{bd} by a factor of ~ 2.5.

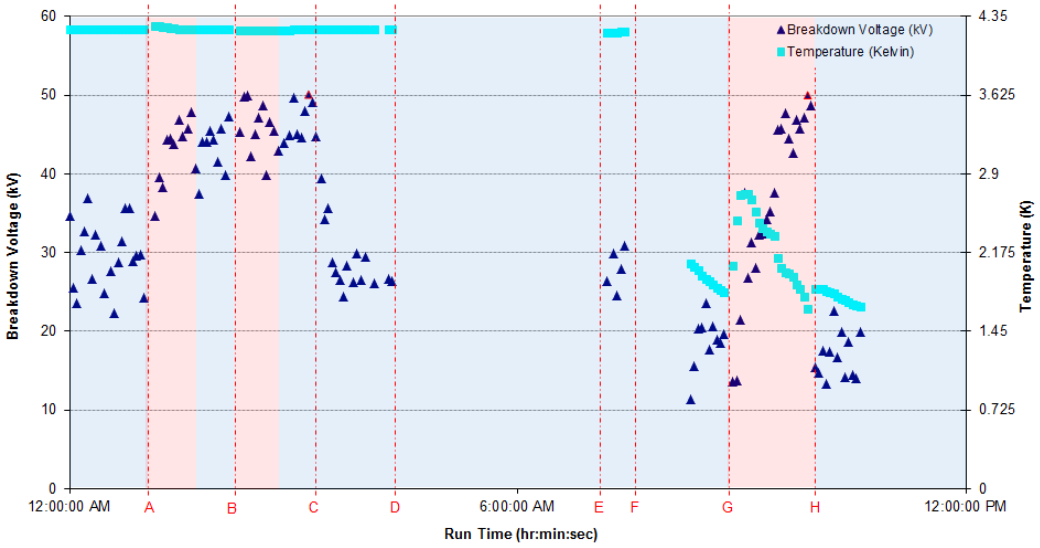

Fig..6.7. Voltage and temperature as a function of run time for PC Run 4. Blue triangle: V_{bd}; Blue triangle with red outside: V_{hbd}; Pale blue square: T_{mb} and therefore temperature of PC (deduced from P_v). In the blue shaded area $P_t = P_c$ (1: PC open to main bath; or 2: PC closed to main bath with He gas fill valve closed with the fill capillary acting as a static line). The red shaded area represents $P_v \leq P_c \leq P_t$ (PC closed to main bath and constantly filling through the fill capillary with room temperature He gas). The relevance of regions A to H is explained in the text.

6.1.5. PC Run 5 (20/04/2010)

The aim of this run was to try and repeat the V_{bd} results obtain in He II in the second section of PC Run 4. The run data is shown on Fig.6.8. and Fig.6.9.

After liquid helium had been successfully transferred into the main bath the bath was pumped on. Some V_{bd} were taken while cooling down (from the start of the run until A). After the helium passed through the superfluid transition (A) P_t was set to ~1200 torr. Over this period the breakdown voltage steadily increased from ~10 kV to ~40 kV. The liquid fill valve on the gas manifold was closed at (B) and there was an observed drop in pressure. This indicated that the PC was not completely full so the fill valve was opened again and two additional data points were taken while the PC was being pressurized.

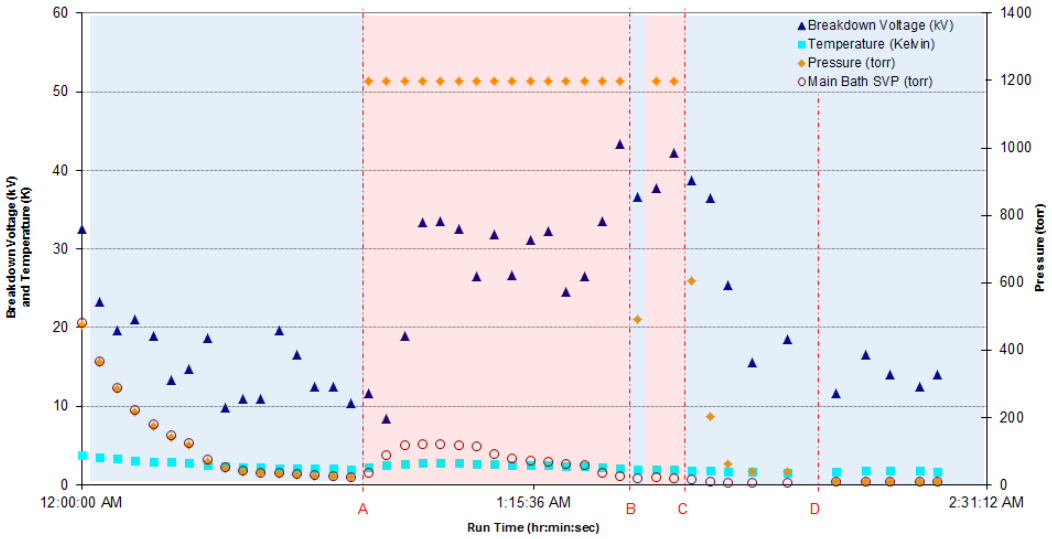

Fig..6.8. Breakdown voltage, pressure and temperature as a function of run time for PC run 5. Blue triangle: V_{bd} ; Orange diamond: P_t, (i.e. at room temperature); Red Circle: P_v; Pale blue square: T_{mb} and therefore PC temperature (deduced from P_v). In the blue shaded area $P_t = P_c$ (1: PC open to main bath; or 2: PC closed to main bath with He gas fill valve closed with the fill capillary acting as a static line). The red shaded area represents $P_v \leq P_c \leq P_t$ (PC closed to main bath and constantly filling through the fill capillary with room temperature He gas). The relevance of regions A to D is explained in the text.

The fill valve was closed off for a second time (C). This caused P_c to drop slowly then settled around ~40 torr. This was higher than the P_V of the main bath which was ~6 torr.

Over this period V_{bd} reduced. The needle valve was opened and L_{fc} vented back to the main bath (D). Five final data points where taken at ~1.7 K under P_v. This set produced similar breakdown voltages to those taken at the start of the run under similar helium conditions. The temperature range of the helium is clearly shown on Fig.6.9.

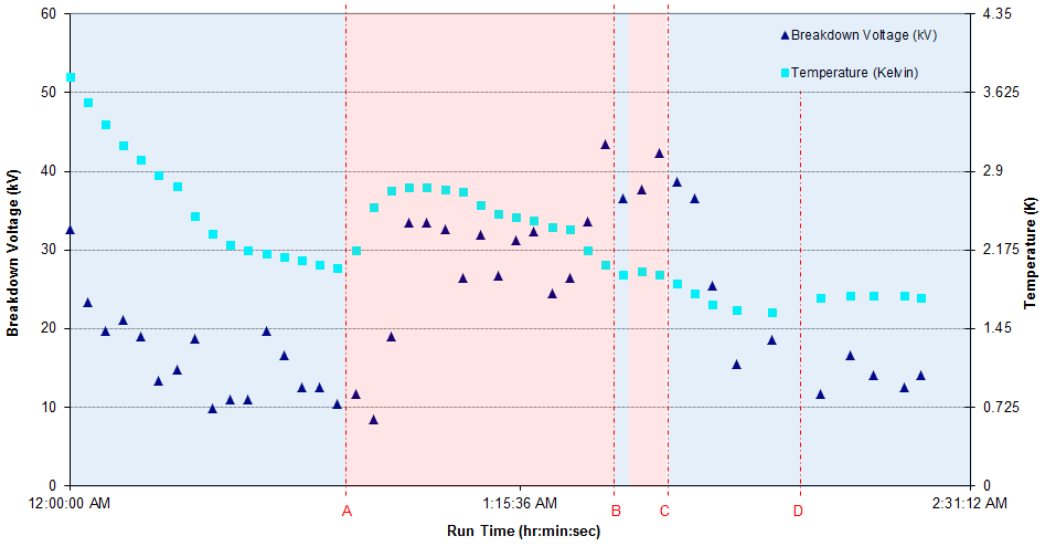

Fig..6.9. Breakdown voltage and temperature as a function of run time for PC Run 5. Blue triangle: V_{bd}; Pale blue square: T_{mb} and therefore temperature of PC (deduced from P_v). In the blue shaded area $P_t = P_c$ (1: PC open to main bath; or 2: PC closed to main bath with He gas fill valve closed with the fill capillary acting as a static line). The red shaded area represents $P_v \leq P_c \leq P_t$ (PC closed to main bath and constantly filling through the fill capillary with room temperature He gas). The relevance of regions A to D is explained in the text.

6.1.6 Summary of PC Runs 1, 2 and 4

A selection of average breakdown data has been plotted against P_t. The data plotted were taken from PC Runs 1, 2 and 4 and it is shown in Fig.6.10. The 2.65 K data from PC Run 3 is not included as it was inconclusive if the cell was breaking down or the end of the grounding on the HV feed (section 6.1.3).

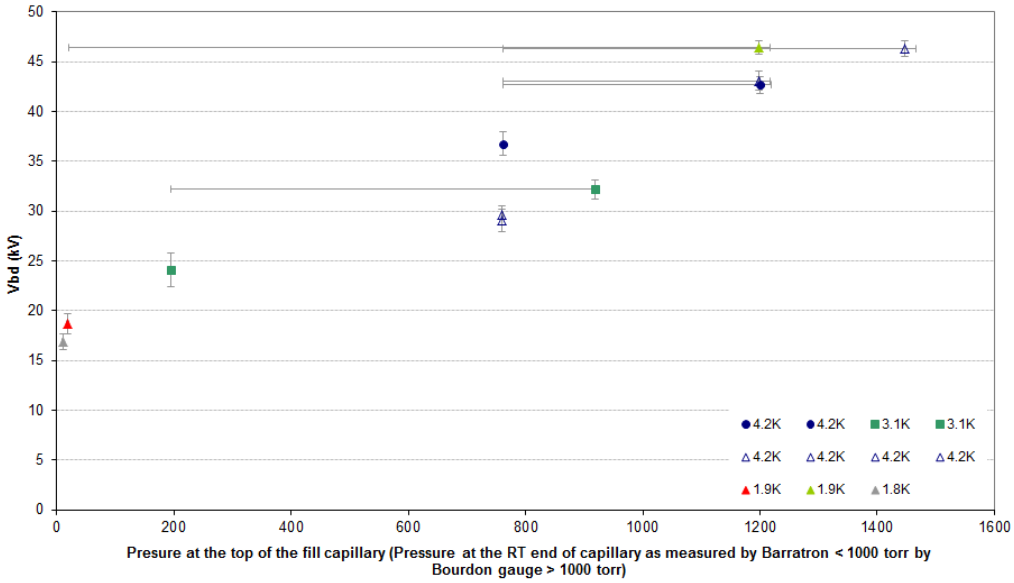

Fig..6.10. Mean Breakdown voltage as a function of pressure at the top of the fill capillary, P_t. Blue circle: 4.2 K data from PC Run 1; Green square: mean temperature 3.1 K, data from PC Run 2; Triangle blue outside: 4.2 K data from PC Run 4; Red triangle: mean temperature 1.9 K, data from PC Run 4; Lime triangle: mean temperature 1.9 K, data taken from PC Run 4; Grey triangle: mean temperature 1.8 K, data from PC Run 4. Error bars shown on breakdown voltage (standard error). The error bars on P_t depict the range of pressure in which the true P_c lies (i.e. $P_v \leq P_c \leq P_t$).

The mean breakdown value and standard error is shown as a function of the pressure recorded on the pressure gauge at the top of the fill capillary, P_t. The pressure error bars are also shown. When $P_t = P_c$, the error bar is given as the standard error on P_t, ∂P. When $P_v \leq P_c \leq P_t$, the error bar is given as the standard error on $P_{t,} + \partial P_t$ / - $(P_t - P_v)$. The Baratron gauge is accurate to 0.01 torr while the bourdon gauge only has an accuracy of ~ 19 torr. Hence, pressure readings > ~1000 torr have a larger measurement error.

The general trend of $V_{bd}(P)$ looks almost linear independent of temperature. The plot shows unequivocally that high voltage breakdown in helium increases with the pressure of the helium and also suggests that the temperature of the liquid helium is much less significant. The data exhibits the same trend for temperatures above and below the lambda point.

6.2. $V_{bd}(P,T)$ – Data taken with Static line

The addition of the static line, L_{st}, enabled P_{cell}, the pressure in the breakdown cell, to be measured accurately at any point during the run, where

$$P_{cell} = P_{st} + P_{hy}$$

P_{st} the pressure at the top of the L_{st} and P_{hy} the hydrostatic correction due to the height of the liquid helium level above the breakdown cell. This arrangement allows V_{bd}, T_{PC}, and P_{cell} to be known accurately at any point during a run.

The following section gives a detailed account of PC runs 6 to 13 carried out between the 15/05/2010 and 11/09/2010, after the addition of L_{st}. The cell geometry for the first seven of these runs remained the same as that set initially for PC Run 1, 12/3/10,i.e. with an electrode separation of 1.27 mm at base temperature.

The aim of PC run 6 was to investigate the effect of varying the pressure in the PC while taking high voltage breakdown data between He II $\leq T \leq$ 4.2 K.

The first part of PC run 7 investigated high voltage breakdown at constant pressure of ~ 1 bar while the temperature was reduced from 4.2 K through the superfluid transition. This would show any significant change in breakdown behavior at the superfluid transition at fixed pressure. When the temperature of the liquid helium was below the λ point the pressure in the PC was released and the high voltage breakdown values monitored.

High voltage breakdown as a function of pressure at fixed temperature was investigated in PC runs 8 to 12, with approximately 5 data points being taken at each set of helium conditions. For each fixed temperature the measurement cycle was started at SVP and the pressure was increased in steps of ~ 200 torr up to 1200 torr and then back to SVP in

the same intervals. This was done in order to investigate any hysteretic behaviour of the breakdown with pressure.

Over the course of the whole data taking period, the later breakdown values were observed to have decreased in comparison to those taken in earlier runs under similar helium conditions. Before PC run 13 (11/09/2010), the cell was dismantled, cleaned, repolished and reassembled. The electrodes were then set to an average separation of 2.9 mm (at RT). PC run 13 investigated if the breakdown voltage increased due to these modifications.

6.2.1. PC Run 6 (15/05/2010)

The voltage, temperature and pressure data for this run is shown on Fig.6.11. and Fig.6.12. Five measurements were taken at 4.2 K, under P_v. The main bath was then cooled. During the pump down $P_c = P_v$, the PC was open to the main bath, as shown on Fig.6.11.

During this period, V_{bd} dropped with reducing temperature and P_v. At (A) the PC was sealed off from the main bath and a pressure of 1200 torr was applied to L_{fc}. A sudden rise in breakdown voltage was observed. Between (A) and (B) the PC pressure increased sharply to ~ 250 torr and then leveled off. T_{mb} initially increased and then reduced slowly. V_{bd} values over this period remain fairly constant at ~33 kV. These breakdown values are similar to those taken at 4.2 K under P_v.

A second dramatic pressure jump was observed at (B). This is correlated to an increase in V_{bd}. The rate of cooling by the bath was also observed to increase at this point. It is evident that increasing the PC pressure will increase V_{bd}. However it is not clear why there were two sudden pressure jumps when a steady rate of helium gas was being supplied to the PC. A possible explanation is to postulate that between (A) and (B) the PC volume is filling and at (B) it has completely filled. This corresponds to a change in the cooling rate of the main bath, shown clearly on figure 6.12. T_{mb} reduced more rapidly after (B). From this it

may also be inferred that the PC was full. A reduction in the amount of warm helium gas flowing into the PC will reduce any heat leak and allow the T_{mb} to drop more quickly. The level of the He II in the main bath dropped below the base of the PC at (C). Hence, it was no longer possible to assume that $T_{mb} = T_{PC}$.

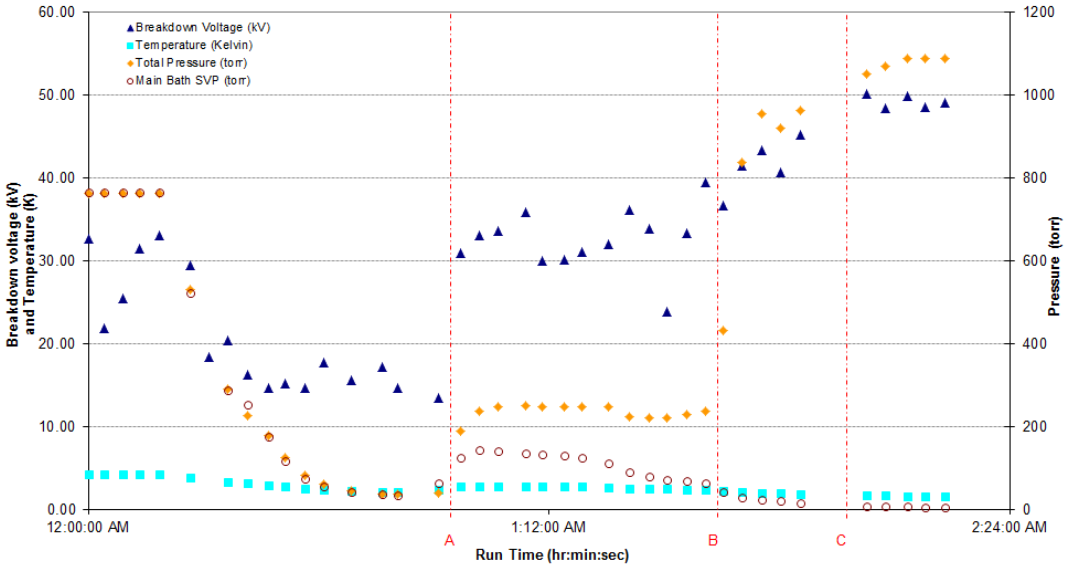

Fig..6.11. Breakdown voltage, pressures and temperature as a function of run time for PC Run 6. Blue triangle: V_{bd}, (breakdown voltage); Orange diamond: P_{cell}, (Pressure of liquid Helium in the breakdown cell. Where $P_{cell} = P_{st} + P_{hy}$, P_{st} is the pressure recorded on the L_{st} and P_{hy} is the hydrostatic correction); Red Circle: P_v, (Main bath SVP); Pale blue square: T_{mb}, (Main bath temperature), and therefore PC temperature (deduced from P_v). Between the start of the run and (A) the bath was cooled from 4.2 K to He II. At (A) the PC was closed of to the main bath and pressurised, $P_t \sim 1200$ torr, (pressure at the top L_{fc}, the fill capillary, at room temperature, RT, was 1200 torr). A sharp increase in pressure is observed at (B). The level of He II in the main bath drops below the base of the PC at (C). Therefore, after (C), T_{PC} (The temperature of the PC) cannot reliably be found from T_{mb}.

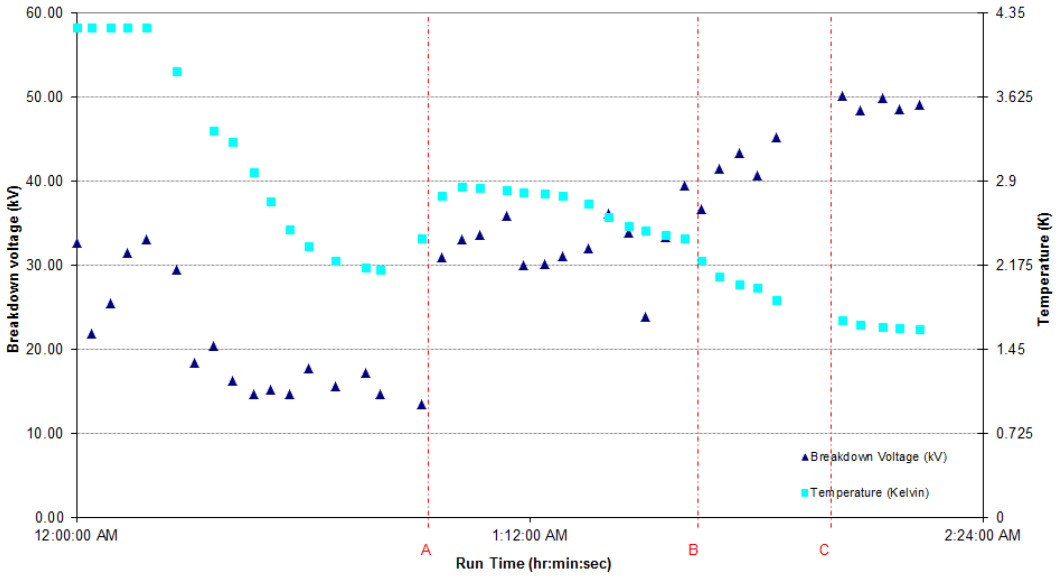

Fig..6.12. Breakdown voltage and temperature as a function of run time for PC Run 6. Blue triangle: V_{bd}; Pale blue square: T_{mb} and therefore T_{PC} (deduced from P_v). Between the start of the run and A the bath was cooled from 4.2 K to below the λ-point. At (A) the PC was closed off from the main bath and pressurised, P_t ~ 1200 torr, (pressure at the top L_{fc}, at RT). A sharp increase in pressure is observed at (B). The level of He II in the main bath drops below the base of the PC at (C). Therefore, after (C), T_{PC} can not reliably be found from T_{mb}.

6.2.2. PC Run 7 (23/05/2010)

In order to improve the run time, the top liquid helium level sensor in the main bath and the cool down method were modified. The top level sensor was moved up to just below the bottom radiation baffle to allow more helium into the main bath during the transfer. The bath was also pumped on very lightly over the entire run. The PC was closed off from the main bath before pumping started and P_t set to approximately 1 atmosphere. Therefore, as the main bath was cooled there was a steady flow of Helium into the PC down L_{fc}. Figure 6.13 and Fig. 6.14. show the data from PC Run 7.

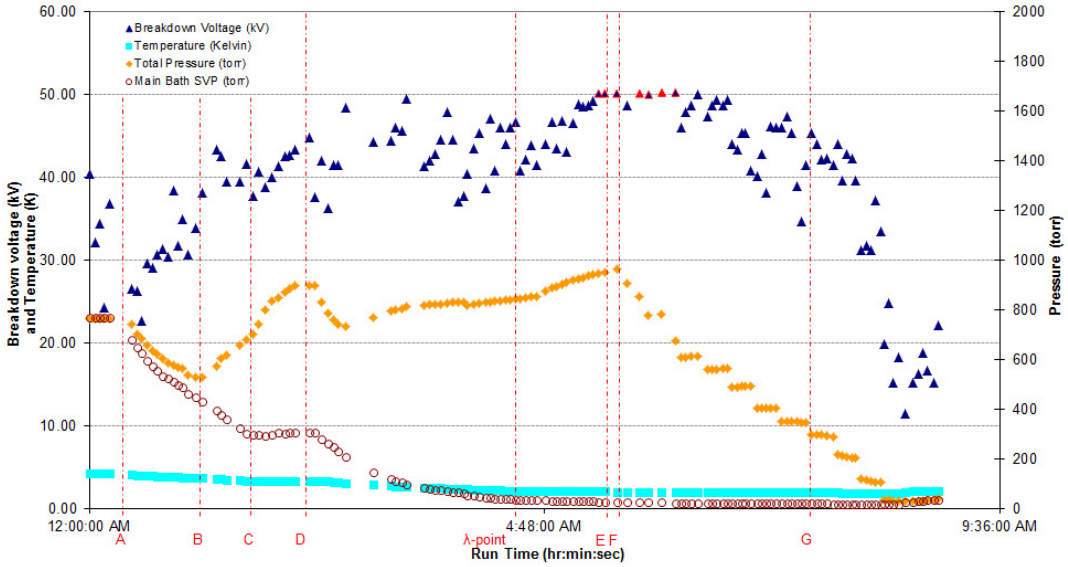

Fig..6.13. Voltage, pressures and temperature as a function of run time for PC Run 7. Blue triangle: V_{bd}; Blue triangle with red outside: $V_{hbd,}$ (Voltage held for a period of time before breakdown); Red triangle: V_h, (Voltage held, it did not breakdown); Orange diamond: P_{cell}, (Where $P_{cell} = P_{st} + P_{hy}$); Red Circle: P_v; Pale blue square: T_{mb}, and therefore T_{PC} (deduced from P_v). Between the start of the run and (A), V_{bd} data taken at 4.2 K under P_v. At (A) the PC was closed of from the main bath, P_t set to ~1 atmosphere and the main bath pumped on. An increase in pressure is observed between (B) and (C). P_v is held at ~ 300 torr between (C) and (D). The bath is cooled throught λ-point between (D) and (E). At (E) the fill valve is closed. From (F) until end of run P_{cell} reduced by releasing pressure through the needle valve into the main bath. The level of He II in the main bath drops below the base of the PC at (G). Therefore, after (G), T_{PC} can not reliably be found from T_{mb}.

The first five breakdown measurements were taken at 4.2 K under P_v. The PC was then closed off from the main bath and light pumping commenced at (A). P_t was set to ~1 atmosphere and the fill valve was opened. P_{cell} was slightly greater than P_v between (A) and (B). The difference between P_v and P_{cell} increased gradually until (B) where a sudden rise in P_{cell} was observed. This was accompanied with an increase in V_{bd} between (B) and (C). P_v was held at ~300 torr while P_{cell} continued to increase to ~900 torr where it then leveled off. The average V_{bd} was ~41 kV at this point.

At (D) T_{mb} was allowed to drop below the λ-point, shown clearly in Fig. 6.14. P_{cell} initially dropped quickly then levelled out and then increased slowly. Between (D) and (E) the breakdown voltage increased slightly. The spread of this data seemed to reduce at (E). Again, the applied voltage was limited to + 50 kV and hence, once V_{bd} is greater than this, the cell holds the voltage.

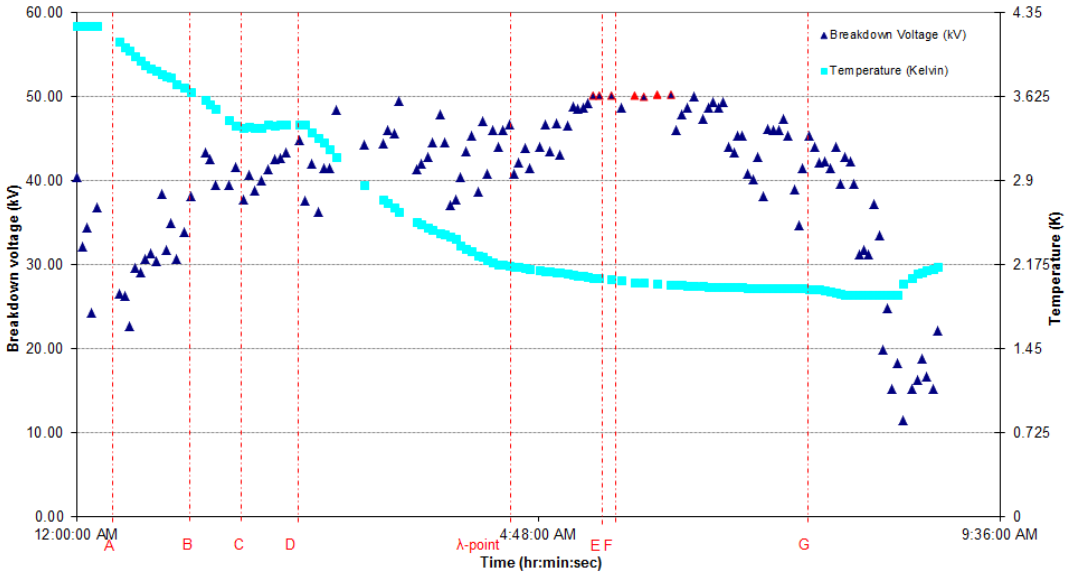

Fig..6.14. Voltage, pressures and temperature as a function of run time for PC Run 7. Blue triangle: V_{bd}; Blue triangle with red outside: $V_{hbd,}$ (Voltage held for a period of time before breakdown); Red triangle: V_h, (Voltage held, it did not breakdown); Pale blue square: T_{mb}, and therefore T_{PC} (deduced from P_v). Between the start of the run and (A), V_{bd} data taken at 4.2 K under SVP. At (A) the PC was closed of from the main bath, P_t set to ~1 atmosphere and the main bath pumped on. An increase in pressure is observed between (B) and (C). P_v is held at ~ 300 torr between (C) and (D). The bath is cooled throught λ-point between (D) and (E). At (E) the fill valve is closed. From (F) until end of run P_{cell} reduced by releasing pressure through the needle valve into main bath. The level of He II in the main bath drops below the base of the PC at (G). Therefore, after (G), T_{PC} can not reliably be found from T_{mb}.

Around (E) the cell was able to sustain 50 kV. To continue taking V_{bd} data, P_{cell} was reduced. The fill valve was closed, (E), which had no effect on reducing P_{cell}. P_{cell} was

therefore reduced in steps by opening the needle value and letting P_{cell} vent into the main bath, from (F) until the end of run. This method showed P_{cell} could be controlled to within ± 2 torr. P_{cell} was reduced until $P_v = P_{cell}$ (i.e. until the PC was open fully to the main bath). Between (F) and the end of the run V_{bd} was observed to decrease with reduced P_{cell}. However, V_{bd} remained high until $P_{cell} \approx P_v$.

At (G) the level of He II in the main bath dropped below the base of the PC and it was not possible to assume that $T_{PC} = T_{mb}$. This data from PC Run 7 suggests that if the PC is kept at a fairly constant pressure then V_{bd} increases slightly when the temperature is reduced. There was no dramatic change to the V_{bd} behaviour as the liquid went through the superfluid transition, suggesting that the breakdown mechanism above and below the λ-point is the same.

6.2.3. PC Run 8 (28/06/2010)

After demonstrating the level of control over P_{cell} during PC Run 7 it was decided to take breakdown measurements at set increments of 200 torr, and at a fixed temperature. The first measurements were taken at P_v then P_{cell} was increased in 200 torr steps. At least five V_{bd} were taken at each step before P_{cell} was increased by an additional 200 torr. This continued until P_{cell} reached 1200 torr.

After reaching 1200 torr P_{cell} was reduced in 200 torr steps and V_{bd} data taken at each step. This method would investigate any hysteresis. P_{cell} was reduced using the needle valve until $P_{cell} = P_v$.

PC Run 8 investigated breakdown at three fixed temperatures, 4.2 K, 3.8 K and 3.5 K and the P_{cell} range was from P_v to ~1200 torr. The data are shown on Fig.6.15.

It is clearly visible that at a fixed T_{mb}, V_{bd} is a function of P_{cell}. It is also evident from these data the high degree of control over the condition of the liquid Helium in the PC. The P_{cell}

can be increased easily using the fill valve and reduced by opening the needle valve. T_{mb} is regulated by regulating the pumping rate on the main bath

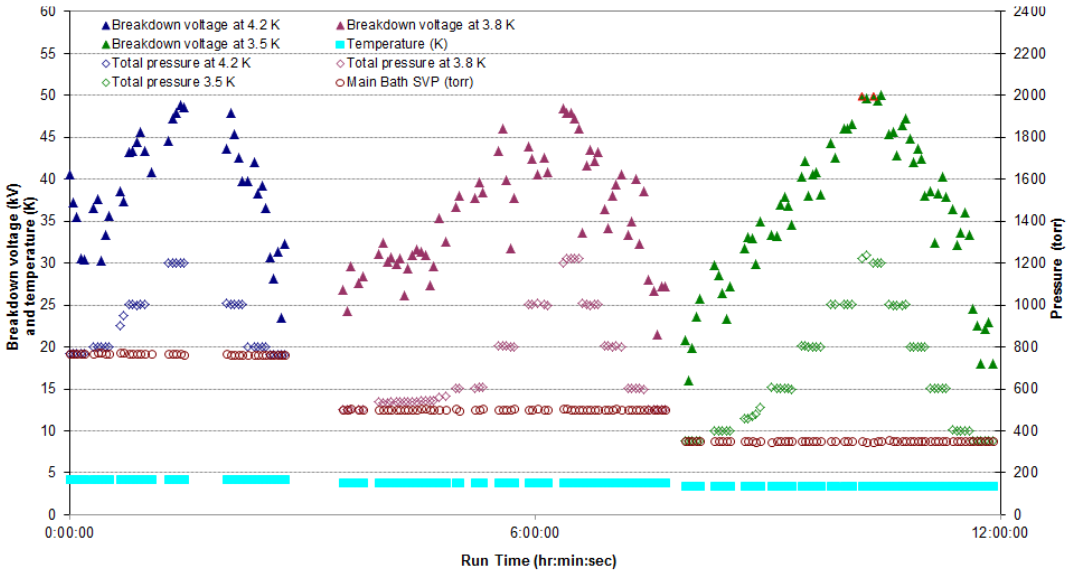

Fig..6.15. Voltage, pressures and temperature as a function of run time for PC Run 8. Blue triangle: V_{bd} at T_{PC} = 4.2 K; Plum triangle: V_{bd} at T_{PC} = 3.8 K; Green triangle: V_{bd} at T_{PC} = 3.5 K; Green triangle with red outside: V_{hbd} at T_{PC} = 3.5 K (Voltage held for a period of time before breakdown); Diamond blue outside: P_{cell} at 4.2 K; Diamond plum outside: P_{cell} at 3.8 K; Diamond green outside: P_{cell} at 3.5 K; Red Circle: P_v; Pale blue square: T_{mb}, and therefore T_{PC} (deduced from P_v).

6.2.4. PC Run 9 (11/07/2010), Run 10 (13/07/2010), Run 11 (22/07/2010) and Run 12 (24/07/2010)

Due to the success in controlling P_{cell} and T_{mb}, and therefore T_{PC}, in PC Run 8 four more runs were carried out using the same method. In each case T_{mb} was decreased to a fixed temperature. V_{bd} data were taken at that T_{mb} for different set values of P_{cell}, from P_v to ~ 1200 torr, in steps of 200 torr, and then back again from ~ 1200 torr to P_v. For PC Run 11 P_{cell} was increased to ~ 1669 torr. At least five V_{bd} points were taken for each T_{mb} and P_{cell}

combination. The run continued until a complete set of data was taken at one fixed temperature or when the level of helium in the main bath dropped below the base of the PC.

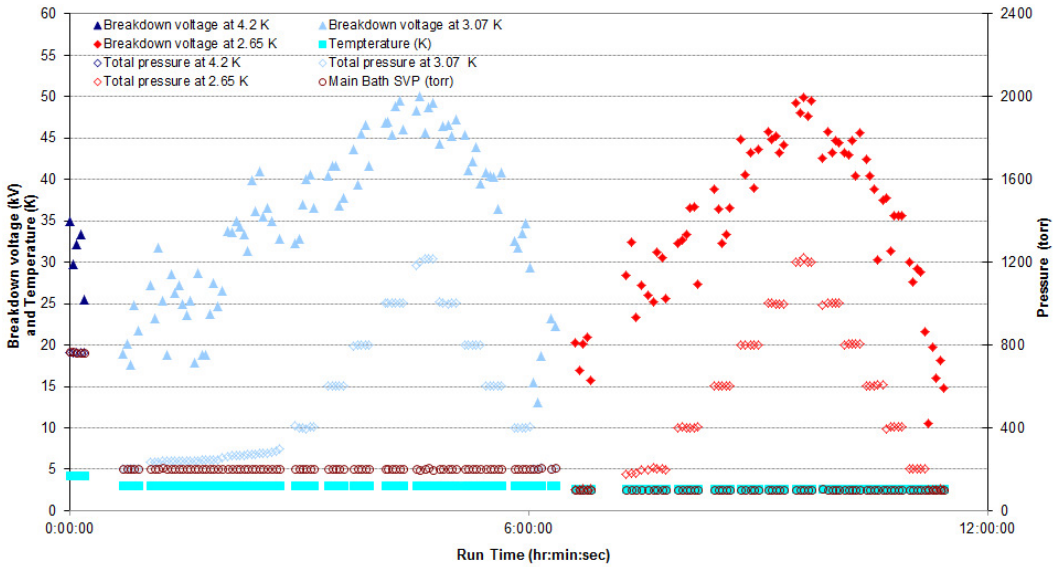

Fig..6.16. Breakdown voltage, pressures and temperature as a function of run time for PC Run 9. Blue triangle: V_{bd} at T_{PC} = 4.2 K; Light blue triangle: V_{bd} at T_{PC} = 3.07 K; Red triangle: V_{bd} at T_{PC} = 2.65 K; Diamond blue outside: $P_{cell} = P_v$ at 4.2 K; Diamond light blue outside: P_{cell} at 3.07 K; Diamond red outside: P_{cell} at 2.65 K; Red Circle: P_v; Pale blue square: T_{mb}, and therefore T_{PC} (deduced from P_v). V_{bd} and T_{mb} are read off y axis 1. P_{cell} and P_v are read off y axis 2.

PC Run 9 took measurements at T_{mb} of 3.07 K and 2.65 K, Fig.6.16. T_{mb} was reduced to 2.2 K, for one set of data, then reduced to just below the λ-point in PC Run 10. The Helium level dropped below the base of the PC before the full set of data could be taken below the λ-point. These measurements are shown on Fig.6.17.

PC Run 11 completed a full set of V_{bd} data in He II. A repeat of V_{bd} measurements at 4.2 K was carried out in PC Run 12. The data obtained from these runs are shown in Figs. 6.18 and 6.19 for PC Run 11 and 6.20 for PC Run 12. In general, the triangles represent V_{bd}, the diamonds P_{cell}, the circles show P_v and the pale blue squares are T_{mb}, and therefore T_{PC}.

Figure 6.16 shows all data taken from PC Run 9. Five breakdown measurements were taken at 4.2 K under P_v. P_v was then reduced to ~ 200 torr and T_{mb} 3.07 K. Measurements were taken at P_v initially and the P_{cell} was then increased with P_t set to ~ 1.3 bar. However it is clear from Fig. 6.16. that P_{cell} did not instantaneously increase to 1.3 bar. It took quite a long time to refill the PC, as shown by the slow increase in P_{cell} from P_v to the target pressure of 400 torr. Over this period there was a sharp rise in V_{bd}. Once the PC is full it is relatively easy increase the PC in steps of 200 torr.

It is clear once again from Fig. 6.16. that V_{bd} is a function of P_{cell} for a fixed temperature. Further data were taken at P_v = 100 torr and T_{mb} = 2.65 K and this time it did not take as long for the PC to refill after pumping down from 3.07 K to 2.65 K. This was because the density change is less than that between 4.2 K and 3.07 K.

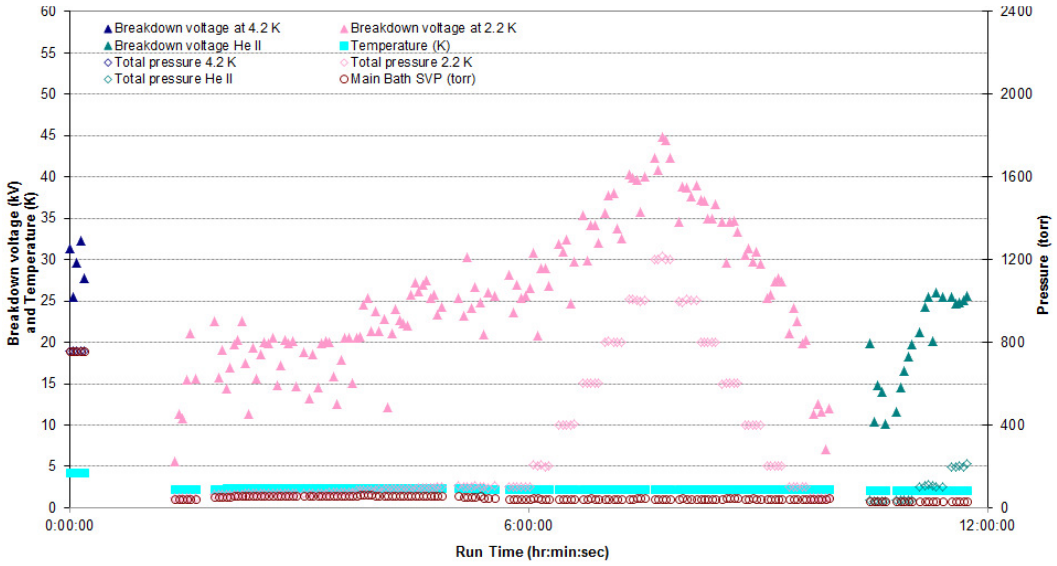

Fig..6.17. Breakdown voltage, pressures and temperature as a function of run time for PC Run 10. Blue triangle: V_{bd} at T_{PC} = 4.2 K; Light pink triangle: V_{bd} at T_{PC} = 2.2 K; Teal triangle: V_{bd} at T_{PC} = He II; Diamond blue outside: $P_{cell} = P_v$ at 4.2 K; Diamond light pink outside: P_{cell} at 2.2 K; Diamond teal outside: P_{cell} at He II; Red Circle: P_v; Pale blue square: T_{mb}, and therefore T_{PC} (deduced from P_v). V_{bd} and T_{mb} are read off y axis 1. P_{cell} and P_v are read off y axis 2.

To investigate any change in V_{bd} characteristics as a function of pressure above and below the λ-point measurements were made at 2.2 K and 2.085 K. In Run 10 a full set of data was taken at 2.2 K. Unfortunately the level of the helium dropped below the base of the PC before a full set of data could be taken at 2.085 K. This run was completed on the 13/07/2010, Fig. 6.17.

The main bath was cooled to 2.2 K and data taken under P_v. P_t was then set to 0.7 bar and it took a long time to pressure the PC to 100 torr. Over this period there was a noticeable increase in V_{bd}. The same 200 torr pressure step cycle to 1200 torr and back to P_v was repeated and it is clear that at 2.2 K V_{bd} is a function of P_{cell}.

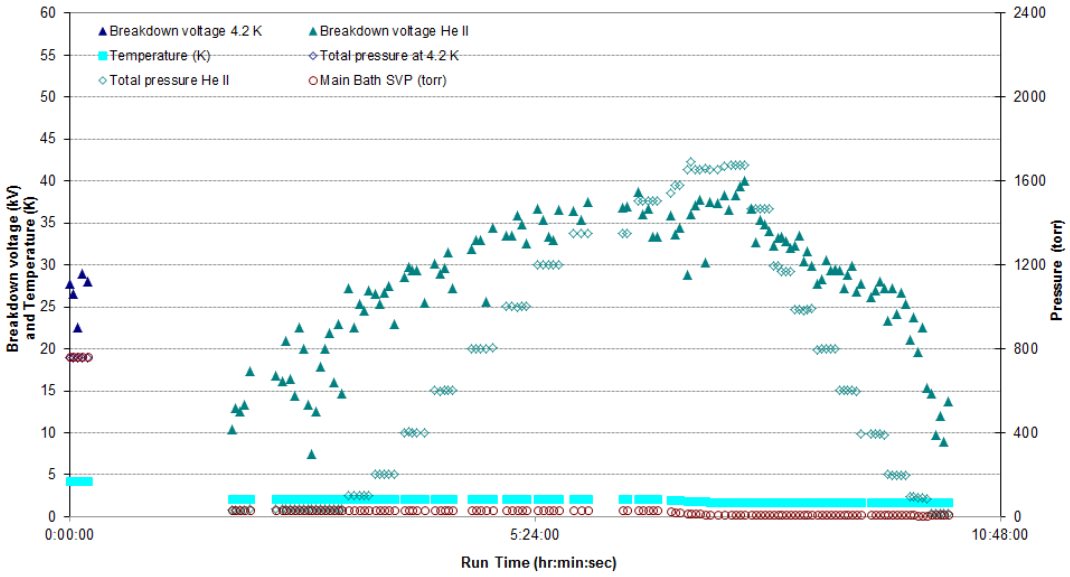

Fig..6.18. Breakdown voltage, pressures and temperature as a function of run time for PC Run 11. Blue triangle: V_{bd} at T_{PC} = 4.2 K; Teal triangle: V_{bd} at T_{PC} = He II; Diamond blue outside: P_{cell} = P_v at 4.2 K; Diamond teal outside: P_{cell} at He II; Red Circle: P_v; Pale blue square: T_{mb}, and therefore T_{PC} (deduced from P_v). V_{bd} and T_{mb} are read off y axis 1. P_{cell} and P_v are read off y axis 2.

The main bath was pumped to below the superfluid transition. Data was taken at P_v, 100 torr and 200 torr. Then the level of Helium fell below the bottom of the PC.

Form this initial data it is clear that V_{bd} in He II is a function of P_{cell}. An increase in V_{bd} of a factor of 2 is observed when P_{cell} is increased by ~ 170 torr above P_v.

A complete set of V_{bd} data was taken in He II in Run 11. The data is shown on Fig. 6.18. The main bath was pumped on until it was He II at 2.1 K. Data was taken under P_v and then in steps of 200 torr up to 1669 torr. It was then reduced in 200 torr steps until $P_{cell} = P_v$. After increasing the pressure to P_{cell} = 1500 torr the temperature was reduced. This was to investigate if the V_{bd} decreased with reducing temperature. The reduction in temperature is clearly shown on Fig. 6.19. This reduction in temperature seems to have little effect on the V_{bd}. After reaching a P_{cell} = 1669 the pressure was reduced in steps down until $P_{cell} = P_v$. This data shows that V_{bd} in He II is a function of P_{cell}. It also shows that there is little effect on V_{bd} when reducing the temperature from 2.1 K to 1.7 K.

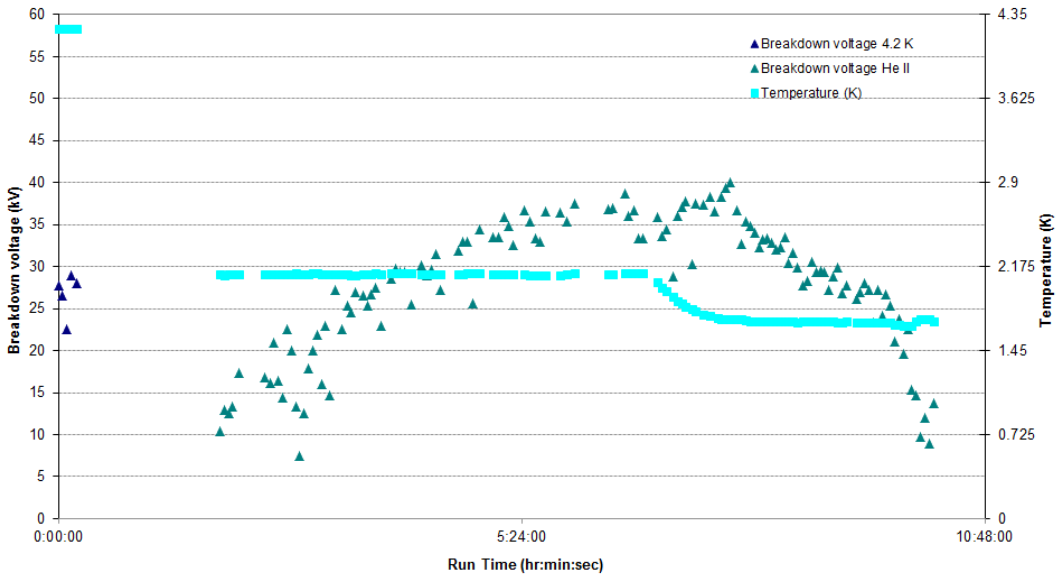

Fig..6.19. Breakdown voltage and temperature as a function of run time for PC Run 11. Blue triangle: V_{bd} at T_{PC} = 4.2 K; Teal triangle: V_{bd} at T_{PC} = He II; Pale blue square: T_{mb}, and therefore T_{PC} (deduced from P_v).

Data taken at a fixed temperature of 4.2 K was repeated, PC Run 12. This was to investigate any change in V_{bd} as a function of integrated running time over all the PC Runs.

This might be expected since sparks will damage the cell and can cause a reduction in $V_{bd.}$ Additionally, every time liquid helium is transferred into the cryostat, and therefore PC, it introduces new impurities.

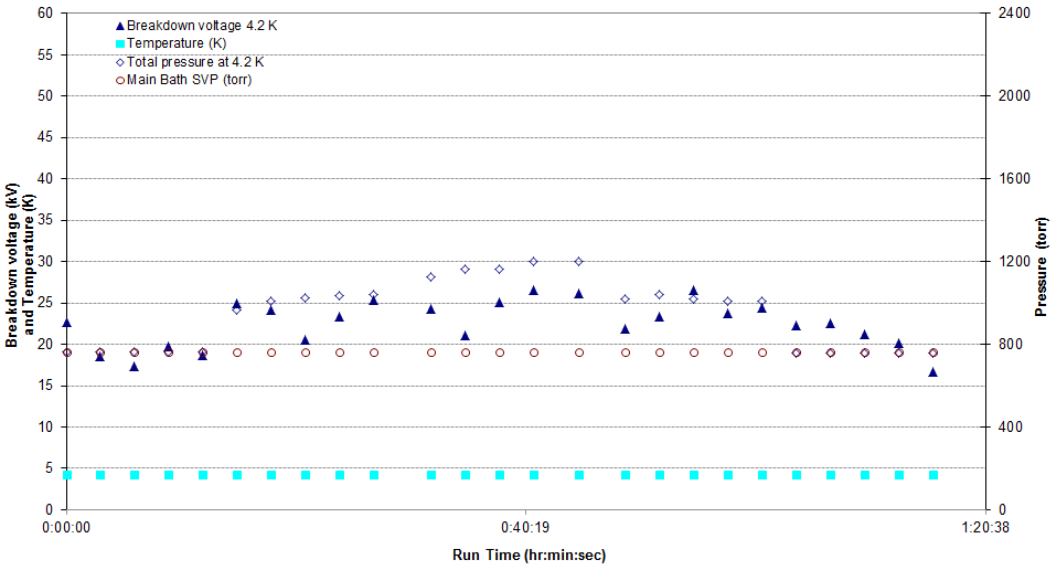

Fig..6.20. Breakdown voltage, pressures and temperature as a function of run time for PC Run 12. Blue triangle: V_{bd} at 4.2 K; Diamond blue outside: P_{cell} at 4.2 K; Red circle: P_v; Pale blue square: T_{mb}, and therefore T_{PC} (deduced from P_v). V_{bd} and T_{mb} are read off y axis 1. P_{cell} and P_v are read off y axis 2.

The temperature was fixed at 4.2 K and the P_{cell} was increased from P_v until 1200 torr and reduced again to P_v. The results are shown on Fig. 6.20. A pressure effect is still evident. However, comparing this set of data to that taken at 4.2 K in Run 8 it is clear that there has been a reduction in V_{bd} at 4.2 K over the PC Runs

6.2.5. PC Run 13 (11/09/2010)

To investigate the drop in V_{bd} as a function of integrated running time, the PC was dismantled and inspected to look for anything obvious. It was clear that breakdown had occurred across the electrodes, with V_{bd} craters being clearly visible. It was also noted that

dust/dirt was now resting on the electrodes. The cell was removed from the apparatus and repolished. Once cleaned it was remounted into the PC and set at a larger average separation of 2.9 mm at RT.

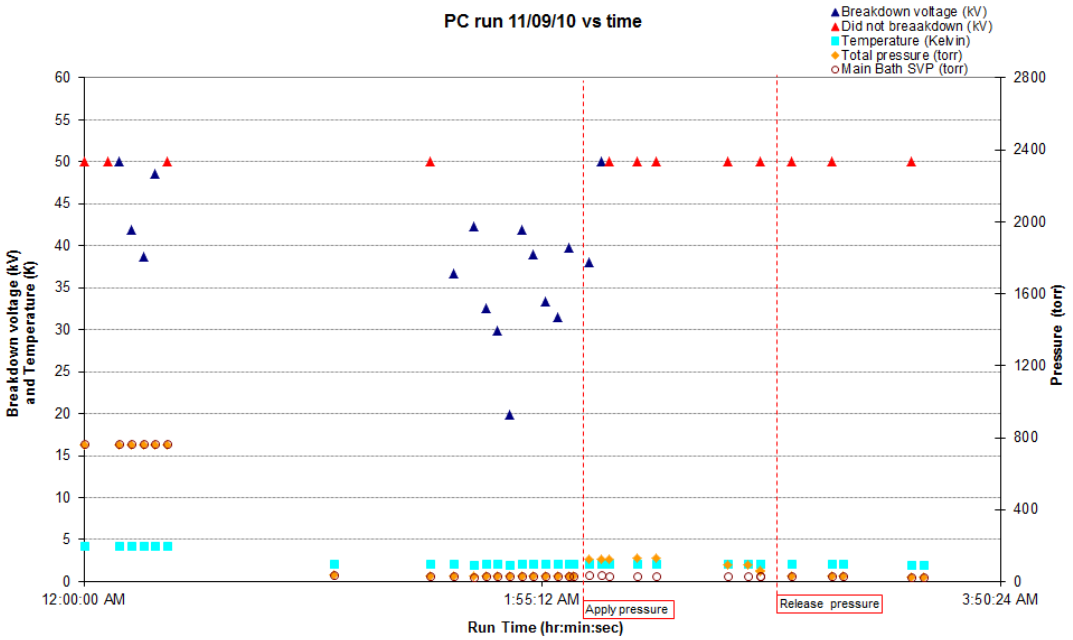

Fig..6.21. Voltage, pressures and temperature as a function of run time for PC Run 13. Blue triangle: V_{bd}; Red triangle V_h; Orange diamond: P_{cell}; Red circle: P_v; Pale blue square: T_{mb}, and therefore T_{PC} (deduced from P_v). V_{bd} and T_{mb} are read off y axis 1. P_{cell} and P_v are read off y axis 2. Also shown are the times when pressure was applied to, P_t = 1.5 bar, and released from the PC.

PC Run 13 was completed primarily to see if V_{bd} would recover to the values ≥ those in the earlier PC runs. The results are shown on Fig 6.21. V_{bd} did increase to 50 kV and hold at this voltage at 4.2 K under P_v and for He II. The cell characteristics had changed and it was no longer possible to investigate V_{bd} as a function of pressure for this separation and surface finish since the voltage could easily increase to 50 kV. This meant that the V_{bd} reduction over many Runs was indeed due to spark damage to the cell or impurities in the cell or a combination of the two.

6.2.6. $V_{bd}(P)$ at constant temperature

To study the effect of PC pressure, P_{cell}, on breakdown voltage, V_{bd}, all V_{bd} data taken at one PC temperature, T_{PC}, was plotted against P_{cell}. Plots of raw data taken at constant temperatures are shown below, Fig. 6.22.

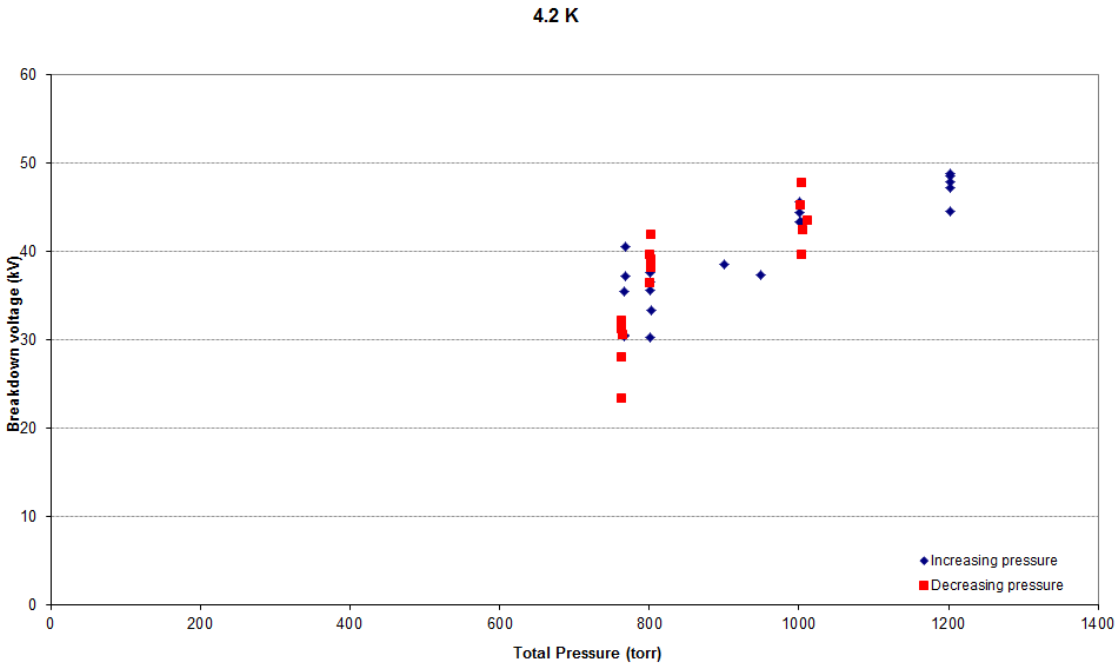

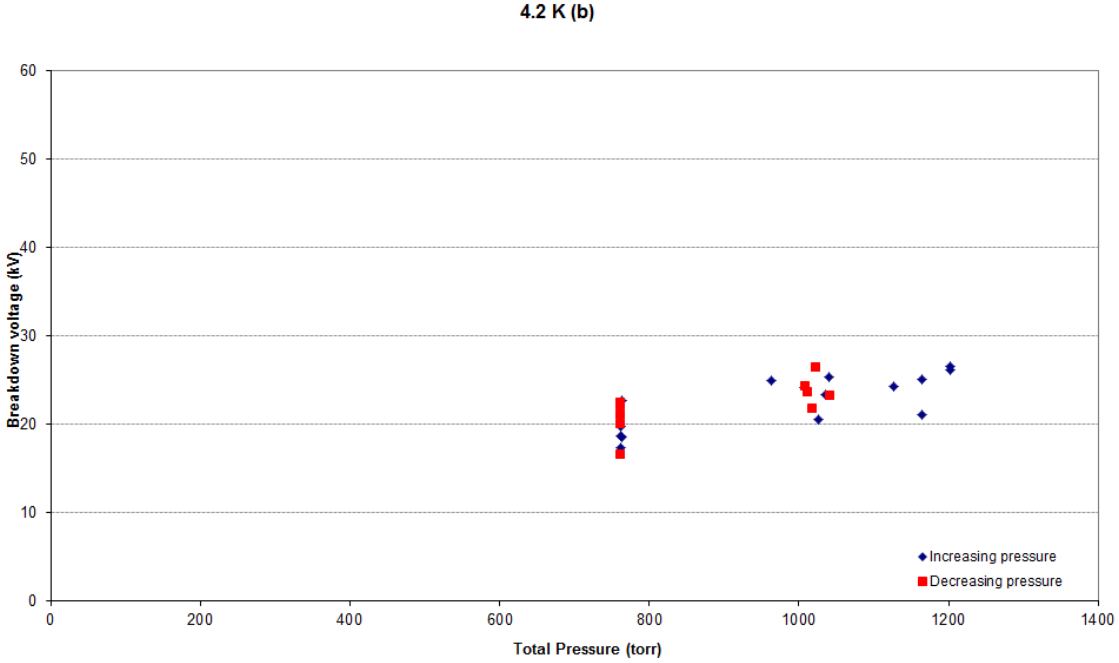

Fig..6.22a. Breakdown voltage as a function of pressure at fixed temperature. Data from PC Runs 8 and 12. Blue triangle: V_{bd} (increasing P_{cell}); Red triangle: V_{bd} (decreasing P_{cell}).

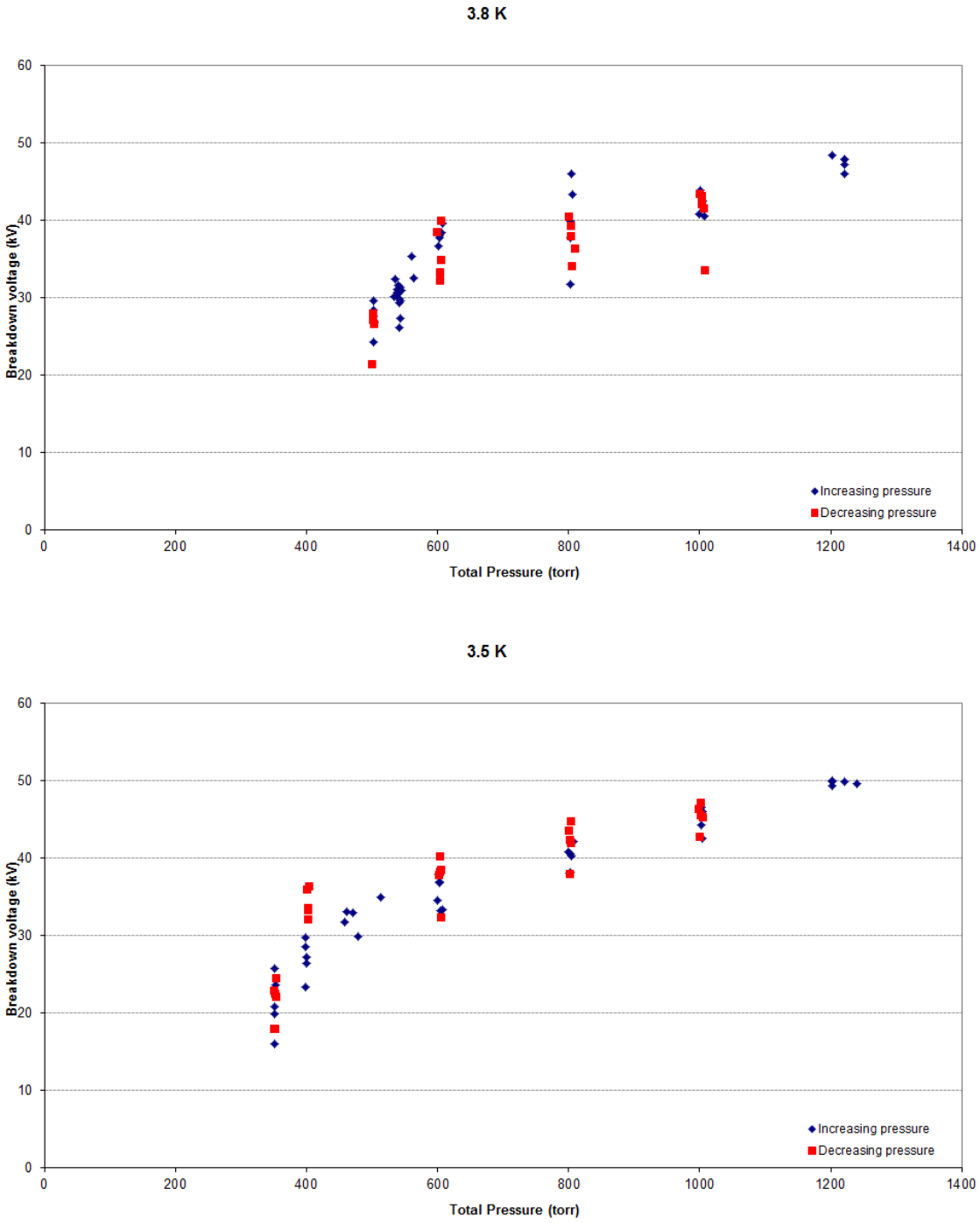

Fig..6.22b. Breakdown voltage as a function of pressure at fixed temperature. Data from PC Run 8. Blue triangle: V_{bd} (increasing P_{cell}); Red triangle: V_{bd} (decreasing P_{cell}).

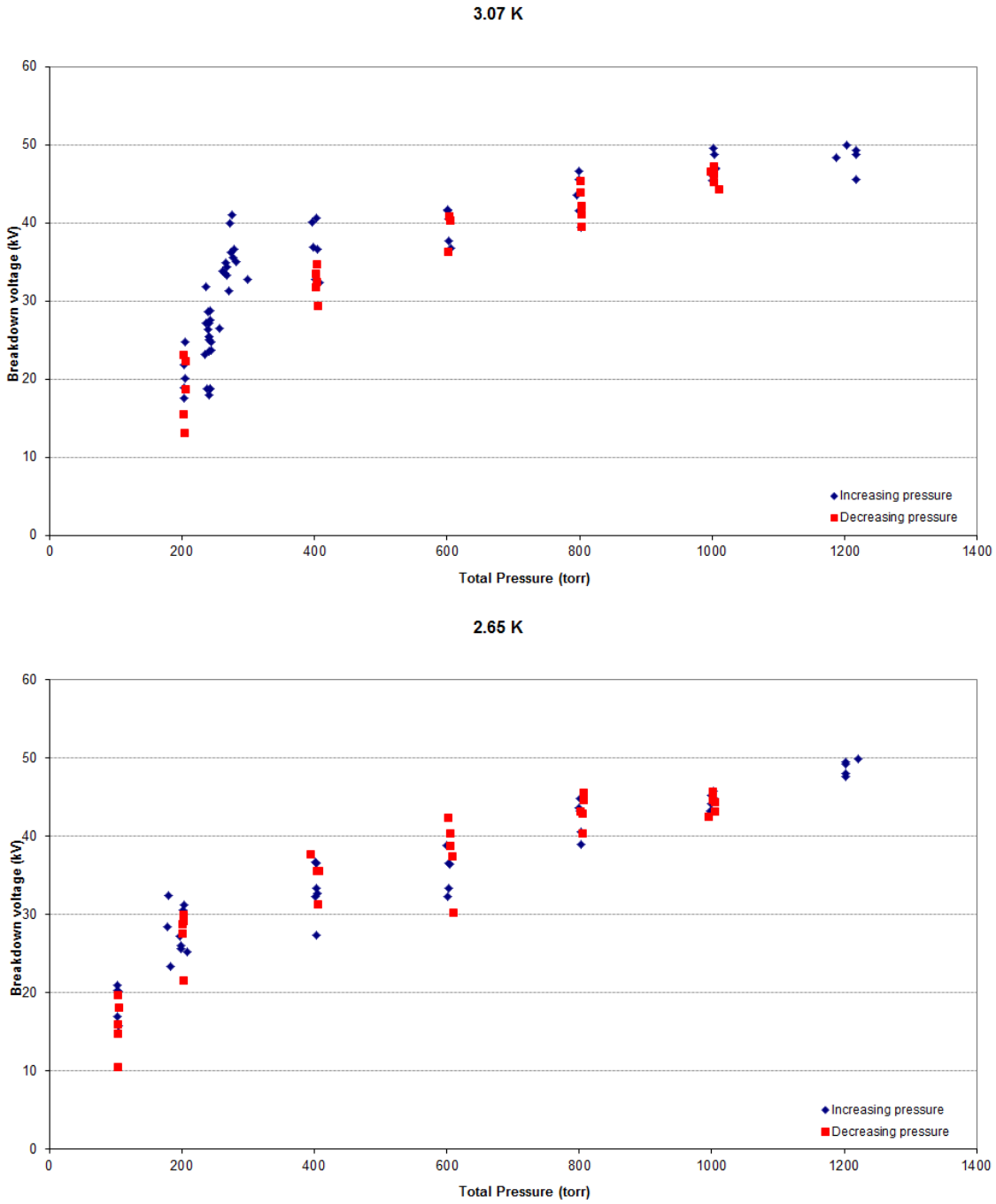

Fig..6.22c. Breakdown voltage as a function of pressure at fixed temperature. Data from PC Run 9. Blue triangle: V_{bd} (increasing P_{cell}); Red triangle: V_{bd} (decreasing P_{cell}).

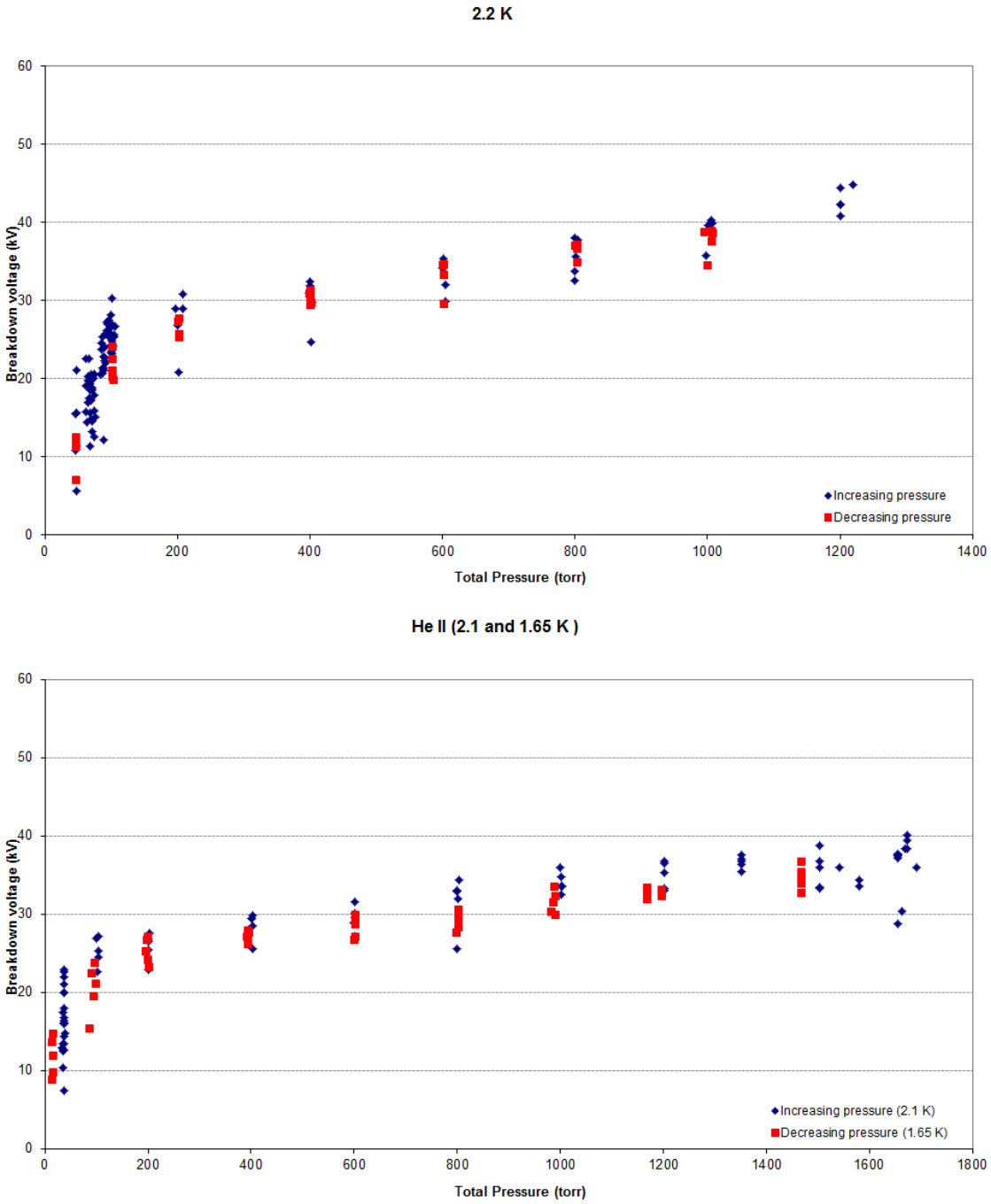

Fig..6.22d. Breakdown voltage as a function of pressure at fixed temperature. Data from PC Runs 10 and 11. Blue triangle: V_{bd} (increasing P_{cell}); Red triangle: V_{bd} (decreasing P_{cell}).

6.3 High Voltage breakdown in He I, He II and LN_2 when a ceramic spacer is added between two Rogowski profile electrodes

Breakdown tests have been carried out using various lengths of Al_2O_3 Alumina ceramic tubes sandwiched between the DKHs and DKHl electrodes. V_{bd} measurements were taking in He I, He II and LN_2.

Section 6.3.1 presents the data from ceramics runs 1, 2, 3, 4, 5 and 6 taken using the DKHs electrodes. These six experiments investigated V_{bd} characteristics as a result of changing the length of Al_2O_3 between the electrodes in both He I and He II. The effect of gold coating the cathode end of the ceramic has been investigated in ceramic run 6.

The data presented in section 6.3.2 is taken from LN_2 runs 1, 2, 3 and 4. The DKHs electrodes were used to carry out V_{bd} measurements on different lengths of ceramic when the cell is submerged in LN_2. We also present here, V_{bd} data using the DKHs electrodes in LN_2 as a function of electrode separation without any ceramic between the electrodes.

Breakdown data taken in He I, He II and LN_2 using the larger DKHl electrodes when a ceramic spacer is sandwiched between the electrodes are presented in section 6.3.3. Some data is also given for V_{bd} between the DKHl electrodes in LN_2 without the inclusion of a ceramic spacer. In comparison to the DKHs electrodes, the surface area of the electrodes and length of the CTJ is increased when using the larger electrodes. The data in section 6.3.3 were taken in ceramic runs 7, 8 and 9 and LN_2 runs 5 and 6.

6.3.1. Ceramic Breakdown tests in He I and He II using DKHs Rogowski profile electrodes

The DKHs electrodes were used to take V_{bd} data in He I and He II as a function of the length of the Al_2O_3 between them. The apparatus and method used to take this data is shown in detail in section 5.7.

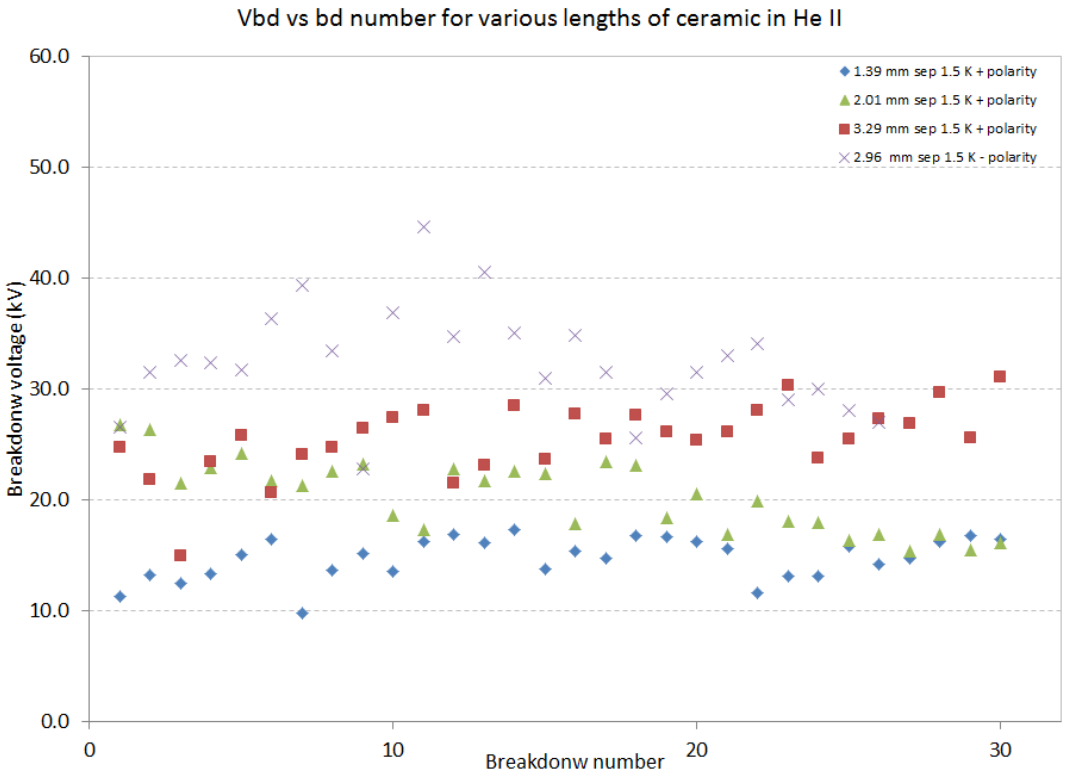

Fig..6.23. Breakdown voltage versus breakdown event number for various lengths of Al_2O_3 between DKHs electrodes submerged in He II at ~ 1.5 K and under P_v. Data from ceramic runs 1, 2, 3 and 4. Blue diamonds: V_{bd}, ceramic run 1 (electrode separation 1.39 mm, positive polarity); Green triangles: V_{bd}, ceramic run 2 (electrode separation 2.01 mm, positive polarity); Red squares: V_{bd}, ceramic run 3 (electrode separation 3.29 mm, positive polarity); Blue crosses: V_{bd}, ceramic run 4 (electrode separation 2.96 mm, negative polarity).

Figure 6.23 plots the V_{bd} data against breakdown event number for ceramics runs 1, 2, 3 and 4. All data was taken in He II at ~ 1.5 K under P_v. The polarity used for ceramic run 4

is negative while that of the others is positive. After subtracting the depth of the DKHs electrode grooves (groove depth 2.27 mm) the true separation between the electrodes was 1.39 mm, 2.01 mm, 3.29 mm and 2.96 mm. For individual lengths the V_{bd} values remained fairly constant as a function of time for all lengths of ceramics.

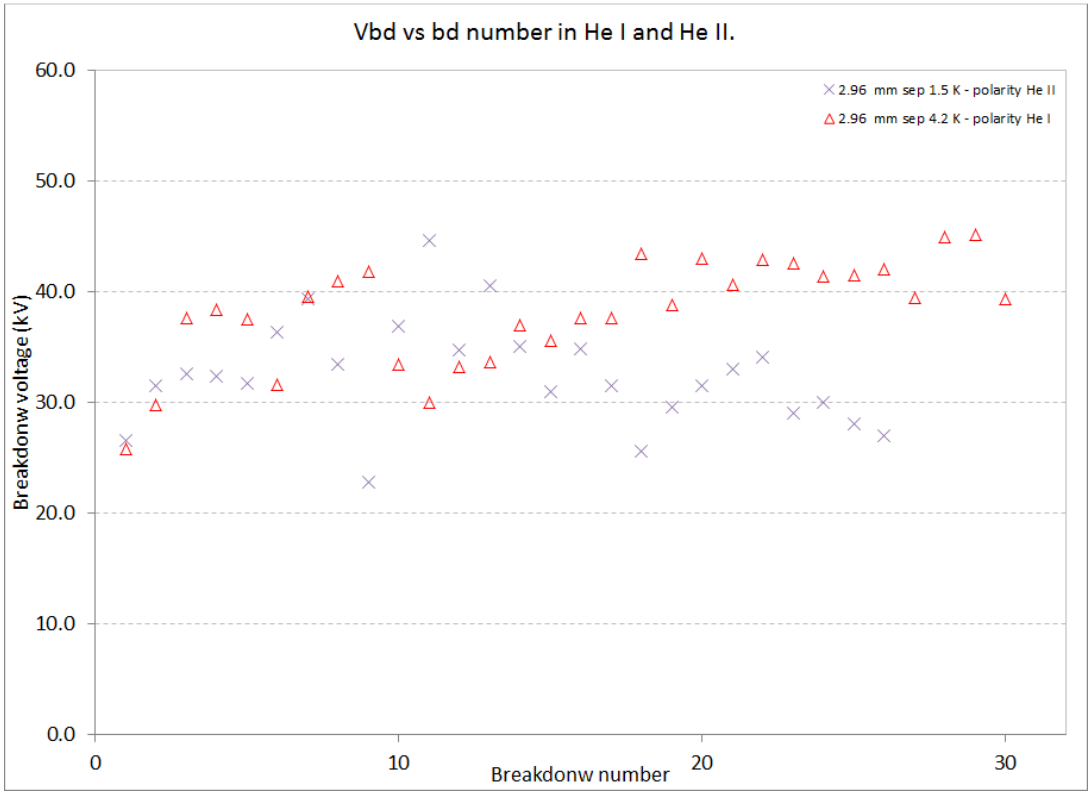

Fig..6.24. Breakdown voltage versus breakdown event number for ceramic runs 4 (He II at ~ 1.5 K under P_v) and 5 (He I at 4.2 K under P_v). There is a separation of 2.96 mm between the DKHs electrodes (total Al_2O_3 length is 7.5 mm). Blue crosses: V_{bd}, ceramic run 4 (negative polarity); Red triangles: V_{bd}, ceramic run 5 (negative polarity).

Two experiments were carried out with the same length of Al_2O_3 between the DKHs electrodes. One in He II at ~ 1.5 K under P_v, ceramic run 4 and the other in He I at 4.2 K under P_v, ceramic run 5. In both cases the HV electrode was negative. Figure 6.24 shows the V_{bd} versus the breakdown event number for both runs. There is no obvious increase or

decrease in V_{bd} data as a function of event number for both He I and He II within scatter. However, both temperatures seem to have larger scatter during the first half of the events. The breakdown voltage then becomes more constant during the second half of events with the V_{bd} in liquid helium at 4.2 K being consistently higher than that at 1.5 K by about ~ 10 kV.

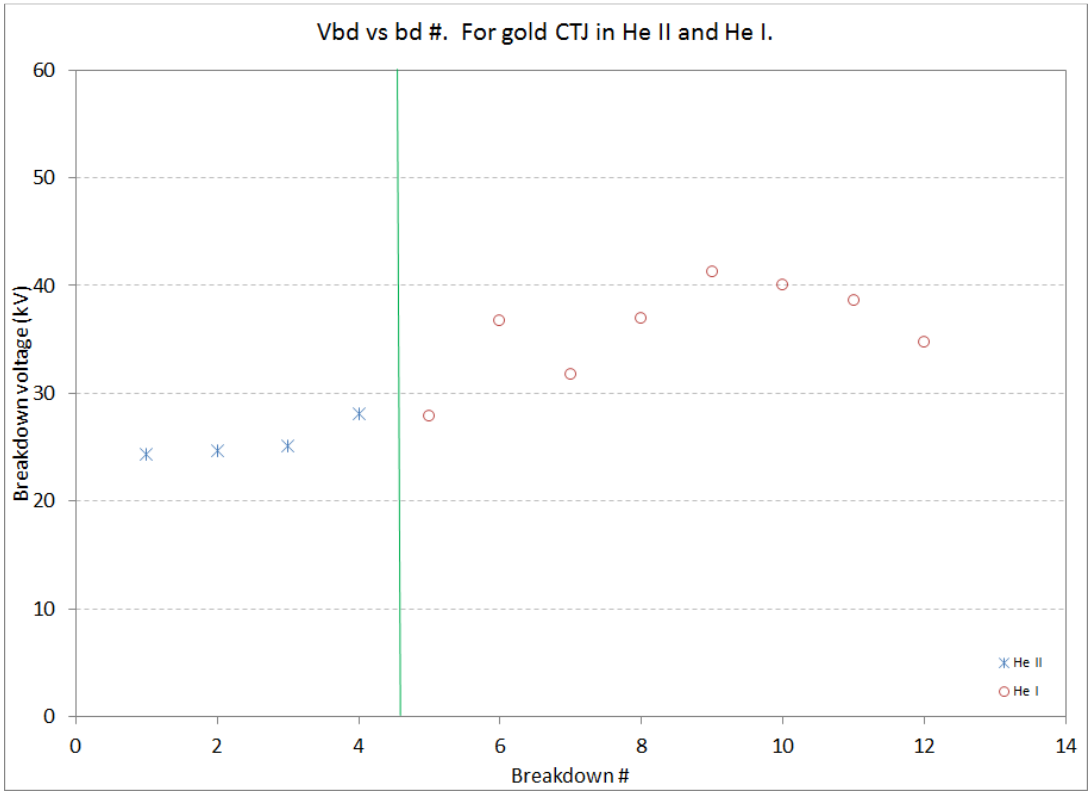

Fig..6.25. Breakdown voltage versus breakdown event number for ceramic run 6. Separation between DKHs electrodes is 3.23 mm (Al_2O_3 length 7.77 mm). The end face of the Al_2O_3 that is in contact with the cathode is coated with gold (gold sputtered on). Blue stars: V_{bd}, (He II at ~ 1.4 K under P_v, positive polarity); Red circles: V_{bd}, (He I at ~ 4.2 K under P_v, positive polarity). Green line indicates the point when the temperature was changed from 1.4 K to 4.2 K.

One ceramic sample had the cathode end coated with Gold. This was to prevent any high E-field regions between the ceramic and the cathode. A breakdown test was carried out on this sample to find out the effect it has on the V_{bd}.

Four V_{bd} measurements were taken when the cell was submerged in He II at 1.4 K. It was then warmed back to 4.2 K and an additional 8 V_{bd} points taken. A slight increase in voltage was observed when the temperature was raised to 4.2 K. In both cases the polarity applied was positive. The results of this run are shown on Fig. 6.25. The cell picked up a high resistance track to ground after the eighth V_{bd} in He I. This limited the voltage on the HV electrode and therefore prevent addaitional V_{bd} measurements.

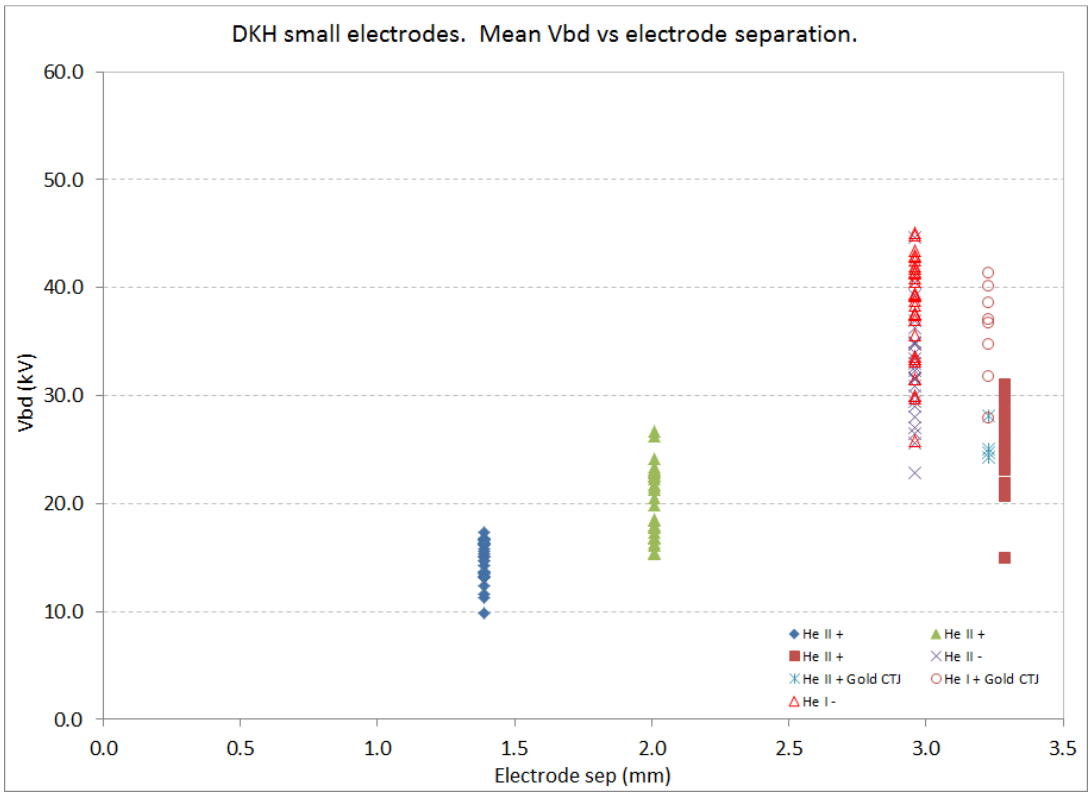

Fig..6.26a. Breakdown voltage (6.26a) and mean breakdown voltage (6.26b) versus separation between DKHs electrodes for various lengths of Al_2O_3. The standard error on the mean breakdown voltage is indicated on 6.26b. Data taken from ceramic runs 1, 2, 3, 4, 5 and 6. Blue diamonds: V_{bd}, ceramic run 1 (He II at ~ 1.5 K under P_v, positive polarity); Green triangles: V_{bd}, ceramic run 2 (He II at ~ 1.5 K under P_v, positive polarity); Red squares: V_{bd}, ceramic run 3 (He II at ~ 1.5 K under P_v, positive polarity); Blue crosses: V_{bd}, ceramic run 4 (He II at ~ 1.5 K under P_v, negative polarity); Red triangles: V_{bd}, ceramic run 5 (He I at 4.2 K under P_v, negative polarity); Blue stars: V_{bd}, ceramic run 6 (He II at ~ 1.4 K under P_v, positive polarity); Red circles: V_{bd}, ceramic run 6 (He I at ~ 4.2 K under P_v, positive polarity).

A summary of all He I and He II data taken with the DKHs electrodes and a ceramic spacer between the electrodes is shown in Fig. 6.26a and Fig. 6.26b. V_{bd} is plotted as a function of the separation between the electrodes and therefore as a function of the length of the ceramic. Figure 6.26a plots the raw data while Fig. 6.26b shows the mean V_{bd}. In general an increase in V_{bd} is observed with an increase in separation. The mean values of V_{bd} in He I are higher than that of the V_{bd} values in He II for a coresponding electrode separation. There seems to be a discrepancy between the 2.96 mm and 3.15 mm data. As a different polarity was used it can be postulated that the CTJ electrostatic are different on each electrode or it could the result of V_{bd} scatter statistics. The V_{bd} values are higher when using negative polarity. This is discussed later in chapter 7.

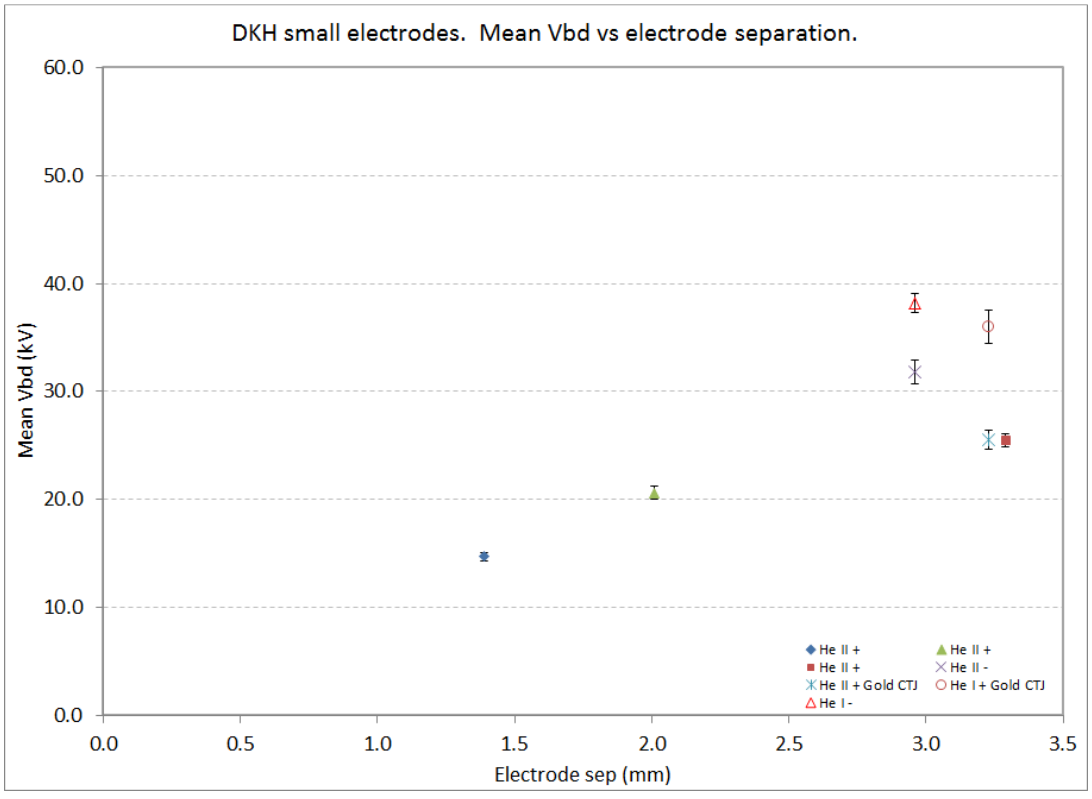

Fig..6.26b. See Fig. 6.26a. for caption.

6.3.2. Ceramic Breakdown tests in LN_2 using DKHs Rogowski profile electrodes

A series of ceramic tests were carried out in LN_2 using the DKHs electrodes to investigate what effect a piece of ceramic has on the breakdown voltage.

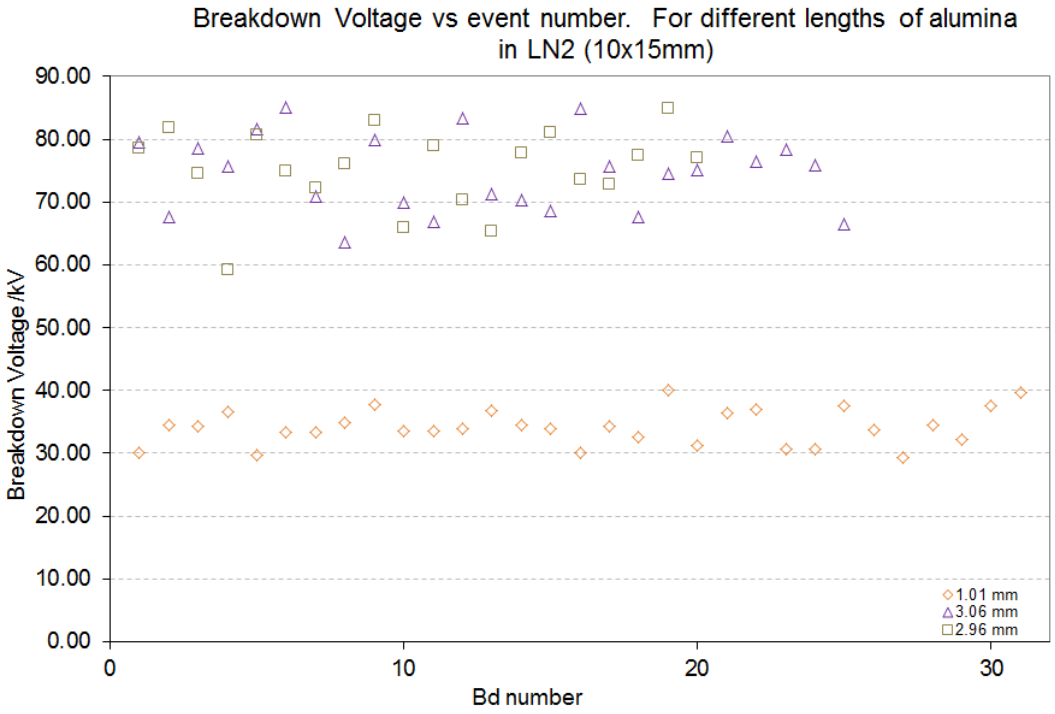

Fig..6.27. Breakdown voltage versus breakdown event number for various lengths of Al_2O_3 between DKHs electrodes submerged in LN_2. Data from LN_2 runs 1, 2 and 3. Orange diamonds: V_{bd}, LN_2 run 1 (electrode separation 1.01 mm, negative polarity); Tan squares: V_{bd}, LN_2 run 2 (electrode separation 2.96 mm, negative polarity); Purple triangles: V_{bd}, LN_2 run 3 (electrode separation 3.06 mm, negative polarity).

Figure 6.27 shows the V_{bd} data as a function of the event number. In general the V_{bd} values are consistent over the run period. Larger separations produced a larger spread in breakdown value. 2.96 mm or greater produced a V_{bd} spread of ~ 20 kV. At a smaller separation of 1.01 mm this spread was only ~ 10 kV.

Breakdown voltage as a function of separation is plotted on Fig. 6.28a. and Fig 6.28b. for breakdown in LN_2 when a ceramic is between the electrodes. Also shown is V_{bd} data taken with the same electrodes but this time no ceramic. The raw data is shown on Fig 6.28a. and the mean on 6.28b. An almost linear increase V_{bd} is observed with separation. The V_{bd} values with and without the ceramic are similar. This indicates the presence of the ceramic has no major effect on the dielectric strength of the cell in LN_2 for this number of breakdown events.

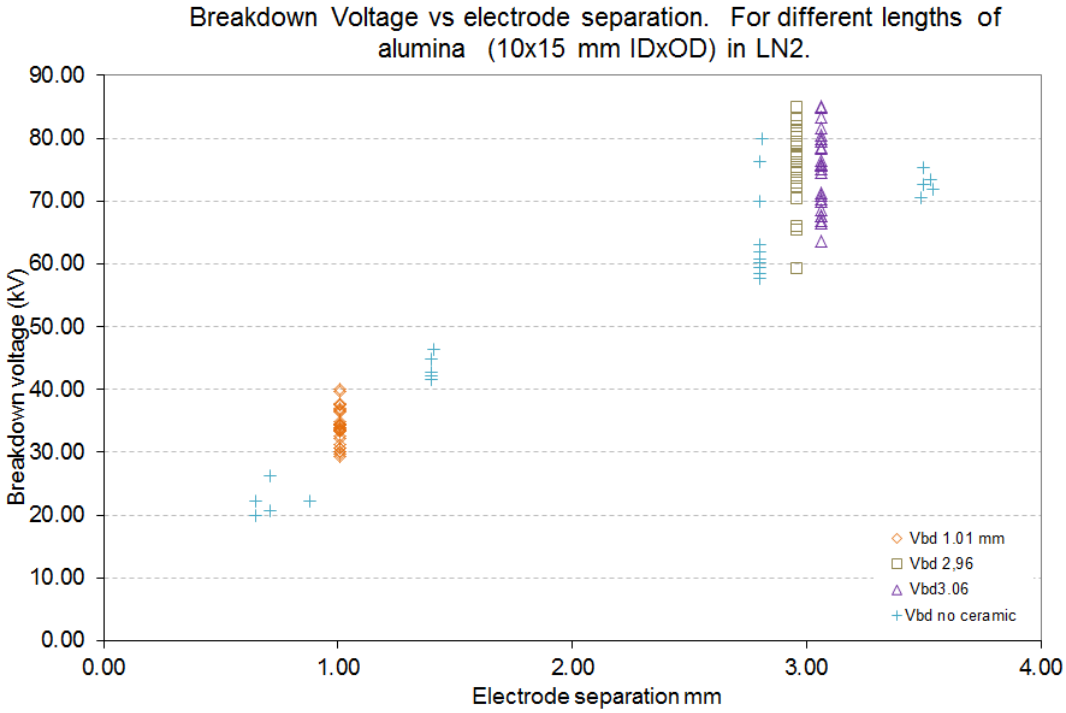

Fig..6.28a. Breakdown voltage (6.28a) and mean breakdown voltage (6.28b) versus separation between DKHs electrodes for various lengths of Al_2O_3 and without any Al_2O_3. The standard error on the mean breakdown voltage is indicated on 6.28b. Data from LN_2 runs 1, 2, 3 and 4. Orange diamonds: V_{bd}, LN_2 run 1 (with Al_2O_3, electrode separation 1.01 mm, negative polarity); Tan squares: V_{bd}, LN_2 run 2 (with Al_2O_3, electrode separation 2.96 mm, negative polarity); Purple triangles: V_{bd}, LN_2 run 3 (with Al_2O_3, electrode separation 3.06 mm, negative polarity); Blue t-crosses: V_{bd}, LN_2 run 4 (without Al_2O_3, electrode separation varies, negative polarity).

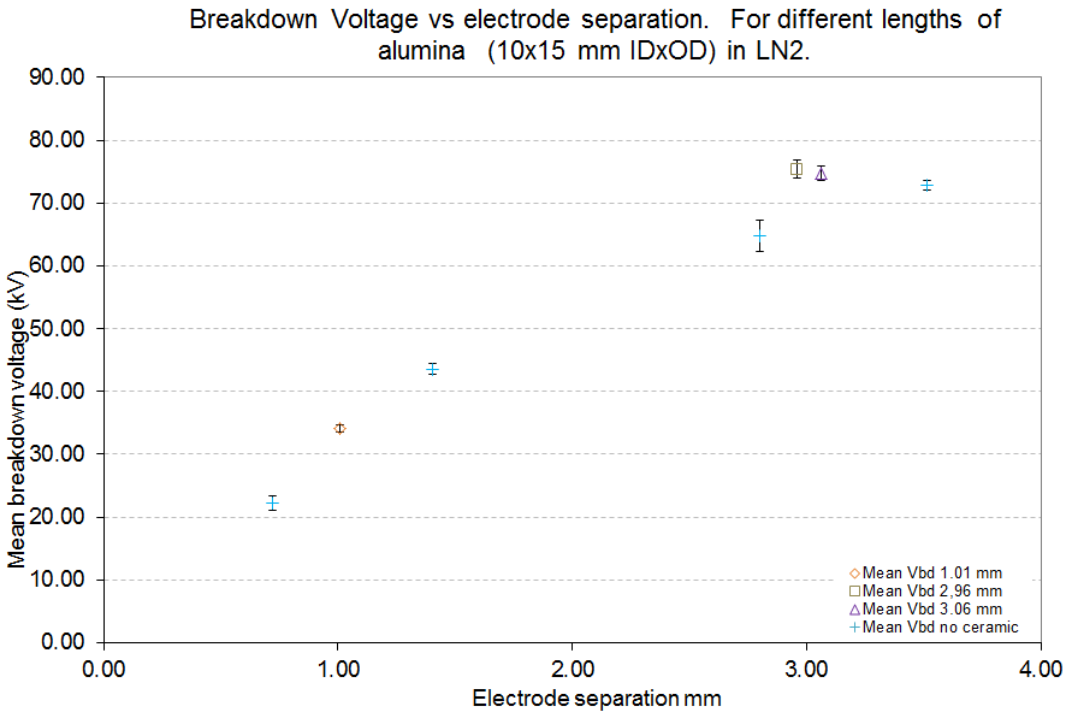

Fig..6.28b. See Fig. 6.28a for caption.

6.3.3. Breakdown with the DKH large electrodes

The DKHl electrodes were used to take data while a piece of ceramic was between the electrodes. Experiments were carried out in He I, He II and LN_2. All data taken from these electrodes has been plotted on Fig 6.29. Figure 6.29 shows the breakdown voltage versus the event number. Only one data point has been taken in He I with electrode separation 13.94 mm. The cell breakdown happened at 99.8 kV then a track to ground was created and the cell would not charge.

The breakdown voltage was scattered around 40 kV when the electrodes were submerged in He II at 1.9 K with an electrode separation of 6.94 mm. Both runs under the same conditions produce very similar results. When the electrode separation is 2.74 mm and the electrodes and ceramic are submerged in LN_2 the breakdown voltage was scattered around 60 kV.

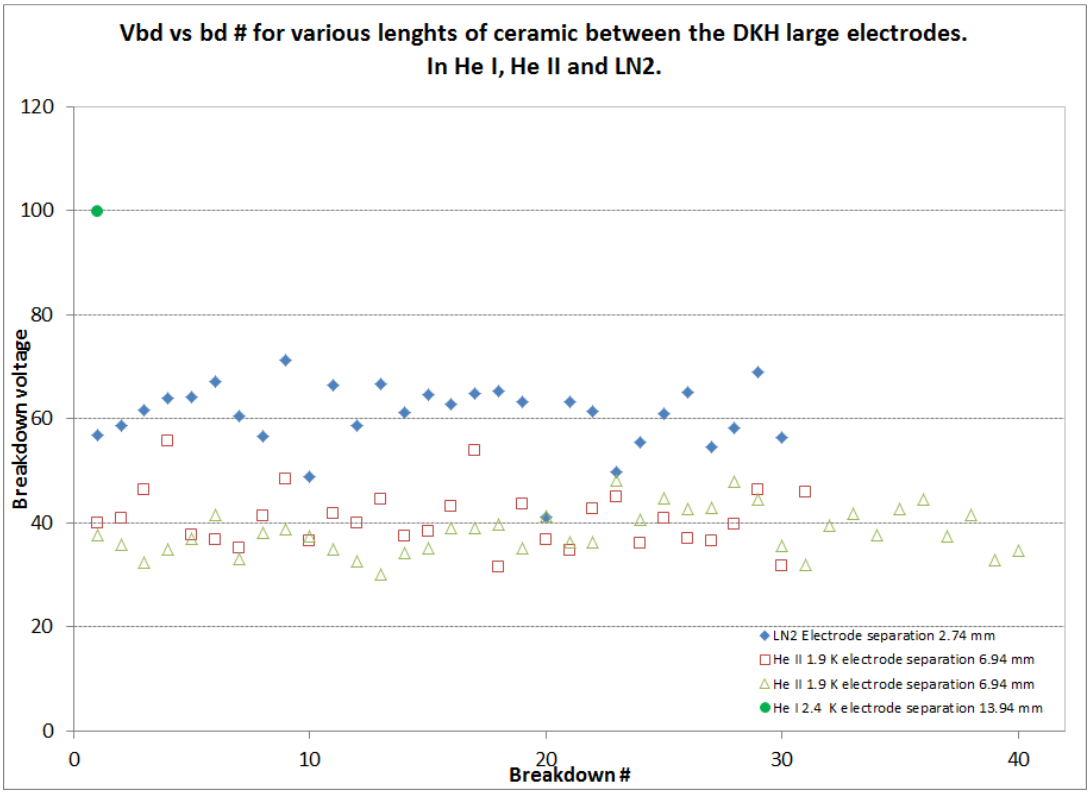

Fig..6.29. Breakdown voltage versus breakdown event number for various lengths of Al_2O_3 between DKHl electrodes in He I, He II and LN2. Data taken from ceramic runs 7, 8, 9 and LN2 run 5. Red squares: V_{bd}, ceramic run 7 (He II at ~ 1.9 K under P_v, electrode separation 6.94 mm, negative polarity); Green triangles: V_{bd}, ceramic run 8 (He II at ~ 1.9 K under P_v, electrode separation 6.94 mm, negative polarity); Green circle: V_{bd}, ceramic run 9 (He I at 4.2 K under P_v, electrode separation 13.94 mm, negative polarity); Blue diamonds: V_{bd}, LN2 run 5 (electrode separation 2.74 mm, negative polarity).

Apart from the one data point taken in He I at 4.2 K at a separation of 13.94 mm all the other tests produced repeatable breakdown data that stayed approximately constant, within the scatter, over the run.

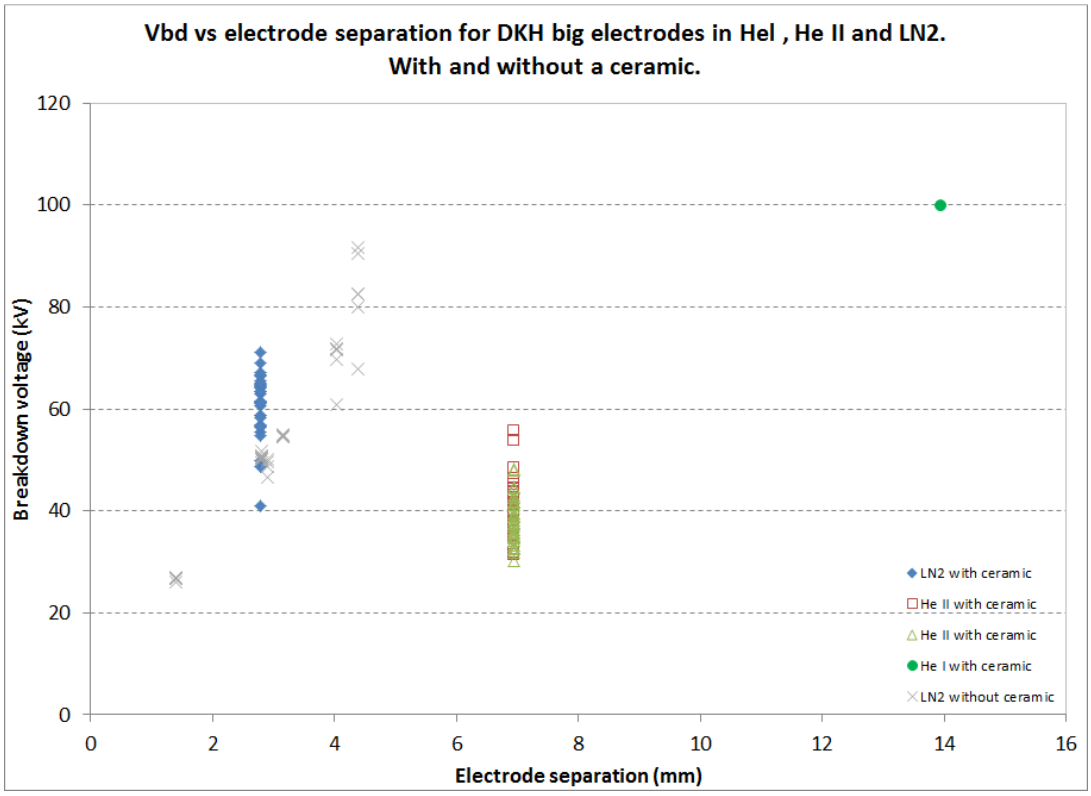

Fig..6.30a. Breakdown voltage versus separation between DKHl electrodes for various lengths of Al_2O_3 and without any Al_2O_3 in He I, He II and LN_2. Data taken from ceramic runs 7, 8, 9 and LN_2 runs 5 and 6. Red squares: V_{bd}, ceramic run 7 (with Al_2O_3, He II at ~ 1.9 K under P_v, electrode separation 6.94 mm, negative polarity); Green triangles: V_{bd}, ceramic run 8 (with Al_2O_3, He II at ~ 1.9 K under P_v, electrode separation 6.94 mm, negative polarity); Green circle: V_{bd}, ceramic run 9 (with Al_2O_3, He I at 4.2 K under P_v, electrode separation 13.94 mm, negative polarity); Blue diamonds: V_{bd}, LN_2 run 5 (with Al_2O_3, electrode separation 2.74 mm, negative polarity); Grey crosses: V_{bd}, LN_2 run 6 (without Al_2O_3, electrode separation varies, negative polarity).

Figure 6.30a and Fig.6.30b show the breakdown voltage as a function of electrode separation, for the DKHl electrodes in He I, He II and LN_2 when a ceramic spacer is between them. Figure 6.30 also includes some data taken using the DKHl electrodes and no ceramic.

In general LN_2 plus the ceramic produces a higher breakdown voltage then He I or He II plus the ceramic. Figure 6.30 shows that the average breakdown voltage for He I at 1.9 K

when the electrode separation is 6.94 mm is ~ 40 kV and that for LN_2 at 2.74 mm is ~ 60 kV. All data was taken using negative polarity.

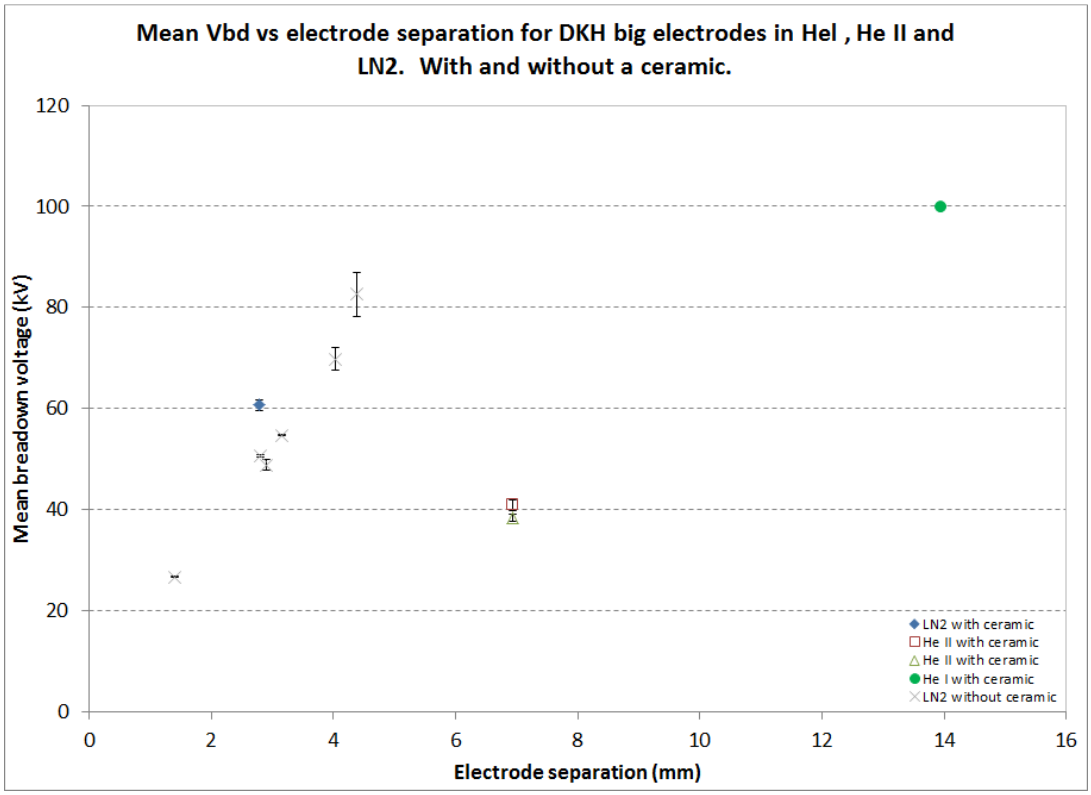

Fig..6.30b. Mean breakdown voltage versus separation between DKHl electrodes for various lengths of Al_2O_3 and without any Al_2O_3 in He I, He II and LN_2. The standard error on the mean breakdown voltage is indicated. Data taken from ceramic runs 7, 8, 9 and LN_2 runs 5 and 6. Red squares: V_{bd}, ceramic run 7 (with Al_2O_3, He II at ~ 1.9 K under P_v, electrode separation 6.94 mm, negative polarity); Green triangles: V_{bd}, ceramic run 8 (with Al_2O_3, He II at ~ 1.9 K under P_v, electrode separation 6.94 mm, negative polarity); Green circle: V_{bd}, ceramic run 9 (with Al_2O_3, He I at 4.2 K under P_v, electrode separation 13.94 mm, negative polarity); Blue diamonds: V_{bd}, LN_2 run 5 (with Al_2O_3, electrode separation 2.74 mm, negative polarity); Grey crosses: V_{bd}, LN_2 run 6 (without Al_2O_3, electrode separation varies, negative polarity).

7 Analysis and Discussion

The first section of this chapter is concerned with the variation with pressure and temperature of the breakdown voltage in liquid helium, using a test cell without any dielectric spacer. The second section considers the effect of a ceramic spacer on the breakdown values. Damage to, and tracking across the spacers is covered in Section 7.3. In the last section of this chapter, we examine the detailed geometry of the grooves in the electrodes and consider how this might affect the breakdown voltages and the damage and tracking observed on the ceramics.

7.1. Analysis of the V_{bd} (P,T) Data

7.1.1. Introduction

This section discusses the variation of the breakdown voltage as a function of pressure in spacerless cells at constant temperatures between 1.7 K and 4.2 K for which data was presented in Section 6.2.

The general form of the variation with pressure and the measurement cycles used to investigate any possible hysteretic behaviour are described first. We next look at the gradual reduction in breakdown voltages seen as function of PC run number. We attribute this to the electrodes suffering damage due to HV cratering and / or debris or dust accumulating on the surface of the electrodes after multiple breakdowns or helium transfers. The lack of hysteresis in our data is then discussed and compared and contrasted with the work of the Indiana group.

The rest of the section is concerned with the particular form of $V_{bd}(T)$ shown in our data. All the data taken both above and below the superfluid transition temperature show a similar variation with pressure. At high pressures, in region 1, a weak linear reduction with

decreasing pressure is observed whereas in region 2, below a temperature dependent "kink" pressure, P_k, there is a much more rapid decrease in breakdown voltage with pressure. Our analysis and parameterisation of this behaviour, and the way in which we took account of the gradual reduction in breakdown voltage with run number, is discussed in detail in Sections 7.1.5 to 7.1.10 inclusive. We briefly consider the variation of $P_k(T)$ in Section 7.1.11 and then compare our analysed results with all available published data in Section 7.1.12. Finally, in Section 7.1.13 we present a possible model to explain our observed $V_{bd}(P,T)$ behaviour and some numerical calculations based upon it.

7.1.2. General form of $V_{bd}(P)$ at Constant Temperature

For any set of breakdown data taken as a function of pressure at any constant temperature between 1.7 K and 4.2 K a general trend is observed. In general an increased in pressure increases the breakdown voltage. At any temperature this dependence exhibits two regimes. A gradually increase in V_{bd} with pressure is observed at high pressures, Region 1. At lower pressure just above SVP a rapidly increasing dependence of V_{bd} with pressure is shown.

To show these regions clearly two dashed lines have been drawn onto the breakdown as a function of pressure plots, figures 7.1, 7.2 and 7.3. The blue dashed line displays Region 1 and the green dashed line Region 2. These trend lines have been fitted using a least square fit linear regression.

The point where these two regimes meet we term the kink pressure (P_k).

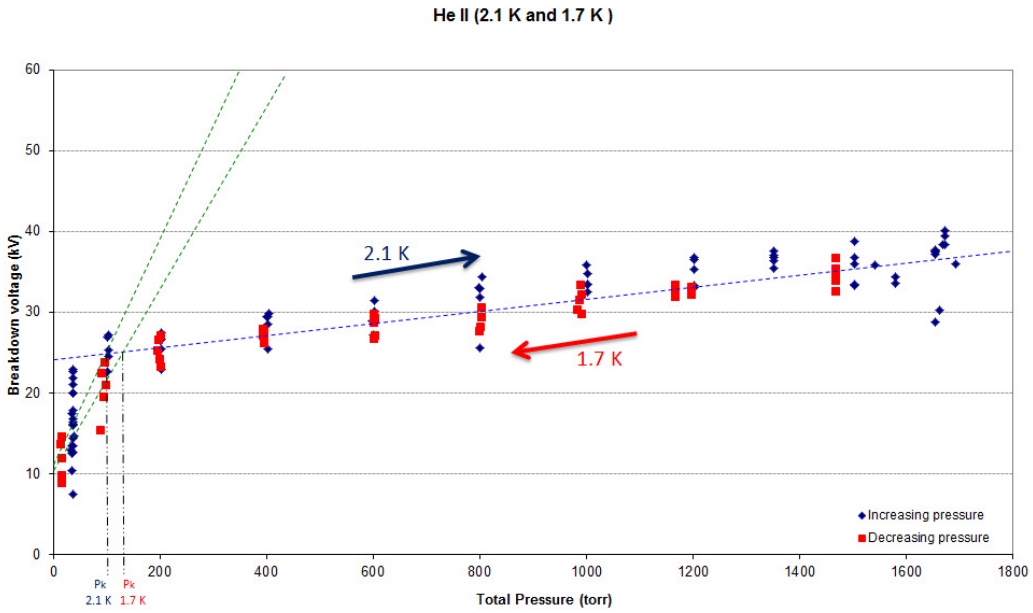

Fig..7.1. Breakdown voltage as a function of pressure at 2.1 K and 1.7 K. PC run 11. Blue triangle: V_{bd} at 2.1 K (increasing P_{cell}); Red triangle: V_{bd} at 1.7 K (decreasing P_{cell}); Blue dashed line: Region 1; Green dashed line: Region 2; Black dashed line: P_k. Blue and red arrows indicate the pressurisation method as a function of run time.

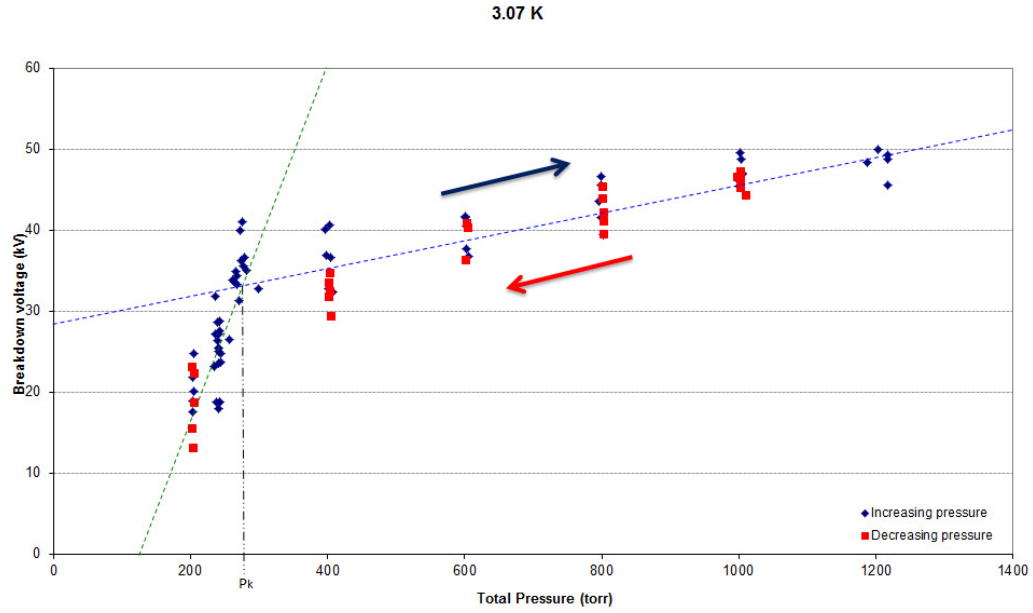

Fig..7.2. Breakdown voltage as a function of pressure at 3.07 K. PC run 9. Blue triangle: V_{bd} (increasing P_{cell}); Red triangle: V_{bd} (decreasing P_{cell}); Blue dashed line: Region 1; Green dashed line: Region 2; Black dashed line: P_k. Arrows indicate the pressurisation method as a function of run time.

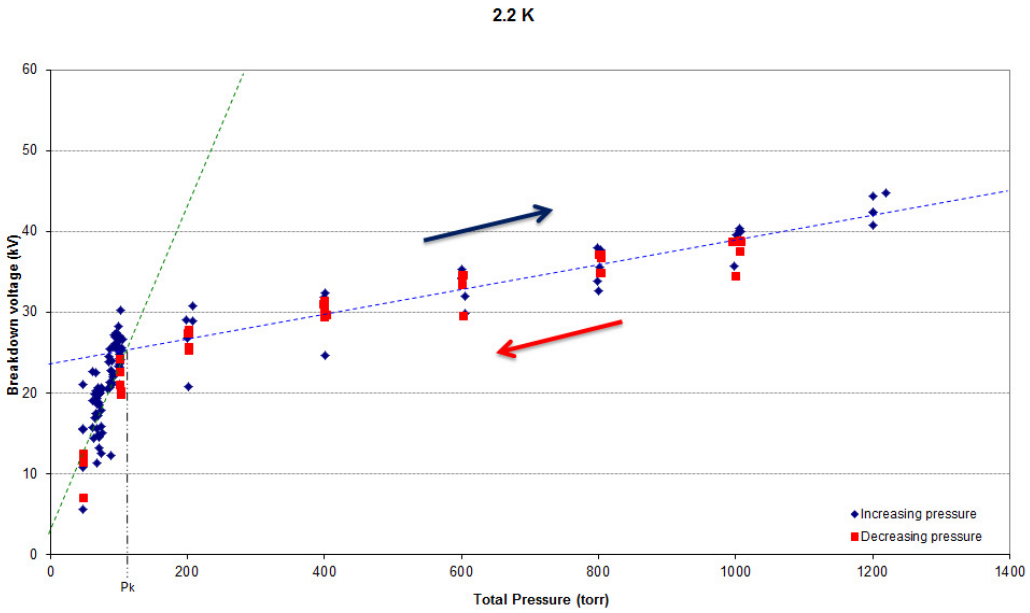

Fig..7.3. Breakdown voltage as a function of pressure at 2.2 K. PC run 10. Blue triangle: V_{bd} (increasing P_{cell}); Red triangle: V_{bd} (decreasing P_{cell}); Blue dashed line: Region 1; Green dashed line: Region 2; Black dashed line: P_k. Blue and red arrows indicate the pressurisation method as a function of run time.

The linear regression was carried over a progressively increasing pressure range, starting from the highest pressure and increasing in steps down to SVP. An example of this analysis on the 2.2 K data is shown in Table 7.1.

As the number of data points is increased from 1200 torr down to 100 torr, the gradient and intercept of the regression line remains approximately the same. The standard error of both and the 95% confidence interval is observed to reduce. The coefficient of determination (R^2) is also shown to be getting closer to 1 with increasing data points. This gives confidence that the additional points are on the same regression line and the accuracy of the fit is improving.

When data over the total pressure range from SVP to 1200 torr is included there is an observed change in the characteristics of the regression line. Both the gradient and the intercept deviate away from their previously stable values, with their standard errors and 95% confidence interval increasing. The R^2 of the fit is reduced. This indicates a change in the

linear behaviour of Region 1 below ~ 100 torr. Thus breakdown as a function of pressure exhibits two characteristic regions, Region 1 and Region 2. This is observed in all data sets at constant temperature above and below the λ-point between 1.7 K and 4.2 K.

Pressure Range	1200 to 800 torr	1200 to 600 torr	1200 to 400 torr	1200 to 200 torr	1200 to 100 torr	1200 to 44 torr
Gradient (kV / torr)	0.0170	0.0151	0.0148	0.01492	0.01574	0.0212
Gradient St error (kV / torr)	0.0024	0.0015	0.0011	0.00087	0.00070	0.0010
95 % confidence interval	0.0050	0.0031	0.0022	0.00174	0.00139	0.0020
Intercept (kV)	22.0	23.9	24.17	24.05	23.36	19.02
Intercept St error (kV)	2.4	1.4	0.87	0.63	0.43	0.47
R^2	0.68	0.74	0.81	0.85	0.87	0.75

Table..7.1. Linear regression analysis of breakdown voltage as a function of pressure at 2.2 K. PC run 10.

7.1.3. Variation in V_{bd} at fixed temperature and pressure as a function of total number of discharges

A discrepancy in breakdown value was observed between PC runs when comparing data taken under the same ^{4}He conditions. At the start of every PC run at least five data points were taken at 4.2 K under SVP, as shown in Fig. 7.4. It is evident that over time there is a reduction in the mean breakdown voltage. Hence, it is therefore not possible to compare directly the raw breakdown data between separate PC runs taken some time apart even if the Helium conditions are the same.

The PC was dismantled after Run 12 to investigate the cause of the observed reduction in breakdown voltage. It was evident that the surface of both electrodes had suffered heavy surface damage, as shown in Fig.7.5. At this point ~ 1165 breakdowns had

occurred across the cell. It was also noted that there was dust and other impurities resting on the ground electrode cup.

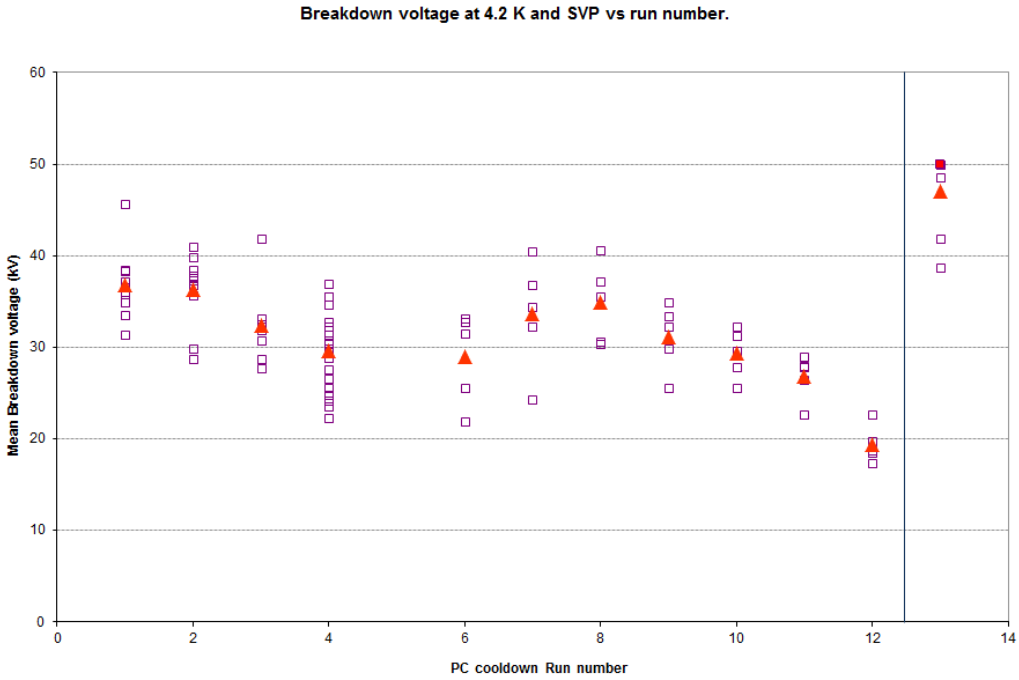

Fig..7.4. Mean breakdown voltage as a function of PC run number. Orange triangle: Mean V_{bd}; Purple square: V_{bd}; Purple square red center: V_h. Line indicates the point when the electrodes were re-polished.

The electrodes separation was measured. It was noted that the electrodes were not quite parallel. The greatest separation was 1.84 mm and the smallest 1.61 mm. It is not surprising that all the discharge events were scattered around the position of least separation. An electrode separation of 1.61 mm at RT reduces to 1.27 mm when at liquid Helium temperatures.

Both electrodes were repolished and cleaned. The cell was reassembled and the electrodes were set to a larger average separation of 2.9 mm at RT. PC run 13 was carried out using the newly polished and cleaned electrodes. An obvious increase in breakdown voltage was observed, figure.7.4.

Fig..7.5. HV Rogowski profile electrode and ground electrode after ~ 1165 discharges. Clockwise from top left: Image 1: Surface of the Rogowski profile electrode; Image 2: Rogowski profile electrode; Image 3: Surface of the PC ground electrode; Image 4: PC ground electrode.

The reduction in breakdown voltage as a function of increasing discharge number is probably caused by the discharge damage to the electrode surface or as a result of the accumulation of dust and impurities in the ^{4}He over running time or a combination of both of these factors.

Gerhold (1989) showed that the overall difference in breakdown voltage between polished and ground electrodes can be as much as a factor of two, (Section 4.1.). Surface roughness has also been investigated by May and Krauth (1981) using spherical 50 mm Nb electrodes which were initially electropolished. After this procedure a pair was chemically etched to produce slight pitting across the surface whilst another set was mechanically polished. In both cases a reduction to the breakdown voltage was observed with respect to

the electropolished sample, (Section 4.2.) Thus, the rougher surfaces produced lower breakdown voltages.

High voltage discharges cause damage to the electrodes. Distinctive cratering is found in all our experiments and the form of this is a function of the breakdown voltage and the electrode material. The observed features of the discharge craters and their variations for different electrode materials are shown in Appendix C.

In our experiments we find in general that one discharge produces one crater. Hence, the overall damage to the electrodes increases with the number of discharges. At first sight it might be expected that the damaged surface would have an increased number of "spikes" leading to an increased local E-fields and hence a reduction in maximum V_{bd} with discharge number. However, if this were the case, we might expect multiple discharges to occur at the same breakdown site but we do not see any evidence for this. There is evidence from the Atomic Force Microscopy measurements of Munday (2010) that material is removed from the surface during the crater formation and it is likely that this will remain within the cell as debris.

The purity of the liquid Helium is also an important parameter. The breakdown field has been shown to reduce by ~ a factor of 2 when comparing purified liquid Helium to commercial grade liquid Helium (Yoshino et al, 1982). It was assumed that the associated impurities become charged and are accelerated in the E-field between electrodes. On impact with the electrode surface these impurities can then initiate bubble formation or electron emission and hence trigger breakdown.

It has also been shown by Yoshino (1982) that as the concentration of Oxygen impurity is increased into liquid Helium the breakdown voltage reduces steady and linearly.

The PC was not opened between Run 1 and Run 12. Therefore, any impurities introduced into the apparatus during either the liquid Helium transfers or as a debris from

crater formation would remain in the PC. The level of such impurities could have steadily built up after every cool down and set of breakdown measurements and resulted in the observed decline in V_{max}.

In conclusion, the observed drop in V_{max} as a function of discharge number may be caused by increased surface roughness as a function of discharge number or by an increase in particulate impurities or by a combination of both.

7.1.4. Lack of evidence for hysteresis in $V_{bd}(P)$

The method used to take measurements at constant temperature was intended to investigate any possible hysteretic behaviour of $V_{bd}(P)$. This was done because Huffer (2008), working at the Indiana University Cyclotron Facility (IUCF), reported that the breakdown voltage of ^4He increased with pressurisation and remained high after it was depressurised.

To investigate this claim, all data taken at constant temperature (Section 6.2) used the same method. Measurements were first taken at SVP and then the pressure was increased in steps to a maximum pressure. This is indicated by the blue diamonds in all Figures in section 6.2.6 and on Fig 7.1, 7.2 and 7.3. The pressure was then reduced via the same pressure steps until it was once again at SVP, represented by the red squares.

It is clear from our data presented in Section 6.2.6, that there is no evidence of any hysteretic behaviour for any constant temperature between 1.7 K and 4.2 K. Given the difference between our data and the results from IUCF group (Huffer, 2008), we now re-examine their work in the light of our own findings.

The initial data presented by Huffer, Fig. 7.6, showed no sign of any hysteresis and only later in his report did he report hysteretic behaviour. Figure 7.7 shows this later data

which indicates that on pressurisation there is a sudden increase in breakdown voltage. These voltage values are all very similar although the pressure is stated as being different.

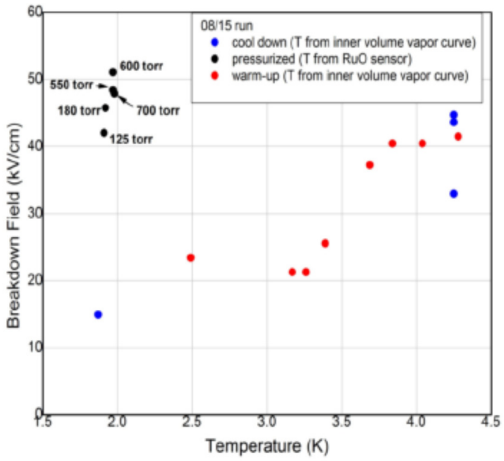

Fig..7.6. Breakdown field measurements as a function of temperature and pressure in liquid ^{4}He. Blue symbols: cooling under SVP; Black symbols: increasing pressure at T >2.17K; Red symbols: warming under SVP. (Huffer, 2008)

Huffer states there is a pressure gauge at the top of their pressurization line but does not make any mention of a second, static line. It is assumed, therefore, that the pressures quoted are from the pressuring fill line. Hence, during any pressurisation process there will be a flow of helium and the pressure in the PC will not be known.

The same effect was observed in the data taken for this thesis. For example, in PC Run 6 the gas pressure at the top of the Helium fill line was initially set to 1200 torr but the pressure recorded at the top of the static line was 250 torr for a considerable period of time while the PC filled and only a small increase in V_{bd} was observed. Once the cell was full there was a sharp rise in pressure and a corresponding increase in V_{bd}.

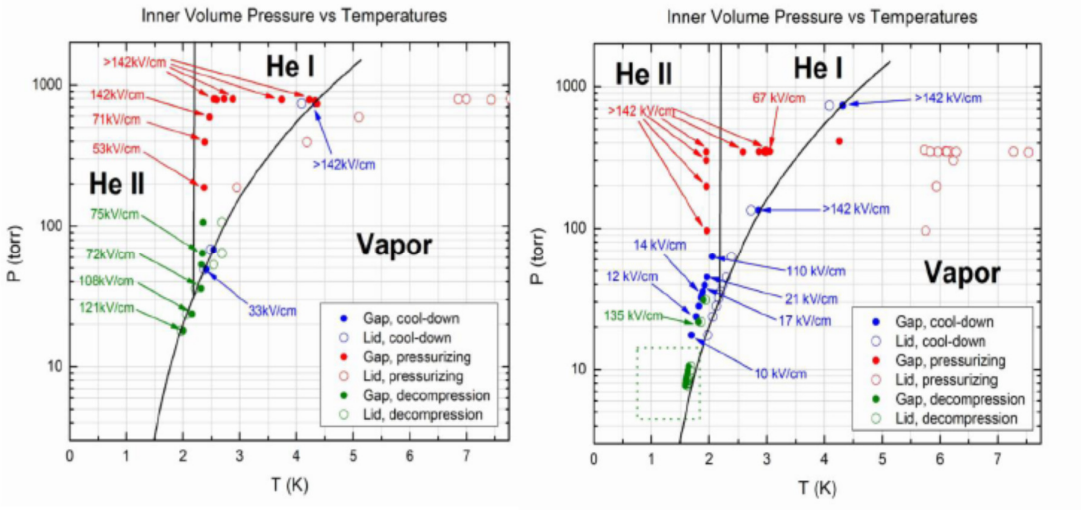

Fig..7.7. Second breakdown field measurements as a function of temperature and pressure in liquid ^{4}He. Blue symbols: cooling under SVP; Red symbols: increasing pressure at T < 2.17K; Green symbols: after depressurisation. (Huffer, 2008)

Huffer's data in Fig. 7.7 shows that once pressurized the electrodes held their voltage and generally did not breakdown. In both data sets in Fig. 7.7 we see that during the cool down the temperature of the electrodes and that of the top of the PC followed each other and were approximately the same. However, these temperatures differed when pressure was applied. We argue that this was due to warm gas filling the pressure cell and causing it to heat up. When the helium gas was shut off the temperatures in the pressure cell again were approximately the same.

A possible reason why the hysteric behaviour was not observed in the initial IUCF run is that only a few measurements made. The data is not plotted against time however, if more data points were taken one could make the assumption that the pressure cell was being pressurized, and therefore filling with helium, for longer. Therefore, when the helium gas was shut off from the pressure cell if it were already full it would have remained at the same pressure and would not have depressurized. This would have given the impression that V_{bd}

remained high with reduced pressure whereas the pressure in the cell would not have decreased.

If indeed the pressure cell was already full and the pressure above the liquid was stable at that of the regulator valve value, then the system would already have been in stable equilibrium. Hence, this is a plausible explanation for the difference in the observation of hysteresis reported by the IUCF group and the lack of any such effect in our data.

7.1.5. Analysis of data from PC Runs 8 and 9 (4.2 K to 2.65 K)

Having ruled out any possible hysteresis, it is now possible to combine all data taken at the same pressure during a run to find an average breakdown voltage. The data from PC runs 8 and 9 is considered. These runs were chosen as they provide a large amount of pressure dependent breakdown data at a number of different fixed temperatures. Also, as these PC runs were taken consecutively the analysis is slightly easier as there is little effect in the degradation of the breakdown voltage with increasing run number (see section 7.1.3). The arithmetic mean breakdown voltage for PC Runs 8 and 9 is shown on Fig.7.8.

At a pressure of 1200 torr, Vmax is ~ 50 kV for all temperatures, there is no evidence of any temperature dependence. Indeed, all measurements taken at the relatively high pressures in Region 1 seem be approximately the same, independent of their temperature.

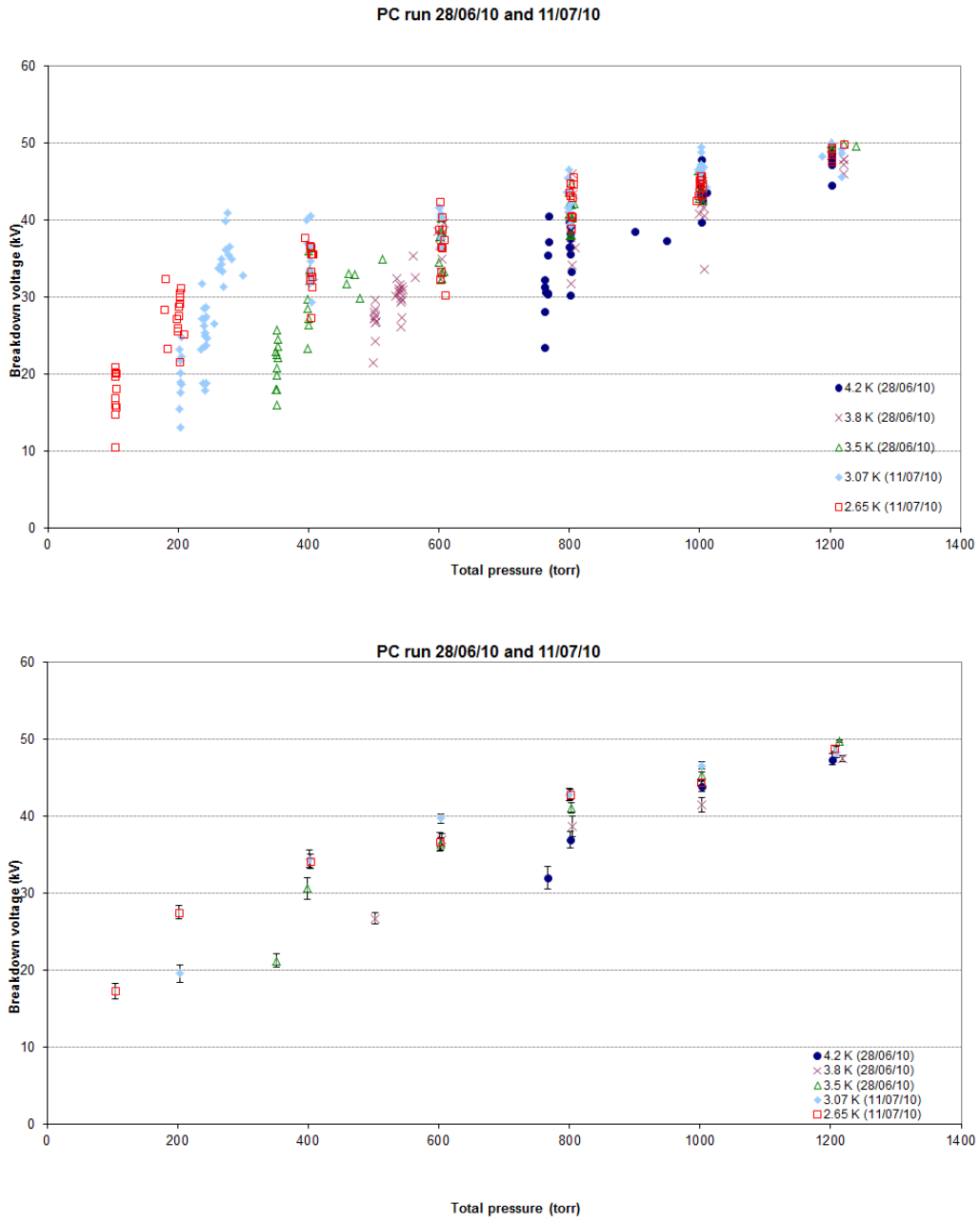

Fig..7.8. Breakdown voltage as a function of pressure. Top : Raw data from PC runs 8 and 9; Bottom: mean valves from PC runs 8 and 9. Blue circles: V_{bd} at 4.2 K; Purple crosses: V_{bd} at 3.8 K; Green triangles: V_{bd} at 3.5 K; Light blue dimonds: V_{bd} at 3.07 K; Red square: V_{bd} at 2.65 K. The standard error on the mean breakdown voltage is indicated on the bottom plot.

7.1.6. $V_{bd}(P)$ in Region 1 from PC Runs 8 & 9 (4.2 K to 2.65 K)

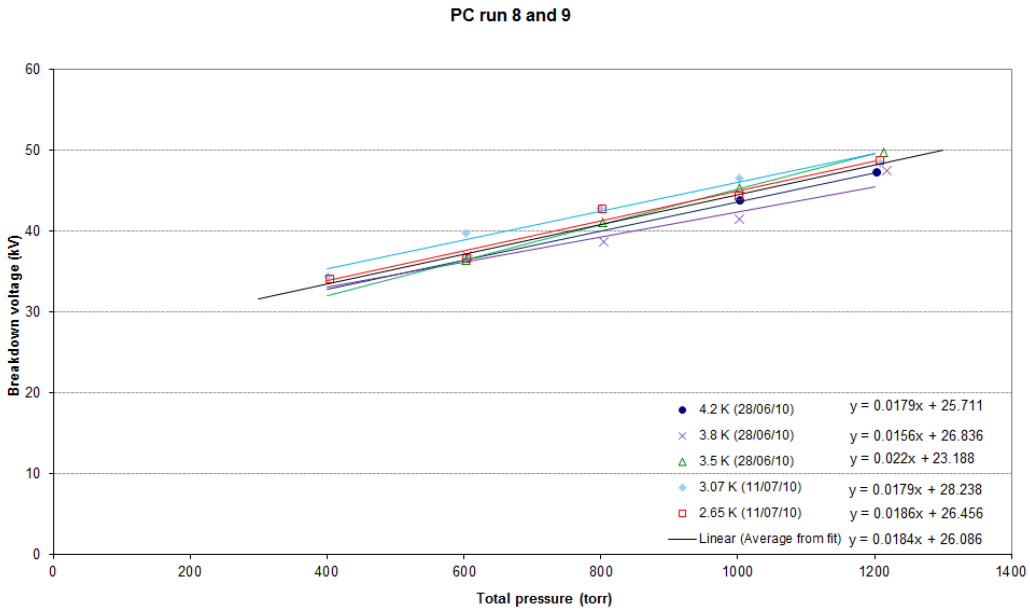

Fig..7.9. Linear regression fits of the breakdown voltage as a function of pressure for Region 1 for PC Runs 8 and 9. Blue circles: V_{bd} at 4.2 K, blue trend line; Purple crosses: V_{bd} at 3.8 K, purple trend line; Green triangles: V_{bd} at 3.5 K, green trend line; Light blue dimonds: V_{bd} at 3.07 K, light blue trend line; Red square: V_{bd} at 2.65 K, red trend line; Black trend line: Average of the linear regression fits of all the temperatures. The equation of each regression line is shown on the right hand side of the legend.

Figure 7.9 shows the data from PC Runs 8 and 9 from Region 1. The data set at each temperature was fit with a linear regression and gave gradients and intercepts which were approximately the same independent of temperature (table.7.2). We infer that $V_{bd}(P)$ in Region 1 is the same for each temperature between 2.65 K and 4.2 K and thus we combine the data to find a common gradient and intercept. This is shown as a black trend line on Fig.7.9 and has a gradient of 0.0184 ± 0.0014 kV/torr and an average intercept of 26.1 ± 1.4 kV.

Temperature (K)	4.2	3.8	3.5	3.07	2.65	Average
Gradient (kV/torr)	0.0179	0.0156	0.0220	0.0179	0.0186	0.0184
Gradient St error (kV/torr)	0.0060	0.0026	0.0016	0.0014	0.0015	0.0014
Intercept (kV)	25.7	26.8	23.2	28.2	26.5	26.1
Intercept St error (kV)	6.5	2.3	1.4	1.1	1.2	1.4

Table..7.2. Linear regression analysis of region 1 for temperatures between 2.65 K and 4.2 K. The gradient and intercept of the region 1 average are also tabulated along with its standard errors.

7.1.7. $V_{bd}(P)$ at Constant Temperature in He II and Normalisation

All measurements in He II (1.7 K to 2.1 K) taken during PC Runs 6, 7, 10 and 11 are shown on Fig.7.10. This data, like that above the λ-point, has two regimes. PC Runs 6 and 7 were carried out earlier than PC Runs 10 and 11 and there is a noticeable reduction in breakdown voltage for the latter (see section 7.1.3).

The data from PC Runs 7 and 11 have been use to fit data lines to both Regions 1 and 2. During PC Run 7 there were occasions when the voltage held for some time before breakdown or it did not breakdown at all. This occurred at pressures ≥ 600 torr (shaded area Fig.7.10). These points represent a different behaviour and hence have not been included in the linear regression fit. The gradients and intercepts of the linear regression along with their standard errors of these fits are shown on table.7.3.

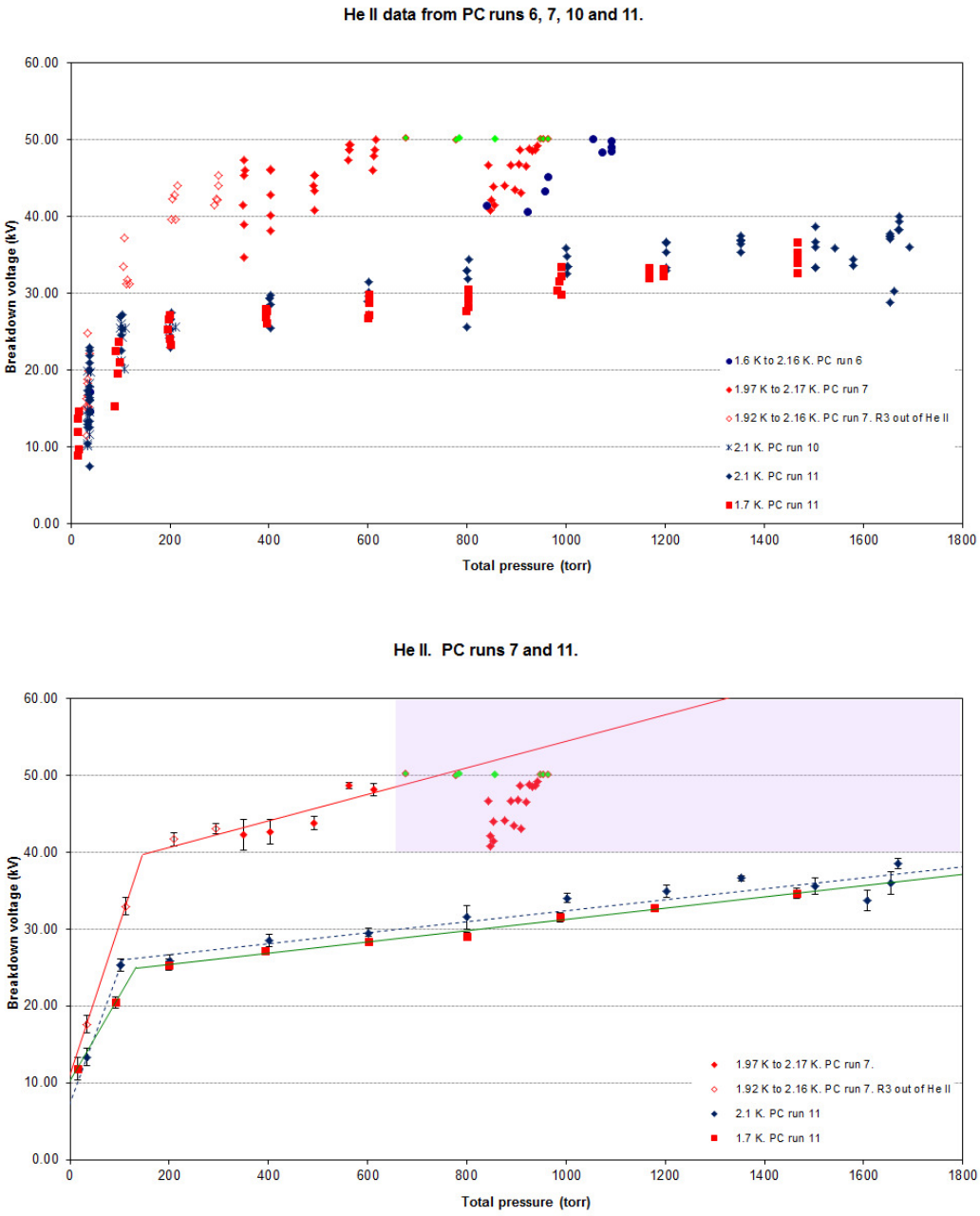

Fig..7.10. Breakdown voltage as a function of pressure in He II. PC runs 6, 7, 10 and 11. Top: raw data; Bottom: Mean V_{bd} at each pressure. Linear regression fits for Region 1 and Region 2. Blue circles: V_{bd} (1.6 K to 2.1 K, PC run 6); Red diamonds: V_{bd} (1.97 K to 2.17 K PC run 7); Red diamonds with a green centre: V_{hbd} (1.97 K to 2.17 K PC run 7); Green diamonds: V_h (1.97 K to 2.17 K PC run 7); Red diamonds with no colour in the centre: V_{bd} (1.92 K to 2.16 K, PC run 7, (main bath level sensor R3 was not in He II); Blue stars: V_{bd} (2.1 K, PC run 10); Blue diamonds: V_{bd} (2.1 K, PC run 11); Red squares: V_{bd} (1.7 K, PC run 11). The standard error on the mean breakdown voltage is shown on the bottom plot.

PC run	7	7	11	11	11	11
Temperature (K)	1.92 to 2.16	1.92 to 2.16	1.7	1.7	2.1	2.1
Region	1	2	1	2	1	2
Gradient (kV/torr)	0.0173	0.195	0.00835	0.113	0.00815	0.140
gradient St error (kV/torr)	0.0037	0.023	0.00047	0.022	0.00072	0.029
Intercept (kV)	37.1	11.1	23.36	10.1	24.87	11.1
Intercept St error (kV)	1.6	1.6	0.47	1.4	0.71	1.6

Table..7.3. Linear regression analysis of Region 1 and 2 for PC runs 7 and 11 for He II in a temperature range between 1.7 K and 2.1 K.

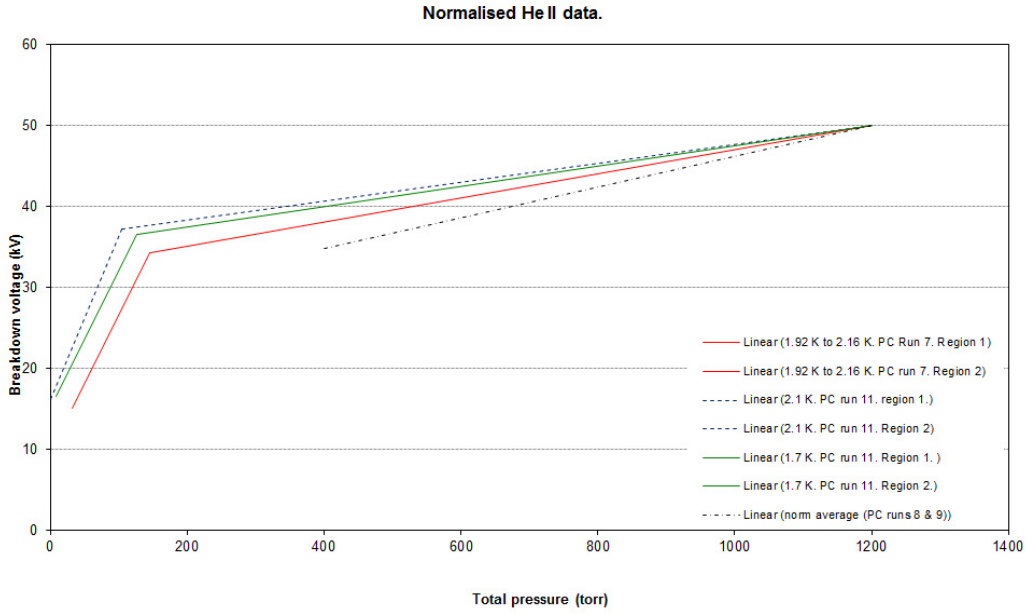

Fig..7.11. Normalised linear regression fits for PC Run 7 and 11. Also plotted is the normalised Region 1 average from PC Runs 8 and 9. All data is normalised to 50 kV at 1200. Red line: 1.92 K to 2.16 K, normalised linear regression, PC Run 7; Blue dashed line: 2.1 K, normalised linear regression, PC Run 11; Green line: 1.7 K, normalised linear regression, PC Run 11; Black dashed line: Normalised region 1 average for PC Runs 8 and 9.

In order to compare the data from PC Run 7 and 11, the Region 1 linear fits were normalised to pass through 50 kV at 1200 torr. For each PC run the Region 2 fits were

normalised by the same factor. This data along with the normalised average Region 1 trend line for PC Runs 8 and 9 are shown on figure.7.11.

The normalised Region 1 trend lines for PC Runs 7 and 11 seem to be approximately the same and are also consistent with the normalised average Region 1 fit from PC Runs 8 and 9.

In conclusion it is assumed that all Region 1 $V_{bd}(P)$ trend lines are the same for any temperature between 1.7 K and 4.2 K after normalisation.

PC run	7	7	11	11	11	11	Average 8 and 9
Temperature (K)	1.92 to 2.16	1.92 to 2.16	1.7	1.7	2.1	2.1	2.65 to 4.2
Region	1	2	1	2	1	2	1
Gradient (kV/torr)	0.0150	0.169	0.01251	0.169	0.0118	0.202	0.0190
gradient St error (kV/torr)	0.0032	0.020	0.00070	0.032	0.0010	0.041	0.0015
Intercept (kV)	32.0	9.6	34.99	15.2	35.9	16.0	27.0
Intercept St error (kV)	1.4	1.4	0.70	2.2	1.0	2.3	1.5

Table.. 7.4. Normalised linear regression analysis of Regions 1 and 2 for PC Runs 7 and 11 for He II in a temperature range between 1.7 K and 2.1 K. Normalised to 50 kV at 1200 torr. Also tabulated is the normalised linear fit of Region 1 average of PC Runs 8 and 9.

7.1.8. Normalisation and Offsetting of all $V_{bd}(P)$ data for Region 1

All data taken at constant temperature between 1.7 K and 4.2 K have been normalised to or offset to 50 kV at 1200 torr, see Fig. 7.12, to find an average $V_{bd}(P)$ line in Region 1 in each case. The normalised data is combined to produce an average Region 1 gradient of 0.01693 ± 0.00092 kV/torr and an average Region 1 intercept of 29.69 ± 0.88 kV. The average gradient for Region 1 from the offset data is 0.01563 ± 0.00090 kV/torr with an

average intercept of 31.24 ± 0.82 kV. Hence, within 1 error bar normalizing and offsetting the data produce the same Region 1 gradient and intercept.

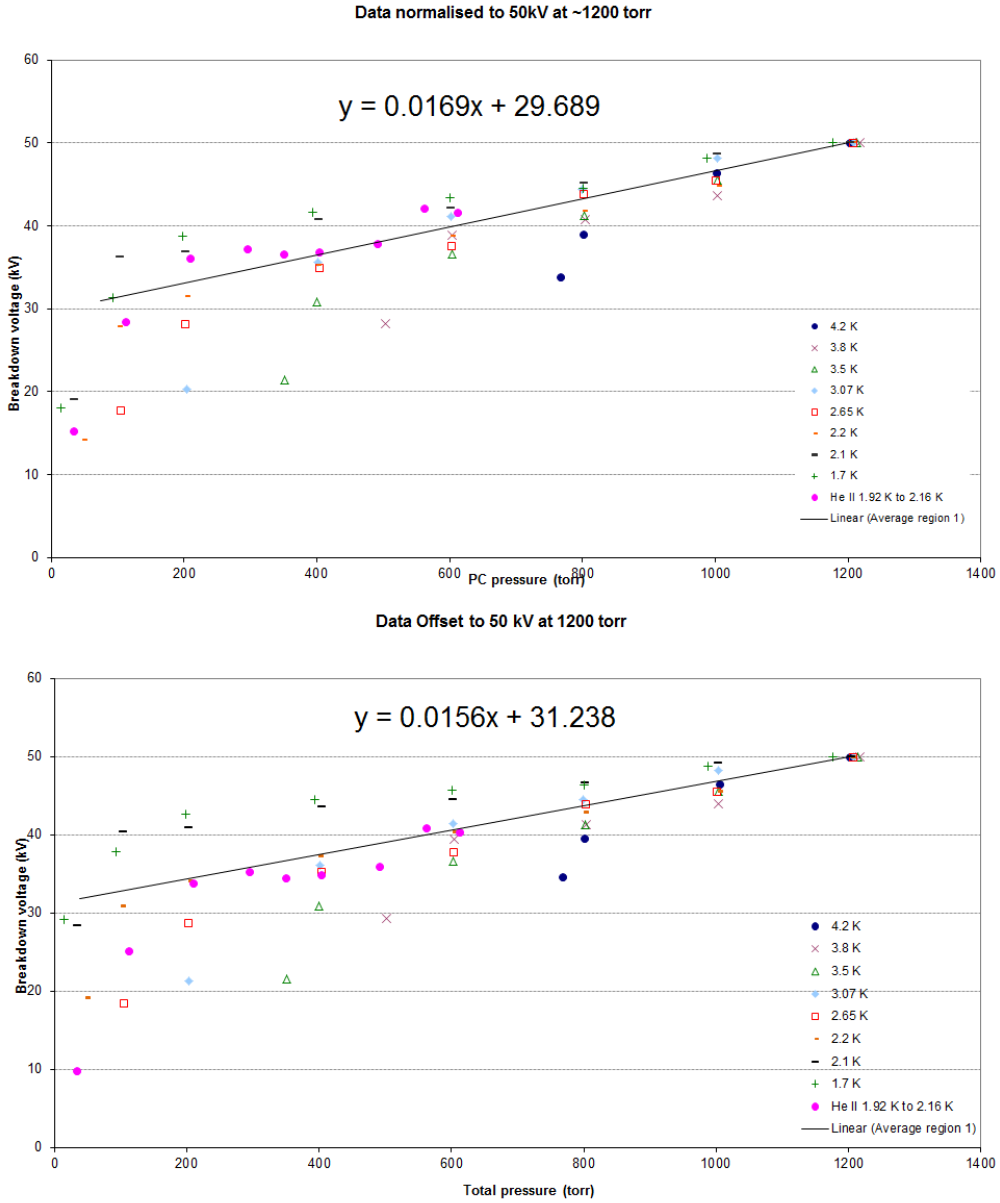

Fig..7.12. Top: Mean normalised breakdown voltage as a function of pressure; Bottom: Mean offset breakdown voltage as a function of pressure for temperatures between 1.7 K and 4.2 K. Blue circles: V_{bd} at 4.2 K; Purple crosses: V_{bd} at 3.8 K; Green triangles: V_{bd} at 3.5 K; Light blue diamonds: V_{bd} at 3.07 K; Red square: V_{bd} at 2.65 K; Orange dashes: V_{bd} at 2.2 K; Black dashes: V_{bd} at 2.1 K; Green t-crosses: V_{bd} at 1.7 K; Pink circles: V_{bd} at 1.92 K to 2.16 K; Black line: Average Region 1.

7.1.9. V_{bd}(P) in Region 2

When the pressure is increased above SVP a sharp rise in V_{bd} is observed. This behaviour is referred to as Region 2. To investigate the characteristics of this behaviour region 2 between 1.7 K and 4.2 K all constant temperature data has been normalised by the same factor as that in Section 7.1.8 (i.e. 50 kV at 1200 torr), and is shown in Fig. 7.13. A linear regression has been fitted to each set of data at constant temperature. The regression line has been extended to clearly show Region 2.

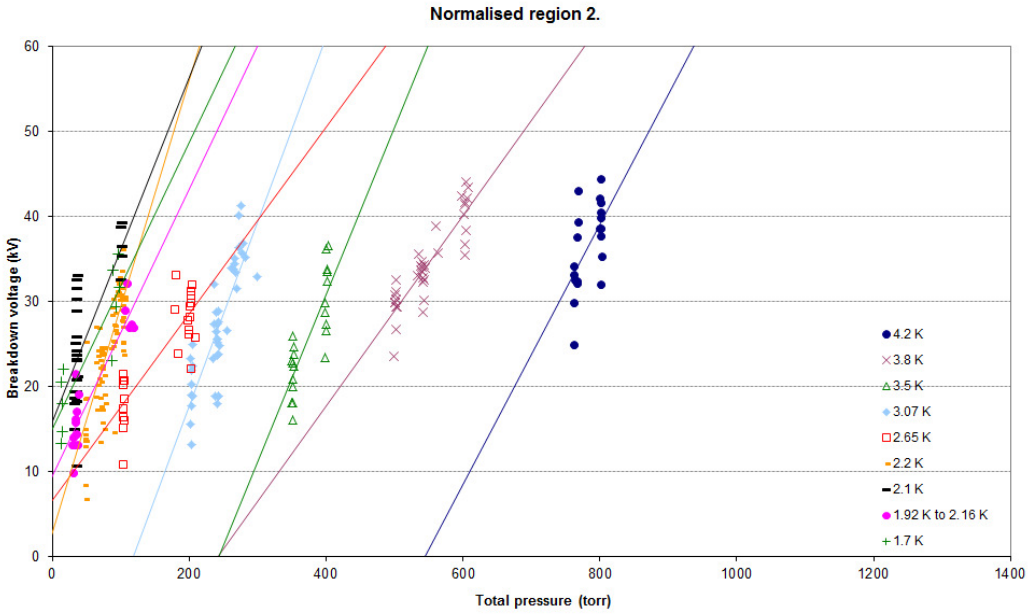

Fig..7.13. Breakdown voltage as a function of pressure. Normalised Region 2 for temperatures between 1.7 K and 4.2 K. Blue circles: V_{bd} at 4.2 K; Purple crosses: V_{bd} at 3.8 K; Green triangles: V_{bd} at 3.5 K; Light blue diamonds: V_{bd} at 3.07 K; Red square: V_{bd} at 2.65 K; Orange dashes: V_{bd} at 2.2 K; Black dashes: V_{bd} at 2.1 K; Green t-crosses: V_{bd} at 1.7 K; Pink circles: V_{bd} at 1.92 K to 2.16 K. A linear regression has been fitted to each data set.

Measurements were initially taken in fixed step pressure intervals. However, in some cases, 3.8 K (purple crosses), 3.07 K (blue diamonds), 2.2 K (orange dashes) and 2.1 K

(Black dashes), many measurements were also made between these pressure intervals. In all cases, Region 2 could be satisfied by a linear relationship, Table.1.5. The average gradient of Region 2 over all temperatures is 0.176 ± 0.0096 kV/torr.

Temperature (K)	4.2	3.8	3.5	3.07	2.65	2.2	2.1	1.92 to 2.16	1.7	Average
Gradient (kV/torr)	0.153	0.112	0.196	0.217	0.110	0.266	0.202	0.169	0.169	0.1762
Gradient St error (kV/torr)	0.052	0.010	0.032	0.024	0.015	0.022	0.041	0.020	0.032	0.0096
Intercept (kV)	-83	-27.0	-48	-25.6	6.6	2.9	16.0	9.6	15.2	
Intercept St error (kV)	41	5.6	12	5.9	2.4	1.8	2.3	1.4	2.2	

Table..7.5. Normalised linear regression analysis of Region 2 for temperatures between 1.7 K and 4.2 K. Also tabulated is the average Region 2 gradient.

7.1.10. Combining Regions 1 and 2

To show an overall account of HV breakdown in ^{4}He between the temperatures of 1.7 K and 4.2 K as a function of pressure, all the normalised data has been plotted on Fig. 7.14. This shows the sharp increase in breakdown voltage with pressure above SVP, in Region 2, combining with the average normalised Region 1 slope. The point the breakdown regime changes from Region 1 to Region 2 we have termed the kink pressure (P_k). The normalised data has been chosen over the offset data as it more closely resembles data taken as a function of SVP (Karamath 2007, Long et al 2006).

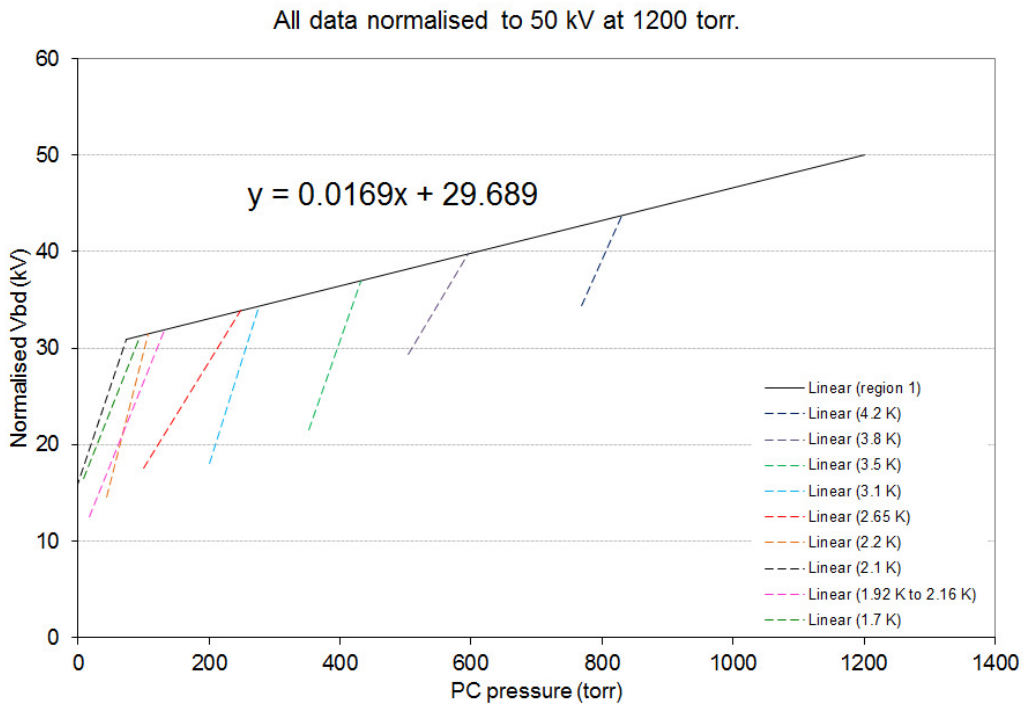

Fig..7.14. Normalised breakdown voltage as a function of pressure. Average Region 1 and individual region 2 data for temperatures over the range 1.7 K and 4.2 K. Black line: Average Region 1; Blue line: 4.2 K; Purple line: 3.8 K; Green line: 3.5 K; Light blue lines: 3.07 K; Red line: 2.65 K; Orange line: 2.2 K; Black line: 2.1 K; Pink line: 2.0 K; Dark green lines: 1.7 K.

7.1.11. $P_k(T)$

Table 7.6 gives the two sets of values of $P_k(T)$ derived from normalising and from offsetting the data, as described in the previous section. Also shown are the two values of $V_{bd}(P_k)$ at each temperature. Again, the values obtained by normalising or offsetting are approximately the same.

To check for any obvious correlations, the two sets of $P_k(T)$ values were plotted against temperature, ^{4}He density and SVP, as shown in Figs. 7.15, 7.16 and 7.17 respectively.

$P_k(T)$ is clearly non-linear but interestingly it's decrease with decreasing temperature mirrors closely the increase in ^{4}He density (Donnelly and Barenghi 1998). The linear

behaviour of $P_k(\rho)$ shown in Fig. 7.16 yields gradients and intercepts of -34.4 ± 1.4 kg $m^{-3}torr^{-1}$ and -35.4 ± 2.1 kg $m^{-3}torr^{-1}$ and 5130 ± 200 kg m^{-3} and 5266 ± 300 kg m^{-3} for the normalised and offset data, respectively.

Temperature (K)	**Norm P_k pressure(torr)**	**Norm P_k voltage(kV)**	**Offset P_k pressure(torr)**	**Offset P_k voltage(kV)**
4.2	830	44	830	44
3.8	596	40	595	41
3.5	431	37	436	38
3.07	277	34	282	36
2.65	248	34	257	35
2.2	108	32	100	33
2.1	74	31	39	32
1.7	96	31	46	32
1.92 to 2.16	132	32	156	34

Table..7.6. $P_k(T)$ and $V_{bd}(P_k)$ values for all normalisation and offset data for temperatures from 1.7 K to 4.2 K.

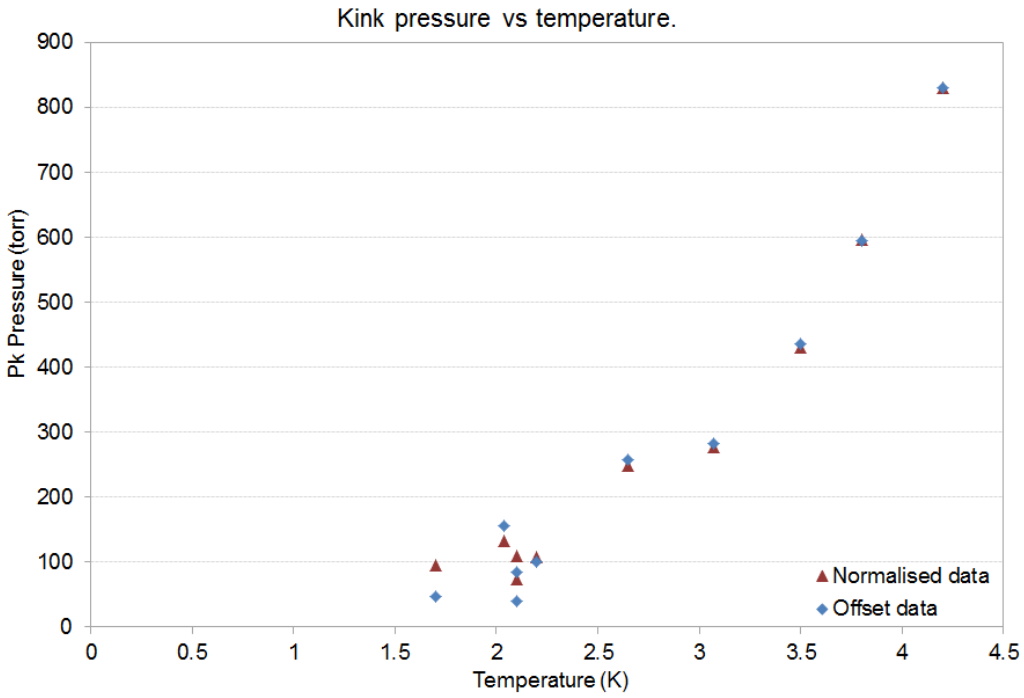

Fig..7.15. Temperature dependence of P_k.

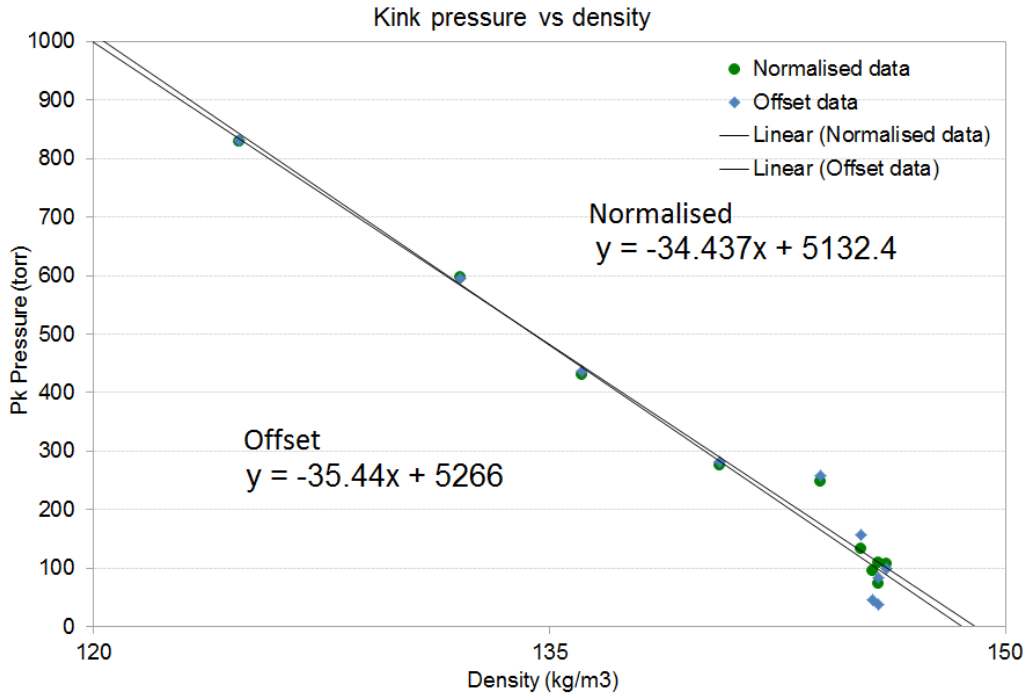

Fig..7.16 P_k as a function of ^{4}He density.

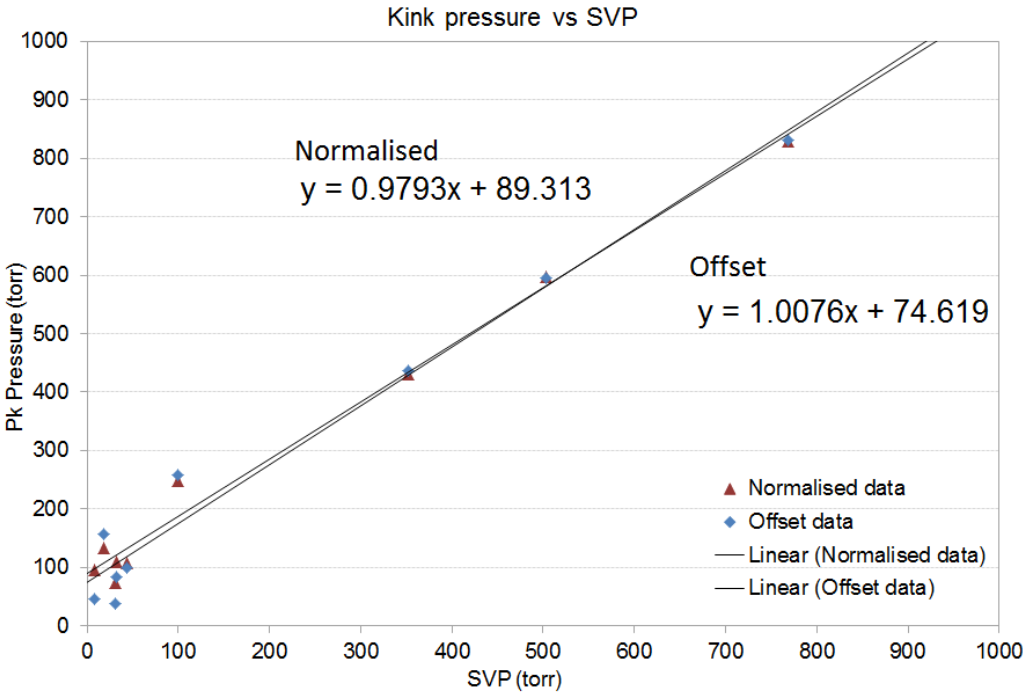

Fig..7.17. P_k as a function of ^{4}He SVP.

A linear dependence is also observed between P_k and the ^{4}He SVP. The normalisation and offset data are the same within one error bar with gradients close to unity. The normalisation data gives a gradient 0.97 ± 0.04 torr^2 with an intercept of 88 ± 13 torr and the offset data a gradient of 1.008 ± 0.061 torr^2 and an intercept of 75 ± 20 torr.

7.1.12. $V_{bd}(P)$ compared with previous ^{4}He data

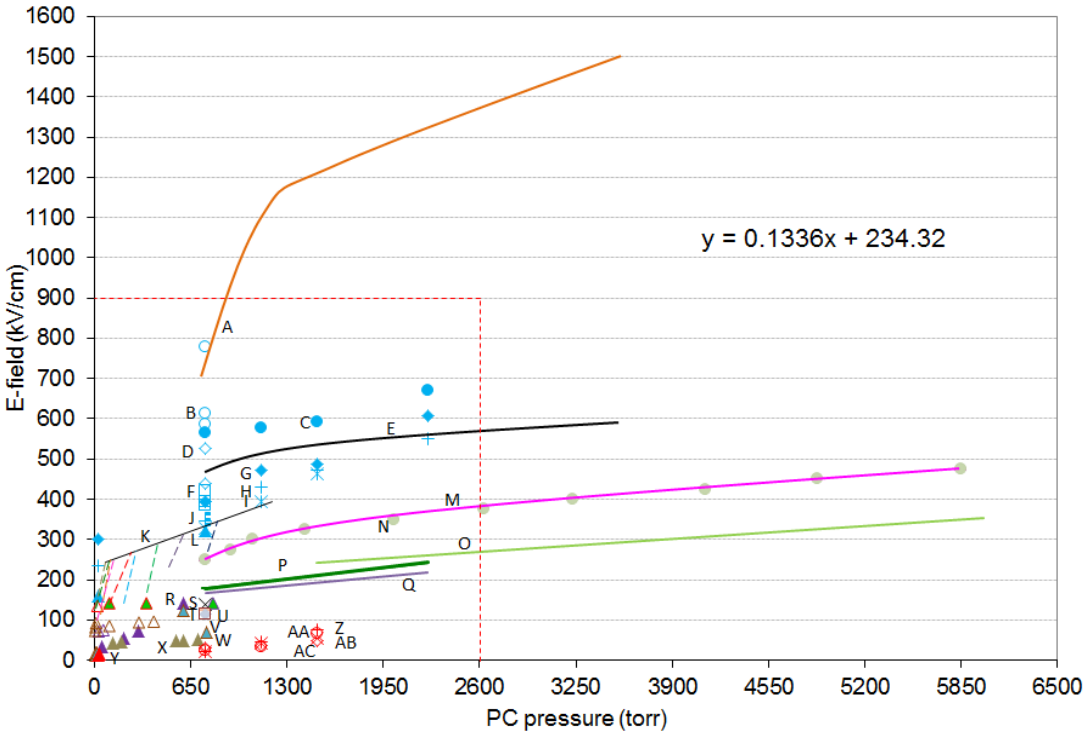

Fig..7.18. Breakdown E-field as a function of pressure for AJD data and previous data. Labels A to AC are explained on Table 7.1.6. The red dashed line indicates the region of data displayed on figure.7.19.

All relevant previous breakdown data in ^{4}He is plotted as a function of pressure along with the data presented in this thesis in Figs.7.18, 7.19 and 7.20. The same data has also been summarised in Table.7.7 and is ordered by breakdown field, E_{bd}, at 760 torr, with data set A being the highest.

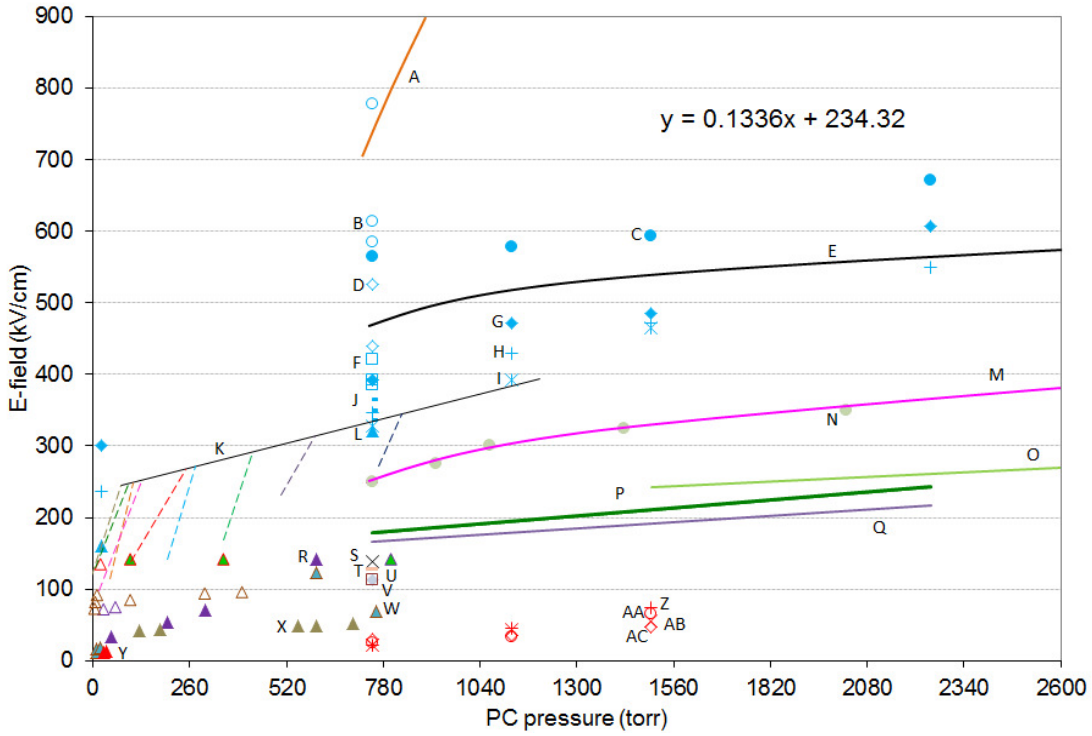

Fig..7.19. Breakdown E-field as a function of pressure for AJD data and previous data. Labels A to AC is explained on Table 7.7.

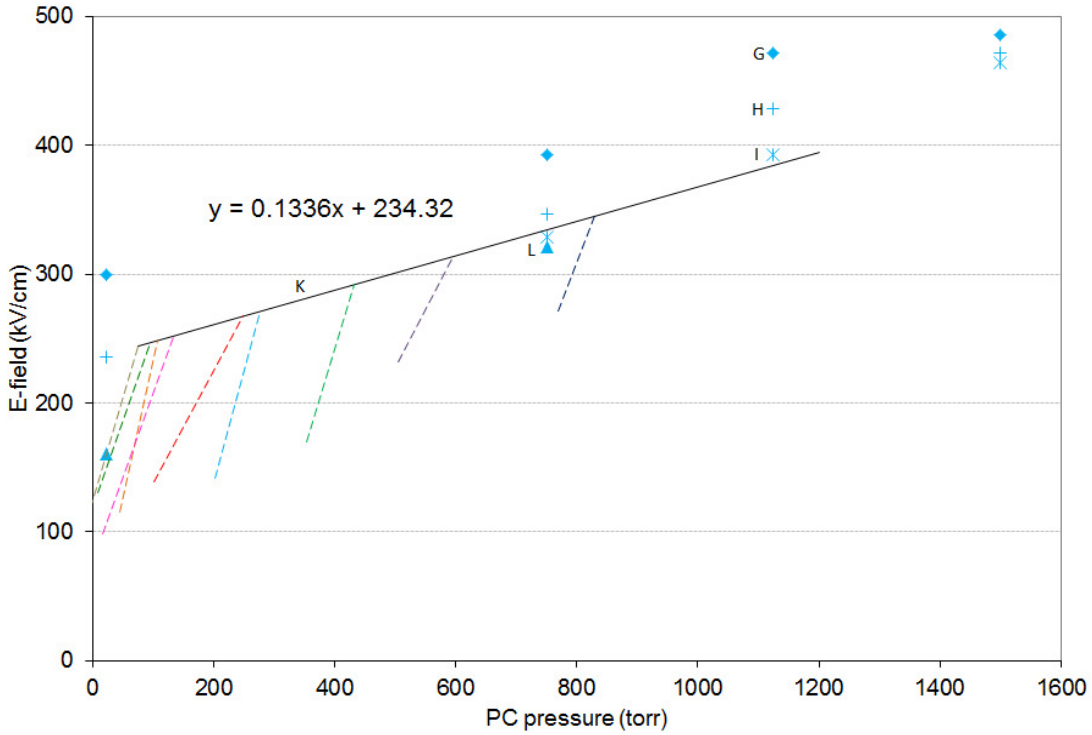

Fig..7.20. Breakdown E-field as a function of pressure for AJD data and previous data. Labels A to L is explained on Table 7.1.6.

Data Set	Symbol	Separation (mm)	Temperature (K)	Electrode Profile	Comments	reference
A	(line)	0.1	4.2	Plane/Sphere	6 µs Pulsed.	Yoshino (1982)
B		0.2	2.1 to 3.8	Sphere/Sphere	25 mm Ø dc	Hara (1993)
C		0.2	1.95	Sphere/Sphere	25 mm Ø dc	Hara (1993)
D		0.5	2.1 to 3.8	Sphere/Sphere	25 mm Ø dc	Hara (1993)
E	(line)	0.5	4.2	Sphere/Sphere	50 mm Ø dc	Gerhold (1989)
F		1	2.9 to 4.2	Sphere/Sphere	25 mm Ø dc	Hara (1993)
G		.5	1.95	Sphere/Sphere	25 mm Ø dc	Hara (1993)
H		1	1.95	Sphere/Sphere	25 mm Ø dc	Hara (1993)
I		1.5	1.95	Sphere/Sphere	25 mm Ø dc	Hara (1993)
J		1.5	2.1 to 4.2	Sphere/Sphere	25 mm Ø dc	Hara (1993)
K	Various	1.27	1.7 to 4.2	Plane/Plane	32.05 mm dc	AJD (2010)
L		2	1.95	Sphere/Sphere	25 mm Ø dc	Hara (1993)
M	(line)	1	4.2	Plane/Plane	60 mm Ø dc	Meats (1972)
N		1	4.2	Plane/Plane	60 mm Ø dc	Meats (1972)
O	(line)	1.7	4.2	Plane/Sphere	15 mm Ø ac	Fallou (1970)
P	(line)	1	4.2	Sphere/Sphere	62.5 mm Ø	Burnier (1970)
Q	(line)	2	4.2	Sphere/Sphere	62.5 mm Ø	Burnier (1970)
R		Not stated	2.3	Not stated		Huffer (2008)
S		0.254	2 to 4.2	Plane/Plane	62.6 mm Ø dc	Wu (1996)
T		0.508	2 to 4.2	Plane/Plane	62.6 mm Ø dc	Wu (1996)
U		1.016	2 to 4.2	Plane/Plane	62.6 mm Ø dc	Wu (1996)
V		1.27	2 to 4.2	Plane/Plane	62.6 mm Ø dc	Wu (1996)
W		Not stated	1.8 to 2.1	Not stated		Huffer (2008)
X		Not stated	2	Not stated		Huffer (2008)
Y		Not stated	1.8	Not stated		Huffer (2008)
Z		5	4.2	Uniform field	Electrode/ Superconducting Wire coil. dc	Chigusa (1999)
AA		3	4.2	Uniform field	Electrode/ Superconducting Wire coil. dc	Chigusa (1999)
AB		7	4.2	Uniform field	Electrode/ Superconducting Wire coil. dc	Chigusa (1999)
AC		9	4.2	Uniform field	Electrode/ Superconducting Wire coil. dc	Chigusa (1999)

Table.7.7. Description of data points A to AC on the breakdown E-field as a function of pressure for AJD data and previous data.

From these plots it is clear that the data presented in this thesis fits into the general trend. Our constant dE_{bd}/dP for Region 1 is in good agreement with other data sets (Hara et al 1993) at comparable separations and increased pressure.

What is clear from the spread of the data is that there is a large volume effect. In general E_{bd} is reduced with increased separation.

The data taken at 4.2 K by Meats (1972), Gerhold (1989) and Yoshino (1982) indicate a departure from Region 1 behaviour close to SVP. However, the only data showing a clear Region 2 dependence, apart from ours, is a single point taken by Hara (1993) at a temperature of 1.95 K with a 2 mm electrode separation. All other data indicates Region 1 behaviour right down to SVP with no apparent change in regime. However, the data taken for this thesis has investigated pressure dependence very near to SVP at constant temperatures between 1.7 K and 4.2 K and shows unambiguously the Region 2 behaviour and the transition to Region 1 at P_k.

Yoshino's (1982) data (A) seems to depart from the general trend. However, this data was taken at 0.1 mm separation and the voltage is pulsed in 6 μs bursts. Measurements by Chigusa (1999) (Z, AA, AB and AC) were made between a plane electrode and a superconducting wire coil wound to have a flat surface. The macroscopic E-field is uniform in the gap. This data was also taken at the largest separations and displayed some of the lowest E_{bd} fields.

7.1.13. A possible model to explain the ^{4}He $V_{bd}(P,T)$ data

The most striking characteristic of the data presented here is the sharp decrease in slope of the $V_{bd}(P)$ characteristic at P_k. There are some hints of this "two-regime" behaviour in some of the other data in ^{4}He, notably in that of Hara (1993), but our data is much more comprehensive. The only other data which appears to clearly show this two-regime behaviour is from transformer oil at room temperature (Cevallos et al 2005a, Fig.4.24 in Section 4.2.6) and from liquid hydrogen (Gerhold, 1979, Fig.4.27. in Section 4.2.6). Cevallos et al's data shows a clear change in slope whereas Gerhold shows only a smooth

trend line but no data points. In both of these cases, the data was taken at only one temperature which thus yielded a single P_k.

The other striking feature of our data is that P_k is always approximately 90 torr above SVP for all temperatures. In addition, it is important to note that for two temperatures $T_1 < T_2$,we find

$$P_k(T_1) < SVP\ (T_2)$$

but that

$$V_{bd}[P_k(T_1)] > V_{bd}[SVP(T_2)]$$

It thus appears that the value of ~ 90 torr is not an absolute pressure which could be related to the onset of some process.

We first recall from the review in Chapter 4 that breakdown in all dielectric liquids seems to follow a very general sequence, independent of the particular geometry used. Following Denat (2011), the possible stages are:

Initiation → Neutral (seed) bubble → Ionised bubble → Streamer → Full bkdwn

The initiation stage has to involve a mechanism to inject heat locally into the liquid. Depending on the geometry and polarity this may involve field emission of electrons, field ionisation or heating by the impact of microscopic particles. A number of authors have calculated the heat input or temperature rise from these various mechanisms (Halpern & Gomer 1969a, McClintock 1971, Zimmerman et al 1976). In each case, they find the heat input to be proportional to the applied field (voltage).

For the highly non-uniform field in point-plane geometry, stable bubbles can be observed around the tip without full breakdown. The optical emission spectra from such bubbles indicate clearly that they contain ionised gas (Li et al, 2009). In contrast, in plane-plane geometries stable bubbles do not generally occur at the initiation point and the sequence from initiation to full breakdown proceeds rapidly.

As discussed in Section 4.3.1, the electrostrictive effect will tend to elongate a bubble in the direction of the field. This is much more pronounced for conducting (ionised) bubble, see Fig.28. In addition, in plane-plane geometry, this elongation will persist in the (uniform) field in the cell whereas it will be restricted to the tip region in a point-plane geometry.

Our general picture for the two regime behaviour in our plane-plane geometry experiments is that above P_k, the dominant effect is field elongation of the bubbles, whereas this effect is negligible below this pressure.

In Region 2, well below P_k the total pressure in the liquid is very close to SVP. Local injection of heat leads to a region of the liquid being superheated and the potential to create a seed bubble. This seed bubble will either grow or collapse, depending on the heat input, the applied pressure and the effect of the E-field in either elongating or causing charge multiplication and further heating. At fixed temperature and pressure, increasing the field increases the heat input to the seed bubble in a linear fashion and hence eventually a field is reached where the transition to full breakdown occurs. Increasing the pressure in this regime means that a higher heat input (and hence voltage) is needed to reach the critical bubble size. Under these conditions, relatively close to the SVP, the bubble might be expected to grow in a chaotic fashion and it is exactly the behaviour observed by Cevallos et al (2005a) shown in Fig.4.33 in Section 4.3.4. At first sight, the strong and roughly linear increase in breakdown voltage with pressure might be expected to continue indefinitely.

We propose that the switch to Regime 1 behaviour, where $\frac{dV_{bd}}{dP}$ falls dramatically, is due to the rapid increase in the elongation of a conducting pre-breakdown bubble by the electrostrictive effect. As Fig.4.28 in Section 4.3.1 demonstrates, this elongation shows critical behaviour essentially above a threshold field when the permittivity of the gas in the bubble becomes large. The Regime 2 behaviour continues only as long as the (uniform) field in the cell is below this critical value. Once the threshold E-field (voltage) has been reached, further increase in applied pressure results in only a small increase in V_{bd}.

Although this model is simplistic, and the lack of much of the necessary data means that any numerical calculation would be hazardous, it offers a mechanism to explain both the behaviour reported here and that of Cevallos et al and Gerhold referred to above.

Unfortunately, this model does not offer an answer to the question of why P_k seems always to occur at SVP + ~90 torr. As noted above, since it is not an absolute pressure, it is unlikely that it is associated with any fundamental process. We are thus left with the idea that this value is dependent on the particular experiment, with some of the potentially important parameters being cell geometry, ^{4}He purity and surface roughness.

For completeness, it is worth noting that the reason for our ability to study $P_k(P)$ over such a wide range is due to the ease with which the SVP of ^{4}He can be varied whilst it remains liquid, certainly when compared to other cryogenic liquids, all of which solidify at relatively high SVP. It is possible that heating an oil to well above room temperature to vary its SVP would lead to similar behaviour to ours being found but this experiment does not appear to have been attempted.

The results of a very preliminary attempt to model the combination of a roughly linear dependence of V_{bd} on pressure close to SVP, followed by an electrostrictive effect dominating at higher pressures is shown in Fig. 7.21. By reproducing Garton and Krasucki (1964) calculations, as shown in Fig. 4.28, the value of the E-field to produce a given bubble

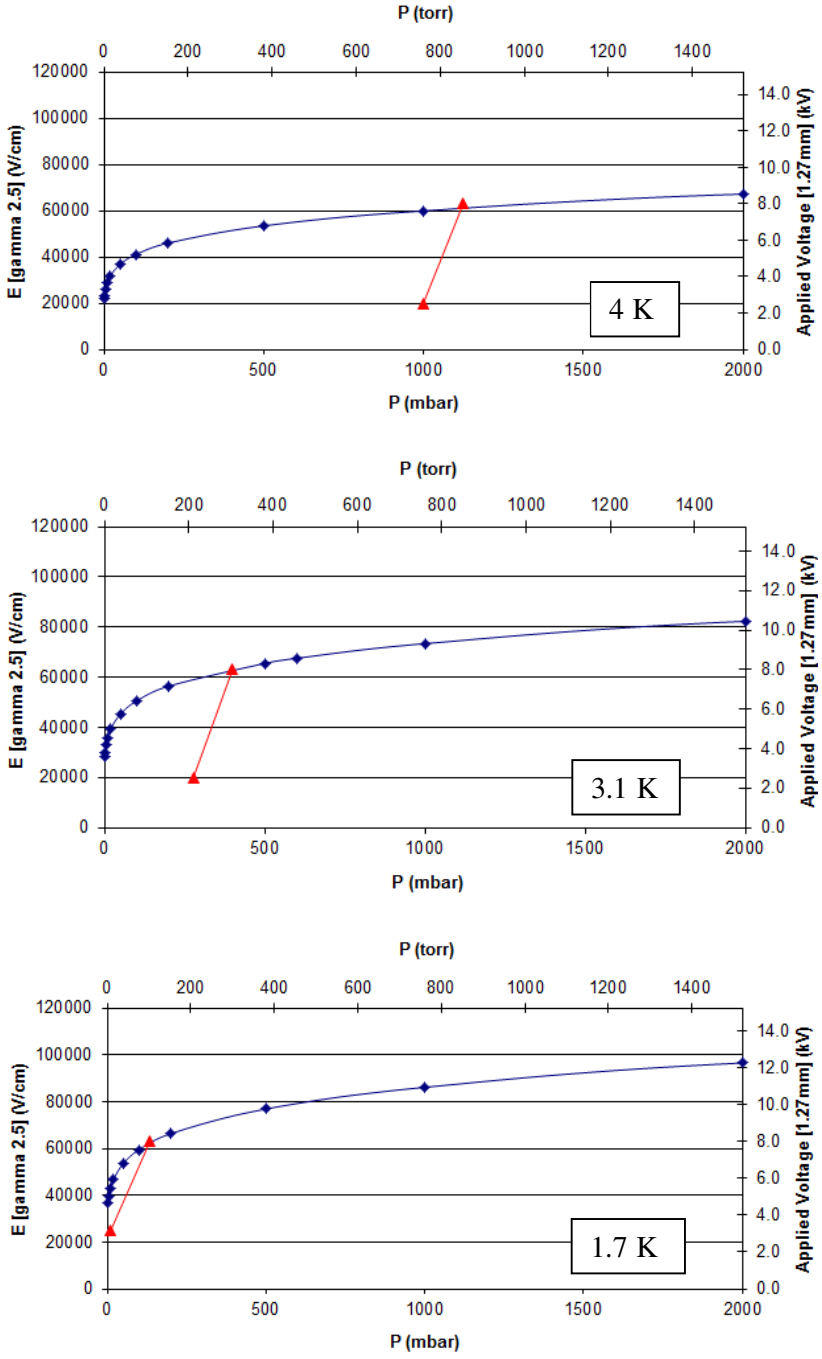

Fig.7.21 Diamond symbols: E-field to produce an elongation ratio of 2.5 in liquid helium as a function of pressure with initial bubble diameter 1 μm, relative permittivity of gas, ε_r = 18 and tabulated values for permittivity and surface tension of the liquid. Red triangle symbols and trend line: Pressures corresponding to SVP and to measured P_k.

elongation was calculated as a function of the pressure for liquid Helium at the three different temperatures. Tabulated values for the liquid dielectric constant and (temperature dependent) surface tension were used. The two other (free) input parameters for these calculations were essentially the (fixed) quantity of gas in the bubble and the dielectric constant of this gas. These were respectively taken to correspond to an initial bubble radius of 1 μm and ε_r of 18 (corresponding to a conducting gas). The results are indicated by the diamond symbols in Fig.7.21. The red triangles on each plot correspond in pressure to the SVP and to the measured P_k values. The proposed linear behaviour at low pressure is shown as the red line.

It can be seen that the overall qualitative experimental behaviour reported here can be simulated with these calculations. It is also worth noting that the absolute values of the fields at which the electrostrictive elongation becomes important is within a factor of five of those we observed experimentally. Given the crudeness of the approximations involved, this is rather encouraging and may be worth pursuing further.

7.2. Analysis and discussion of High Voltage breakdown data in He I, He II and LN_2 when a ceramic spacer is added between two Rogowski profile electrodes

7.2.1. Comparing ceramic V_{bd} data to that with no ceramic

All the data for test cells with a ceramic spacer measured in LHe at Sussex has been collated on Fig. 7.22. This shows the breakdown behaviour at 4.2 K and in He II between 1.4 K and 1.9 K. The electrodes used to take the data are indicated.

When using the DKHs electrodes with a ceramic spacer at separations ranging between 1.39 mm and 3.29 mm and a temperature of ~ 1.5 K, the breakdown occurs at

similar values to that without a spacer. Visual inspection of these samples revealed that breakdown can cause tracks, chipping and damage to the ceramic.

At 4.2 K data taken with the DKHs electrodes shows a reduction in V_{bd} by a factor of ~ 2 when a ceramic spacer is present between electrodes compared to that without a ceramic. Damage and tracks were also observed on these samples.

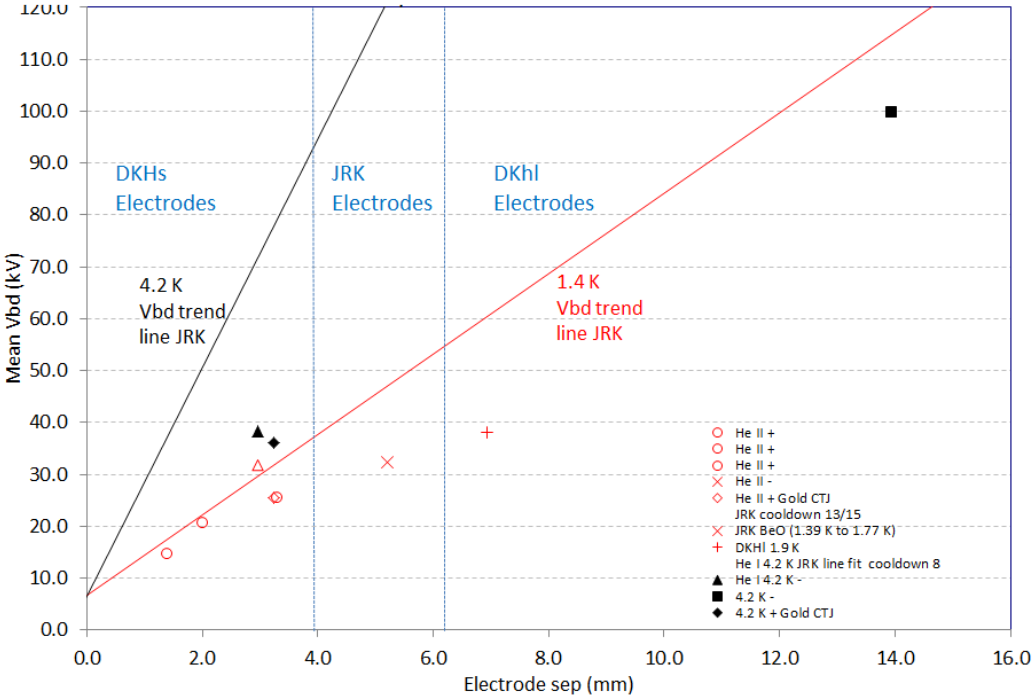

Fig..7.22. Breakdown voltage in liquid helium versus electrode separation for various lengths of Al_2O_3 and BeO spacers between DKHs, DKHl and JRK electrodes under SVP. Data from ceramic runs 1, 2, 3, 4, 6, 7, 8 and 9. Red Circles: V_{bd}, ceramic run 1, 2 and 3, at ~ 1.5 K, positive polarity; Red Triangle: V_{bd}, ceramic run 4, ~ 1.5 K, negative polarity; Red diamond: V_{bd}, ceramic run 6, ~ 1.4 K, positive polarity, Red cross: V_{bd}, BeO run, ~ 1.4 K, from Karamath thesis (Karamath 2007); Red t-cross: V_{bd}, ceramic run 7 and 8, ~ 1.9 K, negative; Black triangle: V_{bd}, ceramic run 5, 4.2 K, negative polarity; Black diamond, V_{bd}, ceramic run 6, 4.2 K, positive polarity; Black square: V_{bd}, ceramic run 9, 4.2 K, negative polarity. Also shown are V_{bd} trend lines for 1.4 K and 4.2 K under SVP from Karamath (Karamath 2007).

The data taken by Karamath (2007) using the JRK electrodes in the temperature range between 1.4 K and 1.8 K and under SVP with a BeO spacer between the electrodes showed a reduction in V_{bd} by ~ 15 kV when compared to the interpolated value for no spacer between the electrodes at the same temperature. The electrode separation was 5.2 mm. Karamath observed many flash over tracks across the surface of the BeO and also chips at the CTJ and ATJ.

Using the larger area DKHl electrodes in He II at 1.9 K when a ceramic spacer is placed between the electrodes at a larger electrode separation of 6.94 mm the V_{bd} value is reduced by a factor of ~ 2/3. Inspection of the ceramics after the experiment revealed there was no sign of damaged or flash over tracks on the ceramic. The number of breakdown craters on the surface of the electrodes match number of breakdowns. Therefore all breakdown events occurred through the He II.

When the separation between the electrodes was increased to 13.94 mm one breakdown event was recorded at 99.8 kV at 4.2 K using the DKHl electrodes. As a result of this breakdown a leakage current flowed through the cell and no futher measurements could be taken as no significant voltage could be applied. On inspection there was one mark on the ceramic that might have been a flashover track across the surface. Flash over tracks and damage to the ceramics are explained in detail in the next section.

In summary, He II at ~ 1.4 K under SVP has similar V_{bd} values for small electrode separations with and without a ceramic spacer. As the separation is increased at the same temperature and under SVP the V_{bd} is reduced when a ceramic spacer is present. However, as the measurements completed with the DKHl large area electrodes showed, no damage to the ceramic occurred when the electrode separation was at 6.94 mm and hence this reduction in V_{bd} may be due to an area or Helium volume effect.

Measurements taken at 4.2 K under SVP with the DKHs electrodes and ceramic spacer show a reduction of ~ a factor of 2 when comparing to data with no ceramic spacer. One data point was record using the larger area DKHl electrodes and at an increased separation of 13.94 mm. After this single breakdown the cell was leaking current and could not be charged. Observation of the ceramic indicated a mark that might have been a track across the surface.

Measurements taken with the DKHs electrodes and the JRK electrodes produced damage to the ceramic. There was no sign of any damage to the ceramic when the DKHl electrodes were used to take data at 6.94 mm at 1.9 K under SVP. However, the breakdown voltages were ~ 2/3 less than those found by Karamath (2007). This might be caused by a possible area or volume effect.

7.3. V_{bd} cracks and tracks sustained to the ceramic surface

When a V_{bd} event occurs across the surface of a ceramic, it can deposit a track and cause damage to the CTJ and the ATJ. To assess these events the ceramic was visually inspected after each cool down. This subsection gives a detailed account of the tracks and damaged formed on the ceramic as a result of V_{bd}.

The next set of figures show the damage and tracked sustained to the ceramic spacers as a result of breakdown. All samples shown were taken using the DKHs electrodes. The first four were taken at ~ 1.5 K and are in order of increasing ceramic length and therefore electrode separation. The fifth shows breakdown damage at 4.2 K. The damaged caused by breakdown on the ceramic sample coated with gold is then shown. This ceramic sample had measurements taken at 1.4 K and 4.2 K. The final investigation was taken from ceramics that had breakdown in LN_2.

7.3.1. Tracks and damage in He II at 1.5 K using the DKHs electrodes

Ceramic run 1 **Ceramic length 5.93 mm, electrode separation 1.39 mm, positive polarity.**

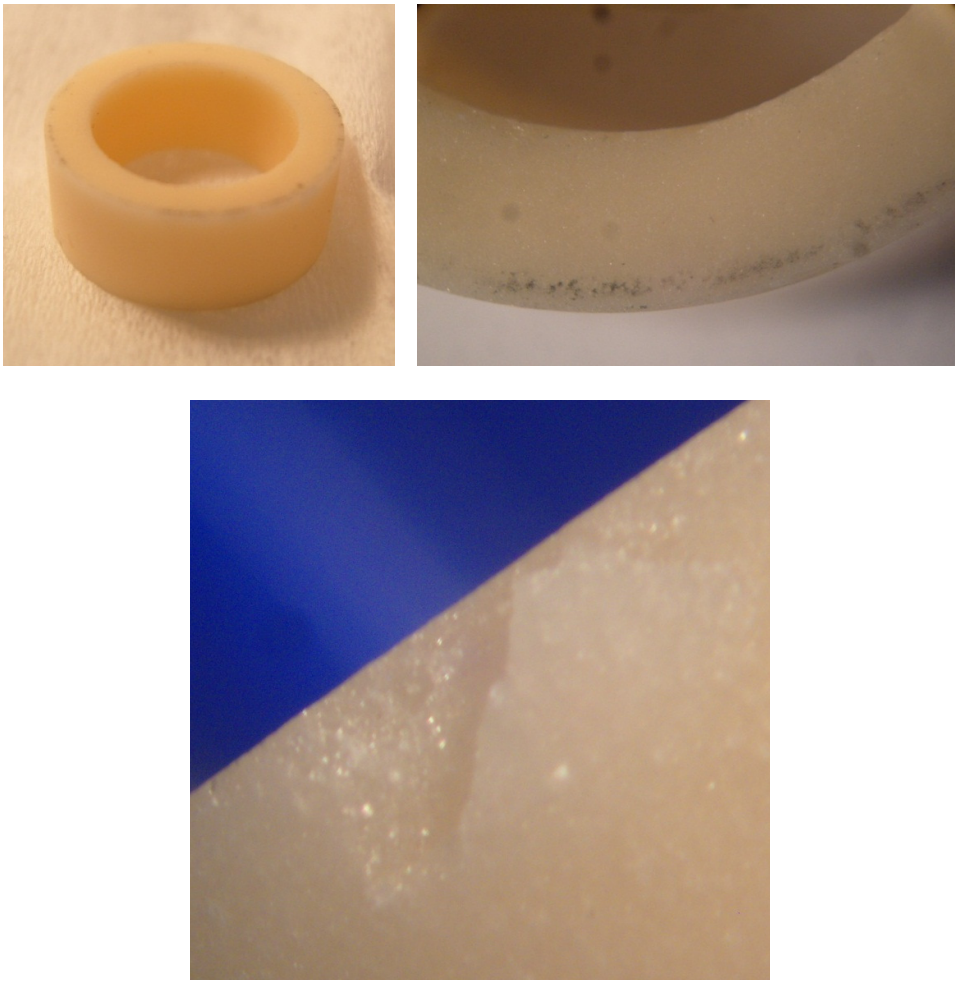

Fig..7.23. Photographs of the ceramic sample from ceramic run 1. The overall length of the ceramic is 5.93 mm with an electrode separation of 1.39 mm. Positive polarity was used. In a clockwise direction starting from top left, Picture 1: the ceramic; Picture 2: Dark marks observed on the end face of the ceramic sample; Picture 3: Chipping to the CTJ.

Figure 7.23 shows images of the damage caused to the ceramic sample in ceramic run 1. The breakdown measurements were taken in He II at ~ 1.5 K under SVP. The average breakdown voltage was 14.7 ± 0.3 kV. There was no obvious sign of any tracking across the ceramic. Chipping and cracks were observed on both the CTJ and the ATJ. Also shown in Fig. 7.23 on picture 2 is a dark region on the ceramic end surface. This is the surface which is in contact with the electrodes.

Ceramic run 2 **Ceramic length 6.55 mm, electrode separation 2.01 mm, positive polarity.**

Breakdown damage and flashover tracks created during ceramic run 2 are shown on Fig. 7.24. The measurements were taken at ~ 1.5 K under SVP and using positive polarity. The average breakdown voltage was 20.6 ± 0.6 kV. Picture 3 on Fig. 7.24 clearly shows flashover tracks running along the surface of the ceramic. The direction of the tracks is that of the applied E-field running from electrode to electrode, as seen on picture 1 Fig. 7.24. Chipping of the CTJ is also shown on picture 2 of Fig. 7.24.

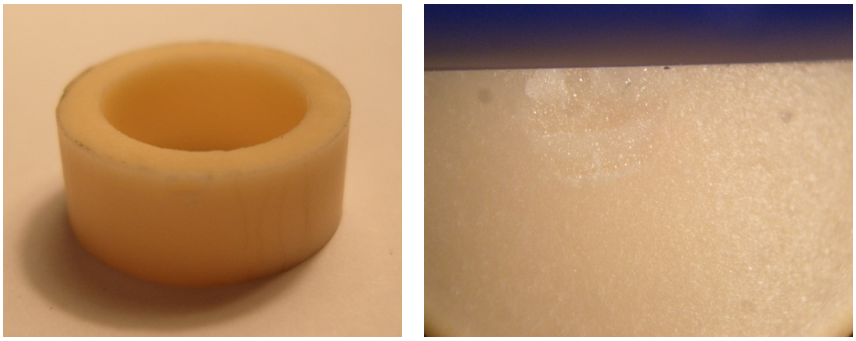

Fig..7.24a. See Fig 7.24b for caption**.**

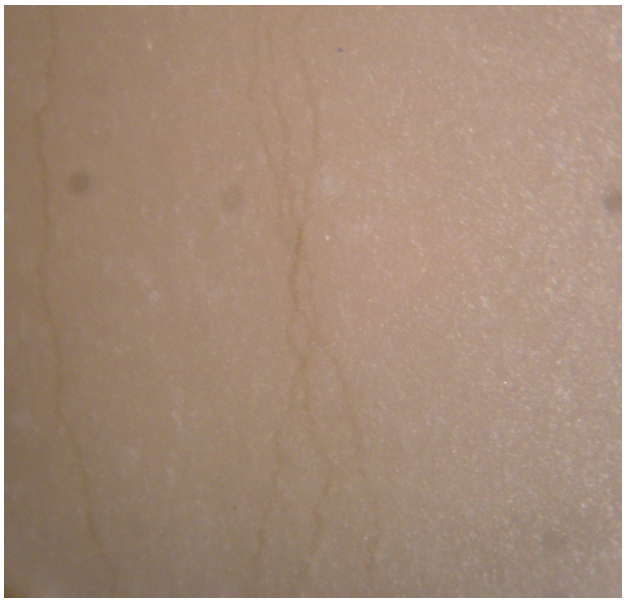

Fig..7.24b. Photographs of the ceramic sample from ceramic run 2. The overall length of the ceramic is 6.55 mm with an electrode separation of 2.01 mm. Positive polarity was used. Left Picture Fig.7.24a: the ceramic; Right Picture Fig.7.24a: Chipping on the CTJ; Picture Above Fig.7.24b: Flashover tracks along the outside surface of the ceramic.

Ceramic run 4 Ceramic length 7.50 mm, electrode separation 2.96 mm, negative polarity.

Figure 7.25. shows the damage caused to the ceramic as a result of breakdown from ceramic run 4. The length of the ceramic was 7.50 mm long with an electrode separation of 2.96 mm. The polarity used to charge the HV electrode was negative. The average breakdown voltage was 31.8 ± 1.1 kV. On picture 1 of figure 7.25 flashover tracks are visible both on the inside and the outside of the ceramic. These tracks run in the direction of the E-field. Approximately 90 % of the breakdowns resulted in tracking. Picture 2 of Fig. 7.25 shows a chip has be removed from the inside edge of the ceramic on the CTJ end. Closer inspection of this same chipped region, picture 3 Fig. 7.25., shows that a piece of the ceramic is missing and a track is running over the chipped surface. This might suggest that the track went under the surface of the ceramic and as a result chipped off the edge.

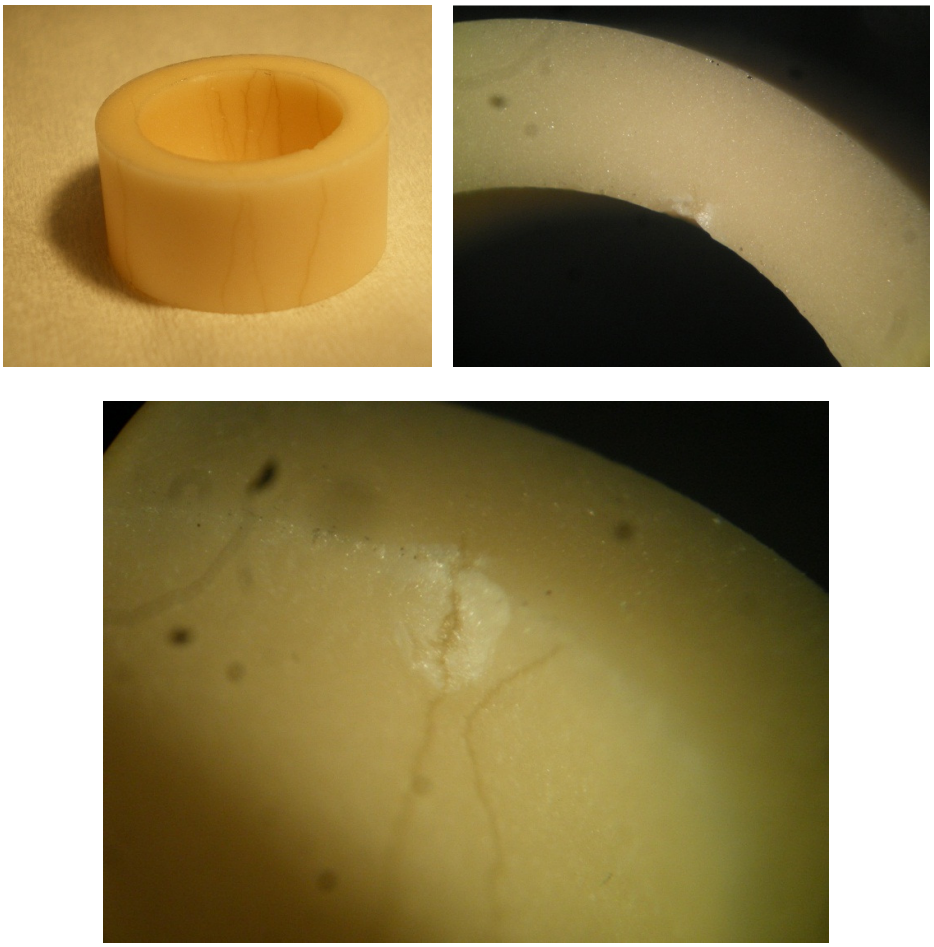

Fig..7.25. Photographs of the ceramic sample from ceramic run 4. The overall length of the ceramic is 7.50 mm with an electrode separation of 2.96 mm. Negative polarity was used. In a clockwise direction starting from top left, Picture 1: The ceramic with tracks visible across the outside and inside surface; Picture 2: Chipping on the inside CTJ; Picture 3: Flashover track damage running through the chipped surface on inside edge of the CTJ.

Ceramic run 3 Ceramic length 7.83 mm, electrode separation 3.29 mm, positive polarity.

Figure 7.26 displays photograph images of damaged caused to ceramic run 3. The measurements were carried out in He II at ~ 1.5 K and under SVP. The total length of the ceramic was 7.83 mm with an electrode separation of 3.29 mm. The average breakdown voltage over this run was 25.5 ± 0.6 kV. Picture 1 of Fig. 7.26 shows tracks running across

the surface of the electrodes in the direction of the applied E-field. Also shown is a dark area on the surface of the ceramic that makes contact with the base of the groove in the electrode. Chipping of both the CTJ and ATJ is also evident. Picture two of Fig. 7.26 shows chips off the outside edge of the CTJ. A track can be seen initiating from the bottom of the chipped edge on Fig. 7.26 picture 3.

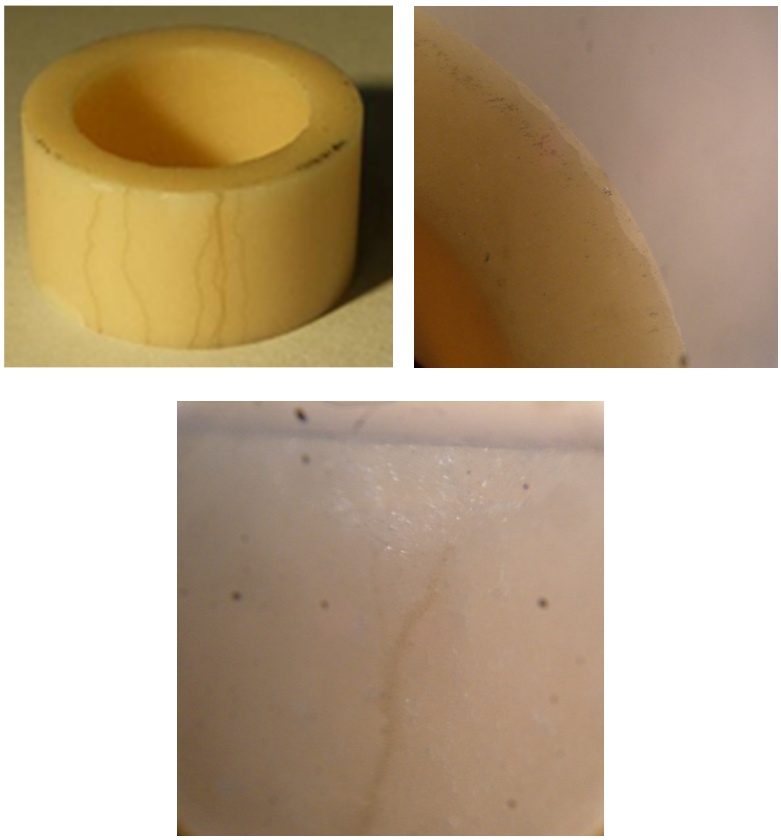

Fig..7.26. Photographs of the ceramic sample from ceramic run 3. The overall length of the ceramic is 7.83 mm with an electrode separation of 3.29 mm. Positive polarity was used. In a clockwise direction starting from top left, Picture 1: Ceramic with track visible across the outside surface. Also observable are dark marks on the ceramic edge and chipping and flaking if the ceramic at the CTJ and ATJ ; Picture 2: Chips off the edge of the ceramic; Picture 3: Flashover track initiating from a chipped region on the outside edge of the ceramic.

7.3.2. Tracks and damage in He I at 4.2 K using the DKHs electrodes

Figure 7.27 shows photographs of the damage caused to a 7.5 mm ceramic sample between the DKHs electrodes (ceramic run 5). These breakdown measurements were carried out in He I at 4.2 K under SVP. A negative polarity was applied. The average V_{bd} value was 38.2 ± 0.9 kV. The probability that breakdown would track across the surface of the ceramic was 77 %.

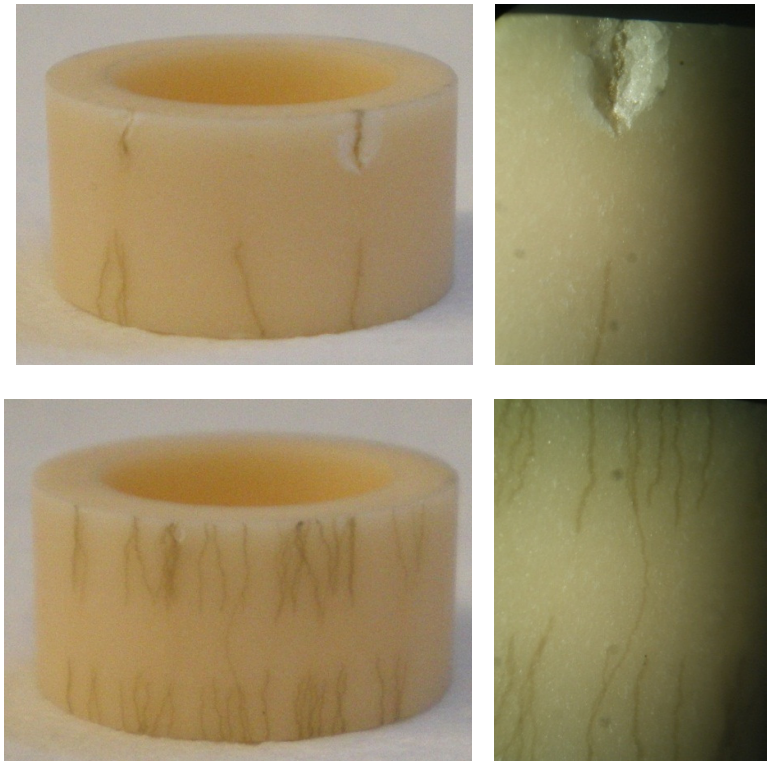

Figure. 7.27. Photographs of the ceramic sample from ceramic run 5. The overall length of the ceramic is 7.50 mm with an electrode separation of 2.96 mm. Negative polarity. In a clockwise direction starting from top left, Picture 1: Ceramic with chips on CTJ. A track can be seen on the chipped area. All the tracks are discontinuous; Picture 2: Enlarged image of the chip seen in picture 1. The track is clearly seen on the surface of the damaged area. This track is discontinuous; Picture 3: The orientation is 180 degrees to that of picture 1 and 2. Many tracks are visible. They all run in the direction of the E-field. Only one track is continuous. All the rest have gaps; Picture 4: same orientation as picture 3. It shows an enlarged image of the continuous track.

The most noticeable feature here is that the majority of the flashover tracks are discontinues. They start at one edge of the ceramic, run down it in the direction of the E-Field, then stops somewhere in the middle. Most of the tracks are discontinuous and show no evidence of any tracking in the mid region of the ceramic. The track reappears and continues until it reaches the opposite edge. Currently we have no clear explanation as to why the tracks displayed this behaviour.

Figure 7.27 pictures 1 and 2 show some of these discontinuous tracks across the ceramic and damage to the CTJ. Pictures 3 and 4 are taken of the opposite side of the ceramic to picture 1 and 2. Many discontinuous tracks are visible. Only one track bridges the gap between the two. The number of tracks found on the cathode side was ~ the same as that found on the anode side, 25 and 24 respectively. The overall number of V_{bd} for this run was 30. This means that one a single breakdown event must have caused both sides of the tracks.

7.3.3. Tracks and damage to a Gold coated ceramic using the DKHs electrodes

In an attempt to prevent high E-Fields in the gap between the ceramic and the electrode, the cathode side of the ceramic was sputter coated with gold. It was assumed that as long as one point of the gold coating on the ceramic sample was in contact with the cathode electrode, the potential of both would be the same. A total of twelve breakdown measurements were taken at 1.4 K and then at 4.2 K. The average breakdown voltage at 1.4 K was 25.6 ± 0.9 kV and the average at 4.2 K and 36.0 ± 1.6 K. The sample was removed after both sets of data had been taken. Therefore, it was not possible to distinguish the damage caused in He I to that in He II.

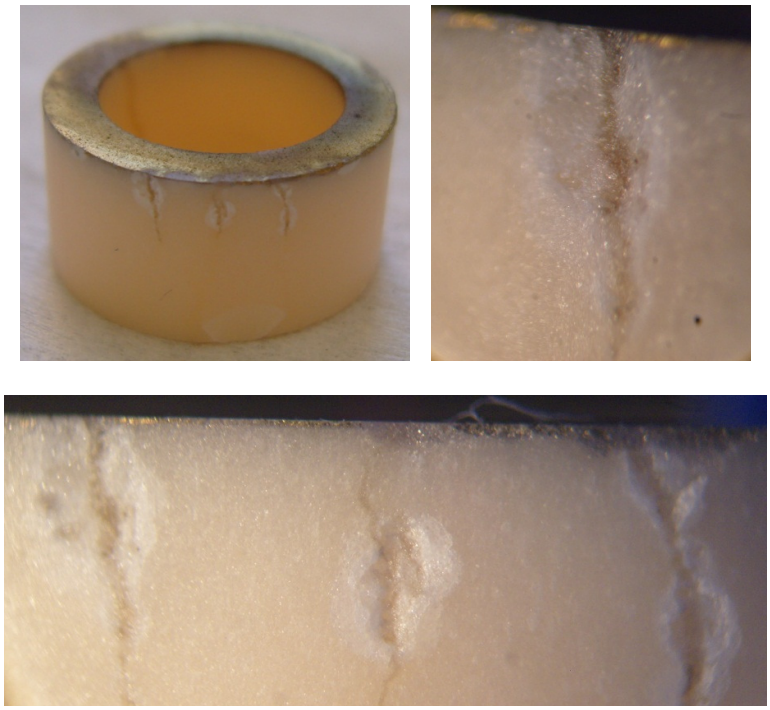

Fig..7.28. Photographs of the ceramic sample from ceramic run 6. The overall length of the ceramic is 7.77 mm with an electrode separation of 3.23 mm. Positive polarity. . Gold has been sputtered onto the gold end of the ceramic sample. In a clockwise direction starting from top left, Picture 1: Ceramic with chips on CTJ. Tracks can be seen running over the chipped area. The gold coating is also shown; Picture 2: Enlarged image of the chip shown in picture 1. The track is clearly seen on the surface of the damaged area. The track appears gold in colour; Picture 3: Enlarged image of the three chip regions shown on picture 1. Through each a chipped area a track is visible across the surface.

Figure 7.28 shows the damage caused to the sample during this run. The gold sputtered surface of the ceramic is visible on picture 1 of figure 7.28. Three tracks are shown to be initiating from the outside edge of the CTJ. These areas have been chipped as a result of the breakdown. Each has a track running over the surface left by the chip. An enlarged chip region is shown on picture 2 of figure 7.28. This image suggests that the discharge has occurred under the surface of the ceramic and chipped off a piece from edge of the CTJ, since the track runs over the surface of the damaged area. The colour of the tracks is visibly gold. The images in figure 7.29 show the opposite side of the ceramic to that in figure 7.28. On

picture 1 of figure 7.29, a gold track is shown over the surface of the ceramic running between the cathode and anode outside edges.

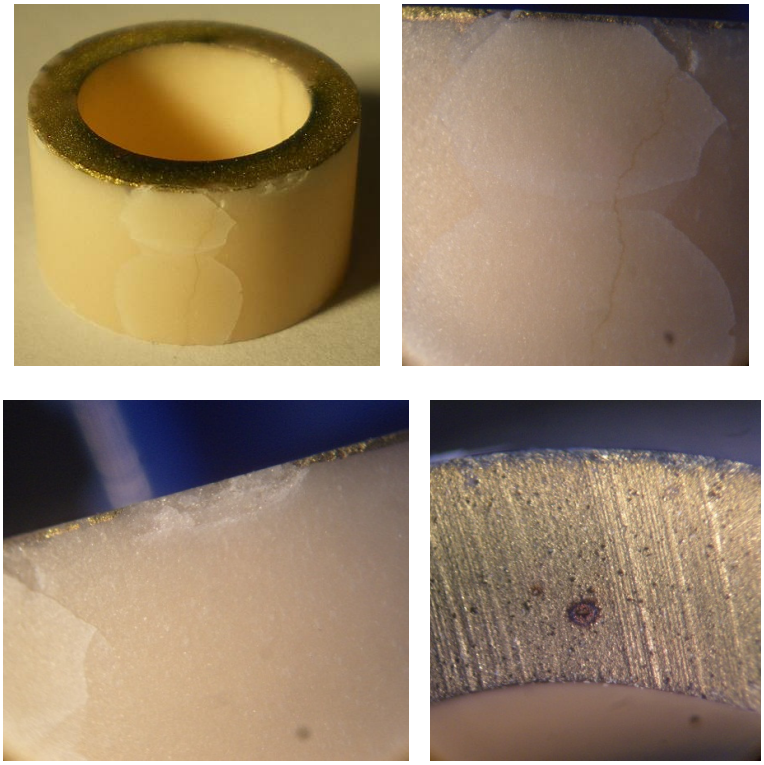

Fig..7.29. Photographs of the ceramic sample from ceramic run 6. The overall length of the ceramic is 7.77 mm with an electrode separation of 3.23 mm. Positive polarity. Gold has been sputtered onto the gold end of the ceramic sample. In a clockwise direction starting from top left, Picture 1: Ceramic with track running across the surface. The ceramic also shows flaking; Picture 2: Enlarged image of track and flaking of the ceramic shown in picture 1; Picture 3: Enlarged image of chipping to the CTJ shown on picture 1; Picture 4: Image of cathode surface coated with gold. Shown in the middle of the surface is a possible breakdown event.

Cracking and flaking of the ceramic surface is also observed. There is a crack that extends right the way across the ceramic surface. Chipping at the CTJ is also visible. This chipping has removed some of the gold from the edge of the ceramic. Figure 7.29 picture 2 is an enlarged image of the cracking and flaking caused to the ceramic. A gold coloured track is also visible.

Additional chipping and damage to the CTJ is shown on picture 3 of figure 7.29. This chipping has removed gold from the edge. Picture 4 of shows a section of the end of the ceramic that was sputtered with gold. A small, round dark area is visible which was not observed prior to making measurements. It is therefore assumed that this is also a result of breakdown.

If, as is suspected, gold is tracking across the surface, it is possible that the tracks found on the other samples were created by electrode material being ejected from its surface on breakdown and then moving over the sample in the direction of the E-field. X-ray Photoemission Spectroscopy (XPS) analysis was carried out at Omicron on the gold-coated and other ceramic samples to try and identify the composition of the tracks. Although there was a clear visual indication that gold tracks were present on the relevant ceramic, the amount of gold picked up in the energy spectrum scan was so small that a 2-D image of the surface did not not show any clear evidence of a gold track.

The ceramic samples used between stainless steel electrodes that had tracks on their surface were also analysed. To identify whether material from the stainless steel had tracked across the surface, Fe was searched for in the energy spectrum, but this was not observed. This is not felt to be surprising given the sensitivity of the XPS instrument used and the fact that tracks were only ~ 10 µm wide.

7.3.4. Tracks and damage in LN_2 using the DKHs electrodes

The damage and tracks created to and across the ceramics as a result of breakdown in LN_2 were also analysed. Figures 7.30 and 7.31 show the damage caused by breakdown.

Breakdown created catastrophic damage to the ceramic sample shown in figure 7.30. The average breakdown voltage for this run was 75.35 ± 1.43 kV. There were 20 breakdown events in total. The breakdown discharge ripped open the surface of the ceramic blowing

pieces of it all over the electrodes. A white ceramic powder is observed on the ground, bottom, and HV, top, electrode. The ceramic had broken into 6 pieces as shown in Fig. 7.31.

Fig..7.30. Photograph of a ceramic sample after breakdown measurements in LN2. The overall length of the ceramic is 7.50 mm with an electrode separation of 2.96 mm. Negative polarity was used. The ceramic has sustained massive amounts of damage over its surface. The surface of the electrodes is covered in a white powder, almost certainly ceramic. Both ground and HV DHKs electrodes are visible in the image.

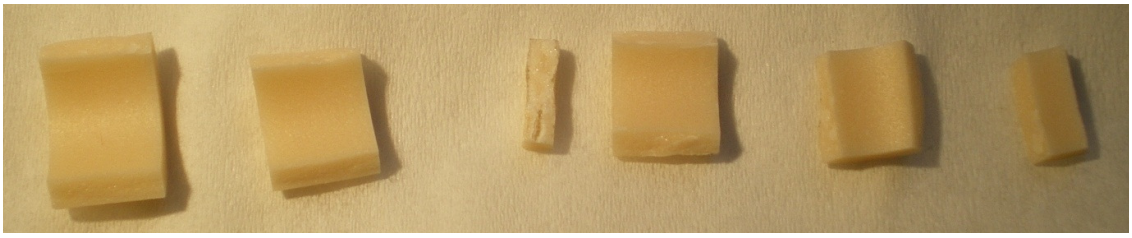

Fig..7.31. Photograph of the ceramic sample shown in figure 7.b.9. The overall length of the ceramic is 7.50 mm with an electrode separation of 2.96 mm. Negative polarity was used. The ceramic has catastrophically split into 6 pieces.

7.3.5. Inspection of large diameter ceramic samples using DKHl electrodes in He I, He II and LN_2

The DKHl electrodes have also been used to take data in He I, He II and LN2. Two experiments have been carried out in He II at 1.9 K using the same 18 mm long ceramic, corresponding to an electrode separation of 6.94mm. The ceramic was inspected after both runs and there was no evidence of any damage. All breakdowns appeared to have occurred through the helium volume and not along the surface of the ceramic.

A breakdown test carried out in He I at 4.2 K. The overall length of the ceramic was 25 mm with an electrode separation of 13.94 mm. Only one breakdown measurement was taken. The cell broke down at 99.8 kV. Then the electrode ceramic cell picked up a resistive track to ground. This prevented the cell from charging.

On inspection of this ceramic there was no real evidence of any significant damage to the ceramic. There was one suspect mark that might have been a track. It ran in the direction of the applied E-field.

One set of breakdown measurements were taken in LN_2 using the DKHl electrodes. The total length of the ceramic was 13.8 mm with an electrode separation of 2.74 mm. The average breakdown voltage was 60.64 ± 1.17 kV. 30 breakdown events were taken.

The electrodes and the ceramic were inspected. There was no evidence of any damage to the ceramic. The number of breakdown events on the surface of the electrodes was the same as the number of discharges. Therefore all the discharges went through the LN_2.

7.3.6. Summary of breakdown damage to Al_2O_3 ceramics

Tracks, chips and catastrophic damage to Al_2O_3 ceramic samples have been observed as the result of high voltage breakdown in He I, He II and LN_2. The numbers of breakdown tracks across two identical 7.5 mm ceramic samples, with electrode separation of 2.96 mm, has been compared.

One measurement set was at 4.2 K under SVP and gave surface tracking for 77 % of the breakdowns. In the second set at 1.5 K and SVP, the proportion of tracking rose to 90 %.

All ceramics used with the DKHs electrodes at separations between 1.39 mm and 3.29 mm had breakdown damage. Chips off the CTJ and ATJ were observed. As the separation between the electrodes is increased the damage to the ceramics is more intense. This is not surprising as increasing the separation also increases the breakdown voltage, thus providing more energy.

Tracks on the surface of the ceramic propagate in the direction of the applied E-field. On a number of occasions tracks are observed on the surface of a chipped area at the CTJ or ATJ. This suggests that the discharge has propagated through the corner of the ceramic, chipping it as it passes through it.

In an attempt to prevent any E-field in the gap between the ceramic and the electrode a ceramic sample had one end sputtered with Gold. The breakdown values for this sample were approximately the same as those taken without any Gold on the ceramic. However, breakdown measurements had to be stopped when the cell developed a high resistance path to ground, limiting the voltage. The ceramic was examined and it revealed that the ceramic sample had been chipped at the CTJ and there was flaking on the surface.

Ceramic breakdown tests with the DKHs electrodes in LN_2 causes catastrophic damage to the ceramic. The breakdown voltage was a factor of ~ 2 higher than that of liquid

helium for similar separations. Higher breakdown voltages provide the discharge with higher energy increasing the probability of damage.

When the DKHl electrodes were used in He II and LN_2 all discharges propagated through the liquid rather than across the surface of the ceramic. The only time there was suspected damage to the ceramic was when the cell was being run in He I at 4.2 K under SVP. One breakdown at ~ 100 kV created a track to ground. On inspection of the ceramic there was one mark on the surface that might have been a possible track. There was no other evidence of damage.

7.4. Measurements of the actual groove profiles of the DKHs and DKHl and Ramsey Cell electrodes

When placing a ceramic spacer between an electrode surface, to some extent a gap will be created between the two. The high permittivity of the ceramic forces a high E-field in the gap. Obviously increasing the E-field enhances the chances of V_{bd} so it is useful to electrostatically model the actual gaps between ceramic and electrode. By using the measured electrode profiles of the DKH electrodes in Opera models, the electric fields generated in the gaps at any given V_{bd} can be established.

7.4.1. Groove profile of the DKHs, DKHl and Ramsey Cell electrodes

Inspection of the surfaces of the DKHs electrode grooves revealed that they were not completely flat (Appendix F). The first measurement of the relative flatness was made at the University of Sussex workshop. A deviation of ~ 80 μm was recorded on one of the DKHs electrodes and ~ 15 μm on the other. The groove surface of the DKHl electrodes was also

measured. These were also found not to be flat. One electrode fluctuated by ~ 75 µm and the other by ~ 105 µm. Both sets of DKH electrodes were taken to RAL for a more precise analysis of the surface. The results of these scans are shown on Fig. 7.32.

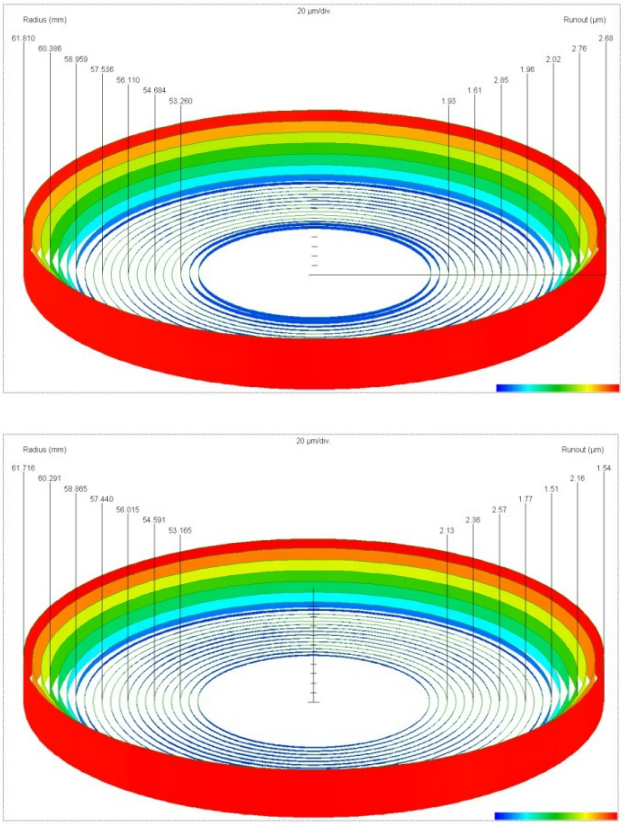

Fig..7.32. DHKl Electrodes. Scan over all of groove. Top: Ground electrode; Bottom: HV electrode. Scan completed at the RAL metrology department.

Both the DHKl electrodes were found to share a similar profile, Fig. 7.32 and Fig. 7.33. The groove surface is deeper and flatter nearer the centre of the electrode. There is a raised slope on the outer radius of the groove. This feature is circumferential and therefore would have probably been created as a result of the manufacture.

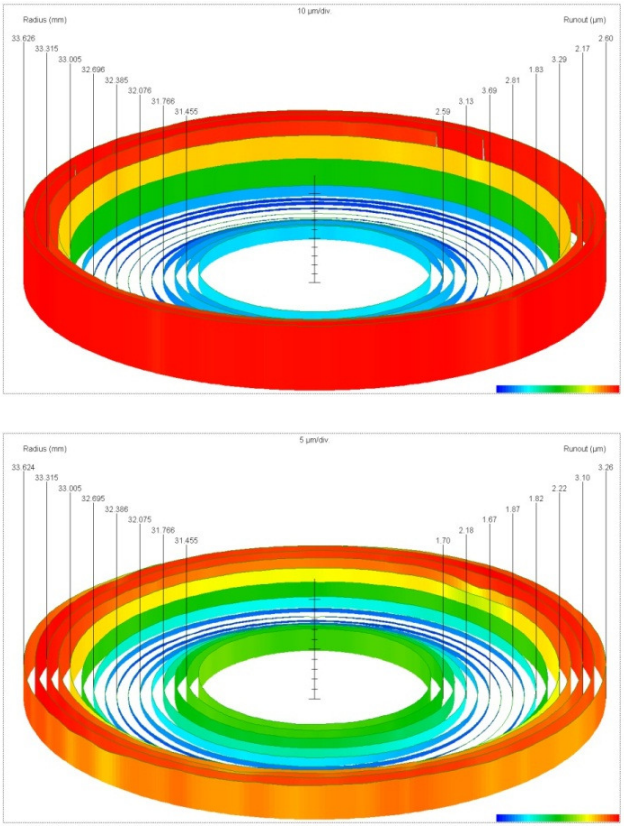

Fig..7.33. DHKs Electrodes. Scan over all of groove surface. Top ground electrode and bottom HV electrode. Scan completed at the RAL metrology department.

7.4.2. Calculations of the Breakdown E-fields on the DKHs. (Opera Vector Field simulations)

The electrode profiles measured at RAL can be used to measure the breakdown E-field from the DKHs electrodes using Opera Vector fields. The data for the DKHs electrodes has been taken from the topography images above and is presented on Fig. 7.34. The electrode groove height versus the radius of the groove. The HV electrode profile is represented by red squares and the ground by blue diamonds.

A curve was fitted to each groove cross section which was then used to produce an accurate E-field model of the base of the grooves of the DKHs electrodes. Figure 7.35 shows

a section through the Opera model of the true groove profile of the DKHs electrodes. The HV electrode groove profile is blue and the ground electrode groove profile is purple. The ceramic is green and liquid Helium is lime.

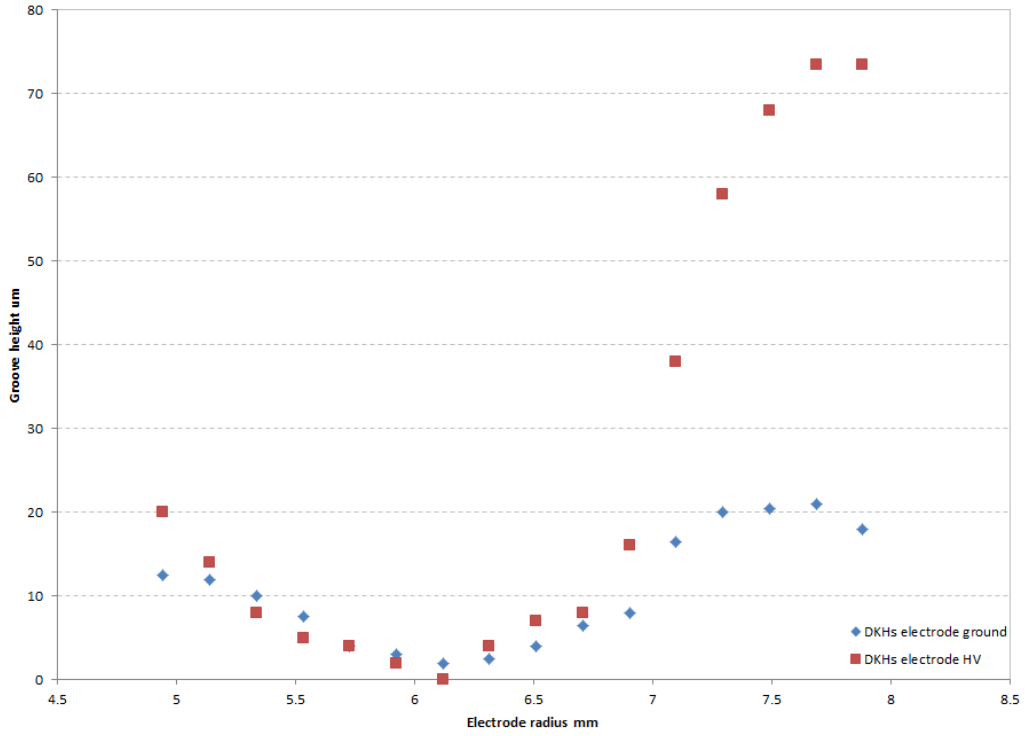

Fig..7.34. DKHs ground and HV electrode groove surfaces as a function of electrode radius.

E-field plots of the DKHs electrode groove profile are shown on Fig. 7.36. They clearly show that the highest field created is in the gap between the ceramic and the electrode.

The Opera model of the DKHs electrode groove profile was used to find the highest E-field produced at breakdown. The average experimental breakdown voltage found for each length of ceramic was used in the model with the correct electrode separation to calculated the magnitude of the E-field produced at breakdown. This data has been summarized on table 7.8.

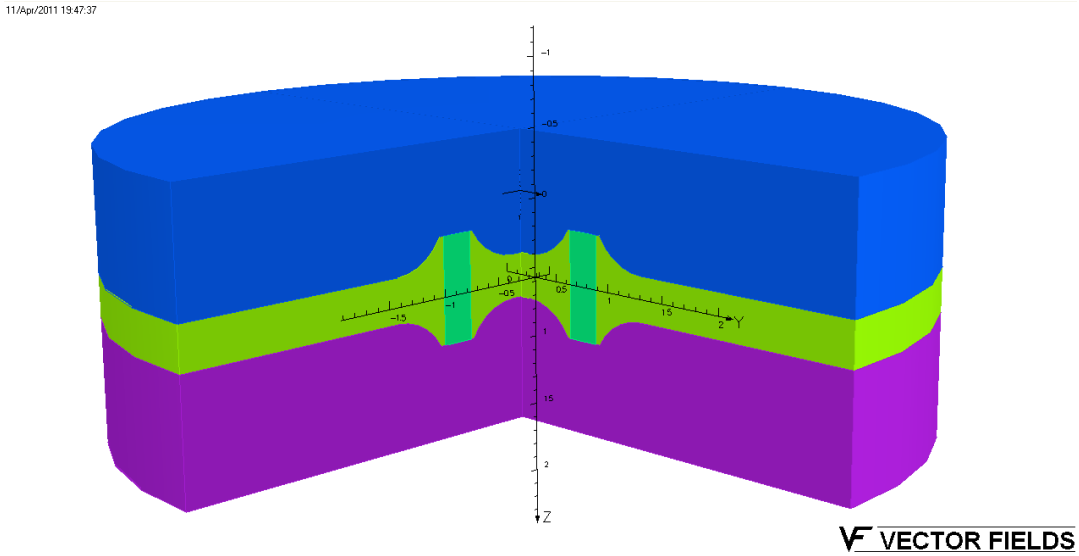

Fig..7.35. Opera model of the groove profile of the DKHs electrodes.

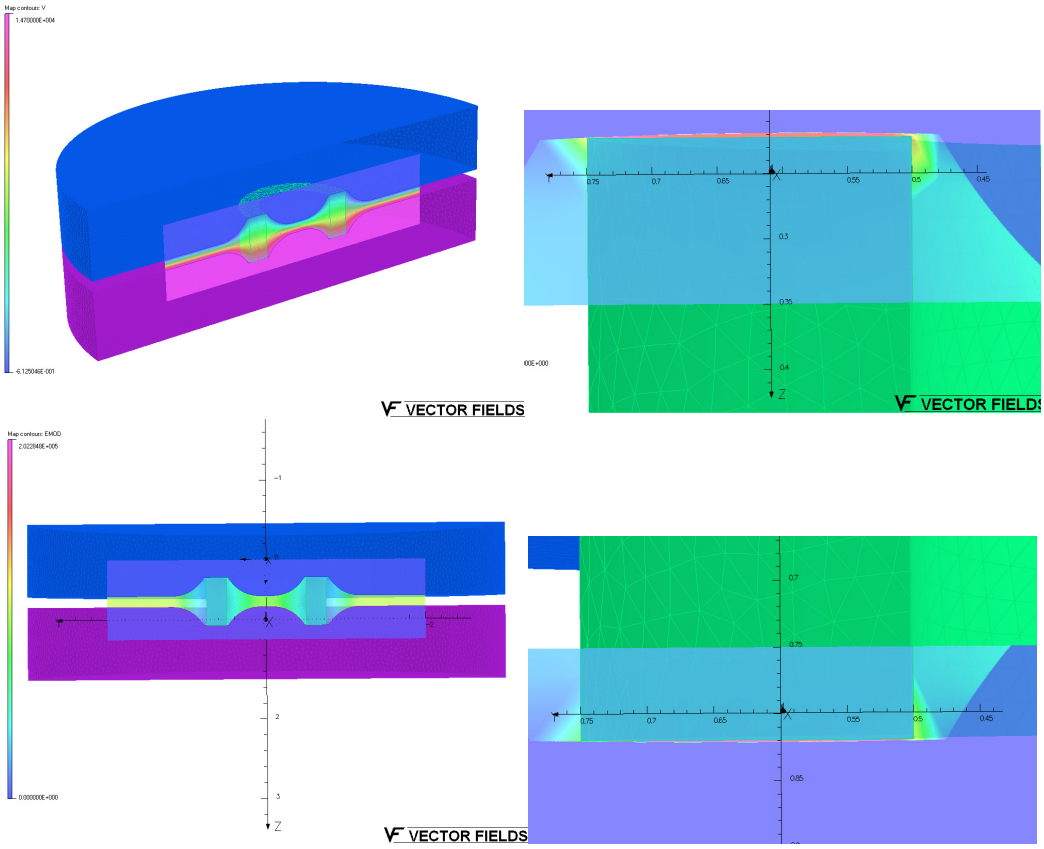

Fig..7.36. Opera model and E-field plots of the DKHs electrodes groove profile. Top left: Potential map; Top right: E-field map of the gap between the ceramic and HV electrode, highest field is shown in red; Bottom left: E-field map; Bottom right: E-field map of the gap between the ceramic and the ground electrode, highest field shown in red.

Average Breakdown Voltage kV	Electrode separation mm	Highest E-field ground V/cm	Highest E-field HV V/cm	HV polarity	E-field between electrodes kV/cm
20.6	2.01	2.72E+05	2.60E+05	+	102.5
14.7	1.39	2.21E+05	2.06E+05	+	105.8
25.5	3.29	2.78E+05	2.64E+05	+	77.5
31.8	2.96	3.62E+05	3.56E+05	-	107.4

Table..7.8. Summary of the experimental and Opera model breakdown E-field for the DKHs electrodes.

From table 7.8 it is clear that although the max E-field created across the electrode is ~100 $kVcm^{-1}$ the E-field in the gap is ~ 3 times that. The E-field in the gap between the ground and the ceramic is always slightly higher than between the HV electrode and ceramic.

In summary, the DKHs and DKHl electrode grooves were scanned at the RAL metrology department which showed that the bottom of the grooves were not flat, and fluctuate in height by ~ 80 μm and by ~ 100 μm, respectively.

It has been observed that the DKHs electrodes breakdown across the ceramic ~ 90 % of the time in liquid helium at ~ 1.5 K under SVP. The experimental data and the groove profile are used to calculate the magnitude of the E-field in the cell at breakdown using Opera vector fields.

The average breakdown E-field across the cell is ~ 100 $kVcm^{-1}$. However the Opera model shows that any gap between the electrode and ceramic produces an average E-field of ~ 275 $kVcm^{-1}$.

7.4.3. Possible V_{bd} Mechanisms and the Physical Geometries of Ceramics

This section considers some mechanisms which might cause the damage to the ceramics shown in the previous sections and then summarise the geometries and results obtained.

Given the importance of bubble formation growth in the breakdown process, cavitation must be considered as a possible mechanism to cause the observed damage to the ceramics. McCluskey and Denat (1996) considered in some detail the effect of shock waves associated with growth of the initial bubble formed just after the initiation phase of breakdown. They considered that this could cause something they called a "vacuole" – a vacuum hole within the liquid. Severe damage to solid surfaces caused by cavitation is very well known in many liquids.

A problem with using cavitation to explain the damage observed here is that there is often evidence of tracking underneath (behind) a chip which has been removed from the surface. This suggests that the ceramic has been blown apart from the inside by a discharge passing through the material, although it is possible that this tracking could have occurred after the initial damage. Such an internal discharge through the actual material of the ceramic seems unlikely. A discharge through liquid within the pores of the ceramic might seem more probable.

We can also make some general statements about relative locations. Damage generally occurs at the end of the ceramic, and more often on the outer circumference. The damage sites at the ends of the ceramic are usually coincident with the beginning of a track, although not all tracks have damage sites associated with them. There are three basic classes of tracks: Starting at the cathode and running the entire length of the ceramic; starting from

	Electrode / Ceramic Combination		
Dimension	DKH small / Alumina	DKH large / Alumina	JRK / Beryllia
	(mm)	(mm)	(mm)
$R_{C\ outer}$	7.5	35	4
$R_{G\ outer}$	7.88	36.76	4
$\delta R_{C\text{-}G\ outer}$	0.38	1.76	0
$R_{C\ inner}$	5	30	
$R_{G\ inner}$	4.75	25.5	
$\delta R_{C\text{-}G\ inner}$	0.25	4.5	
Upper gap	0.075		
Lower gap	0.02		
Possible Radial Separation	C-G can touch only on inside	C-G can touch only on outside	no inner surface of ceramic
	Min C-G gap on outside = 0.13 mm (small)	Min C-G gap on inside = 2.74 mm (large)	Min C-G gap on outside = 0 mm
Vertical Separation	Relatively large vertical gap on inside	Relatively flat bottom to groove	

Table..7.9. Groove-Ceramic Geometry for the Electrode Ceramic combinations used in this work. $R_{C\ outer/inner}$: Outer/inner radius of ceramic; $R_{G\ outer/inner}$: Outer/inner radius of bottom of groove in electrode; $\delta R_{C\text{-}G\ inner/outer}$: Inner and outer separations at the bottom of the groove between the ceramic and the groove edge for concentric alignment.

	Electrode / Ceramic Combination		
Cryogen / K	DKH small / Alumina	DKH large / Alumina	JRK / Beryllia
He II / 1.5K	Tracks (at higher V) Damage (all)	No Tracks No Damage	Tracks Damage
He I / 4.2K	Tracks (both) Damage (both)	No Tracks No Damage Leakage path	
LN2 / 77K	T(all) D(all)	No Tracks No Damage	
Tracking	Much tracking on outside of ceramic, some on inside	No obvious tracking	Much tracking on outside of ceramic

Table..7.10. Summary of tracking and damage for the various combinations of electrode-ceramic cells, cryogens and temperatures.

the cathode and extending only part way along ceramic; starting at the anode and extending only part way.

Table 7.9 summarises some details of the groove-ceramic geometry for the two cells used here and those for Karamath's ceramic tests. The inner and outer separations at the bottom of the groove between the ceramic and the groove edge, $\delta R_{C\text{-}G\ inner}$ and $\delta R_{C\text{-}G\ outer}$, are given for the case when the ceramic and the electrode are concentric. Unless these two values are equal, the ceramic can only touch the groove edge at either the outside or the inside when not concentric. The different degrees of tracking and damage to the ceramic seen when using the same electrode-ceramic combinations in the different cryogens and temperatures is summarised in Table 7.10.

From these Tables, it could be argued that damage and tracks have occurred where the ceramic edge is very close to the curved section of the groove: In the DKHl electrode-ceramic combination both the inner and outer radial separations are relatively large and this combination showed essentially no damage or tracking.

If the, say, inner diameter of the groove is smaller than the inner diameter of the ceramic, but the outer diameters are the same, then on one side (outer) there will be a roughly triangular cross-section gap next to a CTJ, whereas on the other side there will be relatively open (90°) gap. Any shockwave will be more closely confined on the outer side, leading to more cavitation damage. If this argument is correct, then it has clear implications for the main experiment. In this, the ceramic can easily end up with a very narrow gap on the outside of the ceramic on the underside of the Ramsey Cell.

8 Conclusions and suggestions for further work

8.1. Conclusions – Pressure Dependence of V_{bd}

High voltage breakdown measurements as a function of pressure between parallel plate electrodes and at constant temperature between 1.7 K and 4.2 K have been studied. For each temperature similar features are observed. At higher pressures a weak linear dependence is observed, common to all temperatures. This is labelled Region 1. Normalising all data at constant temperature to 50 kV and 1200 torr at 4.2 K produces an average Region 1 gradient of 0.01693 ± 0.00092 kV/torr with average intercept of 29.69 ± 0.88 kV.

At lower pressures the regime changes. The breakdown voltage changes much more rapidly with pressure and this is labelled Region 2. Combining the gradients for all constant temperature data in Region 2 produces an average value of 0.176 ± 0.0096 kV/torr. The point where Region 1 changes to Region 2 is labelled as the (temperature-dependant) kink pressure, P_k.

Plotting P_k against the density of liquid helium produced a linear dependence with gradient of gradient of -34.4 ± 1.4 kg $m^{-3}torr^{-1}$ and intercept of 5130 ± 200 kg m^{-3}.

P_k was also plotted against SVP yielding a gradient consistent with unity to within 1 error bar and intercept of 88 ± 13 torr.

It was observed that the maximum voltage achievable by the cell dropped as a function of run number. Inspection of the PC cell after 12 runs showed the electrodes had sustained large amounts of discharge damage on the surface, and that dust and impurities had built up on the electrodes. It was concluded that the reduction in maximum breakdown voltage as a function of run number was caused either by increasing the surface roughness of the electrodes or by impurities in between the electrodes or a combination of both. Cleaning and repolishing the electrodes restored the previously obtained values.

The method used to investigate any pressure dependence at constant temperature was specifically chosen to investigate hysteretic behaviour. The data from this thesis show that high voltage breakdown in liquid helium shows no hysteresis.

The breakdown fields under SVP observed here are consistent with observations made by others. The two-regime behaviour for $V_{bd}(P)$ at constant temperature reported here has not been clearly identified before in liquid helium. There is some evidence that similar behaviour occurs in some other cryogenic liquids and in transformer oil. A tentative model to explain the behaviour is proposed in which Regime 1 behaviour is attributed to electrostriction elongation of bubbles in the initial phase of breakdown. Preliminary calculations of this effect yield E-fields within a factor of four of those observed experimentally.

8.2. Conclusions – Al_2O_3 Ceramic data

Comparison of breakdown data taken at the same separation in He I under SVP with and without an Al_2O_3 ceramic spacer between electrodes shows the breakdown voltage is reduced by a factor approximately 2 when the Al_2O_3 ceramic spacer is present. A similar comparison of breakdown data taken in He II under SVP shows no sign of any large reduction in V_{bd}. However, breakdown does still initiate at the CTJ ~ 90 % of the time. Examination of the ceramic shows damage to the CTJ and tracks along the surface of the ceramic in both He I and He II.

Gold was sputtered onto the surface of the ceramic to try to eliminate the E-field produced by any gap between the ceramic and the electrode. Breakdown values were approximately the same as that for a ceramic sample without any gold. However, the run ended when the cell formed a high resistance track to ground and could no longer hold voltage. Inspection of the CTJ showed that it was damaged. In some cases Gold tracks

initiated from the damaged regions and propagated over the surface of the ceramic in the direction of the applied field.

The DKHl electrodes have been used to take ceramic data in He II. All breakdowns occurred through the bulk LHe volume and were initiated from the electrode surface. This data was compared to Karamath's (Karamath 2007) and it shows a drop of ~ $\frac{2}{3}$ in V_{bd}. This might be a result of a surface area effect.

Breakdown tests in LN_2 showed catastrophic damage to the ceramic which had been blown apart by the discharge. A load test was carried out to check that the ceramic was not being damaged by purely mechanical forces.

Both DKH electrodes and the Ramsey Cell electrodes were scanned by the RAL metrology department. The scan revealed that gaps up to 100 µm are possible between the end of the ceramic and electrodes. This data was used to produce an E-field model, using Opera vector fields, of the Ramsey Cell. The result showed that when 100 kV is applied across the Ramsey cell an E-field of ~ 100 $kVcm^{-1}$ is formed in any gap (Appendix G).

E-field calculations of the DKHs electrodes, using the observed breakdown values, show the average E-field between the electrodes is ~ 100 $kVcm^{-1}$ at breakdown. This produces an average E-field of ~ 275$kVcm^{-1}$ in the gap between the ceramic and electrode.

8.3. Conclusions – Implications for cryo-edm

It is clear from the work presented in this thesis that increasing the pressure above liquid helium in the temperature range from 1.7 K to 4.2 K increases the breakdown voltage. If this behaviour persists to 0.5 K it could be very beneficial to the cryo-edm experiment as this is the target operating temperature.

It has been shown in this thesis that increasing the pressure of He II between a pair of parallel plate electrodes 1.27 mm to ~ 1.6 bar causes the breakdown voltage to increase from

~ 15 kV to ~ 50 kV. This is a significant increase in normalised E-Field from ~ 120 $kVcm^{-1}$ up to ~ 400 $kVcm^{-1}$.

If the PC data directly scales to the cryo-edm Ramsey cell, increasing the pressure of the helium in to ~ 1.6 bar it would increase the sensitivity by a factor of ~ 3 as the statistical uncertainty on measuring a nEDM is inversely proportional to E.

Even increasing the pressure of the helium to 1 bar to above P_k would still greatly increase the breakdown voltage, by an expected factor of ~ 2.5. However, this will only be the case if the data from the PC electrodes scales directly to that of the cryo-edm apparatus. This is unlikely to be the case as the electrodes of the Ramsey cell have a larger surface area, the separation and thus volume of liquid helium between the electrodes is larger and there is a BeO ceramic spacer sandwiched between the electrodes sitting on an uneven surface. All these factors can lead to a reduced total breakdown voltage.

The PC is cable of creating E-fields of ~ 400 $KVcm^{-1}$ in ~ 1.27 mm gap with no spacer. That is a factor of 40 increases of the current E-field applied to cryo-edm apparatus. If future investigations show the ceramic spacer limits the breakdown voltage, the next generation Ramsey cell might need to be designed such that there is no spacer between the electrodes.

The surface area of the current Ramsey Cell might cause problems. The PC electrodes have been shown to produce an E-field between the electrodes of ~ 400 $kVcm^{-1}$. A compromise might have to be made between the area of the electrodes and the maximum voltage that can be sustained. However, result from electro-polished electrodes show higher breakdown voltages when compared to electrodes that have been mechanically polished. If the Ramsey cell electrodes were electro-polished this might increase the absolute voltage applied to the cell.

Trying to supply 400 kV to any apparatus is problematic. When the cell is in liquid helium at 0.5 K it gets even more complicated. To successfully supply 400 kV to the Ramsey cell a voltage multiplication process might be required (Long et al 2006).

If the absolute voltage into the cell is the limiting factor the experiments can be made more sensitive by reducing the separation between the electrodes. If the voltage to the cell remains constant reducing the separation of the electrodes by 4 will increase the sensitivity by 2 as σ_{d_n} goes with 1/E and 1/√N. The E-field increases by 4 however the volume inside the cell also reduces by 4. This would reduce the volume of helium by 4 but more importantly reduce the number of neutrons by 4.

Increasing the E-field in this way might produce problems with regards to leakage currents if these currents are a function of E-field across the cell. If the leakage current is a function of absolute voltage then reducing the separation of the cell to increase sensitivity would keep leakage currents to a minimum. The origin and magnitude of leakage currents needs further investigation.

It is worth asking the question of what pressuring liquid Helium will do to the UCN production and numbers. Fertl et al (2009) have carried out tests on the single phonon production numbers of UCN as a function of helium pressure at ~ 1.1 K. Their data, shown as a UCN count versus cold neutron wavelength at different pressures is shown in Fig. 8.1.

The wavelength of the single phonon production peak shifts to lower wavelengths as a function of applied pressure. The UCN count rate also decreases with increased pressure. However, this is over a large pressure range, SVP to 20 bar. For significant improvements in the Ramsey Cell the applied pressure needs to be only ~ 1 bar. An increase in helium pressure of ~ 1 bar will reduce the UCN count only by ~ 10 %, figure 8.2. The small percentage of UCN numbers lost from pressurisation will be more than compensated by the additional E-field. In order to get the highest numbers of UCN when using pressurised liquid

helium a very slightly lower cold neutron wavelength collimator should be used, ~ 8.6 Å. However, if the cryo-edm apparatus is moved to a white beam source all neutron wavelengths would be sampled.

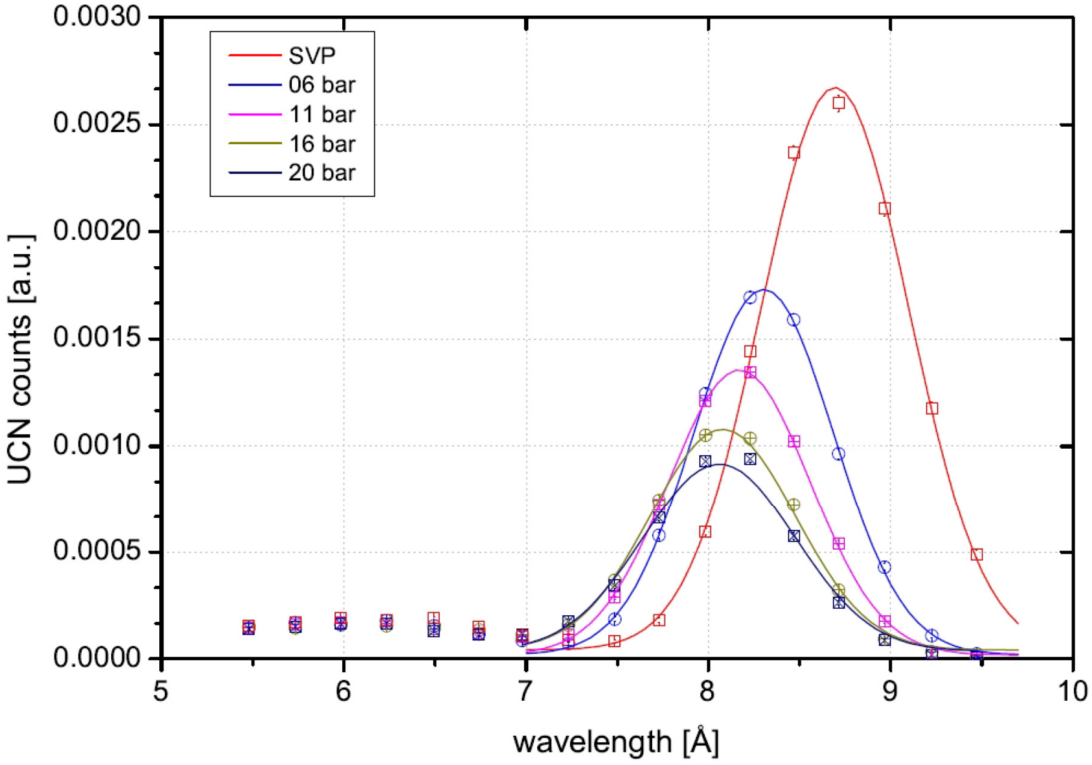

Fig..8.1. UCN count as a function of cold neutron wavelength in He II at 1.1 K for various applied pressures between SVP and 20 bar, (Fertl et al 2009)

Our Opera vector field E-field models of the current Ramsey cell calculates an E-field of ~ 100 kVcm^{-1} in the gap between the ceramic and the electrodes when a voltage of 100 kVcm^{-1} is applied across the cell. Measurements of high voltage breakdown in He II under SVP show that 100 kVcm^{-1} is capable of causing breakdown. On this basis it is predicted that a voltage of 100 kV applied across the Ramsey cell might cause catastrophic breakdown. Thus, voltages applied to the current Ramsey cell design applied under SVP are suggested to be kept below 100 kV.

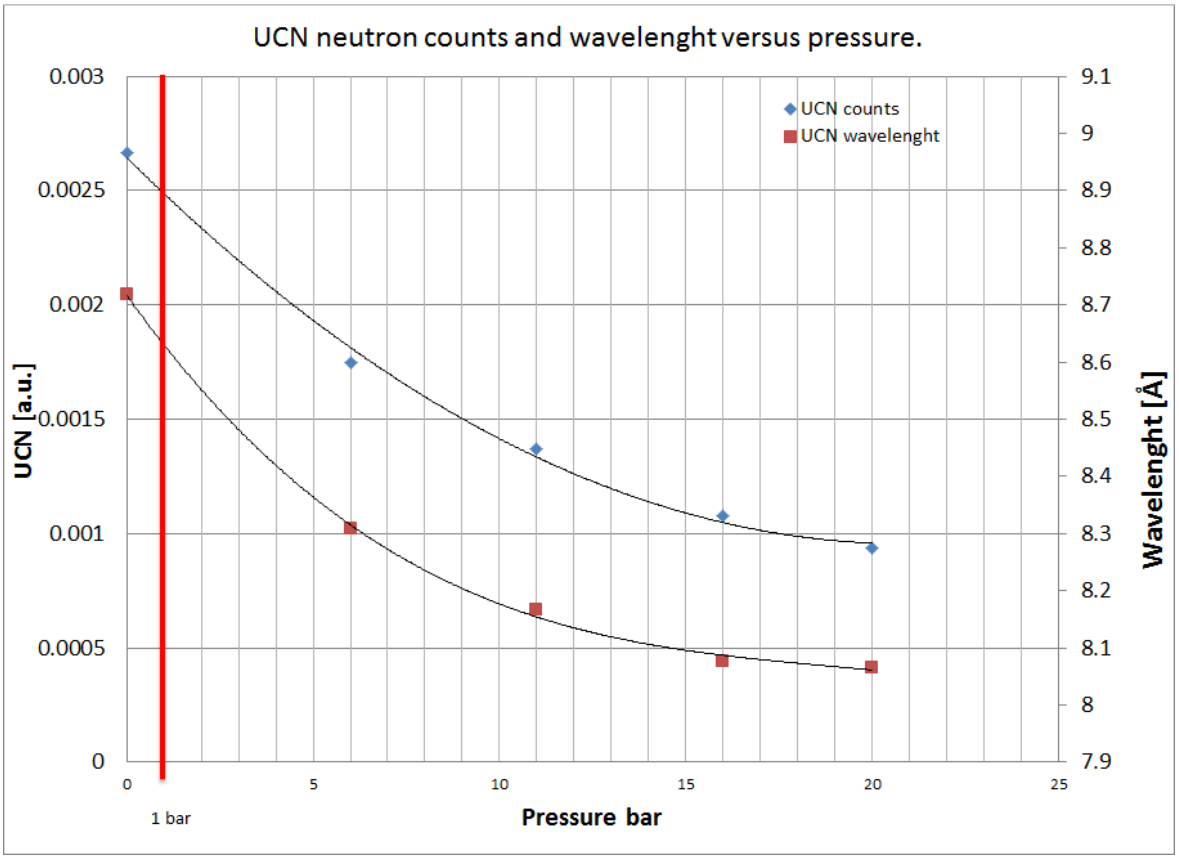

Fig..8.2. UCN counts and UCN wavelength versus He II applied pressure at 1.1 K for various pressures between SVP and 20 bar, Fertl et al, 2009). Red line indicates a liquid helium pressure of 1 bar. Blue diamonds: UCN counts (a.u.) fitted to $y = 4E\text{-}06x^2 - 0.0002x + 0.0026$; Brown squares: UCN wavelength (Å) fitted to $y = -8E\text{-}05x^3 + 0.0045x^2 - 0.091x + 8.7165$.

8.4. Suggestion for further work

In order to reduce the temperature in the current PC setup, the KEK bath cryostat could be connected to an existing Roots pump. To reduce the temperature even further, the PC can be installed onto the dilution fridge. This is a harder task as heat leaks into the cell may prove to be problematic.

The PC has only been used at one separation. There is a lot of parameter space to play with by increasing or reducing the separation when using the same temperature and pressure range. Additionally the PC setup, as it is, can be used to investigate the effect of

surface finish. Electro polished electrodes should be tested in comparison to mechanically polished ones.

Varying the separation will also vary the volume of liquid helium between the electrodes. Thus volume effects can be studied.

Three PC Rogowski profile electrodes made of different material (Stainless Steel, Aluminium and Titanium) already exist. These can be used to test high voltage breakdown as a function of electrode material. Testing Beryllium electrodes would enable direct comparisons to the high voltage performance of the Ramsey cell electrodes. A secondary investigation from these measurements is to analysis the crater damage and profile of each material. Different materials have been observed to produce their own distinct crater characteristics (Appendix C).

Currently the PC is voltage limited by the feedthroughs. The PC should be electrostatically sound to 100 kV. Tests can be carried out at this voltage if 100 kV rated feedthroughs are installed.

Rogowski profile electrodes with varying surface areas, but no larger than the current PC electrode, can be used to investigate any area effect.

An investigation into the observed reduction in voltage as a function of run number can be carried out easily. Once a reduction in maximum voltage is observed the electrodes can be removed and cleaned. The PC setup insures the electrodes are put back in precisely the same position after reinstallation. Once clean, if the voltage remains low it would suggest that electrode damage is the significant cause of the reduction in breakdown voltage. If the voltage increases the dust and impurities in the liquid helium would primarily be responsible for causing voltage reduction.

The pressure range can most certainly be increased above ~ 2.4 bar. The weak point at the moment is the blow off value. This can easily be adjusted to burst at higher pressures.

An investigation of the pressure range that the PC is capable of holding should first be carried out at RT. This can be done by connecting the PC to a gas bottle.

The pressure cell can be used to continue investigating breakdown measurements across a ceramic surface. Two new electrodes would need to be manufactured. These have been designed (Appendix F). These have the same profile as the PC electrodes but include a groove which has the same geometry as the DKHs small electrodes. Between them they will hold a length of 10 × 15 mm Al_2O_3 ceramic tube. The ground electrode can easily be adjusted to be spring loaded.

The PC could be used, without the can, to measure high voltage breakdown across a ceramic as a function of temperature at SVP. The next obvious test is to measure high voltage breakdown across a ceramic as a function of both temperature and pressure. This would indicate if increasing the pressure of the helium increases the breakdown voltage when a ceramic is between the electrodes.

The overall picture of breakdown across ceramic spacers at SVP has gaps in the data. Additional data in He II at larger separations is needed. This would need to be made by either the DHKl electrodes in the KEK or the DKHs electrodes in the KEK as the DKHs electrodes will start to breakdown to the side of the glass cryostat above separations of ~ 3.5 mm. The DKHl electrodes can be used to do breakdown tests at smaller separations. Direct comparison could then be made between data from the DKHl and DKHs electrodes at similar separations. Analysis of the electrodes and ceramic after experimentation would provide clues to any surface area effect, volume effect or the effect of increasing the CTJ.

Breakdown measurements can be made with electrodes with the same dimensions as the Ramsey cell electrodes. This would require a larger test setup, currently under construction at Sussex. This would give direct comparison to the magnitude of E-field capable of being established in the Ramsey Cell of the main experiment.

Appendix A ILL High Voltage Data

High Voltage was applied across the CryoEDM Ramsey Cell in June 2009 and December 2010 at the ILL.

Section A.1 presents data from the June 2009 CryoEDM run. The highest voltage applied across the Ramsey cell was – 30 kV and + 29.5 kV. This produced a maximum E-field of 6.7 $kVcm^{-1}$.

In section A.2 data from the December 2010 CryoEDM run is presented. The Ramsey cell was charged to a maximum voltage of + 47 kV and – 40 kV. This produced a maximum E-field of 10.4 $kVcm^{-1}$ across the Ramsey cell. Also include in this section is an experimental method report from the December 2010 run.

During the high voltage ramping in December 2010 a number of breakdown events were observed. Once the CryoEDM apparatus had warmed back to room temperature an inspection of the CuBe electrodes and BeO ceramic spacers was carried out. Section A.3 outlines the findings of this inspection. An Opera vector fields E-field plot of the Ramsey cell electrodes is also present. This plot shows where the E-field is highest on the Ramsey electrodes.

All plots and data can be found on the cryoEDM internal web page (Davidson 2009, Davidson 2011).

A.1. ILL June 2009

High voltage was applied to the Ramsey Cell in June 2009 by the Sussex group. The high voltage apparatus consisted of a non magnetic G10 feedthrough, two JRK Ti ball electrodes, a JRK PTFE HV feed (± 130 kV), Spellman cable (± 130 kV) and two Spellman power supply (positive and negitive), figure.A.1.

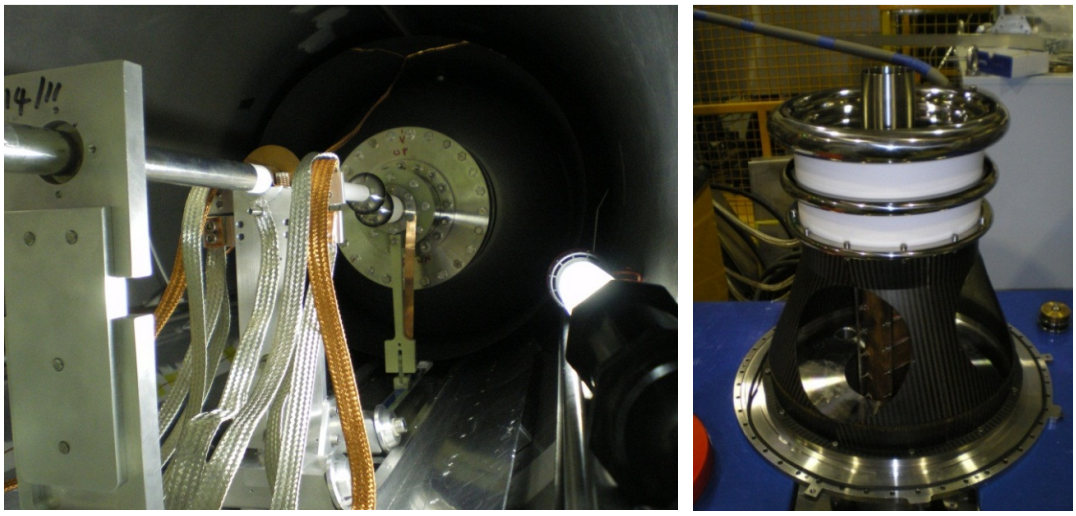

Fig..A.1. Photograph of the HV apparatus on the cryoEDM experiment during assembly 2009. Left: HV apparatus inside the Yoshiki Sheilds; Right: Ramsey Cell with Ti electrodes, HV electrode diameter ~ 30.5 cm, Ground electrode diameter 29.4 cm and the separation between electrodes is 4.5 cm. Also visible are the BeO cylindrical spacers, inner diameter 25 cm and outer diameter 26.1 cm.

Before HV was applied across the Ramsey Cell the feed was ramped up to ± 30 kV. During this time the Ti ball electrodes were ~ 94 mm apart. When charging the feed in positive polarity breakdown did occur at ~15 kV. The voltage recovered and made it to 30 kV where it remained stable.

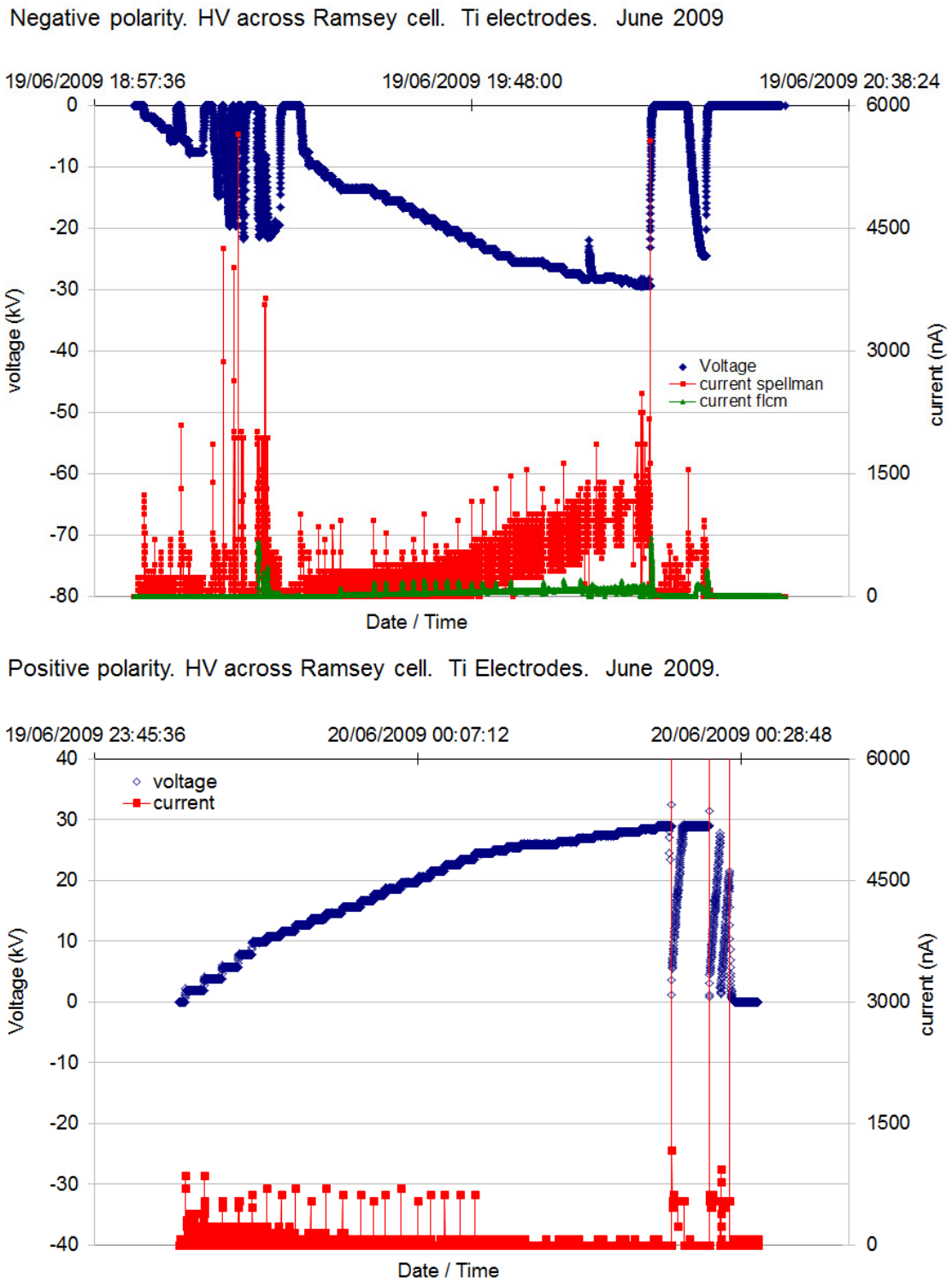

Fig..A.2. High Voltage as a function of time for cryoEDM run June 2009. Top: negative polarity; Bottom: positive polarity.

The capacitance of the feed was monitored as the feed was screwed in. When the two Ti ball electrodes touched there was a change in capacitance of ~ 18 μF. The Ramsey cell was charged to – 30 kV and + 29.5 kV, figure.A.2. Breakdown did occur at + 29.5 kV. At this point the DAQ computers had crashed. On inspection of the data the computers had crashed ~ 2 minutes before the breakdown event. The maximum E-field across the Ramsey Cell during the run was 6.7 $kVcm^{-1}$.

A.2. ILL December 2010

High voltage was applied across the Ramsey Cell in December 2010. The Ramsey Cell electrodes are now made from Be and have a CuBe corona dome, figure.A.3.

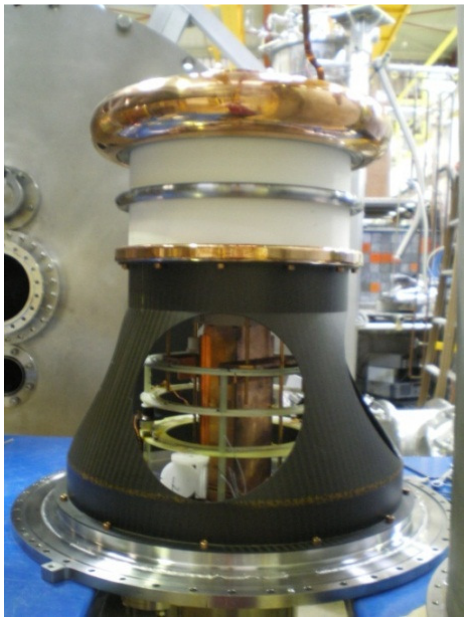

Fig..A.3. Photograph of the Ramsey Cell. Ramsey Cell shown with Be electrodes, CuBe corona dome and BeO ceramic spacers.

The following is the experimental method report on the application of high voltage across the Ramsey cell in December 2010. The highest E-field achieved was 10.4 $kVcm^{-1}$.

Appendix A ILL High Voltage Data

High Voltage applied across the Ramsey cell December 2010 (Reactor Cycle 160).

30/11/10 HV feed moved in until contact with Ramsey cell connector.

The HV feed was moved in and out of contact with the Ramsey Cell connections. The capacitance was measured for 3 different circuits.

Summary below.

SCV temperature before the HV feed was moved 0.57 K.

10:56 HV feed position 250 mm, HV feed not touching. Capacitance 0.06 nF

11:18 HV feed position 213 mm, HV feed in contact. Capacitance 0.26 nF between HV feed and ground. Tiny leak observed on OVC vacuum, this quickly recovered.

11:20 HV feed not touching.

11:26 HV feed not touching. Capacitance 0.05 nF for the meter on its own.

11:26 HV feed position 234 mm, HV feed not touching. Capacitance 0.10 nF between HV feed and return line FT.

11:26 HV feed position 213 mm, HV feed in contact. Capacitance 0.12 nF

HV feed not in contact. Capacitance 0.26 nF between the return line and ground.

HV feed moved in until contact and left in this position, 213 mm.

11:51 Temperature increased to 0.58 K.

01/12/10 Testing spellmans power supplies only.

The negative Spellman power supply was turned on using the optical computer control. The HV computer in the cryoedm cabin was used to operate the Spellman. The Spellman was ramped up to – 10.1 kV. It was not in contact with the cryoedm HV feed. The Spellman was left on at – 10.1 kV over night to insure it could hold voltage for this long period. There were no problems with the HV computer and optical control.

02/12/10 Ramping up The Spellman every 30 s and 300 s to – 10.1 kV

11:24 The Spellman power supply was still at – 10.1 kV. It was turned off then ramped back up to – 10.1 kV.

12:10 The cryoEDM labview programme was set to ramp the Spellman up to - 10.1 kV every 30 s.

12: 46 The cycle time was increased from 30 s to 300 s.

03/12/10 Applying HV across the Ramsey Cell

The HV connector was placed over the HV feed. The HV cable was connected between the positive Spellman power supply and the HV connector. The cryoEDM apparatus was grounded to the Spellman power supplies. Conductivity checks were carried out to check that the apparatus was grounded.

A multimeter was connected in series in the ground return line. From the return line feedthrough to the Spellman power supply. The multimeter was set to volts. When charging the induced charging current is observed as a voltage across the internal impedance of the multimeter.

The HV apparatus is shown in figure.A.4.

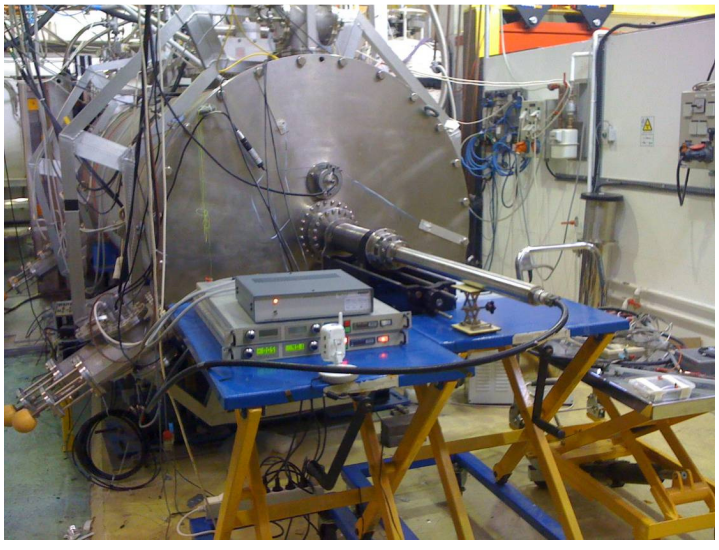

Fig..A4. HV apparatus at the ILL December 2010.

Positive polarity

At ~ 12:05 the HV was turn on. An induced charging current was observed through the ground return line multimeter. Figure.A.5 shows data for the initial positive HV ramp.

The voltage was ramped up in steps of ~ 2 kV. It was then left at that voltage for ~ 3 mins below 30 kV and ~ 5 mins after 30 kV. The voltage was then turned off. The charging current was set to 0.5 µA on the HV computer control. This was actually 0.6 µA as observed on the Spellman power supply. The charging current can be clearly seen in blue in figure.A.5. It corresponds directly to the time the system is ramping up in voltage. After 5 mins at 35 kV the system was programmed to reduce in voltage to 30 kV. At this point a partial discharge occurred. The system recovered to 30 kV and held stable for approximately 3 hours. The voltage was then switched off.

At ~15:57 the voltage was increased. The voltage was ramped up in 2 kV steps and left for 5 mins. At 16:31 when the voltage was at 47 kV the first catastrophic breakdown occurred. This killed the digital multimeter.

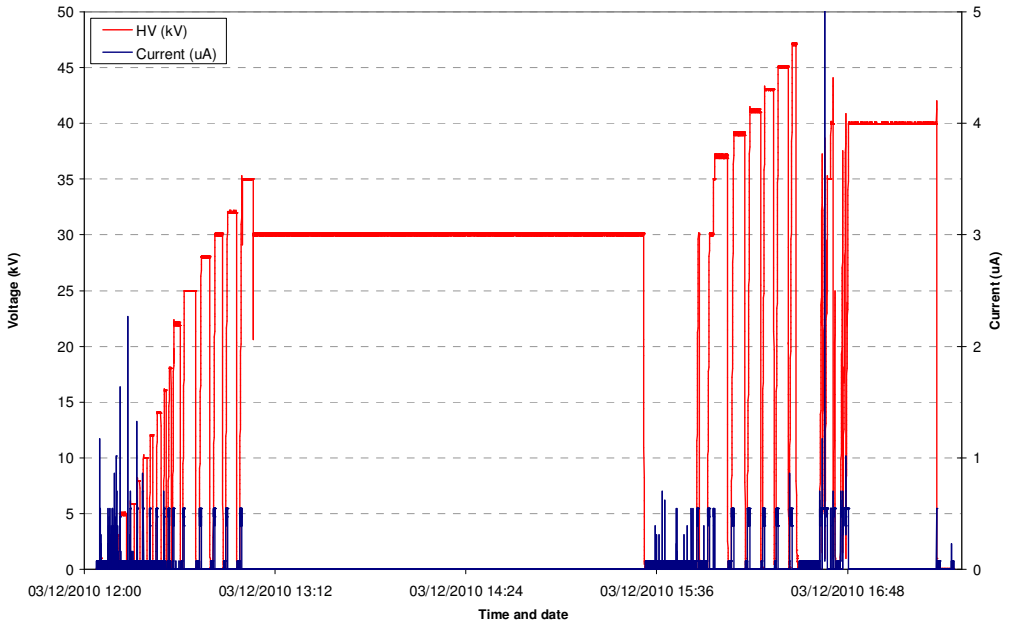

Fig..A.5. Initial positive HV ramp.

After a brief check of instrumentation it was assumed that no instrumentation had been damaged by the HV breakdown apart from the multimeter in the ground return line. The multimeter was then removed from the return line.

The voltage was then set to ramp to 40 kV. However, there were a number of breakdowns and partial breakdowns as it ramped up to 40 kV. These are shown in detail on figure.A.6.

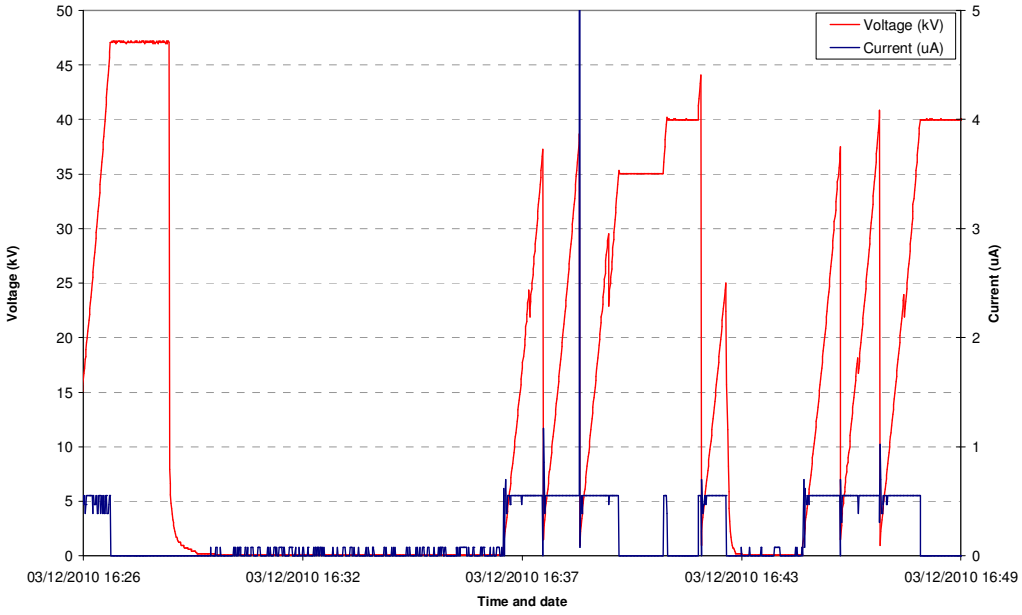

Fig..A.6. Initial positive breakdown events.

Three types of breakdown were observed. The first is a catastrophic breakdown where the voltage drops sharply. The Spellman power supply automatically turns itself off. As the system returns to 0 volts a curved reduction in voltage is observed.

The second type is again a sharp reduction in the voltage. However, this time the Spellman does not turn itself off. It starts to ramp up again (In nearly all cases this type of breakdown is observed in Lab 3A18).

The third type is a partial breakdown where the voltage dropped by only a few kV and then ramps up again.

In total there were 2 of the first type of breakdown 5 of the second and 4 partial events. The system then recovered to 40 kV. When a breakdown event of any type occurred the current reduced to 0 μA.

Negative polarity

The HV cable was removed from the back of the positive Spellman and put into the negative one. The system was turned on and ramped up in – 2 kV steps. It was then left for a period of time, figure.A.7.

The voltage was ramped up in – 2 kV steps and then left for ~ 3 minutes before being turned off. For voltages higher than – 26 kV the voltage was not ramped down in between steps. The breakdown events are clearly shown in figure.A.8.

The negative breakdown events can also be categorised into 3 groups. The maximum voltage reached was - 40 kV. It was stable for ~ 3 mins before being switched off. No breakdown was observed between – 33 kV and – 40 kV.

Overnight positive stability tests.

Two overnight stability tests were carried out. The first, 03/12/10, held 40.1 kV across the cell while the cell valves opened and closed. The second, 04/12/10, held 40.1 kV across the cell. The valves were operational and Neutrons were filling into and emptying from the cells. There were no breakdown events at any point during the run.

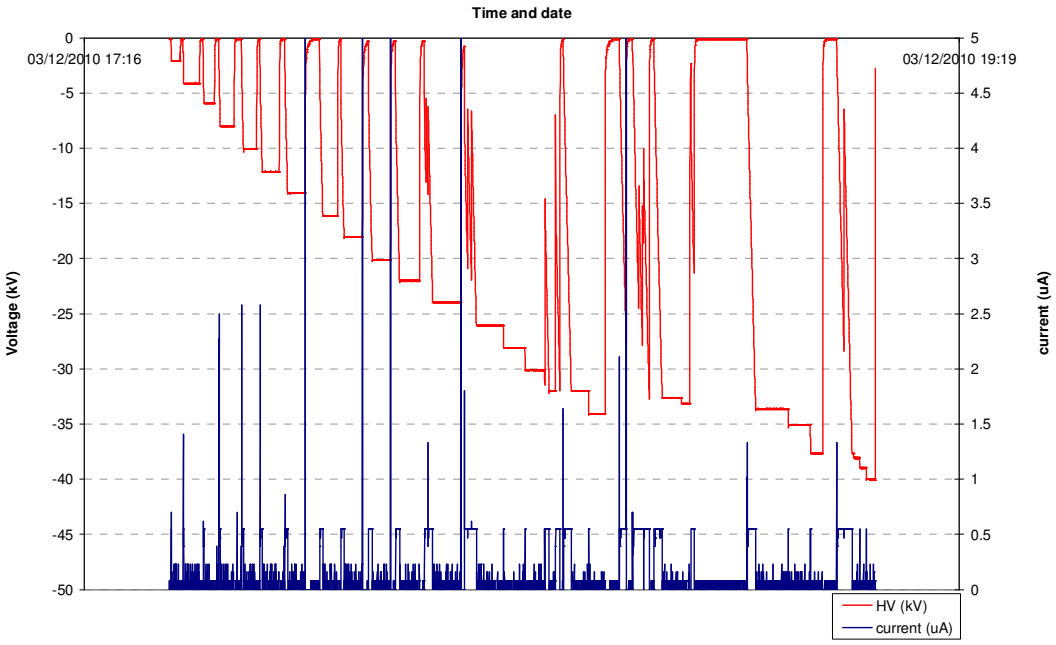

Fig..A.7. Negative HV ramp.

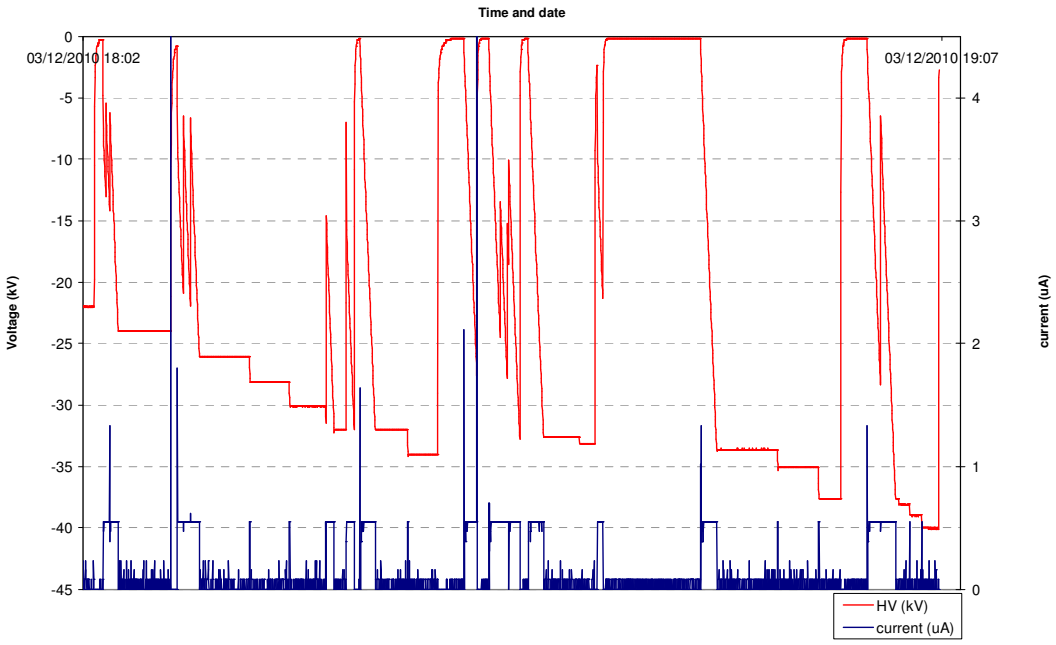

Fig..A8. Negative Breakdown events

A.3. Surface Inspection of Be HV electrode and BeO ceramic April 2011

The surface of the Be HV electrode was inspected after the apparatus had returned to room temperature. A number of features on the surface looked like suspected breakdown damage. Inspection under a microscope showed that the features look like mechanical chips off the surface, figure.A.9. This was probably caused when the electrodes were mechanically polished as the chips were all orientated in a circumferential direction. There was no obvious sign of any breakdown damage to the Ramsey Cell Be electrodes.

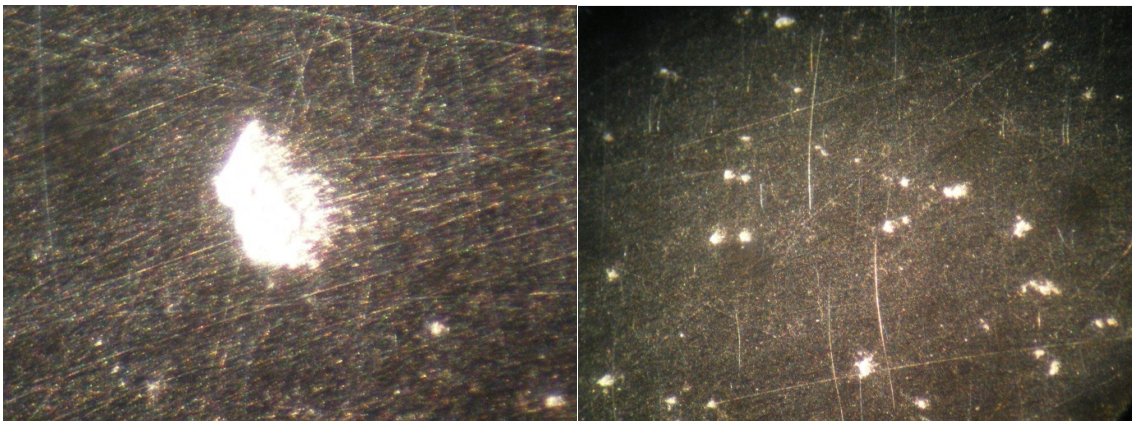

Fig..A.9. Microscopic photograph of the chips found on the surface of the HV Be electrode.

BeO ceramic spacer

Inspection of the surface of the BeO spacer that makes contact with the Be electrode a number of black marks were obsereved, figure.A.10. The black marks occurred at regular spacing. A number of chips off the edge of the BeO cermaic spacer were also observed.

Fig.A.10. Photograph of black marks found on the edge of the Ramsey Cell BeO ceramic spacer.

Visual and microscopic inspection of the CuBe corona dome

It is clearly visible that there had been discharges around the edge of the CuBe corona dome, figure.A.11. Microscopic images show discharges on the surface of the CuBe corona dome had ejected material onto its surface. Jets of material are clearly visible on the surface of the corona dome, figure.A.11, being initiated from a defect on the surface.

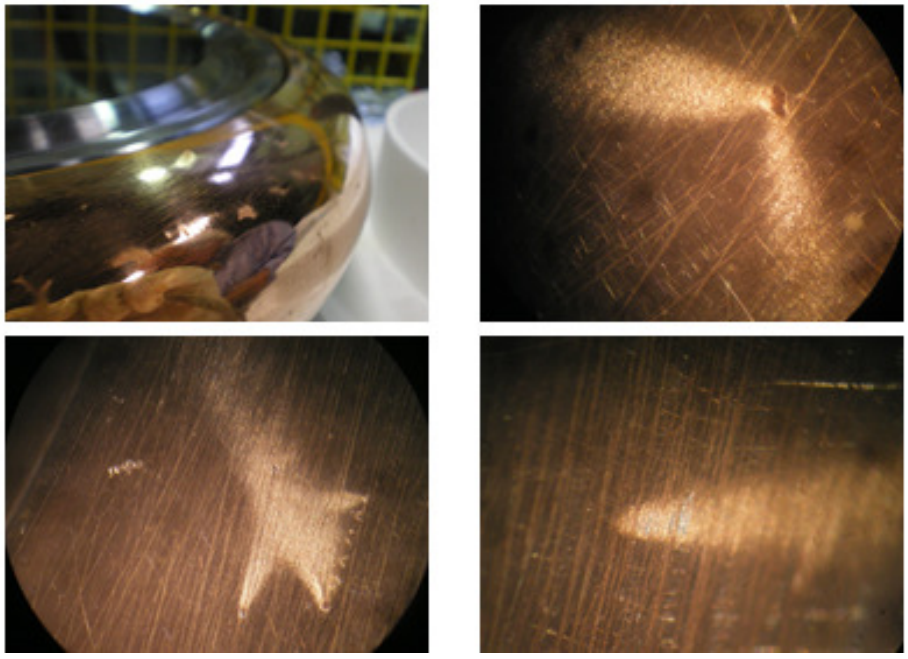

Fig..A.11. Photographs and microscopic photographs of the Ramsey Cell CuBe corona dome.

The Corona dome was made by spinning. This would put strain on the material causing cracks on its edge during manufacture. Mechanically polishing would have covered over the cracks and voids. Under the intense tension of a high E-field material would be ejected from the voids. Inspections of the pits under the microscope suggest the material was molten. Thus, it is probable that the breakdown observed in December 2010 initiated from the corona dome.

E-Field Plot of the Ramsey Cell and Corona Dome

An E-field plot of the Ramsey cell and corona dome was calculated using Opera Vector Fields. When 100 kV is applied across the Ramsey Cell an E-field of ~ 15 $kVcm^{-1}$ to 20 $kVcm^{-1}$ is on the corona dome. The highest E-field is at the egde of the middle electrode, figure.A.12. It has an E-field of ~ 45 $kVcm^{-1}$.

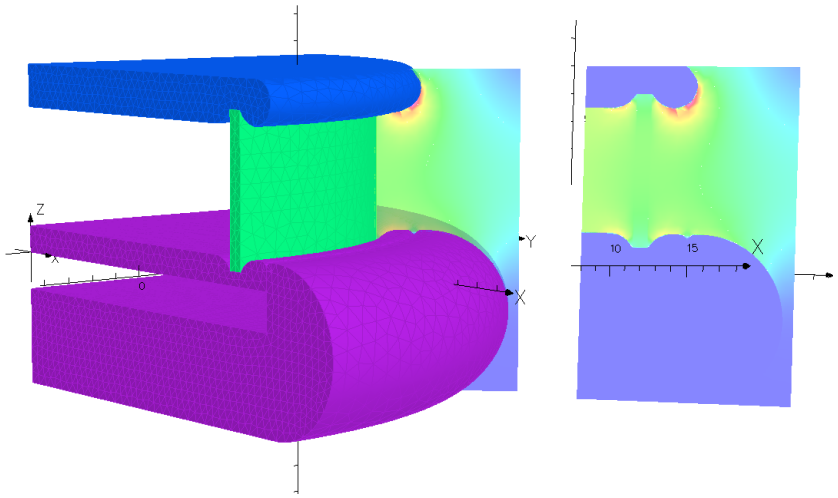

Fig..A.12. Opera vector field plot of the E-field produced on the Ramsey. Highest E-field is shown in red on the outside edge of the ground electrode. The magnitude of the E-field is ~ 45 $kVcm^{-1}$ when 100 kV is applied across the cell.

Appendix B Additional Opera Modelling

Opera Vector Fields was used to investigate the electrostatics of the two ± 30 kV commercial feedthroughs used in the PC. The centre conductor and cap of the ± 30 kV feedthrough is charged to 30 kV. The CF flange is grounded. Figure.B.1. shows the electrostatics profile of the ± 30 kV feedthrough. The highest E-field occurs on the centre conductor between the grounded flange. The magnitude of this E-field is ~ 130 $kVcm^{-1}$.

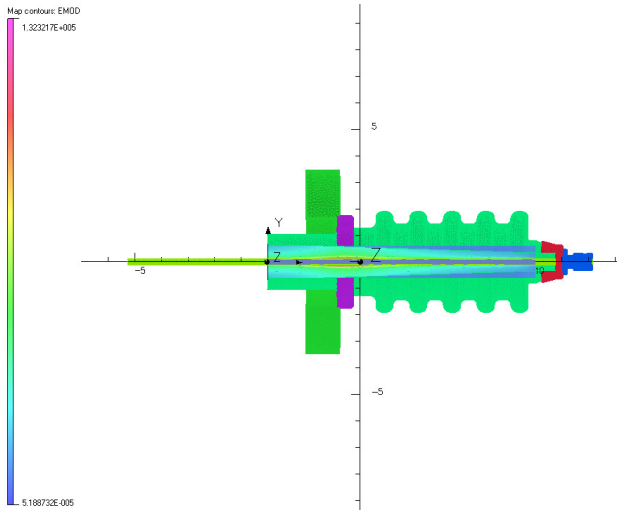

Fig..B.1. Opera Vector Field model of the ± 30 kV commercial feedthrough in a vacuum. Centre conductor and cap charged to 30 kV and CF flange grounded.

In an attempt to reduce the E-field on the centre conductor a PTFE tube has been placed around it. The E-field, calculated by Opera vector fields, has a maximum value of ~ 85 $kVcm^{-1}$, Fig.B.2. For experiments with and without a PTFE sleeve see AJD DPhil experimental lab book number 2 page 57.

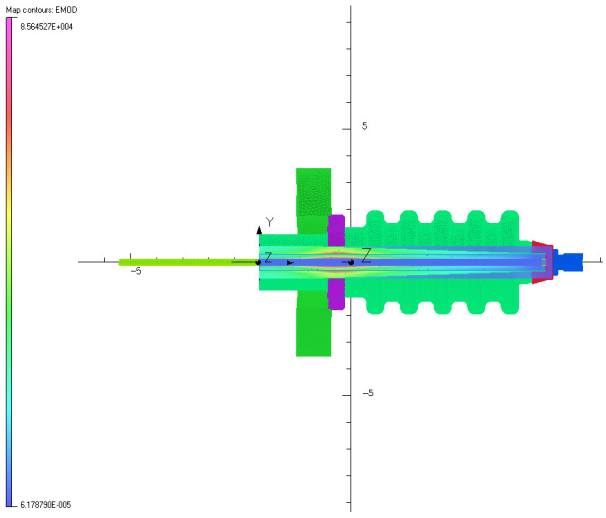

Fig..B.2. Opera Vector Field model of the ± 30 kV commercial feedthrough with a PTFE tube around the centre conductor in a vacuum. Centre conductor and cap charged to 30 kV and CF flange grounded.

Opera Vector Fields was used to model the E-field for a proposed changed to the 2007 SCV. The E-field map, Fig.B.3, showed the electric field at the new modified corner was less than the E-field elsewhere in the experiment so the decision to adapt the apparatus went ahead.

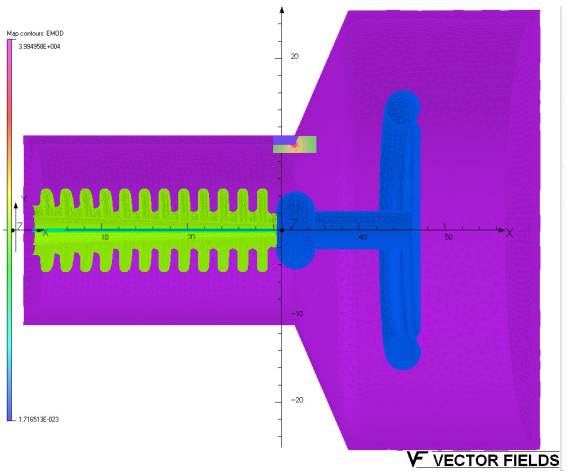

Fig..B.3. Opera Vector Field model of the 2007 SCV. E-field map of the electrostatic environment inside the SCV after modification of the design. The high voltage electrode is set to 160kV. Also included are the HV electrode and a commercial feed through.

Appendix B Additional Opera Modelling

An investigation into the magnitude of the E-field if the BeO ceramic of the Ramsey cell is aligned slightly off centre, either nearer the inside or outside base of the groove, was carried out in collaboration with Lee Suttle using Opera vector fields. This is relevant as the Ramsey cell gets assembled vertically and then gets installed horizontally. During this process it is possible that the BeO might move. The results showed that the off centre ceramic would cause little change to the E-field, ~ 1%. This investigation is covered in detail by Suttle (Suttle 2010).

Appendix C Breakdown Damage to an Electrode Surface

The following report, made during the course of this thesis, is on damage created to the surface of an electrode as a result of high voltage breakdown. This work was carried out in collaboration with Hill (Hill 2009), Suttle (Suttle 2010) and Munday (Munday 2010). All AFM profiles and pictures were produced by Munday.

A number of SEM pictures are presented. They show the crater characteristics for Ti electrodes.

C.1. Investigation of damage to an electrode surface created by high voltage breakdown in liquid helium

When breakdown occurs, it causes damage to the electrode surface as shown in Fig.C.1. These are SEM pictures of damage to a Titanium, (Ti), electrode surface as a result of high voltage breakdown in He I at 4.2K under SVP. This was previously a concern for the cryoEDM experiment as the Ramsey Cell electrodes were made from Ti and coated with a layer of diamond-like carbon, (DLC). The neutrons see a high Fermi potential when hitting the DLC and are reflected back into the cell. However, Ti has a low Fermi potential so if the neutrons hit Ti they will pass through it. If the damage caused to the electrodes' DLC expose the Ti then neutrons will be lost from the cell.

The cryoEDM apparatus has now been upgraded. The new electrode material is Beryllium and hence the problem of crater depth has been removed. However, if when the electrodes are damaged, nano particles are ejected into the helium volume on breakdown, this can cause problems. The very low energy ultra cold Neutrons (UCN) can be up-scattered if they hit a nano particle and then be able to pass through the cell walls.

Appendix C Breakdown Damage to an Electrode Surface

It is therefore important to understand the damage sustained to the electrode surface after breakdown.

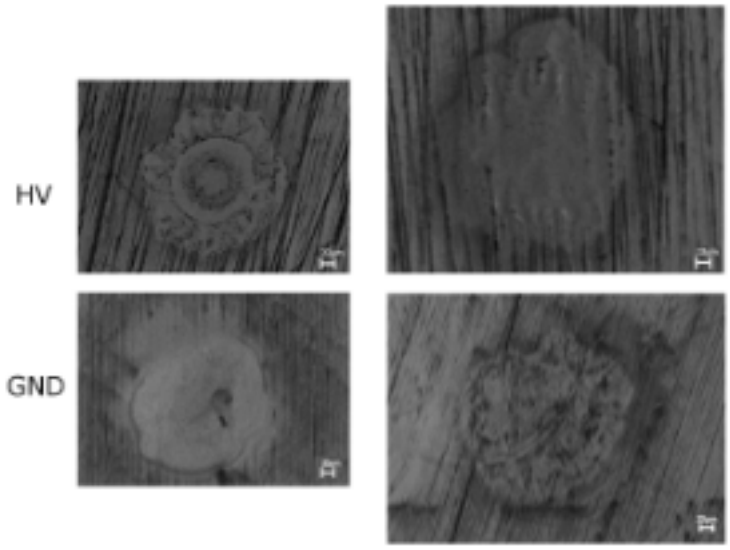

Fig..C.1. SEM pictures of high voltage breakdown damage created to Ti electrodes with and without a 1 GΩ resistor is placed in the HV line (Hill 2009). Left: Breakdown damage to the HV (cathode) and ground (anode) Ti electrodes; Right: Breakdown damage to the HV (cathode) and ground (anode) Ti electrodes when a 1 GΩ resistor is in the HV line.

High voltage breakdown tests indicated there may be a reduction to the damage caused to the electrode surface when a 1GΩ resistor is placed in the high voltage line Fig.C.1. (Hill 2009). The number of discharges with and without the resistor correlated to the number of each type of damage crater. It was observed experimentally that light emission occurred at breakdown. The intensity of light reduced when the resistor block was in the high voltage line. These observations provided evidence to suggest that when a resistor is placed in the high voltage feed line it limits the discharge energy.

Appendix C Breakdown Damage to an Electrode Surface

Experimental Apparatus Development

SEM and optical microscope pictures provide good images of the damage craters. However, they don't give any information about the depth profile of the craters. One method of scanning the profile is by using an AFM. Electrode caps were designed and manufactured (Munday 2010, Suttle 2010) that could be mounted into an AFM. These also screwed onto the small DKHs electrodes Fig.C.2. It was thus possible to measure the depth profile of the damage created to these caps on breakdown.

Fig..C.2. Photographs of the DKHs electrode with caps. Left: DKHs electrode and cap; Right: Cap screwed into the tapped hole in the center of the DKHs electrode.

Data

A number of experiments have been carried out to study breakdown damage to an electrode surface in both He I and He II. The amount of energy available on discharge was varied. Two methods were used to do this. The first by increasing the separation between the electrodes and therefore breakdown voltage and secondly, by adding a large resistor into the high voltage feed line.

The first cap test was in He I at 4.2 K under SVP with no resistor in the high voltage line. The energy available on discharge was varied by choosing two electrode cap separations. These were 1.4 mm and 2.8 mm.

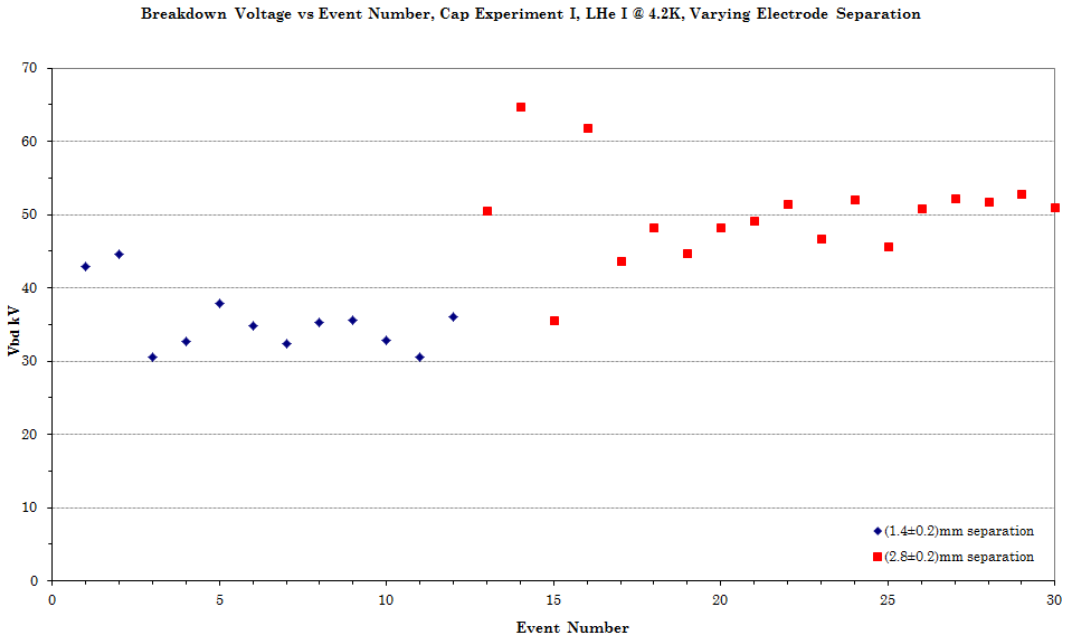

Fig..C.3. Breakdown voltage as a function of event number. Blue diamonds: 1.4 mm electrode cap separation; Red squares: 2.8 mm electrode cap separation.

After the run the caps were removed and the AFM was used to distinguish breakdown damage (Munday 2010). No obvious difference in the depth or diameter of crater was observed. This may not be surprising as there is no clear raise in V_{bd} with increased separation as shown on Fig.C.3. The AFM depth profile plots revealed that the damage craters were formed from multiple smaller craters. A typical 3D scan using the AFM is shown in Fig.C.4 (Munday 2010).

Breakdown damage was investigated in He I and He II with the inclusion of a large 0.5 GΩ resistor in the high voltage line at fixed electrode separation. It was observed that when the resistor was in line it changed the breakdown behavior. On breakdown the voltage did not drop catastrophically to 0 V but instead reduced by approximately 10 kV and then started to charge back up. It was also observed that on breakdown light emission was reduced, suggesting less energy was being discharged.

Appendix C Breakdown Damage to an Electrode Surface

The AFM was again used to analysis the electrode caps. It was observed that there were no significant differences in crater depth or diameter. The damage to the craters again looked like it was made up of a sequence of smaller pits (Munday 2010).

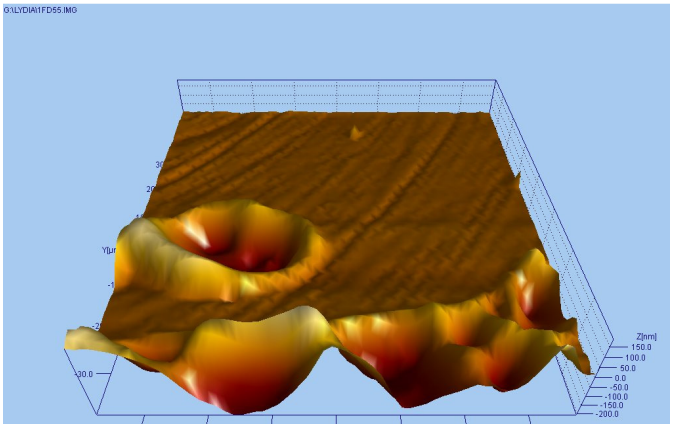

Fig.C.4. AFM profile map of a breakdown carter on the surface of a stainless steel cap (Munday 2010).

These smaller pits suggest the breakdown is not a sudden discharge but a continuous multiple impact discharge. If this is true, then one might expect little variation in the damage depth. The multiple discharges will sweep the surface of the electrode in a localized area causing the damage. One might also expect to see a change in the diameter of the damaged area as the resistor will limit the charge available and therefore turn off the discharge sooner. However, there was no sign of any difference in damage diameter. For more detail see Munday and Suttle (Munday 2010, Suttle 2010)

Summary and further work

Our current understanding is that the high voltage breakdown in LHe is a multiply impact continuous discharge. The AFM depth scans show the damaged area of the electrode surface is itself made up of multiply small craters. When breakdown is triggered the

discharge sweeps the surface of the electrode causing damage to a localised area until it switches off.

The inclusion of a resistor in the high voltage line has experimentally been observed to limit the energy available at discharge. However, AFM scans of the electrode surface have not seen any difference in crater type. This new data contradicts the previous data taken in using the Ti electrodes and a 1GΩ resistor in He I. Two distinct crater types were observed. Further tests with the resistor placed in the high voltage line are needed to investigate what effect this has on breakdown damage.

In these experiments the resistor was positioned between the high voltage feed and power supply. There was a length of high voltage cable connecting the power supply to the resistor and then an additional length connecting the resistor to the feed. On breakdown the capacitance of the length of high voltage cable between the resistor and feed is available for deposition. It would therefore be more advantageous to place a resistor right at the bottom of the feed line between the feed and the electrodes. This would greatly reduce the charge available for breakdown.

SEM pictures of breakdown damage on the surface of Ti electrodes.

SEM pictures of the damage created to a Ti HV cathode and Ti ground anode are shown in Fig.C.5. and Fig.C.6. The shape of the damage caused to the cathode and anode is different. Figure.C.5 shows a circular ring formed on the cathode as a result of high voltage discharge.

Scratches on the surface disappear in the region of the discharge on both the cathode and the anode. This is evidence that the discharge has had enough local energy to melt the surface of the electrode.

Appendix C Breakdown Damage to an Electrode Surface

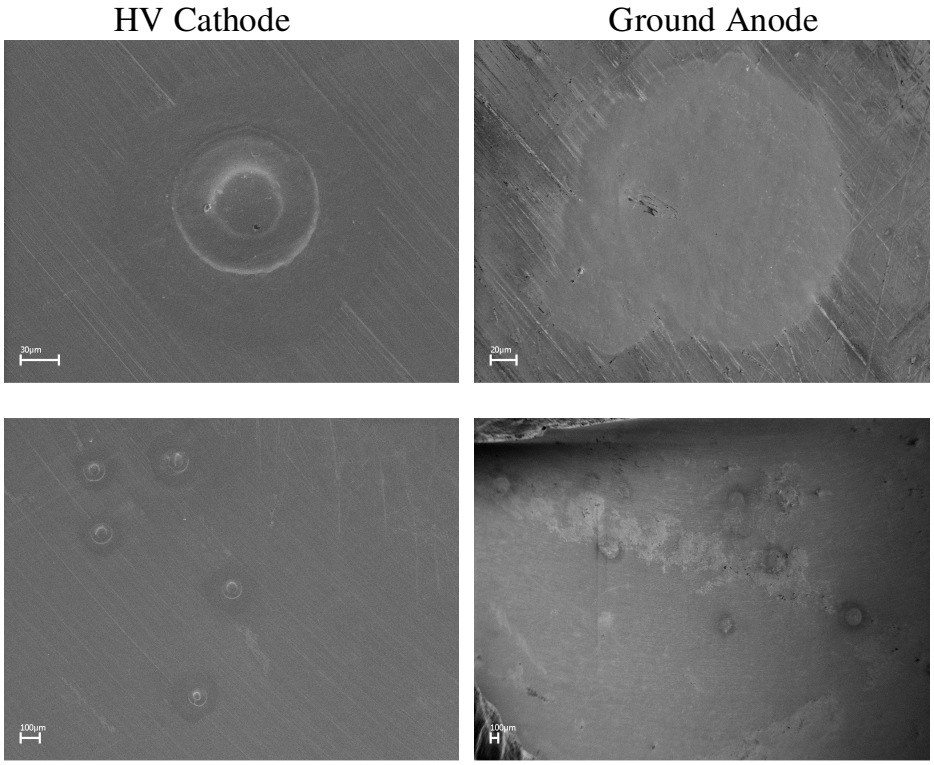

Fig..C.5. SEM pictures of breakdown damage to the surface of Ti electrodes. Left: HV cathode; Right: Ground anode.

Fig.C.6. shows directly opposite areas of the cathode and anode. It is clear that the breakdown patterns match, they are a mirror image. This suggests that the discharge propagates the gap in the direction of the applied E-field.

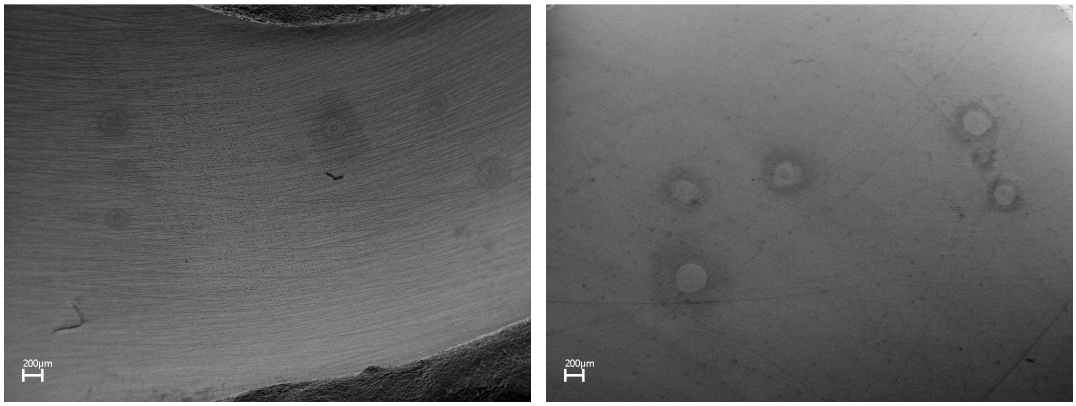

Fig..C.6. SEM pictures of breakdown damage to the surface of Ti electrodes. Left: HV cathode; Right: Ground anode.

Appendix D High Voltage feedthrough leak tests-Superleak

Before installation of any high voltage feedthrough onto either the cryo-edm experiment or the PC experiment the superfluid integrity of the feedthrough has to be tested. In one particular case a ceramic Ti feedthrough was tested and it was found to have a superfluid leak. The results from this superfluid leak test are shown on Fig.D.1.

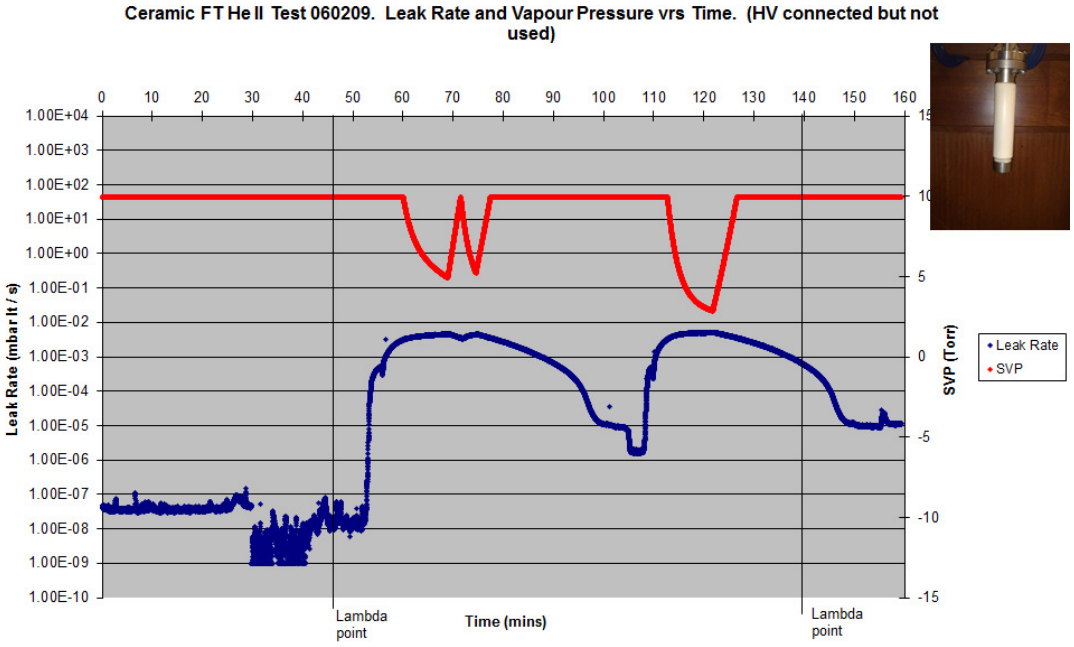

Fig..D.1. Leak rate and SVP, between 0 and 10 torr, versus time of the superfluid integrity of a ceramic Ti feedthough in He II. Blue: leak rate; Red: SVP of the bath between 0 and 10 torr only. The back vertical lines represent the time the temperature of the liquid Helium was at the lambda point.

The feedthrough is mounted onto the end of a hollow stainless steel insert and then inserted into a bath cryostat. The inner volume of the stainless steel tube and feedthrough are evacuated. The leak rate of the inner volume is monitored over the run. From room temperature down to the lambda point the leak rate was ~ 10^{-7} mbar lt s^{-1}. The leak rate is observed to drop by approximately an order of magnitude when the stainless steel tube starts cryo-pumping.

Appendix D High Voltage feedthrough leak tests-Superleak

Just below the lambda point the ceramic Ti feedthrough picks up a leak. The leak rate increases by ~ 5 orders of magnitude to ~ 10^{-3} mbar lt s^{-1}. Reducing the temperature of the bath, shown by the SVP on Fig.B.1, increases the leak rate. Allowing the bath to warm up reduces the leak rate. Figure.B.1. shows a direct correlation between the temperature of the bath and the leak rate. The SVP could only be measured between 0 and 10 torr. Any higher pressure is represented by the flat region on Fig.B.1. The points where the SVP crossed the lambda λ-point are shown.

This observation agrees well with the two fluid model of liquid Helium. As the temperature of the bath reduces the density of the He II increases which causes the leak rate to increase.

Appendix E Rogowski profile electrodes for ceramic tests in the PC

A pair of Rogowski profile electrodes have been designed for the PC, Fig.E.1. They are the same size and profile as the original PC electrodes however the DKHs electrode groove profile is also a feature of their surface. This allows the electrodes to hold a 10 x 15 mm Al_2O_3 ceramic sample. Therefore breakdown tests can be carried out in He I or He II under pressure with the addition of a ceramic between the electrodes. The ground electrode can easily be spring loaded to ensure the ceramic is in contact with both electrodes over the total run period.

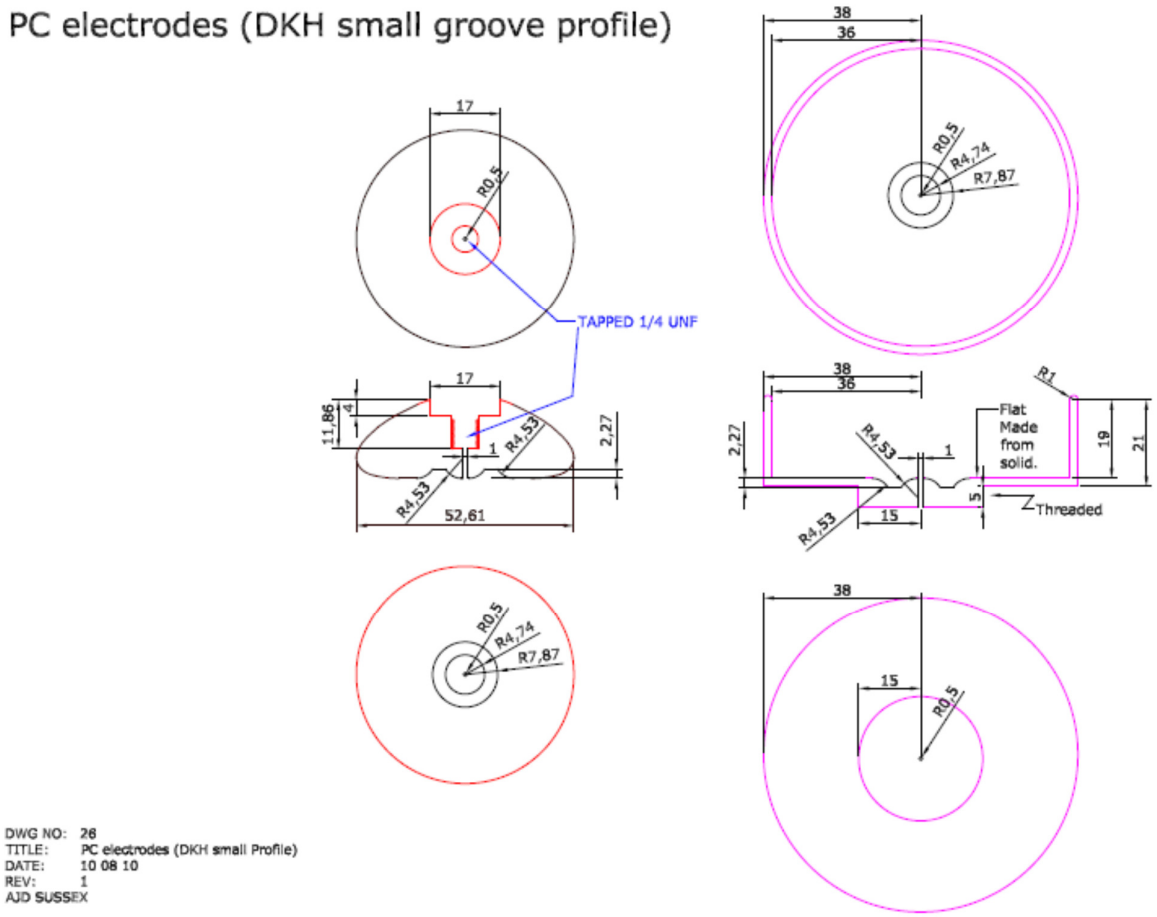

Figure..E.1. AutoCAD drawing of the Rogowski profile electrodes for the PC. The DKHs electrode groove profile is a feature of these electrodes.

Appendix F Dimensions and Drawings of the DKH large and small electrodes

The dimensions of the electrodes used for the ceramic tests, designed by Hill (Hill 2009) are shown below, Fig.E.1 and Fig.E.2. The DKHl electrodes have a radius of 62.5 mm. The groove is 5.53 mm deep and has a radius of curvature of 10.07 mm. The flat surface at the bottom of the groove has an ID of 25.5 mm and an OD of 36.76 mm. The smaller DKHs electrodes have a radius of 29.19 mm. The groove has a radius of curvature of 4.53 mm and is 2.27 mm deep. The groove surface has an ID of 4.75 mm and an OD of 7.88 mm. The DKHl electrodes were design to hold a ceramic tube with diameter 60 × 70 mm and the DKHs electrodes design to hold ceramic tube 10 × 15 mm. Modifications to the original design were made during manufacture, Fig.E.3.

Fig..F.1. The DKHs and DKHl Rogowski profile electrodes.

Appendix F Dimensions and Drawings of the DKH large and small electrodes

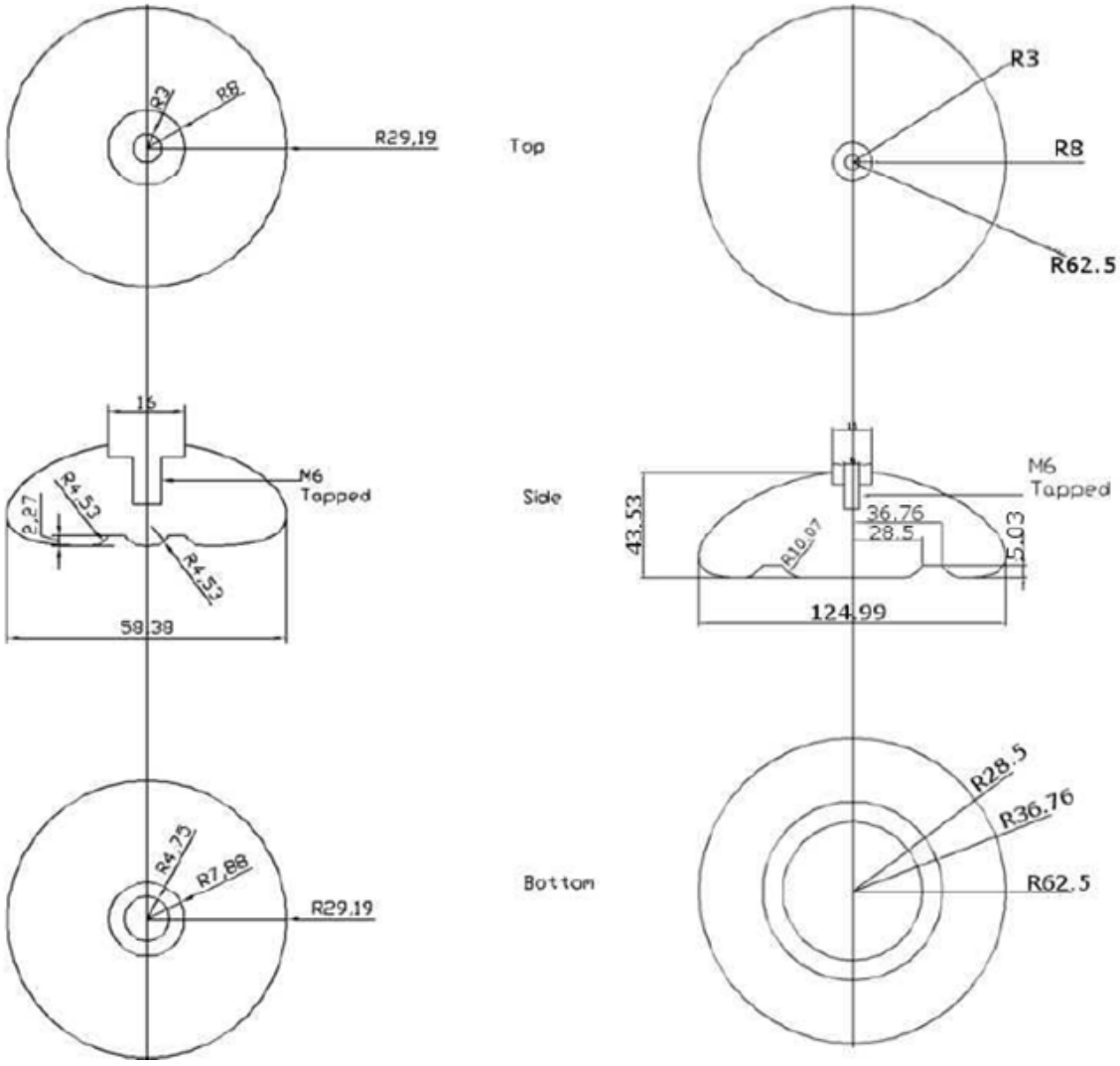

Fig..F.2. Technical drawing of the DKHs and DKHl Rogowski profile electrodes used for the CTJ breakdown tests (Hill 2009).

Appendix F Dimensions and Drawings of the DKH large and small electrodes

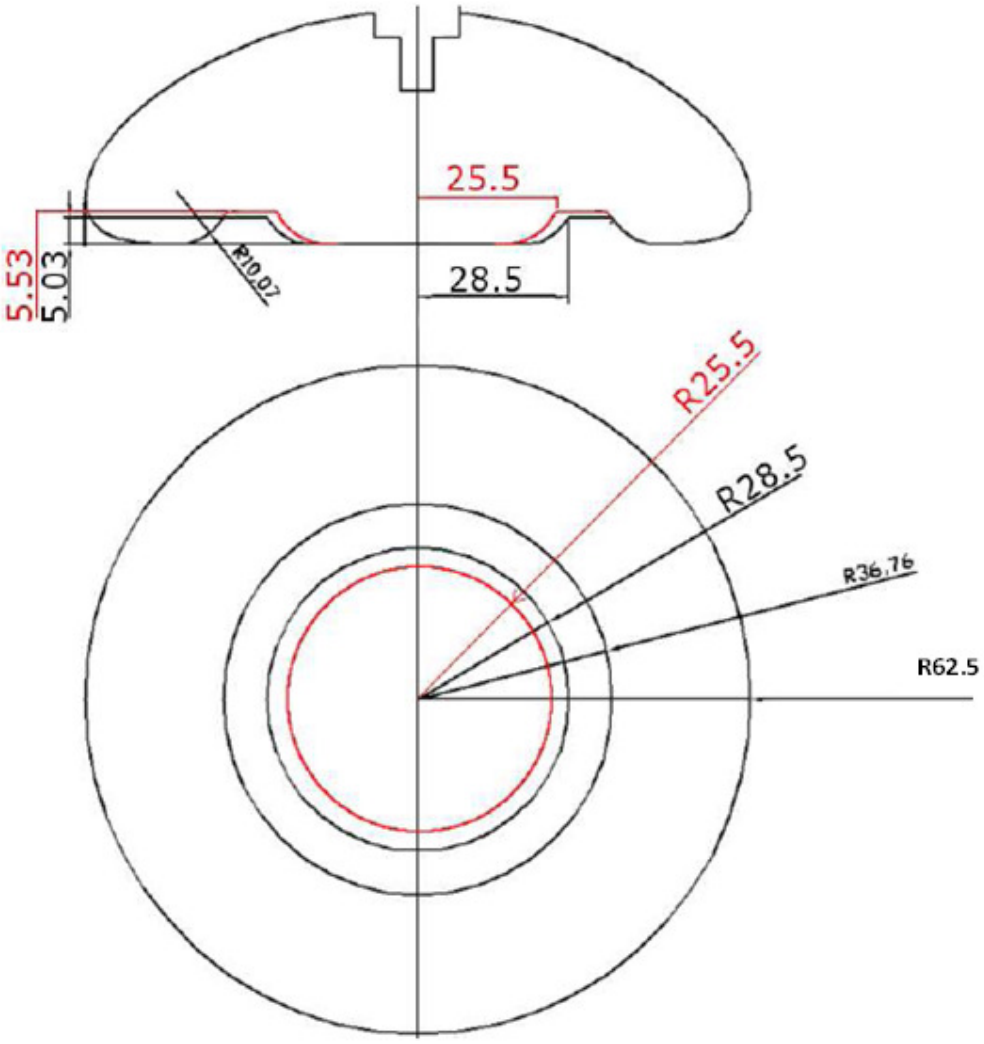

Fig..E.3. Technical drawing of the modifications to the DKHl Rogowski profile electrodes (Hill 2009).

Appendix G E-Field models of the Ramsey Cell

In order to know the extent of the E-field in the Ramsey cell when a voltage is applied across it calculations were carried out using Opera vector fields. In order to produce the most accurate model the HV electrode groove surface profile was scanned at RAL metrology department, Fig.G.1.

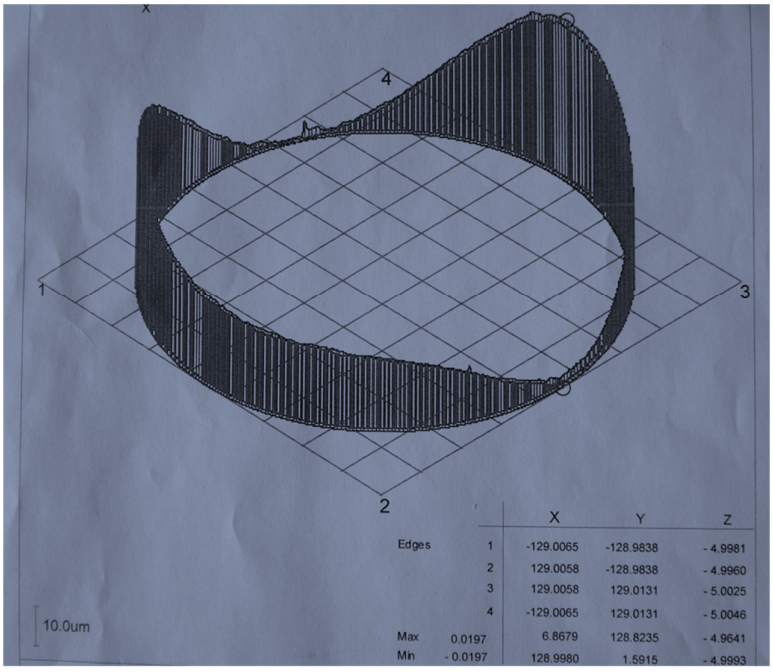

Fig..G.1. Surface scan of the HV electrode taken by the RAL metrology department.

The surface scan was taken at one radius inside the groove of the HV electrode. It clearly shows the depth of the groove changing circumferentially, by as much as ~ 50 µm. It is probably that this feature was caused during the machining process. The electrode was clapped at two opposite sides. This would have put tension on the material while it was being machined. When the clamps were released the material would relax and produce this profile. This profile can now be used to do an accurate E-field calculation.

Appendix G E-Field models of the Ramsey Cell

The Ramsey Cell, Fig.G.2, was modelled using Opera vector fields. The only parts relevant for this E-field calculation were the HV electrode, the middle ground electrode, the ceramic and liquid helium. The Opera model, Fig.G.3, shows the HV electrode (Purple), the middle ground electrode (blue), the ceramic (green) and helium (lime).

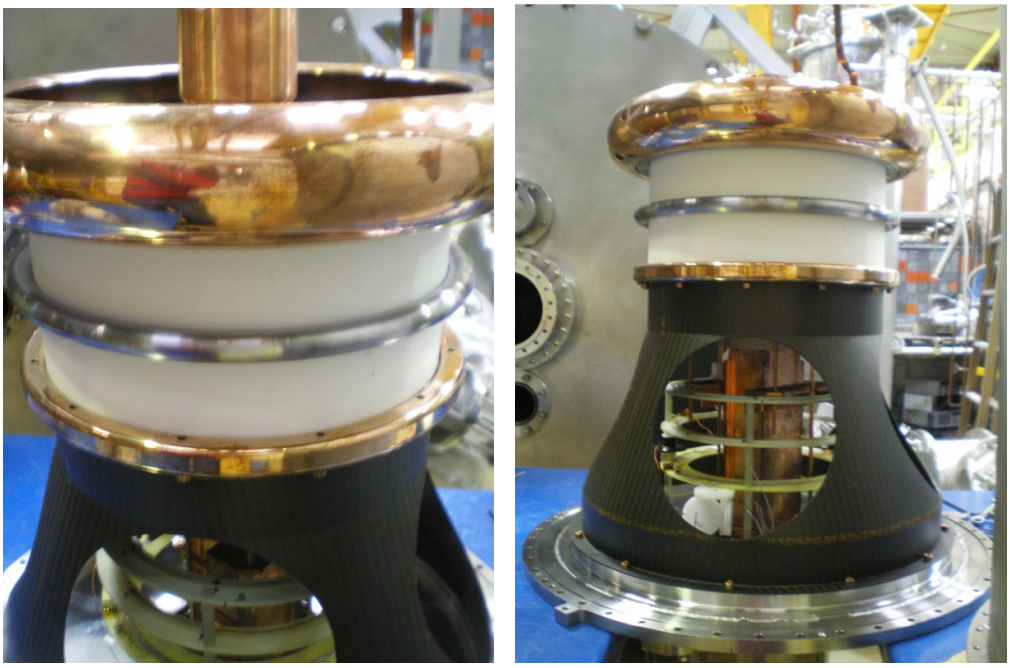

Fig..G.2. Photograph of the Ramsey Cell.

In order to calculate the effect of the gap is was decided the best way to do this was to vary the separation between the ceramic and the HV electrode groove. The ceramic was moved from a separation of 0 to 50 µm in steps of 10 µm to see how the E-field changed inside the gap. A voltage of 100 kV was applied across the Ramsey Cell for all models. Figure G.4 shows the potential map when 100 kV is applied across the electrodes.

It is clear from the E-field models that if a gap is created between the ceramic and the HV electrode the highest field is found in the gap, Fig. G.5. In order to find out the extent of

the E-field in the gap as a function of separation calculations were carried out a various separations. The results are plotted on Fig. G.6.

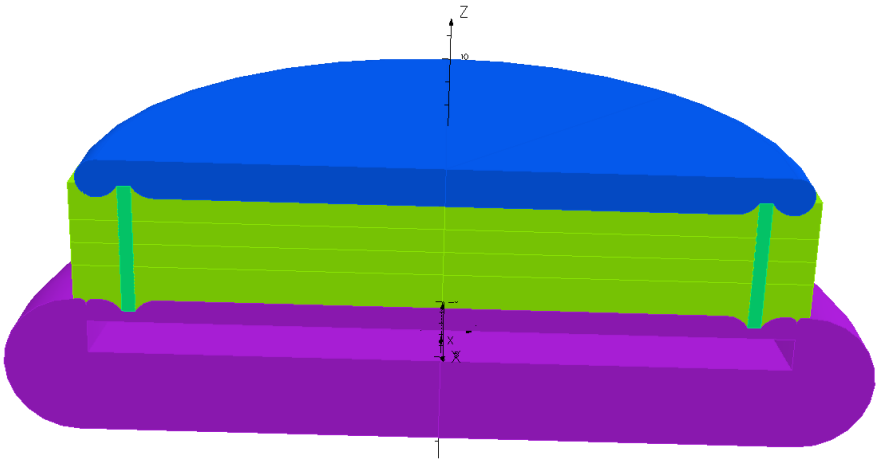

Fig..G.3. Opera model of the Ramsey cell.

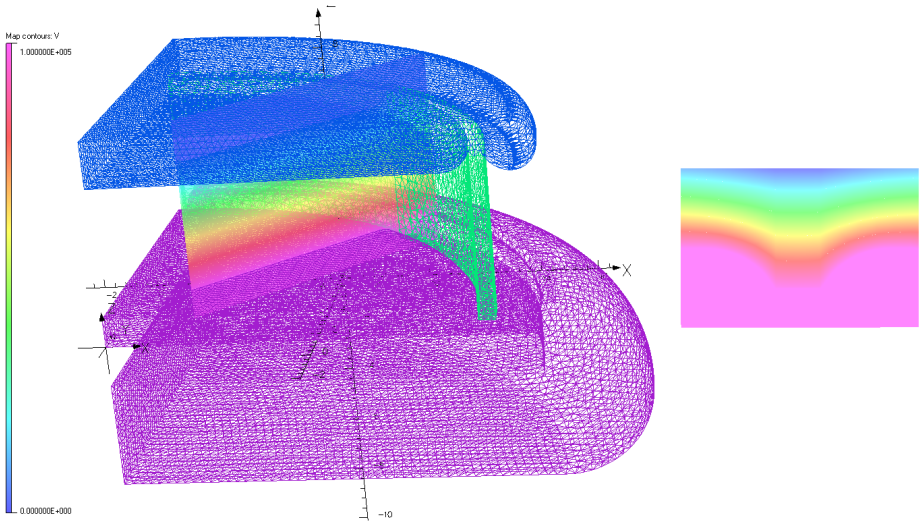

Fig..G.4. Opera Vector Field model of the Ramsey Cell. 100 kV across the electrodes. Left: section through the Ramsey Cell; Right: Voltage potential profile of the groove.

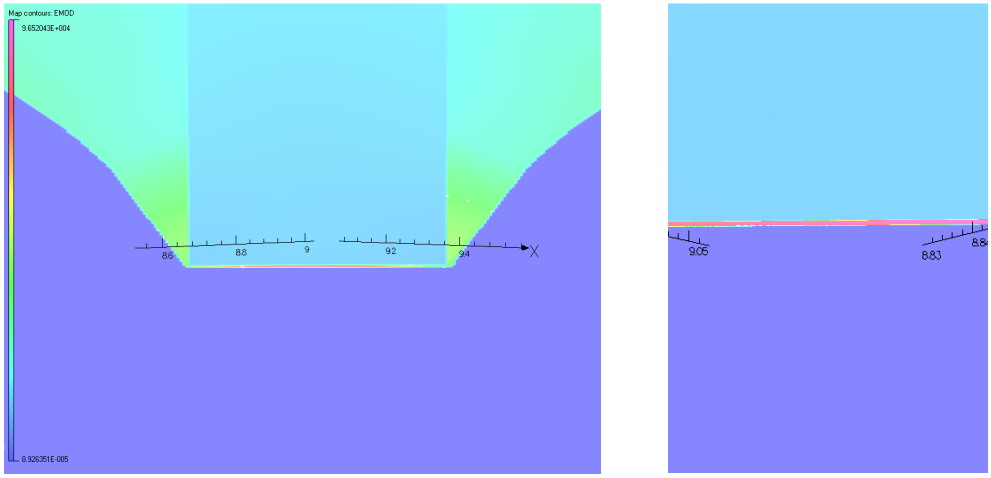

Fig..G.5. Opera Vector Field model of the Ramsey Cell. 100 kV across the electrodes. Left: E-field map of the groove and gap between electrode and ceramic; Right: E-field map of the gap between the ceramic and the HV electrode surface.

Any gap up to a separation of 50 µm produces an E-field which is approximately the same. When 100 kV is applied across the Ramsey cell any gap between the ceramic and the HV electrode will create an E-field of ~ 100 $kVcm^{-1}$. This is a lot higher than the E-field across the Ramsey cell which will only be 22 $kVcm^{-1}$, a factor of ~ 4.5 higher.

This analysis shows that any gap between the ceramic and the HV electrode of the Ramsey cell will produce a very high E-field in the gap. This might suggest that the HV and therefore E-field will be limited as the high E-fields in the gap may cause catastrophic breakdown at lower applied voltages.

In summary, the Ramsey cell high voltage electrode groove profile has been scanned by the RAL metrology department. A fluctuation in height of ~ 50 µm has been observed. The fluctuation occurs circumferentially and is probably a result of the machining process.

The E-field created in the gap between the Ramsey cell high voltage electrode and ceramic have been calculated using Opera vector fields. Any gap in the range 0 to 50 µm will produce an E-field of ~ 100 $kVcm^{-1}$ when a voltage of 100 kV is applied across the Ramsey cell.

Appendix G E-Field models of the Ramsey Cell

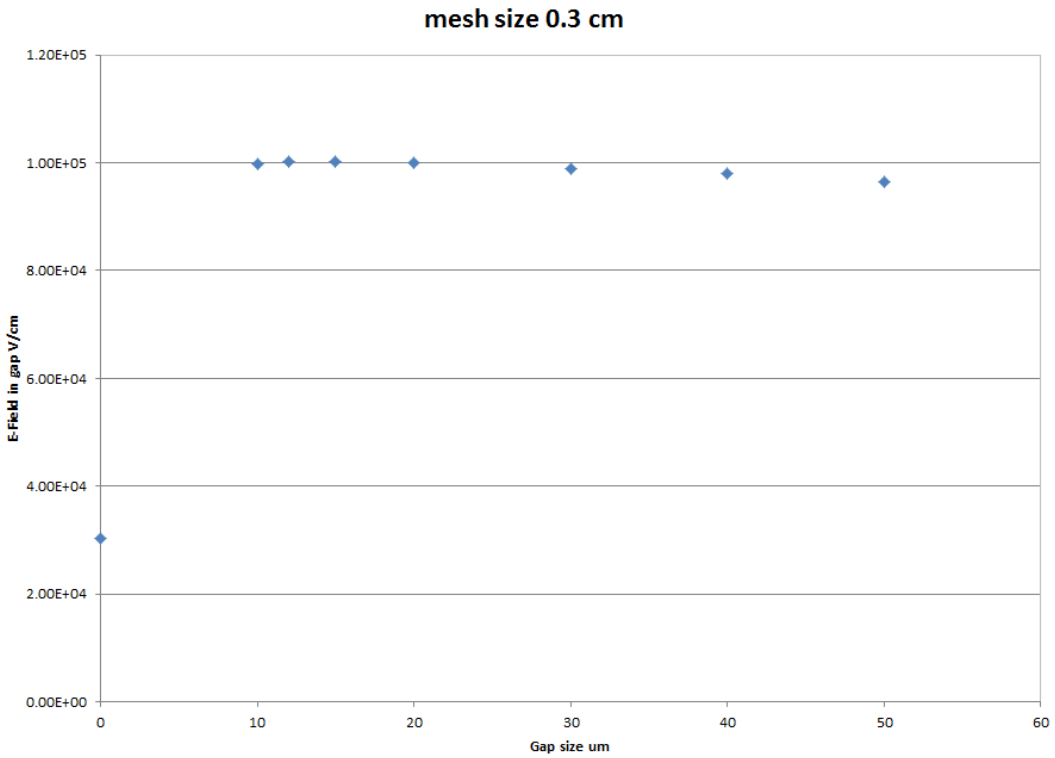

Fig..G.6. E-field versus Gap size between ceramic and HV electrode of the Ramsey cell when 100 kV is applied across the electrodes.

References

Abe H et al 2008 Journal of Fluid Mechanics **619** 261-275

Atkins K R 1959 Liquid Helium Cambridge: Cambridge University Press

Baker C A et al 2003 Nucl Instrum Methods Phys Res A **501** 2/3 517-523

Baker C A et al 2006 Phys Rev Lett **9**13 131801

Baker C A et al 2009 Proceedings of Science EPS-HEP 376

Baker C A et al 2010 Journal of Physics Conference Series **251** 1

Battaglia M et al 2003 arXiv.org hep-ph arXiv:hep-ph/0304132v2 The CKM Matrix and the Unitarity Triangle

Beroual A et al 1998 IEEE Electrical Insulation Magazine **14** 2 6-17

Blank C and Edwards M H 1960 Physical Review **119** 1 50-53

Brennen C E 1995 Cavitation and Bubble Dynamics: Oxford University Press

Buras A J 2002 arXiv:hep/021 0291 v1 The Unitarity Triangle: 2002 And Beyond

Burcham W E and Jobes M 1995 Longman Nuclear and Particle Physics

Burnier P H et al 1970 Advances in Cryogenic engineering **15** 76-84

Butcher M et al 1999a 12th IEEE International Pulsed Power Conference **1** 450-453

Butcher M et al 1999b 1999 Annual Report Conference on Electrical Insulation and Dielectric Phenomena **2** 654-657

Butcher M et al 2006 IEEE Transaction on Plasma Science **34** 2 467-475

Cabibbo N 1963 Phys Rev Lett **10** 12 531-533

Cevallos M et al 2005a IEEE Pulsed Power Conference 1235-1238

Cevallos M et al 2005b IEEE Transactions on Plasma Science **33** 2 494-495

Chadwick J 1932 PRSL **A136** 692

Chigusa S et al 1998 IEEE International Symposium on Electrical Insulation **1**198-199

Chigusa S et al 1999 IEEE Transactions on Dielectrics and Electrical Insulation **6** 3 385-392

Chigusa S et al 2000 IEEE Transactions on Dielectrics and Electrical Insulation **7** 2 290-295

References

Christenson J H et al 1964 Phys Rev Lett **13** 4 138-140

Colletti G et al 1982 Journal of Electrostatics **12** 297-304

Das A and Ferbel T 1994 Wiley Introduction to Nuclear and Particle Physics

Davidson A J 2009 cryoEDM Collaboration meeting Presentation Applying HV across the Ramsey cell. Summary of HV Tests and characteristics of installed Spellman HV Apparatus.

Davidson A J 2011 cryoEDM Collaboration meeting Presentation HV Report May 2011.

Denat, A, 2011, in Proceedings of IEEE International Conference on Dielectric Liquids (IEEE).

Donnelly R J and Barenghi C F 1998 Journal of Physics and Chemical Reference Data **27** 6 1217-1274

Donoghue J F et al 1992 Dynamics of the Standard Model Cambridge University Press

Ellis T and Mc Clintock P V E 1982 Physical Review Letters **48** 26 1834-1837

Fallou B et al 1970 Cryogenics **10** 2 142-146

Fermi E 1936 Ricerca Scientifica **7** 13-52

Fertl M et al 2009 to be published Presentation from 7th International workshop "Ultra Cold & Cold Neutrons Physics & Sources" Saint-Petersburg Russia 8-14 June

Frayssines P E et al 2003 IEEE Transactions on Dielectrics and Electrical Insulation **10** 6 970-976

Garton C G and Krasucki Z 1964 Proc. R. Soc. A **280** 211-226

Glashow S L et al 1970 APS Journals Phys Rev D **2** 7 1285-1292

Gerhold 1972 Cryogenics **12** 5 377-384

Gerhold 1979 Cryogenics **19**10 571-584

Gerhold J 1988 IEEE Transactions on Electrical Insulation **23** 4 765-768

Gerhold J 1989 IEEE Transactions on Electrical Insulation **24** 2 155-166

References

Gerhold J 1991 IEEE Transactions on Electrical Insulation **26** 4 679-684

Gerhold J 1994 IEEE Transactions on Dielectrics and Electrical Insulation **1** 3 432-439

Gerhold J 1998a Hand book of Applied Superconductivity **2** 639-655

Gerhold J 1998b Cryogenics **38** 11 1063-1081

Giansiracusa J 2003 http://maths.swan.ac.uk/staff/jhg/papers/ccft.pdf Looking back at the discovery of the first CP Violation.

Golub R and Pendlebury J M 1977 Physics letters **62A** 5 337-339

Golub R and Pebdlebury J M 1979 Rep Prog Phys **42** 3 439-501

Grozier J 2007 DPhil Thesis University of Sussex The Cryogenic Neutron Electric Dipole Moment Experiments: Magnetic Challenges and Solutions.

Halpern B and Gomer R 1969a The Journal of Chemical Physics **51** 3 1031-1047

Halpern B and Gomer R 1969b The Journal of Chemical Physics **51** 3 1048-1056

Hara M et al 1987 Cryogenics **27** 2 93-101

Hara M et al 1993 Proceedings 8th International symposium on High Voltage Engineering Yokohama, Japan **2** 559-562

Hara M 2008 Proceeding of the 2008 International Symposium on Electrical Insulating Materials 1-9

Harris P 2007 arXiv.org hep-ex arXiv:0709.3100 The Neutron EDM Experiment

Harvard Division of Nuclear Physics www.aps.org/units/dnp/research/harvarducn.cfm

Hayakawa N et al 1997 IEEE Transactions on Dielectrics and Electrical Insulation **4** 1 127-134

Hickson A and McClintock P V E 1971 Physics letters A **34** 7 424-425

Hill D K 2009 MPhys thesis University of Sussex High Voltage Breakdown across Solid Dielectrics in Cryogenic Liquids.

Hills R N and Roberts P H 1971 IMA Journal of Applied Mathematics **9** 1 56-67

References

Hong et al 2003 International Conference on Electrical Insulation and Dielectric Phenomena (CEIDP) IEEE publication number 03CH37471 313-316

Huffer C R 2008 BSc thesis Indiana University Studies of High Voltage Breakdown in Superfluid Helium and SQUID Noise: a R&D Effort to Support the Neutron Electric Dipole Moment Experiment at SNS.

Hwang K F 1978 Adv. Cryo. Eng. **23** 110-117

Karamath J R 2007 PhD thesis University of Sussex He-II under High Electric Field Conditions for the Cryogenic Neutron Electric Dipole Moment Experiment.

Katsika A 2011 PhD thesis University of Sussex Magnetic Aspects of the CryonEDM experiment

Kattan R et al 1989 Journal of Applied Physics **66** 9 4062-4066

Kattan R et al 1991 IEEE Transactions on Electrical Insulation **26** 4 656-662

Kobayashi M and Maskawa T 1973 Prog Theor Phys. **49** 2 652-657

Kok et al 1962 Applied Scientific Research Section B **10** 3-4 257-268

Korobkina et al 2002 Physics letters A **301** 5/6 462-469

Landau L 1941 Phys.Rev. **60** 356-358

Latham R V 1995 Academic Press Inc High Voltage Vacuum Insulation: Basic Concepts and Technological Practice 27

Lavrakas V 1952 Journal of Chemical Education **29** 6 281-283

Lee T D and Yang C N 1956 Phys Rev **104** 1 254-258

Li, Z-L et al 2009 Eur. J. Appl. Phys. **47** 2 1-7.

Liu C Y 2009 Private communication Fundamental Neutron Summer School

Long J C et al 2006 arXiv.org physics arXiv: physics / 0603231v1 High Voltage Test Apparatus for a Neutron EDM Experiment and Lower Limit on the Dielectric Strength of Liquid Helium at Large Volumes

References

Lux J 1998 http://home.earthlink.net/~jimlux/hv/rogowski.htm

Maris H J 2008 Journal of the Physical Society of Japan **77** 11

May D and Krauth H 1981 IEEE Transactions on Magnetics **MAG-17** 5 2089-2092

McClintock P V E 1969 Physics Letters A **29** 8 453-454

McClintock P V E 1971 Physics Letters A **35** 3 211-212

McClintock P V E 1973a Physics Letters A **43** 3 257-258

McClintock P V E 1973b Journal of Physics C: Solid State Physics **6** L186

McCluskey F M J and Denat A 1996 J. Appl. Phys **80** 4 2049-2059

MDC 2010 http://www.mdcvacuum.com/index.aspx 20,000 to 30,000 Volts / 1 Amp / 1 Pin –Del Seal CF Part no. 9442001

Meats R J 1972 PROC. IEE, **119** 6 760-766

Migliori R et al 1978 Cryogenics **18** 7 443-445

Miller C 1989 IEEE Transactions on Electrical Insulation **24** 5 765-786

More T and Johnson K 1998 Cryogenics **38** 9 947-948

Morris J 2002 Review in Undergraduate Research **1** 38-43

Munday L 2010 MPhys thesis University of Sussex Microscopic Investigation of Surface Damage after High Voltage Breakdown in Cryogenic Liquids.

Nakamura K et al 2010 Particle Data Group Journal of Physics G **37** 075021

Ness R M 2008 http://www.nessengr.com/techdata/rogowski/rogowski.html

Niemela J J and Donnelly R J 1995 Journal of Low Temperature Physics **98** 1/2 1-16

Neuber A et al 1999 Journal of Applied Physics **85** 6 3084-3091

Oliver C 1981 IEEE Transactions on Magnetics **MAG-17** 5 2086-2088

Opera v10 Vector fields Opera 3d v10 Vector Fields limited www.vectorfields.com

www.cobham.com/about-cobham/aerospace-and-security/about-us/antenna systems/kidlington.aspx

References

Ostermeier R M 1973 Phys. Rev. A **8** 514-529

Pendlebury J M 1993 Annu Rev Nucl Part Sci **43** 687-727

Perepelitsa D V 2008 Columbia University Department of Physics Sakharov Conditions for Baryogenesis

Phillips A and McClintock P V E 1974 Philosophical Transactions of the Royal Society of London. Series A, Mathematical and Physical Sciences **278** 1281

Poitrenaud J and Williams F I B 1972 Phys. Rev. Lett. **29** 18 1230-1232

Pospeloy M Ritz A 2005 Annals Phys **318** 1 119-169

Ramsey N F 1956 Molecular beams. Oxford University Press

Ramsey N F 1982 Rep. Prog. Phys., **45** 1 95-113

Rayleigh Lord 1917 Philosophical Magazine Series 6 **34** 200 94-98

Rogowski W 1923 Arch f Elekt **12** p 1

Rogowski W 1926a Arch f Elekt **16** p 73

Rogowski W 1926b Arch f Elekt **16** p 76

Rutherford E 1920 Proc Roy Soc **A97** 374

Sakharov A D 1967 Journal of Experimental and Theoretical Physics Letter **5** 24

Schwarz K W 1972 Physical Review A **6** 2 837-844

Schmidt W F 1982 IEEE Transactions on Electrical Insulation **EI-17** 6 478-483

Schmidt W F and Illenberger E 2002 IEEE Proceedings of 14th International Conference on Dielectric Liquids Graz (Austria) July 7-12 159-162

Schmidt W F and Illenberger E 2003 IEEE Transactions on Dielectrics and Electrical Insulation **10** 6 1012-1021

Schools http://schools-wikipedia.org/images/177/17777.png.htm

Sinclair J R 2010 MSc thesis University of Sussex Simulations of Ultra cold neutron

Smith J H et al 1957 Phys Rev **108** 1 120-122

References

Spellman SL10W Part Number SL130PN10/10002 Model SL130PN10/FGLL/230 High Voltage Power Supply Spellman High Voltage Electronics Corporation.

STFC 2009 Precision Experiments: Neutron Lifetime Experiments www.stfc.ac.uk/PPD/resources/.../yr09_lecture13_grinten.ppt

Suttle L G 2010 MPhys thesis University of Sussex High Voltage Breakdown Studies for the Cryogenic nEDM experiment.

Townsley C M 2008 HV Connector 22-4 Connector Insert Drawing No. 00430

Weber K H and Endicott H S 1956 AIEE Transactions of the American Institute of Electrical Engineers **75** 3 371-381

Wilks J and Betts D S 1987 An Introduction to Liquid Helium Second Edition (Oxford: Oxford University Press)

WMAP 2010 Wilkinson Microwave Anisotropy Probe http://map.gsfc.nasa.gov/index.html

Wolfenstein L 1983 Phys Rev Lett **51** 21 1945-1947

Wu et al 1957 PROLA Phys. Rev. **105** 4 1413-1415

Wu J L and Roach J F 1992 Supercollider 4 Plenum Press New York 731-738

Wu J L 1996 Advances in Cryogenic Engineering **41** 1843-1850

Yamamoto O and Takuma T 2000 Electrical Engineering in Japan **131** 3 1-8

Yoshino K et al 1979 Journal of Electrostatics **7** 103-112

Yoshino K et al 1982 Journal of Electrostatics **12** 305-314

Yoshino K et al 1985 IEEE Transactions on Electrical Insulation **EI-20** 2 327-332

Zimmerman P H et al 1976 Physical Review B **15** 5 2630-2650